Searching for Deviations from the Standard Model in Top Decays and Prompt $e^{\pm}\mu^{\mp}$ Events with the ATLAS Experiment

Nikhul Dev Patel

THE UNIVERSITY OF
SYDNEY

A thesis submitted in fulfilment of the requirements
for the degree of Doctor of Philosophy
August 2014
School of Physics, Faculty of Science, University of Sydney

Preface & Statement of Contribution

The ATLAS Collaboration at the LHC comprises over 3,000 physicists organised into groups and sub-groups that undertake specific physics or detector performance analyses, as well as run ATLAS detector operations. Due to the scale and complexity of any given analysis at ATLAS it is necessary to collaborate closely — distributing parts of an analysis to individuals involved in the relevant sub-group, and drawing on the relevant expertise of other groups within ATLAS, in order to bring all the work together as a whole for publication. This thesis presents the author's own contributions to the presented analyses, and as such focuses on the aspects of these analyses undertaken by the author over the course of the PhD. Contributions from others are cited in the main text as they arise, and any figures or tables that are the work of others are cited in the corresponding captions. Any Monte Carlo simulated data used in the studies presented here are provided by the ATLAS MC production group unless explicitly stated in the main text.

In this thesis, the necessary theoretical background and experimental details are provided in Chapters 2 and 3 respectively.

Chapter 4 comprises a study conducted by the author for the ATLAS SemiConductor Tracker (SCT) group in 2009 [1], on the potential for damage to the ATLAS silicon micro-strip tracker in the case of LHC beamloss in the vicinity of the ATLAS detector. This study was partially motivated by the LHC accident in September 2008, whereby serious damage was done to the collider, requiring over a year of repairs. The GEANT4 simulated events used in the study (described in Section 4.3) were provided by the SCT group, while the study itself (Sections 4.4, 4.5 and 4.6) was conducted by the author.

Chapter 5 covers the light charged Higgs search that took place towards the end of 2010 and throughout 2011, while the author was a member of the ATLAS charged Higgs group [2, 3]. Motivation for the light charged Higgs search is provided by predictions from theoretical models containing two Higgs doublets (outlined in Section 5.1), with the limits set by previous experimental charged Higgs searches discussed in Section 5.2. The two ATLAS $H^+ \to \tau_{\text{had}}\nu$ analyses are presented in Sections 5.3 and 5.5, as the collective work of the two $H^+ \to \tau_{\text{had}}\nu$ analysis teams. As all group members must necessarily converge on the object and event selections (outlined in Section 5.3) in order to perform the required studies on backgrounds and sources of systematic uncertainty consistently, software to implement these selections in data and MC was written by the author. However, the selections themselves were largely optimised and set for the analysis of 2010 data, in which the author was not involved. The rest of the chapter focuses on the specific contributions of the author on behalf of the analyses on 2011 data. Section 5.4, consists of an attempt by the author to identify a discriminating variable to separate a potential H^+ signal from the major Standard Model backgrounds in order to improve the sensitivity of the analyses. The charged Higgs signal events used in this study were generated by the author using PYTHIA and the ATLAS ATHENA framework. As no strongly discriminating variable could be identified, attention turns to the effects of systematic uncertainties on the modelling of the major SM background. The focus is therefore shifted in Section 5.6 to a study conducted by the author into the uncertainty in analysis acceptance arising from the Monte Carlo used to model the major SM background process. Another important systematic effect that must be considered is the rate at which electrons are mis-identified as hadronically decaying taus. This mis-identification probability is estimated by the Tau working group using $Z \to ee$ events in data, and Section 5.7 consists of a study conducted by the author into whether the use of scale factors based on this mis-identification probability can be justified when the electrons in question are produced via $t\bar{t}$ events (which will have different kinematics in general). The exclusion limits on the existence of a light charged Higgs, set by the $H^+ \to \tau\nu$ analyses, conclude the chapter in Section 5.8.

Over 2012 and the first half of 2013 the opportunity arose to join the AIDA group, working within both the ATLAS top group and ATLAS Standard Model group. AIDA is An Inclusive Dilepton Analysis that provides a simultaneous measurement of the $Z/\gamma^* \to \tau\tau$, $t\bar{t}$ and WW production cross sections, as well a more global test of the Standard Model[4]. Section 6.1 presents the AIDA method for measuring the $Z/\gamma^* \to \tau\tau$, $t\bar{t}$ and WW production cross sections — these cross section measurements are the collective work of groups at Duke, Sydney and Melbourne, where the author has been part of the Sydney effort. The codebase for the AIDA cross section measurements at ATLAS consists of object/event selection, template production, fitting and shape systematic evaluation — the majority of this was written by Kevin Finelli and Antonio

Limosani, and utilised by the author with some modifications in Sections 6.1 and 6.2. Section 6.2 outlines the author's initial attempt at testing the goodness-of-fit between data and the SM expectation within the context of AIDA, and the fitting procedure for the cross section analysis is partially reproduced here. The remainder of the chapter — Sections 6.3 and 6.4 — present work conducted by the author towards improvements in the evaluation of the goodness-of-fit using code written by the author, utilising templates sets generated for the AIDA cross section analysis that were not produced by the author.

Acknowledgements

I would like to thank my supervisors Kevin Varvell and Aldo Saavedra for their guidance over the *many* years I've been a student — all the way back to undergraduate particle physics lectures and projects, through to being given the opportunity to work on the first data from the LHC. Thank you to Mark, Ian, Cameron, and Curtis for the thousands of coffees/lunches/drinks and occasional physics discussions that provided some escape from the crushing fear and self-doubt, and to everyone else in the Sydney High Energy group for providing such a supportive working environment.

I am grateful to Dave Robinson, for making sure I didn't break the SCT; and to Martin Flechl, for his perspective and understanding during a stressful time. Thanks also go to Tony Limosani, Anna Phan and Martin White for introducing me to life at CERN; Charlie Isaksson, for a particular conversation about life and expectations; and Valentina, Lewis, Serena, Tom and Shervin for the best times I've ever had at a golfing resort.

Finally, I would like to thank my brother for employing me when I was broke, and express my profound gratitude to my parents for their unconditional support throughout this PhD — particularly towards the end where this support was the difference between finishing and not.

Contents

"Human knowledge had become too great for the human mind. All that remained was the scientific specialist, who knew 'more and more about less and less,' and the philosophical speculator, who knew less and less about more and more. The specialist put on blinders in order to shut out from his vision all the world but one little spot, to which he glued his nose. Perspective was lost. 'Facts' replaced understanding; and knowledge, split into a thousand isolated fragments, no longer generated wisdom. Every science, and every branch of philosophy, developed a technical terminology intelligible only to its exclusive devotees; as men learned more about the world, they found themselves ever less capable of expressing to their educated fellow-men what it was that they had learned."

— Will Durant (The Story of Philosophy)

Chapter 1.

Introduction

Our notions of matter, forces and energy are bound up as the core of current understanding about the wider universe, and this understanding comes from embedding these ideas in self-consistent mathematical models that represent (we hope) an objective reality that exists independently of ourselves. Testable theories, that can be expanded to fold in ever more observations, bring us closer to forming an accurate picture of the universe in so far as it is possible for us to perceive it. The ultimate goal of physics in the early 21st century is the reconciliation of our current models of particle physics and cosmology. In order to reach such a goal we attempt to move beyond our current understanding by searching for new phenomena outside the scope of current models, as well as searching for deviations from the models' description of known phenomena. Particle physics is at the stage today where the large quantities of new experimental data are likely to provide hints for how to proceed theoretically.

To date, all known fundamental particles and their interactions are incorporated into the Standard Model of particle physics (SM). The existence of Dark Matter (which only interacts gravitationally) as inferred from astronomical observations, as well as the the existence of neutrino masses inferred from their mixing in flight, are the main pieces of experimental evidence so far at odds with the Standard Model (Chapter 2). Producing a Dark Matter candidate "in the lab" (inferred from missing momentum in particle collisions) is therefore one of the major remaining tasks for the Large Hadron Collider (LHC).

The LHC at the European Organisation for Nuclear Research (CERN) today sits at the energy frontier of particle physics, and its detectors began taking physics data from proton-proton collisions at a 7 TeV centre of momentum energy in 2010. As any hints of such new physics will first show up as an inconsistency between the data observed and the expectation predicted by the SM, it is important to take full advantage of the unprecedented collision energies at which the LHC operates to explore as many physics processes as possible (Chapter 3). The physics studies able to be conducted are completely dependent on the quality of the data collected by the ATLAS detector, and in such a complex experiment the detector hardware, operation, performance, data quality, and the physics analysis cannot be separated from one another. This thesis presents a study, conducted before data taking began, into the possible vulnerability of the ATLAS SemiConductor Tracker to a potential LHC beamloss accident (Chapter 4). In order to advance the physics goals of the LHC, this thesis will focus on a search for physics beyond the SM in top quark decay (Chapter 5), as well as testing the consistency of the SM using events containing an oppositely charged electron and muon (Chapter 6), in data collected by the ATLAS detector.

Chapter 2.

Theoretical Background and Motivation

The Standard Model of Particle Physics is currently our best description of the fundamental constituents of matter and their interactions via the strong, weak and electromagnetic forces. This chapter provides an overview of the necessary theoretical background and overarching motivations for the work described in this thesis as well as the majority of the physics program at the Large Hadron Collider. Section 2.1 attempts to place the Standard Model (SM) of particle physics in context with respect to the rest of fundamental physics with a brief description of the model provided in Section 2.2. Finally, Section 2.3, covers the shortcomings of the SM which act as broad motivation for Chapters 5 and 6 that detail investigations in to physics beyond the SM, and SM consistency, using ATLAS data.

It should be noted that natural units, $c = \hbar = 1$, will be used from this point onwards when discussing particle physics, while SI units will be used to describe macroscopic objects, such as those in the experimental setup — the convention used should be clear from the context, but where it is not it will be made explicit. The Einstein summation convention is assumed, with Greek indices used for Minkowski spacetime, and Roman indices for Euclidean dimensions, i.e.

$$\begin{aligned} A_\mu A^\mu &\equiv \eta_{\mu\nu} A^\mu A^\nu \equiv A_0^2 - A_1^2 - A_2^2 - A_3^2 \quad , \\ A_i A^i &\equiv \delta_{ij} A^i A^j \equiv A_1^2 + \cdots + A_n^2 \quad . \end{aligned}$$

2.1. What is the Lagrangian of Nature?

If we consider some object travelling from a point A to a point B, there are some very general steps that can be used to work out the dynamics of such a system — in this case the path the object might traverse between the two points. These steps are as follows:

1. Determine the Lagrangian, L, that incorporates everything that is known about the physics of the system.
2. Define the action, S, as an integral over this Lagrangian, this is then associated with *how* the object gets from A to B.
3. Associate quantities corresponding to the extremum of S with the most likely dynamics of the system.

This simple case however is not well defined as the physics one needs to consider varies wildly depending on the scale and energy of this "object".

2.1.1. Scale and Energy Regimes

In physics to date there are generally four regimes that we consider in terms of the size and energy of the system under consideration (see Figure 2.1). The case of an object moving from a point A to B is vague because the interpretation, concepts and definitions used to describe such a scenario change depending on the regime we are in. The four regimes are conceptually very different, however, the analysis of each case is based on the common framework listed above.

The regime first considered was that of large low energy mechanical systems, as these are at the scales and energies that we can directly perceive through our senses. The Lagrangian reformulation of Classical Mechanics (CM) to describe the behaviour of such systems was developed over the late 18th century by Lagrange and Euler, almost one hundred years after Newtonian mechanics. The wildly different behaviour of large scale high energy systems and small scale low energy systems were discovered and formalised independently at the beginning of the 20th century as General Relativity (GR) and Quantum Mechanics (QM) respectively. The Lagrangian formalism was carried over to these regimes, and proved remarkably capable of incorporating the new physics. This required huge conceptual shifts in terms of the physics incorporated into the Lagrangian (in the case of GR) or the interpretation of the action (in the case of QM) but the

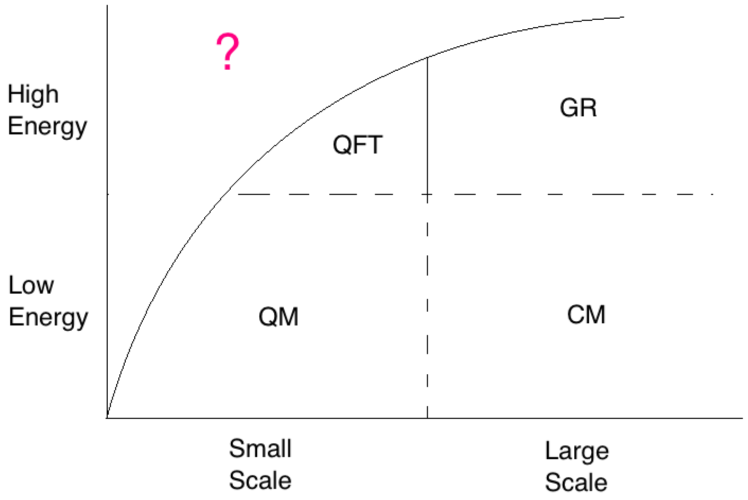

Figure 2.1.: Scale and energy regimes in the physical world and the corresponding physical theories used to understand and calculate the dynamics of systems in them: Classical Mechanics (CM); General Relativity (GR); Quantum Mechanics (QM); and Quantum Field Theory (QFT).

fundamental procedure remained the same. In the regime where relativistic effects become important in defining the motion (of a macroscopic object), time and space can no longer be treated separately and the object's motion relative to the observer as well as the particular geometry of spacetime must be considered. The notions of kinetic and potential energy in relation to gravitation are not so useful in GR as kinetic energy is relative, while gravitational potential energy becomes geometry. Thus, if no other forces are acting the object follows a geodesic path through spacetime — the structure of which, is encoded in the metric tensor. Whereas in QM there is no longer a single solution to the equations of motion defining the path of the object as every possible path will have some probability of being traversed, with the amplitude for any particular path $\propto e^{iS[\text{path}]}$. Thus the action must be considered over all possible paths, with the path that minimises the action simply being the most probable, with other paths also possible.

Quantum Field Theory was developed over the course of the 20th century in order to combine QM and Special Relativity (SR), to move some way to covering the fourth small scale and high energy regime which is relatively difficult to access experimentally. It formulates the Lagrangian in terms of fields defined over all of (flat) spacetime, as opposed to discrete objects at points in spacetime. The "object" is now considered to be an excitation of a field and therefore the sum over all paths to calculate an amplitude in QM becomes a sum over all possible field configurations that result in the excitation existing at point A and point B in spacetime. With

$$S[\phi] = \int \mathcal{L}\left(\phi(x), \partial_\mu \phi(x)\right) \, d^4x \quad ,$$

where $\mathcal{L}$ is the Lagrangian density at a spacetime point, x, defined in terms of the field, $\phi(x)$, and its spacetime derivatives. The equations of motion for a particle are expressed as quantised field equations and largely sever the connection to the idea of an object moving between two points.

2.1.2. Symmetries

An important relationship that emerges from the formulation of physics in terms of an action principle is the linking of certain symmetries to physically observed conservation laws, indicated by degrees of freedom in choosing the Lagrangian. Proved by Emmy Noether in 1918 [5], Noether's theorem states that any differentiable symmetry of the action defines a corresponding conservation law. For example, in Special Relativity (SR), the invariance of the action under rotations, translations, or Lorentz boosts can be expressed as Poincaré transformations and correspond to the conservation of 4-momentum, the three components of angular momentum, and the three components of the velocity of the centre of mass. The Poincaré symmetry is postulated for all relativistic quantum field theories in order to incorporate these conserved quantities, and as a result, whether the fields are scalar fields, spinor fields, vector fields, or tensor fields determines how they transform under the group. Thus, 'spin' is a fundamental property of a field in a relativistic QFT and what we generally consider to be a particle is just an irreducible unitary representation of the Poincaré group. Another fundamental symmetry that applies to all relativistic QFTs is invariance under the CPT transformation, which is a discrete symmetry involving: the inversion of all charges (C) such that particles become anti-particles; as well as time (T) reversal and parity (P) inversion, $(x^0, x^1, x^2, x^3) \rightarrow (-x^0, -x^1, -x^2, -x^3)$. Although CPT invariance is a fundamental property of relativistic QFTs [6], it has been experimentally observed that P is violated [7], as is CP [8].

A gauge theory is a type of relativistic QFT from which our current models of particle physics are built, in which the Lagrangian is invariant under a continuous group (Lie group) of *local* transformations occurring at a given spacetime point in addition to the global Poincaré and CPT symmetries. These additional local symmetries are incorporated by requiring that the fields form a representation of the symmetry group of the theory. Though Noether's theorem still requires that invariance under some transformation lead to a conserved current associated with a particular symmetry, the gauge transformations require an additional modification of the regular derivative operator, ∂_μ, to a gauge covariant derivative operator, D_μ, such that it retains the behaviour of a vector operator locally. The simplest example of such a gauge theory is Quantum Electrodynamics (QED), which describes the electromagnetic (EM) interaction between the 4-component spinor representation of the fermion field, $\psi(x)$, and the 4-vector gauge field of the theory, $A_\mu(x)$. The symmetry group of the theory is $U(1)$,[1] with elements of the group represented by points on the unit circle, which can be labeled by some phase at each spacetime point x. The Lagrangian is therefore invariant under local transformations of the fermion field of the form $\psi(x) \rightarrow e^{iQ\alpha(x)}\psi(x)$, which requires a corresponding transformation of the gauge field (the vector potential that defines the EM field) of the form $A_\mu \rightarrow A_\mu - Q\partial_\mu\alpha(x)/e$. The particular gauge boson[2] associated with the gauge field in this case is the photon and the Lagrangian for QED takes the form:

$$\mathcal{L}_{QED} = \bar{\psi}(i\gamma^\mu)(D_\mu)\psi - m\bar{\psi}\psi - \frac{1}{4}F_{\mu\nu}F^{\mu\nu} \quad , \tag{2.1}$$

where the Dirac spinor representation of the Lorentz symmetry is realised by the matrices, γ^μ, with $\bar{\psi} = \psi^\dagger\gamma^0$. The free photon field is described by $F_{\mu\nu}F^{\mu\nu}$[3] and $D_\mu = \partial_\mu + ieQA_\mu$ is the covariant derivative — ensuring the Lagrangian is invariant under local $U(1)$ transformations. The quantities Q and m represent the electric charge and mass of the fermion field respectively, with e the normalisation factor such that $Q = -1$ for the electron. The first term in the Lagrangian, $\bar{\psi}(i\gamma^\mu)(D_\mu)\psi$, represents a kinetic term for the fermion field and an interaction term between the fermion field and the gauge field that corresponds to the interaction vertex $f\bar{f}\gamma$. Though very successful for describing electrodynamics, QED is itself the result of a larger broken symmetry which unifies quantum electrodynamics with the weak interaction at higher energy scales as part of the Standard Model of particle physics which will be discussed next.

---

[1] One dimensional *unitary group*, the irreducible representation of which is the set of all 1×1 unitary matrices, $[e^{i\theta(x)}]$.

[2] It is a boson because the gauge field transforms as a vector under Lorentz transformations.

[3] Which can be written in terms of divergences of the vector potentials with $F_{\mu\nu} = \partial_\mu A_\nu - \partial_\nu A_\mu$.

2.2. The Standard Model of Particle Physics

The Standard Model (SM) is currently the most successful framework for describing nature at its most fundamental level, incorporating strong, weak and electromagnetic interactions between the known fundamental particles so far discovered. It describes the interactions observed experimentally between the fundamental fermions and bosons. The fermions fall into two categories depending on whether they interact via the strong force. The quarks: up (u), down (d), charm (c), strange (s), top (t), and bottom (b) — interact via the strong, weak and electromagnetic forces, and as a result of the strong interaction form bound states[4]. The leptons: electron (e), muon (μ), tau (τ), electron neutrino (ν_e), muon neutrino (ν_μ), and tau neutrino (ν_τ) — do not interact via the strong force. The SM itself is constructed as a non-abelian[5] quantum gauge field theory obeying certain symmetries, along with a built-in symmetry-breaking mechanism responsible for generating masses for the fundamental particles. The fundamental particles of the SM, then, are only 'fundamental' under a particular representation of one of the symmetry groups of the model. For example, the b quark mass eigenstate is not the same state that results from a weak interaction — the fundamental objects are the fields and the symmetries of the Lagrangian apply to these fields. The theory can be thought of as a combination of Yang-Mills theories,[6] generalising and extending QED to include the strong and weak interactions as well as self-interactions among the gauge fields that mediate the interactions. The particles of the SM can be thought of as excitations of superpositions of the fundamental fields that appear in the Lagrangian. The SM Lagrangian representing these fields and their interactions is invariant under transformations within the group $\mathbf{R}^{1,3} \rtimes$[7]$SO(1,3) \times SU(3)_C \times SU(2)_L \times U(1)_Y$ — which combines the global Poincaré symmetry (translations, $\mathbf{R}^{1,3}$, and rotations and boosts, $SO(1,3)$), colour symmetry ($SU(3)_C$), weak isospin and weak hypercharge symmetries ($SU(2)_L \times U(1)_Y$). By requiring invariance of the Lagrangian under these symmetry groups all the observed SM interactions can be derived. The 12 massless gauge fields involved in the interactions are listed in Table 2.1 along with the corresponding covariant derivative and form of the gauge transformation (represented as a unitary matrix) following the same steps as in QED. Where a labels the eight gluon fields, and b labels the three W fields. The six quark fields are denoted by q, and the six lepton fields by l

---

[4] The exception to this is the top quark which decays before such bound states can form.

[5] Group elements do not commute.

[6] Gauge theories based on a compact semi-simple Lie group, $SU(N)$ for example.

[7] Semi-direct product, rather than direct product as the translations subgroup is normal while the Lorentz group is not.

with their left- and right-handed helicity states denoted by L and R respectively. No right handed helicity states for the neutrinos have been observed. The coupling constants g and g' are related via the Weinberg angle: $\tan\theta_w = g'/g$. The Hermitian matrices λ^a (Gell-Mann matrices) and σ^b (Pauli matrices) are the generators of the non-abelian $SU(3)_C$ and $SU(2)_L$ respectively and Y is the generator of $U(1)_Y$. α_a, α_b and α here are continuous real parameters.

Gauge Group	Gauge Fields	Gauge Covariant Derivative	Unitary Transformation
$SU(3)_C$	G^a_μ	$\partial_\mu - \frac{i}{2}g_s\lambda^a G^a_\mu$	$e^{i\lambda^a\alpha_a(x)}$
$SU(2)_L$	W^b_μ	$\partial_\mu - \frac{i}{2}g\sigma^b W^b_\mu$	$e^{i\sigma^b\alpha_b(x)}$
$U(1)_Y$	B_μ	$\partial_\mu - \frac{i}{2}g'YB_\mu$	$e^{iY\alpha(x)}$

Table 2.1.: Gauge groups of the SM and the corresponding gauge fields and fermion fields with a non-trivial representation under these groups.

The overview of the SM provided here uses [9, 10] as primary references, and these should be consulted for further detail than can be provided here.

2.2.1. The Strong Interaction

The motivation for QCD came in an attempt to explain the observation of the $\Delta^{++}(uuu)$, a state that would be forbidden by the Pauli exclusion principle unless some additional degree of freedom for quarks existed [11]. This extra degree of freedom provides a “colour” charge for the quarks that binds them into colour neutral mesons ($q\bar{q}$) and bosons (qqq, $\bar{q}\bar{q}\bar{q}$) The strong interaction, or quantum chromodynamics (QCD) is formulated as a non-abelian gauge theory but is largely separate from the electroweak part of the SM and like QED, it represents an unbroken symmetry with massless gauge bosons (gluons) interacting with quark fields. All other fields that do not interact via the strong interaction have a *singlet* (trivial) representation under the symmetry group.[8] QCD is based on the $SU(3)$ gauge group represented by a linearly independent set of complex unitary 3×3 matrices with determinant zero (i.e. 3×3 Gell-Mann matrices, equivalent to the 2×2 Pauli matrices). There are 8 such matrices which form an *adjoint* representation of the gluon states and these states may operate on themselves (gluon self-interaction) or on triplet states of quarks, the so-called *fundamental* representation (smallest irreducible representation) whimsically labeled by three colours r, g, b. These states may be denoted

---

[8] The representation under the group is the set of 1×1 matrices that are the number 1.

by

$$\psi_q \equiv \begin{pmatrix} d_r \\ d_g \\ d_b \end{pmatrix}, \begin{pmatrix} u_r \\ u_g \\ u_b \end{pmatrix}, \begin{pmatrix} s_r \\ s_g \\ s_b \end{pmatrix}, \begin{pmatrix} c_r \\ c_g \\ c_b \end{pmatrix}, \begin{pmatrix} b_r \\ b_g \\ b_b \end{pmatrix}, \begin{pmatrix} t_r \\ t_g \\ t_b \end{pmatrix} . \tag{2.2}$$

The Lagrangian of QCD is very similar to that of QED (Equation 2.1), taking the familiar form:

$$\mathcal{L}_{QCD} = \overline{\psi}_q^{\,i}(i\gamma^\mu)(D_\mu)_{ij}\psi_q^{\,j} - \frac{1}{4}F^a_{\mu\nu}F^{a\mu\nu} \quad , \tag{2.3}$$

with the covariant derivative, $(D_\mu)_{ij}$, this time given by $\delta_{ij}\partial_\mu - \frac{i}{2}g_s\lambda^a_{ij}G^a_\mu$, and the free and self-interacting gluon field terms $F^a_{\mu\nu} = \partial_\mu G^a_\nu - \partial_\nu G^a_\mu - g_s f^a_{bc}G^b_\mu G^c_\nu$. The normalisation, g_s, is the strong coupling constant (which runs with energy) and λ^a are the traceless Hermitian Gell-Mann matrices. The structure constants f^{abc} are determined by the commutation relations between the Gell-Mann matrices which constitute the generators of the group, with $[\lambda_a, \lambda_b] = if^{abc}\lambda_c$. The indices i, j represent the three colour states $i, j = r, g, b$; while indices a, b, c label the gluon states, $a, b, c = 1, \ldots, 8$. As in QED there is also a gluon field term, $\frac{1}{4}F^a_{\mu\nu}F^{a\mu\nu}$, containing a free and self-interacting part. No mass term is included here as (unlike in QED) such a term would break local gauge invariance. Thus, mass terms for the fermions must be generated in a different way, to be discussed next as part of the electroweak theory.

An important property of QCD interactions that results from the strength of the coupling constant g_s is that of confinement. QCD is very similar to QED in terms of the structure of the Lagrangian but the strength of the interaction ensures that only colour neutral states are observed in nature, quarks and gluons are only considered free at high energies and the coupling strength runs down with energy (so called asymptotic freedom) — this is a crucial point in relation to hadron collider experiments — as it is only in this perturbative (small coupling constant regime) that cross section calculations for QCD interactions can be computed.

2.2.2. Electroweak Theory

In the 1960s and 1970s the electric interaction and weak interactions, which are responsible for radioactive decay, were unified into a single electroweak (EW) interaction at high energy ($\sim 100\,\text{GeV}$). This unified interaction is described by a non-abelian gauge theory based on the $SU(2) \times U(1)$ gauge group. The initial unification proposal by Glashow [12] and incorporation of an electroweak symmetry breaking mechanism by Weinberg [13] and Salam [14] led to the three sharing the 1979 Nobel prize with the discovery of the predicted massive W and Z bosons occurring at CERN in 1983[9] [16–19], also leading to a Nobel prize. The mechanism used to break the electroweak symmetry down to the electric and the weak forces as we observe them at lower energies was that devised also in the 1960s by Higgs [20]; Brout and Englert [21]; and Guralnik, Hagen and Kibble [22], subsequently referred to as the Higgs mechanism and resulting in the prediction of a new boson that came to be known as the Higgs boson. Higgs and Englert won the 2013 Noble prize for this work after the boson was discovered in 2012, again, at CERN [23, 24]. This 50 year journey resulted in the SM as we know it today.

Electroweak Unification: $SU(2)_L \times U(1)_Y$

The Lagrangians for QED and QCD are invariant under parity but this is not the case for the EW interaction where the fundamental representations of the fermion fields for the $SU(2)_L$ part of the interaction are doublets of lepton or quark fields where only the left-handed helicity states have a non-trivial representation of the group. There are four gauge fields associated with the combined $SU(2)_L \times U(1)_Y$ symmetry. The three fields, W^1_μ, W^2_μ, W^3_μ, are the gauge fields of $SU(2)_L$ and B_μ is the gauge field associated with $U(1)_Y$. Before symmetry breaking (discussed next) the gauge bosons of these four fields are massless, much like the gluons in the strong interaction. The interacting fields are in the (fundamental) Weyl spinor representation of $SU(2)$, whereas the right-handed states are singlets:

---

[9] Weak neutral currents were in fact first observed in the Gargamelle bubble chamber at CERN in 1973 [15].

$$\psi_L \equiv \begin{pmatrix} \nu_{eL} \\ e^-_L \end{pmatrix}, \begin{pmatrix} \nu_{\mu L} \\ \mu^-_L \end{pmatrix}, \begin{pmatrix} \nu_{\tau L} \\ \tau^-_L \end{pmatrix}, \begin{pmatrix} u_L \\ d_L \end{pmatrix}, \begin{pmatrix} c_L \\ s_L \end{pmatrix}, \begin{pmatrix} t_L \\ b_L \end{pmatrix}, \tag{2.4}$$

$$\psi_R \equiv \nu_{eR},\ \nu_{\mu R},\ \nu_{\tau R},\ e_R,\ \mu_R,\ \tau_R,\ d_R,\ u_R,\ s_R,\ c_R,\ b_R,\ t_R \ . \tag{2.5}$$

Only the ψ_L states of the fermions may interact under the full $SU(2)_L \times U(1)_Y$ symmetry, while right handed states only interact under the $U(1)_Y$ part. Due to the chiral nature of the symmetry, mass terms for the fermions cannot be included as such terms would need to couple left- and right-handed states with different representations and therefore break the symmetry. Thus, at this stage the fermion fields are all massless and there is no notion of mass eigenstates as these are generated after symmetry breaking, discussed in Subsection 2.2.3. The Lagrangian for the electroweak part of the SM describing interactions between left- and right-handed fermion fields (ψ_L, ψ_R) with the electroweak gauge fields ($W^1_\mu, W^2_\mu, W^3_\mu, B_\mu$) is shown below in Equation 2.6.

$$\begin{aligned} \mathcal{L}_{EW} = \overline{\psi}_L{}^i \left(i\gamma^\mu\right) &\left[\delta_{ij}\partial_\mu - \frac{i}{2}g\sigma_{aij}W^a_\mu - \frac{i}{2}g'Y\delta_{ij}B_\mu\right]\psi_L{}^j \\ &+ \overline{\psi}_R \left(i\gamma^\mu\right)\left[\partial_\mu - \frac{i}{2}g'YB_\mu\right]\psi_R \\ &- \frac{1}{4}W_{a\mu\nu}W^{a\mu\nu} - \frac{1}{4}B_{\mu\nu}B^{\mu\nu} \ , \end{aligned} \tag{2.6}$$

with the covariant derivative this time given by $\delta_{ij}\partial_\mu - \frac{i}{2}g\sigma_{aij}W^a_\mu - \frac{i}{2}g'Y\delta_{ij}B_\mu$ for the left handed fermion doublets and $\partial_\mu - \frac{i}{2}g'YB_\mu$ for the right handed fermions which have singlet representations under $SU(2)_L$. The electroweak gauge field terms are composed of $W^a_{\mu\nu} = \partial_\mu W^a_\nu - \partial_\nu W^a_\mu - g\epsilon^a_{bc}W^b_\mu W^c_\nu$, where ϵ^a_{bc} is the fully anti-symmetric tensor; and $B_{\mu\nu} = \partial_\mu B_\nu - \partial_\nu B_\mu$. The normalisations, g, g', are the coupling constants to the W^a_μ and B_μ fields respectively and σ^a are the three traceless Hermitian Pauli matrices, $\sigma^1, \sigma^2, \sigma^3$. The fields ψ_L have indices to indicate weak isospin, $i, j = 1, 2$, while indices a, b, c label the three gauge fields, $a, b, c = 1, 2, 3$. The free and self-interacting field terms for the gauge fields are given by the $\frac{1}{4}W_{a\mu\nu}W^{a\mu\nu}$ and $\frac{1}{4}B_{\mu\nu}B^{\mu\nu}$ terms.

Note that neither the fermion fields nor the gauge fields have mass terms yet, as adding such terms at this stage would break the gauge invariance of the Lagrangian and we would not have a unified theory. As the weak boson and fermion states we observe are indeed massive, we require a way to generate their masses spontaneously, such that the electroweak symmetry is preserved at high energy (required for a renormalisable theory) but breaks at some lower energy, generating the masses we observe in the process.

Electroweak Spontaneous Symmetry Breaking: $SU(2)_L \times U(1)_Y \rightarrow U(1)_{EM}$

Now, how to get from the unified electroweak picture painted above to the electromagnetic and the weak interactions as we observe them at low energy, with a massless photon, but massive weak bosons? The weak force interactions as we know them at low energies are inconsistent when extended to high energies (~ 1 TeV), for example, massive bosons imply that the scattering of longitudinally polarised W^+W^- bosons will eventually break unitarity (i.e. the probability for the scattering process will exceed 1) as the energy of the interaction increases. Thus some new type (or types) of interaction must come into play, before any unitarity violations occur, that act to cancel such anomalies.

The fix for this problem, as well as a way to generate masses for the fermions, comes in the form of the Higgs mechanism, in which the electroweak symmetry is broken down to the $U(1)_{EM}$, resulting in massive gauge fields and the coupling of ψ_L and ψ_R states to produce fermion mass terms in the process. For the first step of the Higgs mechanism we can introduce a doublet of complex scalar fields under $SU(2)_L \times U(1)_Y$, and writing in terms of four real scalar fields $\Phi = \frac{1}{\sqrt{2}}(\phi_1 + i\phi_2, \phi_3 + i\phi_4)^T$, the Lagrangian for Φ will include an invariant kinetic term along with some potential term, $V(\Phi^*_i\Phi^i)$:

$$\mathcal{L}_{Higgs} = (D_{\mu}{}^{i}_{j}\Phi^j)^*(D^{\mu}{}_{ik}\Phi^k) - V(\Phi^*_i\Phi^i) \quad , \tag{2.7}$$

with the $SU(2)_L \times U(1)_Y$ covariant derivative introduced in Equation 2.6, $(D_\mu)_{ij} = \delta_{ij}\partial_\mu - \frac{i}{2}g\sigma_{aij}W^a_\mu - \frac{i}{2}g'Y\delta_{ij}B_\mu$. The potential term is postulated to be of the form

$$V(\Phi^*_i\Phi^i) = \mu^2(\Phi^*_i\Phi^i) + \frac{\lambda}{2}(\Phi^*_i\Phi^i)^2 \quad , \tag{2.8}$$

with real parameters μ^2 and λ. The potential minimum at $V = 0$ will therefore occur when

$$(\Phi_i^*\Phi^i)_{min} \equiv (\phi_1^2 + \phi_2^2 + \phi_3^2 + \phi_4^2)_{min} = -\frac{2\mu^2}{\lambda} \quad . \tag{2.9}$$

This minimum of the potential is in the form of a 4-dimensional hypersphere, and we are free to choose any point we wish on this hypersphere as the vacuum state without loss of generality. Therefore, choosing a point with three of the four scalar fields set to 0 we have, at the minimum,

$$\phi_{1,min}^2 = \phi_{2,min}^2 = \phi_{4,min}^2 = 0 \tag{2.10}$$

$$\phi_{3,min}^2 = -\frac{2\mu^2}{\lambda} = v^2 \Longrightarrow \langle 0|\Phi|0\rangle = \begin{pmatrix} 0 \\ \frac{v}{\sqrt{2}} \end{pmatrix} \tag{2.11}$$

where v is the vacuum expectation value for the field ϕ_3 in this case, though the choice is arbitrary. Expanding about the potential minimum at this point there are three free degrees of freedom that allow us to remain at the potential minimum and one massive scalar field associated with the second derivative of the potential in the direction away from the potential minimum (the Higgs field). If we consider the interaction terms in the kinetic part of the Lagrangian in equation 2.7, after a vacuum expectation value for the field has been set we get

$$(D_{\mu}{}^{i}_{j}\Phi^{j})^{*} = \frac{-ig}{2\sqrt{2}} \begin{pmatrix} W_\mu^3 + \frac{g'}{g}YB_\mu & W_\mu^1 + iW_\mu^2 \\ gW_\mu^1 - giW_\mu^2 & -W_\mu^3 + \frac{g'}{g}YB_\mu \end{pmatrix} \begin{pmatrix} 0 \\ v \end{pmatrix}$$

$$(D^{\mu}{}_{ik}\Phi^{k}) = \frac{ig}{2\sqrt{2}} \begin{pmatrix} W^{3\mu} + \frac{g'}{g}YB^\mu & W^{1\mu} - iW^{2\mu} \\ gW^{1\mu} + giW^{2\mu} & -W^{3\mu} + \frac{g'}{g}YB^\mu \end{pmatrix} \begin{pmatrix} 0 \\ v \end{pmatrix}$$

$$i.e. \;\; (D_{\mu}{}^{i}_{j}\Phi^{j})^{*}(D^{\mu}{}_{ik}\Phi^{k}) = \frac{g^2v^2}{8}\left[(W_\mu^1)^2 + (W_\mu^2)^2 + \left(\frac{g'}{g}YB_\mu - W_\mu^3\right)^2\right] \tag{2.12}$$

Now, from the form of Equation 2.12 we can see that there will be mass terms generated for all four of the gauge fields of the form $\frac{g^2v^2}{8}W_\mu W^\mu$, but we only want three massive bosons and one massless one with Z_μ and A_μ uncharged under $U(1)_{EM}$. Thus rotations between W^3_μ & B_μ as well as between W^1_μ & W^2_μ are applied such that

$$Z_\mu \equiv \cos\theta_w W^3_\mu - \sin\theta_w B_\mu \tag{2.13}$$

$$A_\mu \equiv \sin\theta_w W^3_\mu + \cos\theta_w B_\mu \tag{2.14}$$

$$W^\pm_\mu \equiv \frac{1}{\sqrt{2}}\left(W^1_\mu \mp W^2_\mu\right) \tag{2.15}$$

These linear combinations of the electroweak vector fields are chosen such that we get a massless photon field, massive W and Z fields and W bosons with electric charges ± 1 as observed. In terms of the electric coupling constant, e (normalised such that the charge of an electron is -1), it is related to the coupling constants of $SU(2)_L$ and $U(1)_Y$ by $e = g\sin\theta_w = g'\cos\theta_w$, where θ_w is known as the weak mixing angle[10]. This non-zero vacuum expectation value (vev) for the Higgs field also allows us to create mass terms for the fermions, by coupling left- and right-handed states through this vev in the form $y_1\overline{\psi}_L{}^i\Phi_i\psi_R + y_2\overline{\psi}_R\Phi^*{}_i\psi_L{}^i$. The massive scalar boson associated with the field that gets the non-zero vacuum expectation value can be seen in the expression for the potential Equation 2.8 as $\frac{\lambda v^2}{2}\phi_3^2$. The process of EW symmetry breaking described above is thought to have happened when the universe cooled enough for a non-zero vacuum expectation value for the Higgs field to spontaneously 'freeze out' (i.e. fall into some minimum of the potential) as the universe cools after the Big Bang.

2.2.3. Particle Content of the SM

The mass eigenstates we generally consider as particles, with masses generated after EW symmetry breaking, are the things particle physics experiments generally look for, with the caveat that in the case of weak interactions the mass states do not align with the 'flavour' states that take part in the interaction. Beginning with the discovery of the electron in 1897 [25], which was the first of the fundamental particles that comprise the Standard Model to be discovered, to the 2012 discovery of the Higgs boson, all predicted SM particles have now been experimentally discovered (unless one were to include right handed neutrinos, though it is not clear how they could be detected directly). The particle content that results from the dynamics of the fundamental fields of the

---

[10] Or as the Weinberg angle.

SM contains: $3 \cdot 2 \cdot 6 = 36$ quarks; either 9 or 12 leptons (depending on whether-or-not neutrinos are their own anti-particles); a single scalar Higgs boson; the 3 massive Z and $W^{\pm}$ vector bosons; the massless photon; and 8 gluons. So at most, 61 particles comprise the SM, the spins and masses of which are listed in Table 2.2.

spin-0	Mass (GeV)	spin-$\frac{1}{2}$	Mass (GeV)	spin-1	Mass (GeV)
h	126	ν_1	$< 2.3 \times 10^{-9}$	γ	0
		ν_2			
		ν_3			
		e	5.11×10^{-4}		
		u	2.3×10^{-3}	g	0
		d	4.8×10^{-3}		
		s	9.5×10^{-2}		
		μ	1.06×10^{-1}		
		c	1.28	W	80.4
		τ	1.78		
		b	4.2	Z	91.2
		t	173		

Table 2.2.: Approximate masses of the particles of the SM (i.e. after EW spontaneous symmetry breaking), with the massless photon and gluons corresponding to the unbroken $U(1)_{EM}$ and $SU(3)_C$ symmetries respectively.

The fermions of the SM and their quantum "numbers" under the gauge groups $SU(3)_C$, $SU(2)_L$, $U(1)_Y$ and $U(1)_{EM}$ are listed in Table 2.3, split into left- and right-handed helicity states and three generations that share quantum numbers but correspond to different mass eigenstates. The z-components of weak isospin states are labeled T_3, with $T_3 = \frac{\sigma_3}{2}$. Along with hypercharge, Y, these values determine the electric charge after spontaneous symmetry breaking as $Q = T_3 + \frac{Y}{2}$. With the discovery of the Higgs boson (h) in 2012, for the first time the SM is over-constrained and best fits to the parameters will be able to shed light on its self-consistency [26].

Due the nature of the weak interaction, the fermion mass states as listed in Table 2.2 are not the same as the flavour states that interact via the weak interaction. These flavour states correspond to linear combinations of the mass eigenstates and are related by a unitary matrix. The mixing matrix that transforms between the flavour and mass eigenstates of the quarks is known as the Cabibbo-Kobayashi-Maskawa matrix (CKM matrix). It contains 9 complex entries, implying CP violation in the quark sector for weak interactions [27, 28], with the d', s', b' states listed in Table 2.3 given by

Fermion Generations			Quantum Numbers				
I	II	III	C	T	T_3	Y	Q
$\begin{pmatrix}\nu_e\\ e^-\end{pmatrix}_L$	$\begin{pmatrix}\nu_\mu\\ \mu^-\end{pmatrix}_L$	$\begin{pmatrix}\nu_\tau\\ \tau^-\end{pmatrix}_L$		$\frac{1}{2}$	$+\frac{1}{2}$ $-\frac{1}{2}$	-1	0 -1
$\nu^*_{e\,R}$ e^-_R	$\nu^*_{\mu\,R}$ μ^-_R	$\nu^*_{\tau\,R}$ τ^-_R		0	0	0 -2	0 -1
$\begin{pmatrix}u\\ d'\end{pmatrix}_L$	$\begin{pmatrix}c\\ s'\end{pmatrix}_L$	$\begin{pmatrix}t\\ b'\end{pmatrix}_L$	🟥🟩🟦	$\frac{1}{2}$	$+\frac{1}{2}$ $-\frac{1}{2}$	$-\frac{1}{3}$	$+\frac{2}{3}$ $-\frac{1}{3}$
u_R d_R	c_R s_R	t_R b_R		0	0	$+\frac{4}{3}$ $-\frac{2}{3}$	$+\frac{2}{3}$ $-\frac{1}{3}$

Table 2.3.: Quantum numbers of the SM fermions not including their corresponding anti-particle states. Fermions with the same quantum numbers are split into 3 generations. Note: the right handed neutrino states (*) have not been observed.

$$\begin{pmatrix} d' \\ s' \\ b' \end{pmatrix} = \begin{pmatrix} V_{ud} & V_{us} & V_{ub} \\ V_{cd} & V_{cs} & V_{cb} \\ V_{td} & V_{ts} & V_{tb} \end{pmatrix} \cdot \begin{pmatrix} d \\ s \\ b \end{pmatrix} \quad , \tag{2.16}$$

where the entries are proportional to the amplitudes for the transition of a down-type quark (d, s, b) to transition to an up-type quark (u, c, t) in a weak interaction.

With the discovery of neutrino oscillations via the detection of solar neutrinos, reactor neutrinos and accelerator produced neutrinos, it has been found that neutrinos produced in their flavour eigenstates, oscillate in flight between these states [29]. Thus, a mixing matrix corresponding to the CKM matrix also exists in the lepton sector, and is known as the Pontecorvo-Maki-Nakagawa-Sakata matrix (PMNS matrix) [30–32]. It relates the neutrino flavour states $(\nu_e, \nu_\mu, \nu_\tau)$ that participate in the weak interaction to their mass eigenstates (ν_1, ν_2, ν_3).

$$\begin{pmatrix} \nu_e \\ \nu_\mu \\ \nu_\tau \end{pmatrix} = \begin{pmatrix} U_{e1} & U_{e2} & U_{e3} \\ U_{\mu1} & U_{\mu2} & U_{\mu3} \\ U_{\tau1} & U_{\tau2} & U_{\tau3} \end{pmatrix} \cdot \begin{pmatrix} \nu_1 \\ \nu_2 \\ \nu_3 \end{pmatrix} \quad . \tag{2.17}$$

with the parameters of the PMNS not as well measured as those of the CKM matrix, it is unclear at this stage whether or not CP violation also exists in the lepton sector. However the fact that neutrinos are massive, but right-handed neutrinos are not observed (as the weak interaction maximally violates parity) suggests that the SM is not complete and at this time massive neutrinos lie just outside the scope of the SM.

Therefore, in terms of experimentally measurable free parameters of the SM we so far have: 12 fermion masses; 3 mixing angles and 1 complex phase coming from parameterisation of the CKM matrix; 3 mixing angles and at least 1 complex phase coming from parameterisation PMNS matrix; 3 coupling constants for the strong, weak and electromagnetic interactions; 1 vector boson mass (m_Z); and 1 scalar boson mass (m_h). All other values in the model can be fixed from knowledge of these parameters, and so far all except the neutrino masses and mixing phases have been experimentally measured. Outside of the neutrino sector, the SM is over-constrained and primed for consistency tests.

2.3. Shortcomings of the SM

Though incredibly successful at describing physics over many orders of magnitude on energy scales up to $\sim 1\,\text{TeV}$, and predicting the existence of massive W and Z bosons as well as the Higgs boson, there are theoretical/philosophical reasons as well as recent experimental results that lead us to believe that the SM cannot be the full story.

As mentioned in the previous section there are at least 25 free parameters in the SM itself, and these parameters are many orders of magnitude apart (see Table 2.2 for example). If we assume that there is indeed some fundamental unified theory of nature, a number of problems with the SM begin to arise from a purely theoretical standpoint. The fact that there are so many parameters that are not set by the theory itself but must be measured by experiment seems to require some explanation. Apart from having to be measured experimentally, the values these parameters take do not possess the quality of naturalness that we expect of physical theories, in which quantities in the theory should be of order 1 relative to some scale set by the theory.

The energy scale of the theory also becomes a problem in the context of gravity, the behaviour of which is currently formulated as a classical theory that deals with the geometry of spacetime. Now, the SM itself does not attempt to describe gravity which is only expected to become strongly coupled at energies close to the Planck scale, $\sim 10^{19}$ GeV.[11] The question that arises (known as the Hierarchy problem), is why the mass of the Higgs boson ($m_h \approx 126$ GeV) is so low and not somewhere near the Planck scale? As the Higgs is a scalar its mass is particularly sensitive to Feynman diagrams containing fermion loops, and thus cannot strictly be calculated in the SM as there is no low energy cut-off for the amount of 4-momentum that can run in these loops. Therefore, we would naively expect these loop corrections to the Higgs mass to take the measured mass up to the Planck scale where (presumably) gravity would somehow come into play and prevent the Higgs mass blowing up to infinity, yet the Higgs mass remains anchored at the electroweak scale. This is the primary reason for expecting new physics to exist somewhere between the electroweak scale and the Planck scale. A widely studied theoretical framework that incorporates a solution to the Hierarchy problem by postulating such new physics is Supersymmetry [33]. Supersymmetric theories stabilise the Higgs mass by introducing super-partner fields for each of the SM fields such that quantum corrections to the masses of scalar particles in the theory will cancel each other and remove the need for such fine tuning of the Higgs mass. However, in order to cancel additional anomalies arising from triangular fermionic loops in Supersymmetric theories (as a result of the addition of a spin-$\frac{1}{2}$ higgsino super-partner to the Higgs) a second Higgs doublet of complex fields is required [34, 35]. Such "two Higgs doublet models" will be discussed further in Chapter 5.

In terms of astronomical/cosmological data the SM also falls short. The most glaring omission from the SM as it is currently formulated is the existence of Dark Matter. From the rotation curves of spiral galaxies, to weak gravitational lensing through clusters of galaxies and strong lensing around galactic centres, to lensing around a collision of two galaxies (the bullet cluster), evidence is mounting that the centre of gravity of galaxies and clusters of galaxies is inconsistent with the distribution of visible matter within the galaxies, implying the existence of some form of non-relativistic Dark Matter [36, 37]. Many models that propose physics beyond the SM are constructed to contain one or more Dark Matter candidates [38]. One possibility suggests itself through the fact that neutrinos are massive, implying that there exist right handed neutrino states that would not interact via any of the gauge fields of the SM (so-called sterile neutrinos), and would only connect to the SM through coupling to the Higgs field. Such massive right handed neutrinos with masses large enough ($\sim$ keV) to play the role of a viable Dark Matter candidate are but one option that must be considered as a dark matter candidate.

---

[11] The Planck energy scale is a back of the envelope "what if" a particle has a de-Broglie wavelength equal to the Schwarzschild radius corresponding to its mass. i.e. $E_p = G^{-\frac{1}{2}} \sim 10^{19}$ GeV.

Another important astronomical observation to occur within the last 20 years is that the rate of expansion of the universe seems to be accelerating [39–41]. This provides direct evidence for the existence of some form of Dark Energy (energy with positive energy density but negative pressure), however the vacuum energy that arises from the fields of the SM is some 120 orders of magnitude too large and would require additional fields and new physics in order to provide cancelations to bring it into line with observations. Recent high precision mapping of the Cosmic Microwave Background (CMB) by the Planck telescope [42] confirms that the energy density of the universe is split between three main categories: Baryonic Mater ($\sim 5\%$); Dark Matter ($22.7 - 26.8\%$); and Dark Energy (68.3%).

All of this is simply to point out that the SM is by no means a complete theory of nature, but the experimentally valid low energy effective theory to which any theory beyond the SM must converge to at the electroweak energy scale. Based on the observations outlined above it is likely that there exists some more complete theory beyond the SM and searches for inconsistencies in the SM predictions at the LHC energies provide the opportunity to expose points of weakness in the model where new types of interactions would need to fill the gap. Searching for inconsistencies in the SM predictions is the focus of Chapters 5 and 6. Chapter 5 concerns the search for inconsistencies in the predicted decay of top quarks to tau leptons ($t \to bW^+ \to b\tau^+\nu_\tau$) and whether or not this is better explained by models that contain an extended Higgs sector (to be discussed in Section 5.1). Chapter 6 describes the effort to test the distribution of events in the LHC data containing an electron and oppositely charged muon, with the expected distribution for such events under the SM.

Chapter 3.

The ATLAS Experiment at the LHC

This chapter provides information on the experimental effort currently underway to explore particle physics at the TeV scale. It covers the general setup and aims of the LHC physics program and provides an overview of the ATLAS experimental setup, with a focus on data taking by ATLAS during 2010 and 2011, as the research presented in later chapters only includes ATLAS data collected at 7 TeV. Due to the complexity of the LHC and the ATLAS detector, along with their multitudes of subsystems, only a brief overview is given in this chapter in order to provide enough background for the chapters that follow.

3.1. The LHC

The Large Hadron Collider (LHC) [43] is a proton-proton (pp) synchrotron that currently sits at the energy frontier in experimental particle physics. Hadron colliders at the energy frontier are colloquially referred to as "discovery machines", as they deliver parton-parton interactions (usually from pp or $p\bar{p}$ collisions) at a continuum of energies, up to a significant fraction of the energies of the colliding hadrons. As this parton-parton interaction energy can reach into an as yet un-probed energy regime, any undiscovered resonance that can be produced in the available phase space should eventually be discovered at an LHC experiment.

3.1.1. Goals of the LHC

The primary goals of the LHC program are: to discover/confirm the mechanism of electroweak symmetry breaking in the SM; and ideally to discover inconsistencies in the SM itself as there is no *a priori* reason for it to be valid above the electroweak scale. As of the time of writing (2014) this first goal has been achieved, as what appears to be the SM Higgs boson has been discovered using the LHC, thus validating the Higgs mechanism for electroweak symmetry breaking. The LHC will also hopefully provide hints of physics beyond the SM, and some measurements to motivate new models that can account for some of the outstanding questions in fundamental physics, questions such as:

- What is Dark Matter?
- Is it the SM Higgs that has been discovered?

These questions could be related, so any direction that can be provided by experimental results from the LHC would greatly advance theoretical efforts towards a more fundamental theory of the universe.

3.1.2. The LHC Chain

The LHC machine itself accelerates protons (or lead ions) in two counter-circulating beams and brings them into collision at interaction points (IP) within the four main LHC detectors ATLAS, CMS, LHCb and ALICE. The “LHC” acronym is also often used as an umbrella term covering everything to do with physics at the LHC: the injector chain; the LHC machine; the LHC experiments – ATLAS [44], CMS [45], LHCb [46], ALICE [47], TOTEM [48], LHCf [49] and MoEDAL [50]; as well as the Worldwide LHC Computing Grid (WLCG) [51] – used to store and analyse the vast quantities of data produced by the experiments.

The injector chain through to the LHC machine along with the four main experiments are shown in Figure 3.1 as part of the accelerator complex at CERN. For *pp* collisions this chain begins with hydrogen gas released into Linac 2, the linear accelerator that ionises the hydrogen atoms and accelerates the resulting protons to 50 MeV at which they enter the Proton Synchrotron (PS) Booster. The PS Booster consists of four synchrotron rings that further accelerate the protons to 1.4 GeV using RF cavities that produce two bunches of protons per ring. Sets of six of these bunches are then injected into the

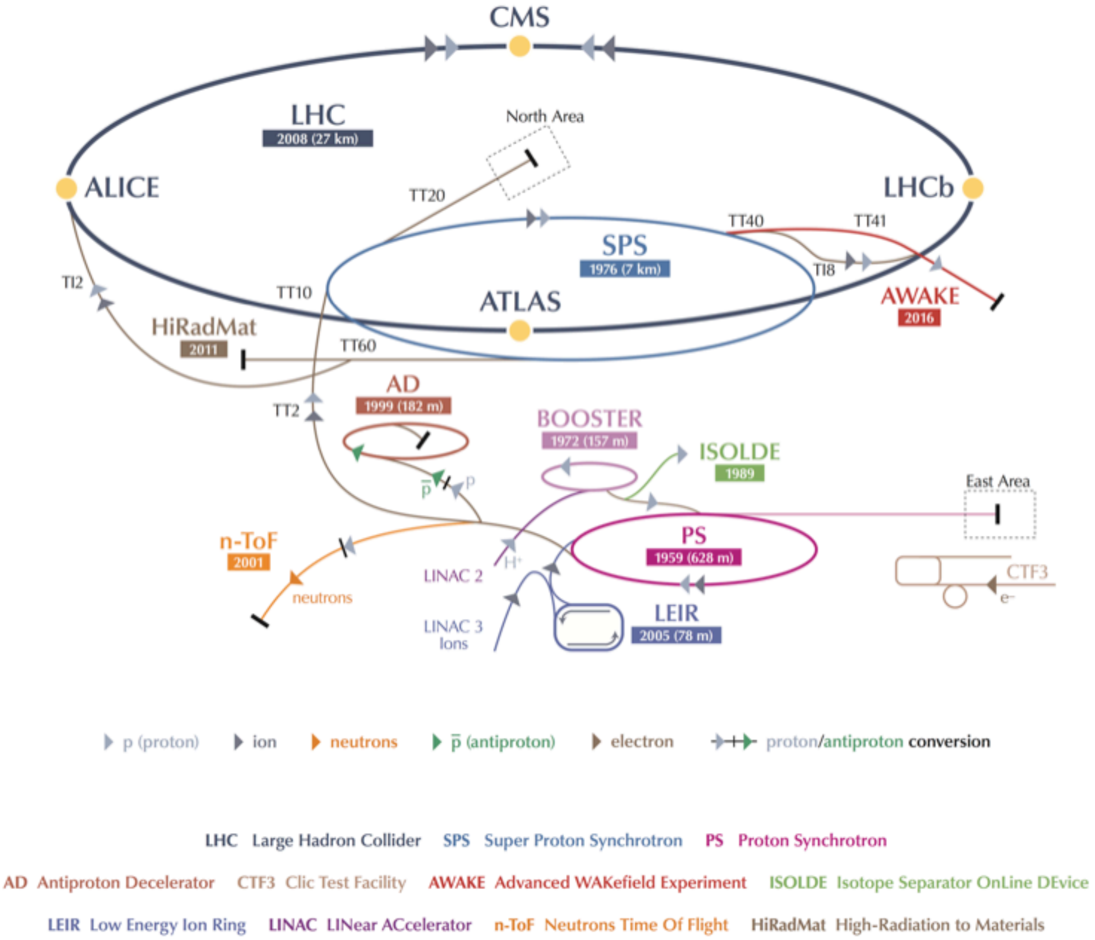

Figure 3.1.: Schematic of the CERN accelerator complex [52].

PS. The PS accelerates the protons up to 26 GeV and is responsible for the ultimate longitudinal bunch structure of the LHC beams. Of the six bunches injected initially, each bunch is split into three and each of these is split again into four by varying the RF harmonic numbers. The resulting set of 72 bunches are then sent (via the TT2/TT10 transfer line) to the SPS. The Super Proton Synchrotron (SPS[1]) accelerates the protons to 450 GeV, ready for injection into the LHC rings. The LHC itself consists of two beam pipes that pass through the 1232 superconducting dipole magnets necessary to produce the (up to $\sim 8\,\mathrm{T}$) magnetic fields required to constrain the proton beams (up to the nominal 7 TeV beam energies) to the 27 km long tunnel originally built to house the LEP Collider [54]. Thousands more (8361) magnets around the ring act to focus the beams. That the magnets be superconducting in order to produce the large magnetic

---

[1] Previously the $Sp\bar{p}S$ at which the UA1 and UA2 experiments discovered the W and Z bosons [53].

fields required, creates the need for a complex liquid helium based cryogenic system, and the entire LHC therefore operates at a temperature of just 1.9 K. After successful circulation of proton beams in September 2008 one of the connectors between two of the magnets lost superconductivity and vaporised, ultimately resulting in a large loss of helium causing many of the magnets to quench [55]. As a result the LHC was shut down for repairs until the end of 2009, with short commissioning and physics runs at the end of 2009 with 1.18 TeV beams, moving to 3.5 TeV beams (half the design energy) in March 2010 and continuing to run at this energy through 2011, and increasing to 4 TeV for runs throughout 2012.

3.1.3. The Experiments

ATLAS and CMS are general purpose detectors optimised for discovery of potential new physics signals resulting from pp collisions delivered by the LHC. These experiments and the respective experimental collaborations (comprising approximately 3000 physicists each) conduct a wide variety of SM measurements and new physics searches to advance our understanding of fundamental physics in this new energy regime. This was demonstrated in stunning fashion with the 2011/2012 buildup-to and announced-discovery-of a previously unobserved spin-0 resonance, consistent with the SM Higgs boson, with an invariant mass of $\sim$125 GeV at both ATLAS and CMS [23, 24]. LHCb is a more specialised detector intended to study heavy flavour physics (particularly B meson systems) during pp running. While ALICE (A Large Ion Collider Experiment) is a dedicated heavy-ion detector used during the $PbPb$ and pPb runs which have taken place towards the end of each year after pp running, it aims to determine properties of quark gluon plasmas.

3.1.4. LHC pp Physics Runs in 2010 & 2011

The 2010 and 2011 pp runs at the LHC relevant to this thesis took place with a centre of momentum collision energy of 7 TeV, however the machine parameters, and therefore the conditions for pp collision events recorded by ATLAS varied drastically between the start of 7 TeV operation in March 2010 and the end in October 2011. The focus here will be on luminosity delivered to the ATLAS detector at the 7 TeV collision energy, as this is the data used for the analyses described in Chapters 5 & 6. The major change over 7 TeV data taking periods was due to the effort to increase instantaneous luminosity to reach a target of 5 fb^{-1} of delivered integrated luminosity by the end of 2011 (Figure 3.2).

With much of the attention on discovering or excluding the SM Higgs below ∼600 GeV at ATLAS and CMS.

Beam Information	2010	2011	Nominal
Transverse Emittance, ε (μm)	$2.4-4$	$1.9-2.3$	3.75
Amplitude Modulation at IP1, β^* (m)	3.5	1	0.55
Maximum Colliding Bunch Pairs	368	1380	2808
Protons per Bunch	1.2×10^{11}	1.5×10^{11}	1.15×10^{11}
Bunch Spacing (ns)	150	50	25
Peak Instantaneous Luminosity ($\mathrm{cm}^{-2}\ \mathrm{s}^{-1}$)	2.07×10^{32}	3.65×10^{33}	1×10^{34}

Table 3.1.: The parameters listed are for collisions with stable 3.5 TeV proton beams during 2010 and 2011 [56], with the nominal values provided for reference.

The large increases in the number of protons per bunch (see Table 3.1) between the start and end of 7 TeV running, as well as further squeezing[2] of the beams at the interaction point caused a large increase in the number of inelastic *pp* collisions occurring during any given bunch crossing (in-time pileup) shown in Figure 3.3. The mean number of such *pp* interactions in a given bunch crossing, μ, is given by

$$\mu = \frac{\mathcal{L}\sigma_{\mathrm{inel}}}{n_b f_r} \quad , \tag{3.1}$$

where $\mathcal{L}$ is the instantaneous luminosity; σ_{inel} is the cross section for inelastic *pp* collisions; f_r is the revolution frequency around the accelerator ring; and n_b is the total number of bunches crossing at the interaction point [57]. The increase in μ value over during 2010 and 2011 can be seen clearly in Figure 3.3, with examples of interaction vertices reconstructed by ATLAS in 2010/2011 shown in Figure 3.4.

3.2. The ATLAS Detector

ATLAS (A Toroidal LHC ApparatuS) [44] constitutes the equipment utilised by the ATLAS Collaboration to record *pp* collisions provided by the LHC. The design of ATLAS has been driven by the harsh operating environment expected from LHC. It is composed

---

[2] The width of the beams at the interaction point is proportional to $\sqrt{\varepsilon\beta^*}$, and so squeezing is achieved by decreasing β^*, which is the longitudinal distance from the focus point to a point at which the width of the beam is twice as large.

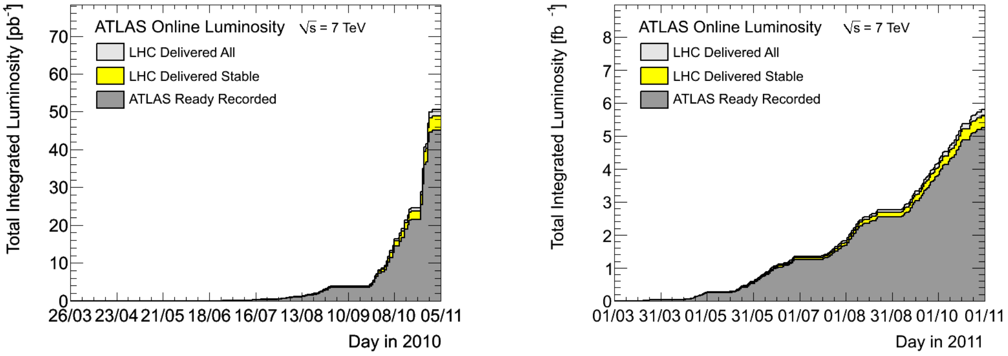

(a) 2010 **(b)** 2011

Figure 3.2.: Total integrated luminosity for $\sqrt{s} = 7\,\text{TeV}$, pp collisions delivered at the ATLAS interaction point (IP1) by the LHC and the amount recorded by ATLAS [58].

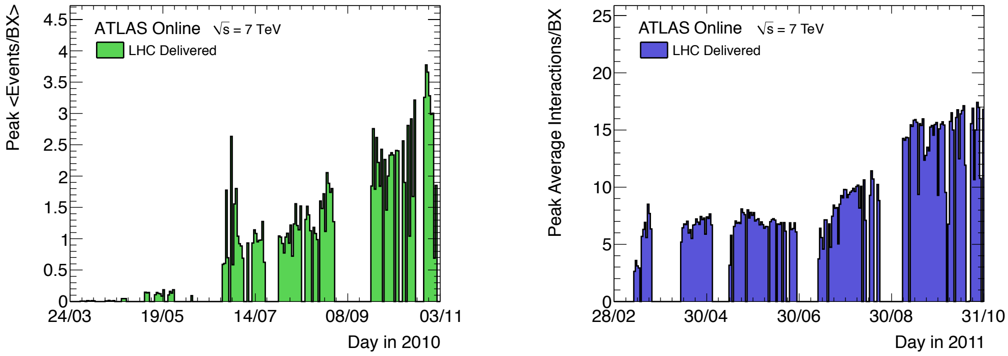

(a) 2010 **(b)** 2011

Figure 3.3.: The maximum mean number of events per beam crossing versus day. The plots show the maximum average value for all bunch crossings over a luminosity block (10 sec–1 min time period) during a given run. The online luminosity measurement is used for this calculation as for the luminosity plots 3.2 [58].

of various subsystems that are each designed to detect, measure and identify specific types of particles produced in a collision. Also part of ATLAS is a complex trigger system and computing centre designed to cope with writing pp collision event data to disk given the high collision rate.

The ATLAS detector itself is a multi-purpose particle physics detector with a forward-backward cylindrically symmetric geometry. The reference system used is a right-handed Cartesian co-ordinate system, with the nominal collision point at the origin. The anti-clockwise beam direction (looking down on the ring) defines the positive z-axis, while the positive x-axis is defined as pointing from the collision point to the centre of the LHC

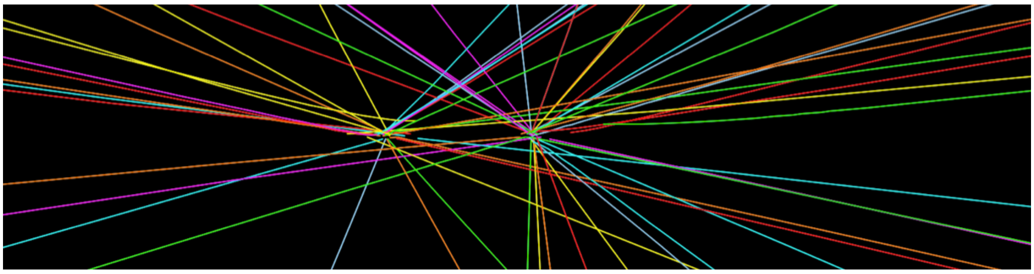

(a) March 2010 (Run: 152166, Event: 467774) – 7 TeV collision event at ATLAS with 2 reconstructed interaction vertices.

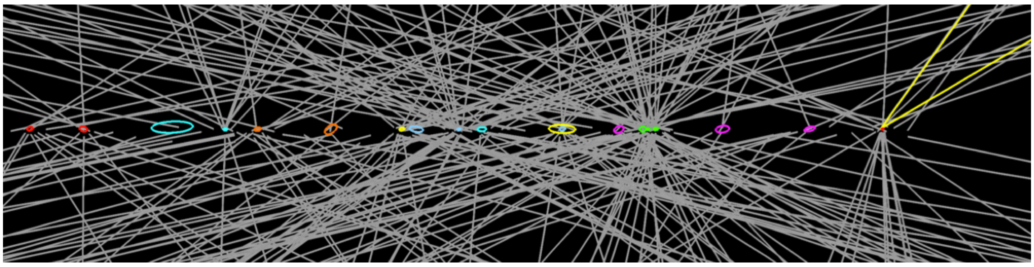

(b) September 2011 (Run: 189280, Event: 1705325) – 7 TeV collision event at ATLAS with 20 reconstructed interaction vertices (circled).

Figure 3.4.: The change in pileup conditions, as shown by *pp* collisions in two bunch crossings reconstructed by ATLAS between start of 2010 and end of 2011, due to increasing luminosity provided by the LHC [59]. Note the large increase in track multiplicity.

ring and the positive y-axis points upwards. In spherical polar co-ordinates the azimuthal angle, ϕ, is measured around the beam axis ($x - y$ plane), and the polar angle, θ is the angle measured with respect to the z-axis. However, in considering physics processes that take place during collisions, use of the polar angle is not ideal due to the fact that in a hadron collider the parton momentum along the z-axis is unknown. As a result a transformation of θ to a new variable that is invariant (in the limit of massless particles, but well approximated when a particles mass is small relative to its momentum) under Lorentz boosts along the z-axis. This variable, called pseudorapidity, is defined as

$$\eta = -\ln \tan(\theta/2) \quad . \tag{3.2}$$

Using this, a measure of separation (ΔR) can be defined in pseudorapidity–azimuthal space that is also invariant under boosts along the z-axis, with

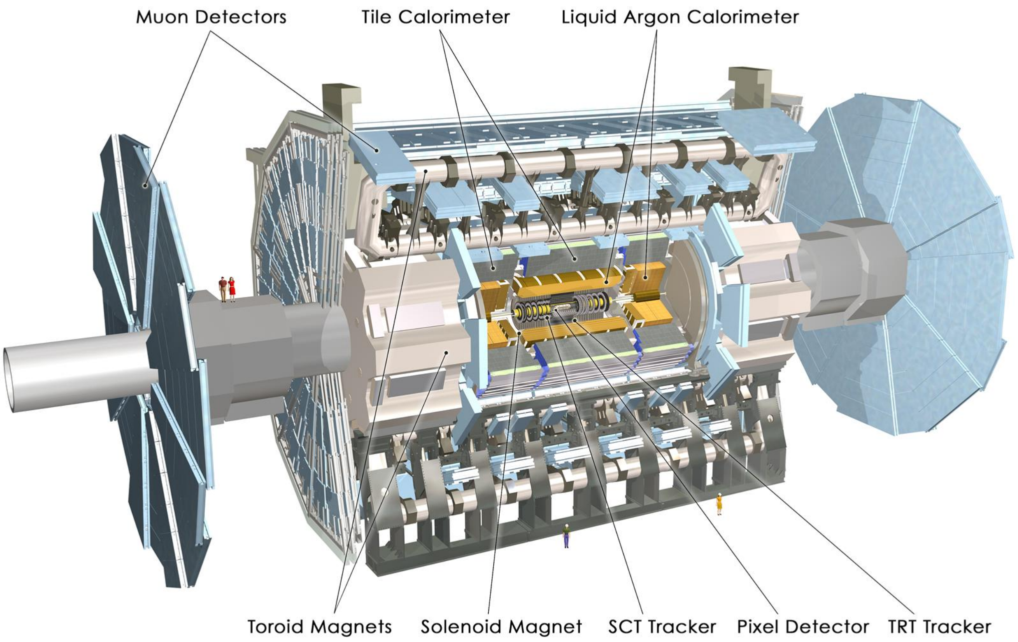

Figure 3.5.: Cutaway schematic of the ATLAS detector [60], with the main sub-detectors and magnets that comprise the overall ATLAS detector listed.

$$\Delta R = \sqrt{\Delta\eta^2 + \Delta\phi^2} \quad . \tag{3.3}$$

Transverse momentum and energy are defined as $p_{\mathrm{T}} = p \sin\theta$ and $E_{\mathrm{T}} = E \sin\theta$, respectively. E_{T} is a purely experimental quantity derived from energy measurements in the calorimeter cells, using the azimuthal direction of the calorimeter cells themselves in terms of the co-ordinate system defined from the interaction point, while p_{T} is a quantity derived primarily from tracking information.

3.2.1. Inner Detector

The ATLAS inner detector (ID) is an approximately cylindrical tracking system, 7 m in length with a radius of 1.15 m immersed in a 2 T axial magnetic field produced by the superconducting solenoid that surrounds it. The ID provides tracking information for charged particles in the pseudorapidity range $|\eta| < 2.5$. It consists of a silicon pixel detector, a silicon microstrip detector (SCT), and a drift-tube-based transition radiation tracker (TRT). It provides for measurement of charged particle momenta as well as vertex reconstruction, which is crucial when there is more than one pp interaction per bunch crossing (pile-up). Precise vertexing also allows for identification of B mesons and τ leptons which produce secondary displaced vertices close to the main interaction vertex. A cross sectional schematic of the ID system is provided in Figure 3.6.

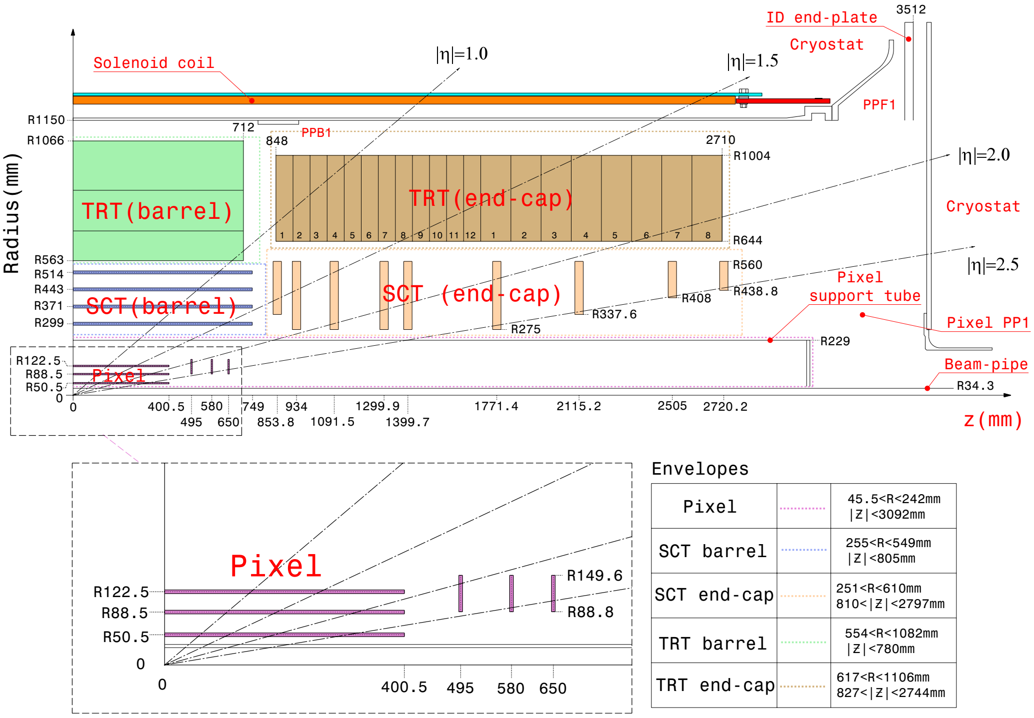

Figure 3.6.: Schematic of the ATLAS inner detector and solenoid [44] — only a quarter of the ID is shown due to its cylindrically symmetric geometry.

The Pixel Detector

The Pixel sub-detector [61, 62], as it's name suggests is composed of doped silicon pixel sensors over a total active area of 1.7 m^2. This is the highest resolution sub-detector in ATLAS and is located closest to the interaction point (see Figure 3.6). It achieves precision vertexing of charged tracks with a transverse impact parameter resolution of better than $\sim 15\,\mu$m, and longditudinal impact parameter resolution of better than ~ 1 mm allowing for reconstruction of multiple primary verticies. In addition to withstanding the high particle fluxes, it is crucial in resolving secondary vertices from taus or B mesons and the multiple primary vertices that result from the high pileup environment. The innermost barrel layer (known as the B-layer) with a radius of 50.5 mm is closest to the collision point, and provides the space point most important for high precision vertexing. This vertex resolution became increasingly important over 2010/2011 as the pileup increased, as shown in Figure 3.4. In all, the 3 co-axial barrel layers and 6 end-cap discs provide ~ 80 million readout channels, with each pixel sensor (nominally $50 \times 400\,\mu\text{m}^2$) connected to a dedicated readout channel by solder bump bonding it to an element of the readout electronics. The arrangement for the Pixel detector as described was used up to the end of data taking in 2012, after which an insertable B-layer and new beam pipe section were added during the long shutdown over 2013–2014.

The SemiConductor Tracker

The SemiConductor Tracker (SCT) is the second of the silicon sub-detectors, sandwiched between the Pixel and TRT and consisting of 4 barrel layers and 2 end-caps (with 9 wheels each). The barrel and end-caps are composed of 2112 and 1976 double sided modules respectively: the arrangement of the barrel (end-cap) layers (wheels) can be seen in Figure 3.6. The SCT sits relatively close to the beam pipe, with the inner barrel layer only 200 mm away from the beam axis. The barrel extends out radially in the range $255\,\text{mm} < r < 549\,\text{mm}$, and has a total length of $|z| < 805\,\text{mm}$, while the end-caps have a minimum inner radius of 251 mm and a maximum radius of 610 mm and lie in the range $810\,\text{mm} < |z| < 2797\,\text{mm}$ (Figure 3.6). The double sided modules, with strips offset at an angle of 40 mrad between one side and the other providing stereo information in the readout, produce space points to be used in the tracking algorithms. Further detail on the SCT detector modules is provided in Chapter 4 in relation to a study on effects of LHC beam loss on their on-board readout electronics.

The Transition Radiation Tracker

Surrounding the SCT is the Transition Radiation Tracker (TRT) [63], which is composed of ‘straw’ tubes, 4 mm in diameter. It consists of a barrel (52,544 straws 144 cm in length oriented parallel to the beam) and two end-caps (122,880 straws 37 cm in length radially aligned to the beam axis), see Figure 3.6. This provides a large number of space points used for charged particle tracking as particles must pass through $35 - 40$ straws. The tubes are made from carbon fibre reinforced kapton surrounding an aluminium cathode (at 1.5 kV), with a gold-plated tungsten wire anode (earthed) running through the centre of each tube. Tubes contain a gas mixture composed of Xe(70%), CO_2(27%) and O_2(3%) that gets ionised by traversing charged particles, with the resulting electrons drifting to the wire anode. This signal is amplified and compared against a 300 eV reference threshold — if the signal passes, it constitutes a "low-threshold" hit. A parallel process exists for high-threshold hits, with a 6 keV reference threshold. Transition radiation (soft X-rays, $5 - 30$ keV) is produced as charged particles traverse polymer fibres (in the barrel) and Al foils (in the end-caps) interspersed between the straws, with the amount of radiation dependent on the traversing particle's relativistic gamma factor, $\gamma = E/m$. This transition radiation excites the Xe, resulting in more high-threshold hits. As electrons have the largest gamma factors, the ratio of low-threshold to high-threshold hits can be used to identify them, and in particular distinguish them from charged pions. Refer to [64] for further information on TRT performance.

3.2.2. Calorimetry

The ATLAS calorimeter system covers the pseudorapidity range $|\eta| < 4.9$, and provides energy and position measurements of particles emerging from the interaction point via measurement of the electromagnetic and hadronic showers they induce. It is composed of five sub-systems, all sampling calorimeters, that use alternating layers of absorber material (to induce showers) and an active readout material (to measure energy loss). This also means that, although the intrinsic energy resolution improves with particle energy ($\propto 1/\sqrt{E}$), the ultimate resolution is limited by sampling fluctuations. The five sub-systems, arranged as shown in Figure 3.7, are: the Liquid Argon (LAr) Electromagnetic Barrel Calorimeter; the LAr Electromagnetic End-cap Calorimeters; the Tile Hadronic Calorimeter (barrel and extended barrel sections); the LAr Hadronic End-cap Calorimeters (HEC); and the LAr Forward Calorimeters (FCal). The design of these sub-systems is driven by the differing resolution and radiation hardness requirements that vary with the position in $|\eta|$ and distance from the interaction point. The EM and Hadronic Calorimeters cover $|\eta| < 3.2$, while the (radiation hard) FCal spans $3.1 < |\eta| < 4.9$. High energy resolution is required for $|\eta| < 2.5$, as this corresponds to the inner detector coverage, and as such, tracking information can be combined with (higher resolution) calorimeter information for precision measurement of charged particle 4-vectors. Coverage up to high $|\eta|$ is required for accurate jet multiplicity measurements as well as valid calculation of missing energy due to particles that escape the detector such as neutrinos. As a result of this requirement, higher radiation hardness is required for the large particle fluxes in these forward regions and hence LAr is used as the active readout for both EM and hadronic sections of the Forward Calorimeters.

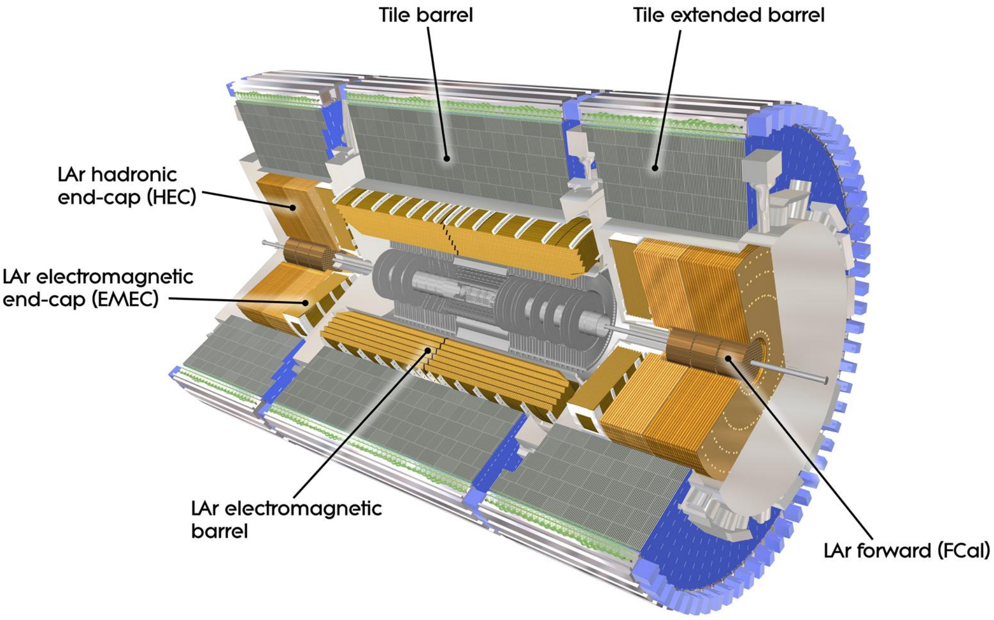

Figure 3.7.: The full ATLAS calorimeter system [65], with the five sub-systems that compose it listed .

EM Calorimeters

The EM Calorimeters are sampling calorimeters utilising alternating layers of lead absorber material to induce EM showers and liquid argon as the active read-out material in which the lengths of particle ionisation trails are proportional to the energy loss of the particle. The measurement relies on high energy charged particles (overwhelmingly electrons) losing energy via bremsstrahlung ($e\gamma^* \rightarrow e\gamma$) and high energy photons losing energy by producing e^+e^- pairs. This is the primary way in which the EM shower evolves (alternating bremsstrahlung and pair production) until the energies of the shower constituents are $< 10\,\text{MeV}$, at which point ionisation becomes the dominant mode of energy loss. This energy loss of the shower constituents, via ionisation of the LAr, is what is measured as the high bias voltage across the LAr results in a pulse with a steep rise and slowly falling tail produced at the readout electrodes for a given ionisation trail. The energy resolution for electrons ranges from $9 - 22\%/\sqrt{E}$ while for photons it is between $8 - 14\%/\sqrt{E}$. The range in resolution is due to the calorimeter geometry, with the largest resolution uncertainty occurring close to the transition region of the barrel and end-cap calorimeters where the amount of passive material in front of the calorimeter is the largest. The LAr EM barrel consists of two half barrels with a small ($\sim 4\,\text{mm}$)

gap separating them at $z = 0$. They use an accordion geometry (see Figure 3.8(a)) with towers etched into the material that flay out with η (see Figure 3.8(b)), with lead sampling layers sandwiched between stainless steel with honeycomb spacers to produce the gap for the LAr and support the electrodes that produce a bias voltage of 2000 V across the LAr. For $|\eta| < 2.5$ (the precision region), the EM Calorimeter is segmented in three layers 3.8(b), with the first layer having a thickness of ~ 6 radiation lengths (X_0), and acting as a pre-shower detector and has a resolution fine enough to discriminate between $\pi^0 \to \gamma\gamma$ and hard γs from the interaction point. For $2.5 < |\eta| < 3.2$, only the back two layers are present, resulting in a coarser granularity.

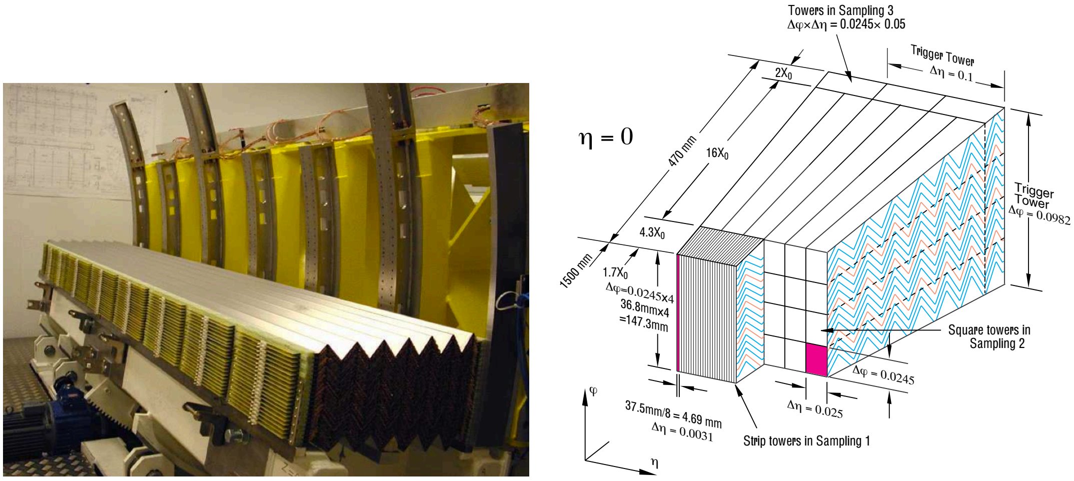

(a) Photo of a LAr barrel EM module and steel ring support structure.

(b) Schematic of the cell layout of the EM calorimeter modules.

Figure 3.8.: Section of the ATLAS LAr barrel calorimeter [66].

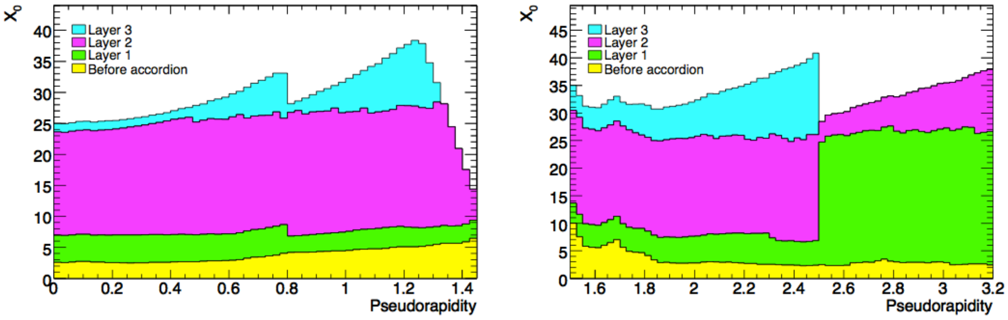

Figure 3.9.: Radiation lengths (X_0) for EM interactions due to detector material, as a function of $|\eta|$ [44].

Hadronic Calorimeters

The Barrel Tile Calorimeter (barrel and extended barrel) consists of plastic scintillating tiles as the active medium, sandwiched between steel absorbers. The scintillator tiles lie radially to the beam line with their faces in the $r-\phi$ plane (see Figure 3.10(a)). They use wavelength shifting fibres to capture the light signals from the tile edges, with the signals read out by two photomultiplier tubes (one per side), and the resulting analogue pulse (after shaping and amplification) is digitised at a frequency of 40 MHz. The energy loss during hadronic showers happens primarily via neutral pions which produce EM showers and other hadrons that also interact with nuclei in the absorber material, and these can both be measured. Energy loss also comes from nuclear binding energy/nuclear recoil, soft neutrons, neutrinos and muons, but this is lost completely. The non-compensating nature of the calorimeter implies that the response to hadronic showers is not fully captured as the ratio of energy lost through EM interactions (i.e. how many π^0s are produced) vs hadronic interactions cannot be known ahead of time and must be corrected for afterwards by calibration to the so-called jet energy scale. The energy resolution is between $2-3\%$ for the calorimeter response over η, however the additional energy scale uncertainty associated with the jet energy scale calibration is $\sim 4\%$ [67]. In this case the necessary calibration from the EM energy scale to a jet energy scale is determined for the average shower through momentum balancing in photon + jet events [68].

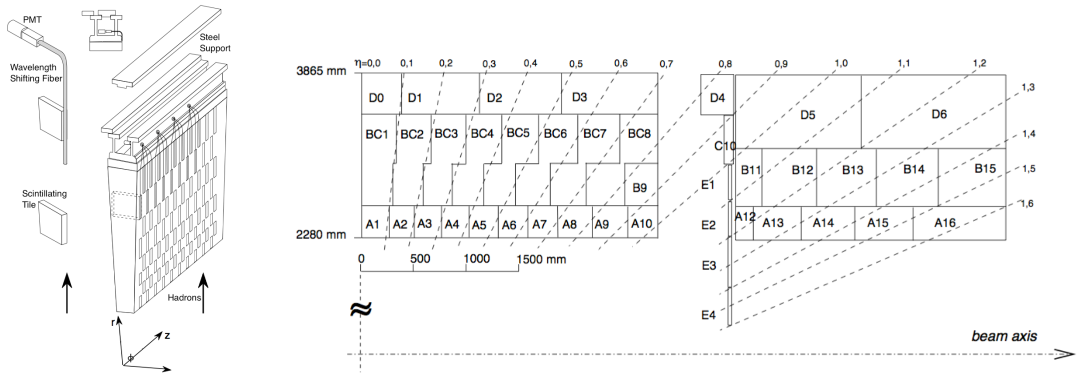

(a) Wedge section ($\Delta\phi \sim 0.1$) of the Tile Calorimeter [66].

(b) Quarter cross section of the Tile Calorimeter in the $r-z$ plane [44].

Figure 3.10.: Tile calorimeter schematics.

Liquid Argon is used as the active readout medium in the Hadronic End-cap Calorimeters to provide radiation hardness to the much higher hadron fluxes (plastic tiles would not last long in this environment: $1.5 < |\eta| < 3.2$).

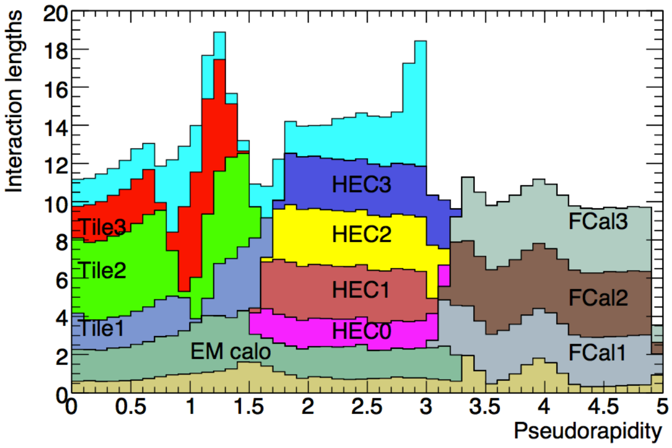

Figure 3.11.: Interaction lengths (λ) for hadronic interactions due to detector material, as a function of $|\eta|$ [44].

Forward Calorimeters

The Forward Calorimeters [69] are located 4.7 − 6.1 m from the interaction point in the range $3.1 < |\eta| < 4.9$ (see Figure 3.12). They are composed of three sections: the first (FCal1) is an EM calorimeter, with Copper absorber (for optimal resolution and heat removal) and LAr readout (but much thinner LAr gaps than in the main LAr calorimeters); the other two (FCal2 and FCal3) mainly use Tungsten as the absorber to minimise the lateral spread of the hadronic showers. The depth in hadronic interaction lengths (λ) corresponding to the material in the calorimeter system, including the FCal is shown in Figure 3.11, the depth of $\geq 10\lambda$ was chosen to ensure high energy hadronic jets are fully contained by the calorimeter and do not pass through into the muon system.

3.2.3. Muon Spectrometer

Surrounding the calorimeters is the muon system consisting of the Muon Spectrometer (MS) and the three Toroidal Magnets [70]. It is designed to provide momentum measurements for muons, which travel through the calorimeters as they do not typically lose energy via bremsstrahlung in the EM Calorimeter (compared to electrons, energy loss

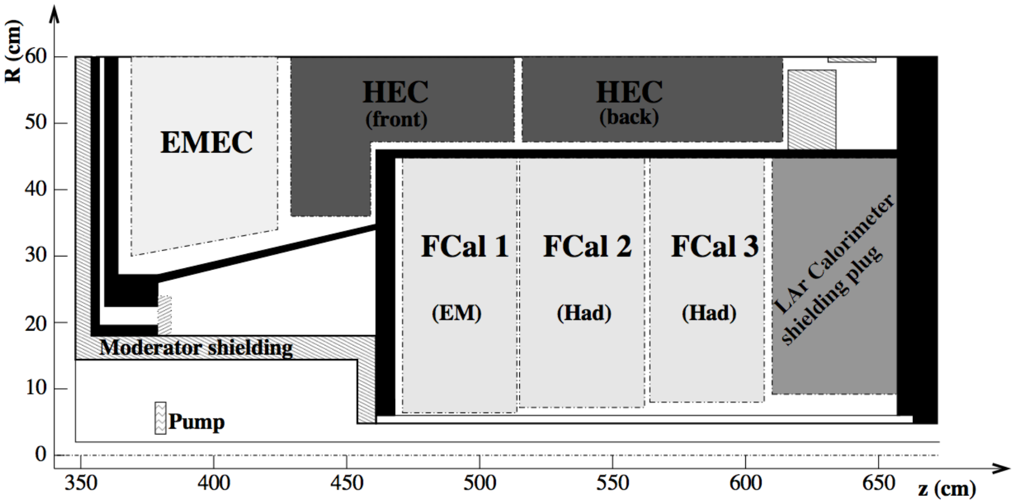

Figure 3.12.: Schematic of the ATLAS LAr FCal [44].

due to bremsstrahlung for muons is a factor $\frac{m_e^4}{m_\mu^4}$ less), and as they are leptons, they do not interact via strong interactions in the Hadronic Calorimeter.

The entire muon system extends out to $|\eta| < 2.7$, with the ability to trigger on muons passing p_{T} thresholds in the range $|\eta| < 2.4$. The magnetic fields produced by the toroids bend muons in the $r - z$ plane for charge and momentum measurements. These fields are provided by a large barrel 'air-core' toroid ($|\eta| < 1.4$) and two smaller end cap toroids ($1.6 < \eta < 2.7$), with the magnetic field in the transition region ($1.4 < \eta < 1.6$) provided by a combination of both the barrel and end cap magnets. The vast majority of momentum measurements are provided by Monitored Drift Tubes (MDTs) that operate in the range $|\eta| < 2.7$ and form the bulk of the MS (see Figure 3.13(a)). The basic detector elements of the MDT chambers are $\sim$3 cm diameter pressurised drift tubes filled with Ar (93%) and CO_2 (7%) at 3 bar. The electrode running through the centre of each tube is a 50μm thick, gold-plated tungsten-rhenium wire kept at a potential of 3080 V and there are a total of 354,384 tubes in total [71]. Due to the high particle fluxes in the range $2.0 < |\eta| < 2.7$, the innermost MDT end cap layer extends only to $|\eta| < 2.0$, with the remaining coverage provided by Cathode Strip Chambers (CSCs) which are able to withstand the higher rates while still providing the necessary resolution. Triggering, bunch crossing identification and additional coordinate measurements are provided by Resistive Plate Chambers (RPCs) in the range $|\eta| < 1.05$ and end cap Thin Gap Chambers (TGCs) for $1.05 < \eta < 2.4$.

The design of the MS has been driven by the goal of attaining stand-alone resolution of $\sim 10\%$ on 1 TeV muon tracks, corresponding to a 50μm uncertainty on a sagitta[3] of $\sim 500\,\mu$m along the $z-$axis. In order to obtain this nominal resolution, constant monitoring of the MDTs' relative positions as well as accurate mapping of the magnetic field is required. As a result the MDTs use 12,000 optical alignment sensors to monitor their relative positions and the magnetic field from the toroids is measured/monitored with ~ 1800 Hall sensors.

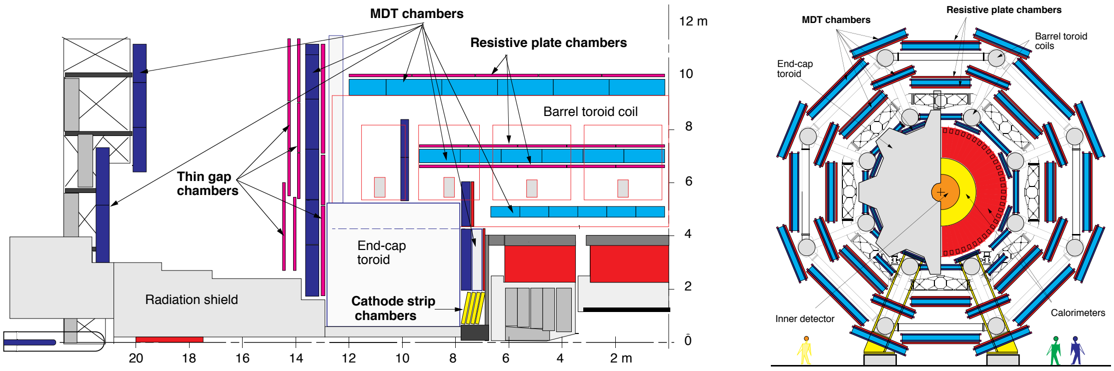

(a) Quarter cross section schematic view of the Muon Spectrometer and magnets.

(b) Transverse cross sectional schematic of the MS and toroids.

Figure 3.13.: The ATLAS Muon System [70].

3.2.4. Trigger and Data Acquisition System

The nominal bunch crossing rate at ATLAS is 40 MHz, and taking into account pileup interactions at each crossing, the expected event rate is of order ~ 1 GHz. In order to reduce this rate to one able to be saved to disk (at a maximum rate of 600 Hz in 2011) most *pp* collision events must be discarded. To perform this task a multi-stage Trigger and Data Acquisition system (TDAQ) is employed, a schematic representation of which is given in Figure 3.14. The TDAQ sifts through the multitudes of detector information to select the "interesting" event data to write to disk for offline analysis. The Trigger is currently split into three stages, a Level-1 trigger (L1), Level-2 trigger (L2) and Event Filter (EF), with refinement of event selection and background rejection (as well as the amount of computing required) increasing at each stage. The DAQ system buffers event data for readout and passes it back and forth through the triggers, logging the final

---

[3] Depth of the bending arc.

events by the types of triggers they pass and sending the event data to the CERN data centre to be written to disk (again, see Figure 3.14).

The majority of pp collision events are rejected at L1, which is a hardware based trigger using custom electronics with input from only the calorimeters (EM, Hadronic and FCal) and muon detectors (RPCs and TGCs). It must reject events if they do not pass preset E_{T} or p_{T} thresholds or $\sum E_{\mathrm{T}}$ or missing transverse energy requirements in less than 2.5μs of the bunch crossing time, reducing the rate of events passed to L2 by a factor of ~ 1000. The L1 decision (along with a timing signal) is broadcast to all the front-end electronics (FE) of the detector subsystems, and determines whether the event data can be pushed to read-out drivers (RODs). These RODs provide $\sim 1-2\%$ of this data to L2 to analyse the Regions of Interest (RoI) identified at L1. The L1 trigger uses a coarser calorimeter granularity than is available to make a quick decision, integrating the energy collected over ‘trigger towers’, $\Delta\eta \times \Delta\phi = 0.1 \times 0.1$ blocks of calorimeter cells, depicted in Figure 3.8(b). The L1 decisions from the muon detectors are based on coincidences of hits in the RPCs and TGCs to identify muon candidates, as well as uniquely identify the corresponding bunch crossing (L1ID). This L1ID for a given event is matched to the Bunch Crossing Identifier (BCID), based on clock signals from the LHC, by the ATLAS Timing, Trigger & Control system (TTC).

The High Level Trigger (HLT), consisting of L2 and EF, is a software system running on a PC farm containing dedicated EF compute nodes and XPUs (eXchangable Processing Units) which can be configured to perform L2 or EF processing on a run by run basis [72]. In total, there are $\sim 17,000$ CPU cores available at the HLT with L2 and EF decision times taking ~ 40 ms and ~ 4 s respectively. At L2 the RoI ($\eta - \phi$ coordinates from the nominal interaction point) identified at L1 are scrutinised using higher granularity information from the relevant detector subsystems *including* tracks built from hits in the ID. After L2 acceptance the whole event is built using the online reconstruction algorithms (essentially the same as the offline ones) and passed to the EF to impose more global requirements on the events. The trigger system is designed to select events by identifying high-p_{T} muons, electrons, photons, hadronically decaying taus, jets, and B hadron candidates, as well as using global event signatures, such as the total scalar sum of transverse energy ($\sum E_{\mathrm{T}}$) or the missing transverse energy, defined as $E_{\mathrm{T}}^{\mathrm{miss}} = \sqrt{(\sum E_x)^2 + (\sum E_y)^2}$. Over 2011 the TDAQ system operated with an overall efficiency of 94%, while the trigger criteria, so-called trigger menus, were updated as luminosity increased in order to keep event rates at each stage within acceptable limits. This generally required increasing trigger thresholds as luminosity increased. However, certain triggers may also be removed entirely, or multiple triggers combined based on the physics case made in support of a particular trigger or set of triggers. The triggers are inclusive, so events need only pass a single trigger chain to be saved to disk, thus a broad menu ensures that events featuring most physics of interest are saved.

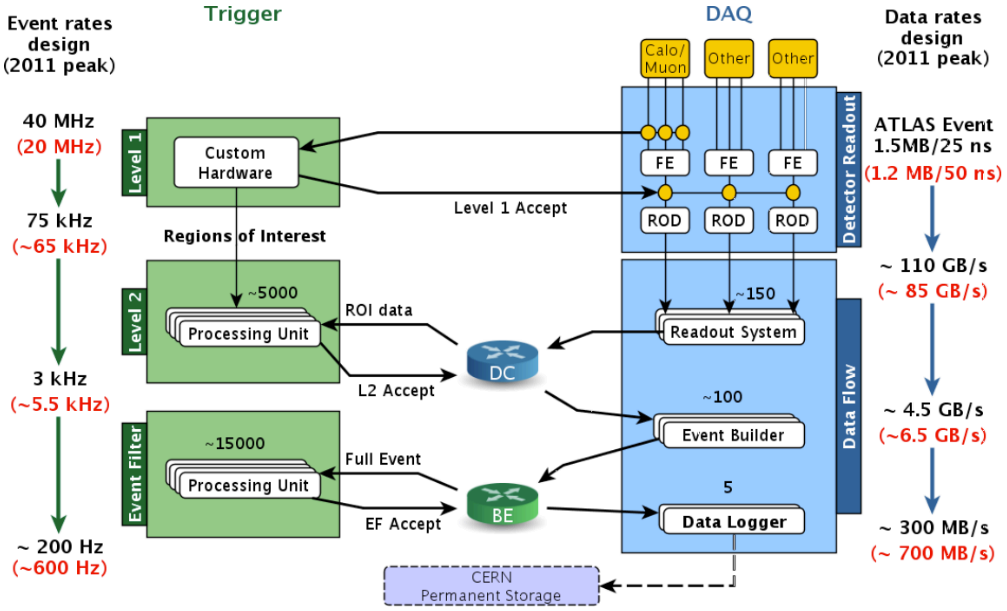

Figure 3.14.: Schematic representation of the ATLAS TDAQ system, with maximum rates for 2011 shown in parentheses [73].

3.3. Data and Monte Carlo Modelling

3.3.1. Data

The raw event data output by the TDAQ system, along with conditions and information on detector calibration and beam conditions, is processed initially within the Tier-0 data centre at CERN, the first of the four tiers that comprise the WLCG distributed computing infrastructure [74]. The Tier-0 consists of $\sim 10,000$ cpu cores and handles data recording, calibration, prompt event processing during physics runs, and data distribution to Tier-1 sites. There are 10 Tier-1 sites around the world ($\sim$35,000 cpu cores), responsible for: data reprocessing[4]; higher level processing by official ATLAS

---

[4] For example, if significant changes to a particular reconstruction algorithm are made all previously saved data will need to be reprocessed using the new algorithm.

physics groups; as well as permanent data storage. A further 70 Tier-2 centres ($\sim 65,000$ cpu cores) perform Monte Carlo modelling, end-user physics analysis and also provide storage for all of these datasets. An additional ~ 100 Tier-3 computing clusters are also used for end-user physics analysis.

The initial processing of the data requires saving reconstructed events built from digitised outputs of the detector (RAW data) for each event that passes one or more of the trigger chains. Such events have already been reconstructed to some extent at the Event Filter level and are further processed into the Event Summary Data (ESD) format, with each saved event taking ~ 700 KB. The D3PD data format used for analyses in Chapters 5 and 6 is derived from the Analysis Object Data (AOD) format which is itself distilled from the ESD, such that only the minimum information required is used for physics analysis – this is analysis dependent.

Data taking in a given year is split into periods, listed in Table 3.2 for 2011, for which significant changes in either ATLAS or the LHC operating parameters have occurred. Many of the measures used to characterise the *pp* collisions and detector status during a given run[5] are defined at a granularity of 1 Luminosity Block (LB), which is a 10 s–1 min interval over which any time-dependent measures can be integrated and averaged, and flags can be set for things like the SCT data quality for example. Luminosity measures, average pile-up per bunch crossing, run conditions, detector subsystems' status, trigger status and data quality are all considered on a per-LB basis. For analysis, Good Runs Lists are created from the lists of runs and LBs for which the LHC is providing stable colliding beams and all required detector sub-systems are operating as expected and at high efficiency (typically $> 96\%$).

3.3.2. ATLAS Event Simulation

To provide an expectation that can be compared with data in terms of known physics, or to optimise the searches for new physics and extract signals, Monte Carlo modelling of events is undertaken by first generating and then simulating the particle interactions as the protons collide and the products propagate out through the ATLAS detector. These simulated events also allow for evaluation of detector efficiencies and systematic uncertainties as the truth of the initially generated event is known. Producing simulated events is a multi-stage process (summarised in Figure 3.15) incorporating all of our current

---

[5] One full cycle of LHC fill → magnet ramp → stable beams and collisions → beam dump.

Period	$\mathcal{L}_{max}$ (10^{30} cm^{-2} s^{-1})	$\int \mathcal{L}\, dt$ (pb^{-1})	μ_{max}	Bunch Spacing (ns)
A	154	8.7	7.1	50
B	247	18	9.2	
D	659	182	7.3	
E	832	52	7.6	
F	1100	156	8	
G	1263	566	7.9	
H	1264	283	6.8	
I	1887	406	9.1	
J	1995	237	9.6	
K	2328	676	11	
L	3252	1599	16	
M	3848	1160	32	25

Table 3.2.: List of 2011 7 TeV *pp* ATLAS data taking periods with relevant collision information in terms of instantaneous luminosity, $\mathcal{L}$, and the maximum pile-up for a given run averaged over all runs in the period, μ_{max}.

understanding of particle physics – QCD in particular. The key technique allowing this modelling of the hadron collisions at the LHC is *factorisation*, in which the treatment of particle interactions is split into different regimes according to the size of the momentum transfer that takes place in a given interaction which is necessary due to the running of the strong coupling constant with the scale of momentum transfer, $\alpha_s(Q^2)$.

For cases of high momentum transfer such as the hard interaction, the quarks/gluons within the colliding protons interact to produce a small number of high energy quarks, leptons, Higgs or vector bosons. In this case the matrix element (as discussed in Section 2.2) can be computed at some scale, Q^2, to leading order (LO), next-to leading order (NLO) and even next-to-next-to leading order (NNLO) in some cases, using perturbative QCD and EW theory. In cases of low momentum transfer (~ 1 GeV), such as hadronisation consisting of non-perturbative QCD interactions, modelling cannot proceed from first principles and therefore must rely on phenomenological models that require tuning to data [75]. Finally there is the intermediate regime, set by the factorisation scale parameter μ_F, with $\sim 1\,\text{GeV}^2 < \mu_F^2 < Q^2$ – where the transition from one scheme to the other occurs as the parton shower progresses through to hadronisation. There are many methods by which general-purpose event generators deal with this, using general models of shower evolution with a number of tuneable parameters that must be obtained from data [76].

The production of simulated events begins by setting the content and momentum distribution of partons that make up the colliding protons. The Parton Distribution

Functions, and the DGLAP[6] equations describing the evolution of these functions with energy, determined from fits to deep inelastic scattering data [77] are used to set the composition of the colliding protons. Testing and validation of the evolution equations is primarily from the results of deep inelastic scattering experiments [78].

The hard interaction is simulated to a given order in perturbation theory with one of the main MC generator packages incorporating the latest theoretical calculations for the process being modelled. The hard interaction can also be modified by the addition of (high-p_{T}) gluon radiation from any coloured objects in the initial state (ISR) or final state (FSR) – usually treated separately.

In addition to the hard interaction, lower energy interactions between the other partons in the two colliding protons are considered as what is known as the underlying event. As the partons in the underlying event are colour connected to the partons involved in the hard interaction, they shower by radiating gluons as the energy of the products decreases up to the point where the QCD interactions become strongly interacting. The properties of this process are parameterised with the parameters determined from data, for example, the 2011 ATLAS MC produced with the general purpose event generators PYTHIA and HERWIG rely on the AUET2B [79] and the AUET2 [80] ATLAS Underlying Event Tune parameter sets respectively based on 2010 data. Additional soft *pp* interactions, 'pile-up', are modelled using parameter sets tuned using the most common types of *pp* interactions, so-called minimum bias data [75]. Modelling of all these soft processes is necessary because they occur with a frequency orders of magnitude greater than the hard processes of interest and therefore form a large background to most studies.

The products of these *pp* collisions and their interactions with the ATLAS detector are modelled with a full GEANT4 simulation of the detector itself [81, 82]. This simulation of the interactions and the resulting detector 'hits' – readout signals from the sub-detectors, and the digitisation of these detector hits, puts the simulated event on par with data as far as the physics object reconstruction algorithms go.

3.4. Physics Object Definitions

In particle physics experiments the reality of what happens in a given interaction is inferred from particular signatures in the readouts of the various sub-systems that

---

[6] Dokshitzer-Gribov-Lipatov-Altarelli-Parisi

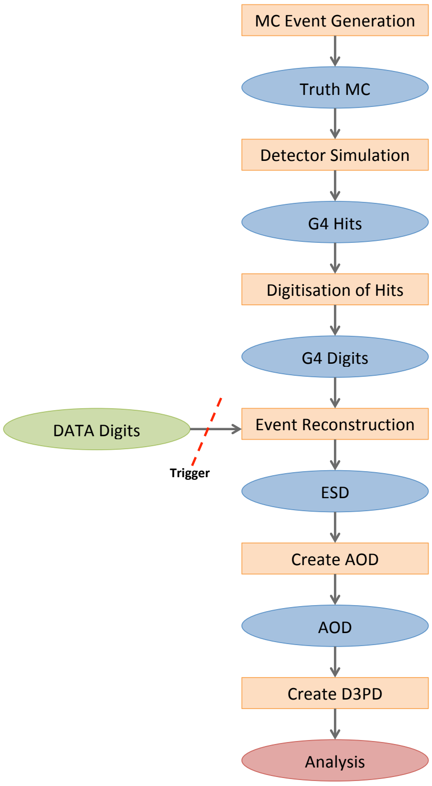

Figure 3.15.: Summary schematic of the ATLAS Data/MC event chain. The trigger is only applied to data, where events are discarded. MC events are not discarded, but instead contain what the trigger decisions would have been.

constitute the detector. This requires analyses be conducted on detector objects that have a certain probability of representing the actual particles that gave rise to their associated detector signatures.

In practice, the goal is to start with sets of tracks associated with charged particles traversing the detector, formed from hits in the Inner Detector and the Muon Spectrometer, and clusters of cells in the Calorimeter system in which energy has been deposited in order to reconstruct the 4-vectors of the various physics objects to be used for analysis [84, 85].

Objects are selected via various reconstruction and identification algorithms in order to cover different levels of purity (proportion of selected objects that are real) vs efficiency

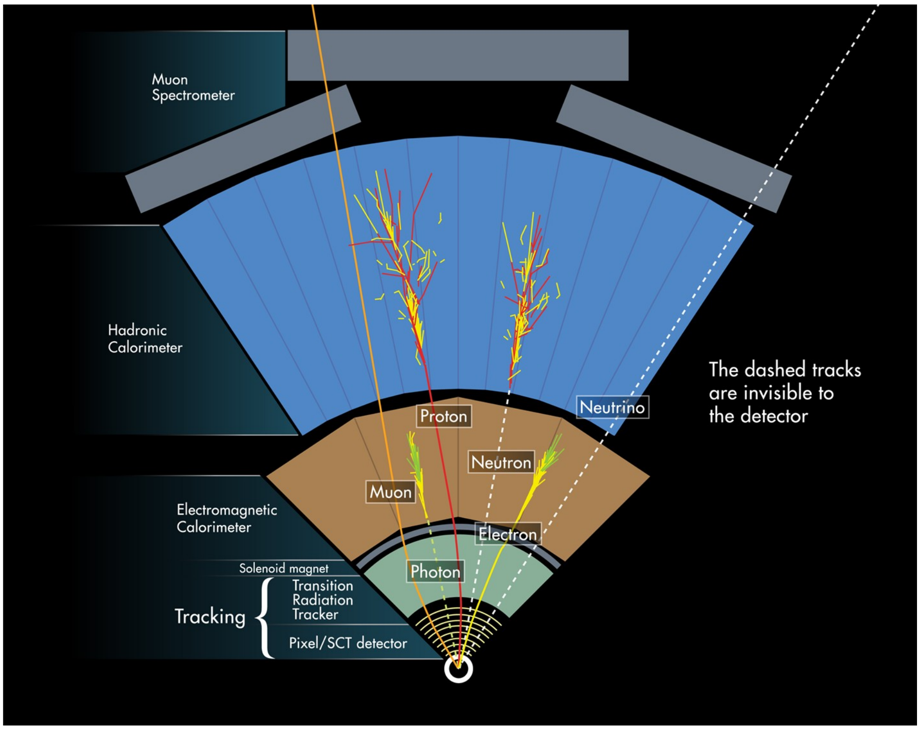

Figure 3.16.: Cutout cross section of the ATLAS detector indicating detector signatures of final state particles [83].

(proportion of real particles that are selected). Final object selection then occurs at the analysis stage depending on the particular requirements of the analysis. In this case reconstruction/identification/selection are covered here as they are applied in both Chapters 5 and 6. The physics objects used are those recommended by the ATLAS Top Working Group for use in 2011 data and these are outlined below with references provided for further details.

3.4.1. Primary Vertex

An event, as a single *pp* collision, is produced from a hard scatter between partons at a position defined by reconstruction of the primary event vertex. This reconstruction is based on two steps. First reconstructed tracks are associated to vertex candidates for a given bunch crossing using a vertex finding algorithm, this is based on the track impact parameter values to the candidate vertex. If tracks are incompatible with having originated from the same vertex they are used to seed a new vertex. Next the positions of the vertices (and corresponding uncertainties) are determined by a fit, using not only the relative associated track positions, but also constraining the vertex position in the transverse plane to the beam spot [86].

3.4.2. Electrons

Electron object reconstruction starts as a cluster of EM Calorimeter cells built out from a central "seed position", determined by a sliding-window algorithm[7]. Track matching to the cluster is then performed, where the reconstructed tracks are required to be within $\Delta\eta < 0.05$, and $\Delta\phi < 0.05$ ($\Delta\phi < 0.1$) if the track is bending away from (towards) the cluster seed to allow for bremsstrahlung effects. If there is more than one matching track the closest is chosen, and electrons in the forward region, $|\eta| > 2.5$, that cannot be matched to Inner Detector tracks are not considered in the analyses presented in Chapters 5 or 6. After track matching, the cluster energy is recalculated to account for energy deposited outside of the original cluster, after which the 4-momentum is formed using the final cluster energy and the 3-momentum as calculated from the track. The identification criteria that are used to classify reconstructed electron objects for 2011 analyses fall into three categories, `ElectronLoose++`, `ElectronMedium++` and `ElectronTight++`, which use cut-based quality requirements on the reconstructed electron object to achieve set working points for selection efficiency and purity (i.e. background rejection), with jet rejection factors of approximately 500, 5000, 50000, respectively [87].

The electron selection used requires `ElectronTight++` objects.The cluster position must lie within $|\eta_{\text{cluster}}| < 2.47$, excluding the transition region between the barrel and end-cap EM calorimeters, $1.37 < |\eta_{\text{cluster}}| < 1.52$. Additional requirements include ensuring that the electron candidate is isolated from additional jet activity present in the event via a cut on the ratio of energy deposited around the cluster position (in the range $0.2 < \Delta R < 0.3$) to that of the cluster itself, such that 90% of true prompt electrons satisfy the requirement. Also, a cut on the transverse energy, defined as $E_{\text{T}} = E_{\text{cluster}}/\cosh(\eta_{\text{track}})$, is set at 20 GeV.

Though electron objects are generally well modelled in MC simulation, it is necessary to correct for differences in identification efficiency between data and MC. For this purpose scale factors are calculated from data using a tag-and-probe method to form di-electron pairs produced from on shell Z decays to determine what the efficiency should be [87].

---

[7] Photons are reconstructed using the same clustering method.

3.4.3. Muons

Muon tracks are reconstructed independently in the Muon Spectrometer and the Inner Detector, then combined to form the muon candidate [88] – so-called “combined” muons, constructed via the MUID algorithm [89]. Low backgrounds ensure the purity and efficiency for reconstructing muons are high due to the requirement of a track in the Muon Spectrometer, while the Inner Detector track allows for precise vertexing and momentum measurements at low p_{T}. However the Inner Detector track requirement for the combined muons used in this case limits the acceptance to, $|\eta| < 2.5$.The momentum resolution for muons in this central region ranges from $\sim 1.7\%$ for muons with $p_{\mathrm{T}} \approx 10\,\mathrm{GeV}$ to $\sim 4\%$ when $p_{\mathrm{T}} \approx 100\,\mathrm{GeV}$.

In addition to this “tight” identification, additional quality requirements from the Inner Detector are included in the selection of muon objects. For example they must produce at least 7 hits in the SCT and Pixel detectors, with one of these hits in the Pixel B-layer. The ratio of the number of TRT hits that are outliers (hits that do not lie along a smooth track trajectory when pixel and SCT measurements are included) to the total number of TRT hits associated with the track must be less than 90%, with at least five hits (if $|\eta| < 1.9$) to form a smooth trajectory with the Pixel and SCT hits, and suppress fake tracks in the TRT. In order to reduce the backgrounds from muons produced in heavy flavour jets, isolation requirements in the calorimeter and tracking are also specified such that $E_{\mathrm{T}} < 4\,\mathrm{GeV}$ within a cone of $\Delta R < 0.2$ and $p_{\mathrm{T}} < 2.5\,\mathrm{GeV}$ within a cone of $\Delta R < 0.3$ around the track. The selected muons are then required to have $p_{\mathrm{T}} > 15\,\mathrm{GeV}$ (Chapter 5) or $p_{\mathrm{T}} > 20\,\mathrm{GeV}$ (Chapter 6). As for electrons, the identification efficiency for muons (shown in Figure 3.17) is scaled to that of muons in data using a tag-and-probe method with di-muon pairs, again, from the Z peak.

3.4.4. Jets

Hadronic jets resulting from colour recombination as high energy quarks or gluons produced in an interaction hadronise are constructed from groupings of calorimeter cells. Such objects are reconstructed using the anti-k_t clustering algorithm [91] from topological clusters in the calorimeter (approximately within a cone of $\Delta R < 0.4$), the algorithm allows small energy deposits from neighbouring jets to be allocated to the jet containing the nearest large deposit, altering the neighbouring jet’s shape if need be. The jet energy is calculated first at the EM scale, and then energy deposited in the Hadronic Calorimeter

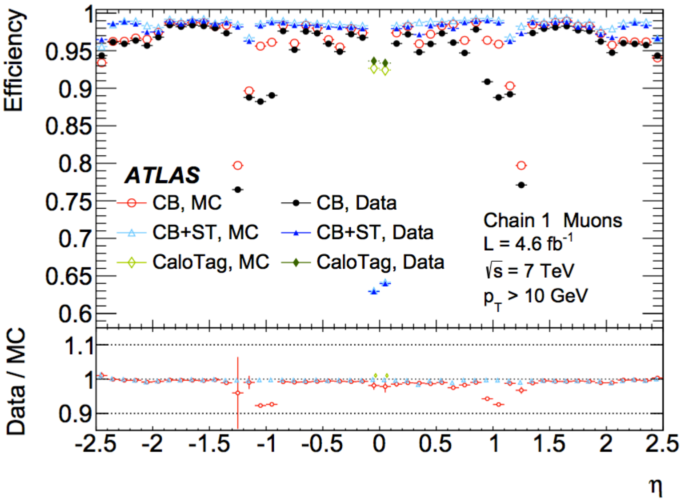

Figure 3.17.: Muon reconstruction efficiencies as a function of η as measured from $Z \rightarrow \mu\mu$ events in the 2011 data sample [90]. The combined muons used here are labeled "CB". Note: that the dips in efficiency at $|\eta| \approx 1.2$ in 2011 were due to some MDT chambers that had not yet been installed.

is calibrated using p_{T} and η dependent correction factors to restore the jet's true energy at the Jet Energy Scale [92, 93]. In order to select jets originating from the primary vertex, tracks pointing to the calorimeter clusters are combined to derive a probability that a given jet originated at a particular vertex, the so-called Jet Vertex Fraction (JVF).

A cut on the JVF ($|\mathrm{JVF}| > 0.75$) is important for separating jets from the primary vertex in high pile-up environments in which multiple secondary vertices lead to large numbers of additional jets [94], especially as it is insensitive to the absolute number of additional pile-up vertices. The selected jet objects are then required to have $p_{\mathrm{T}} > 20$ GeV (Chapter 5) or $p_{\mathrm{T}} > 30$ GeV (Chapter 6).

The selection of jets resulting from b quarks, necessary for the Charged Higgs analysis of Chapter 5, requires an additional tag on the selected jet objects based on reconstruction of a displaced vertex (due to the propagation of the B-meson formed from the b quark) close to the primary vertex. The tagger used is called `MV1`, which is a neural network-based combination of the outputs from three different algorithms (`IP3D`, `SV1` and `JetFitterCombNN`) – with the most important physical variables used for tagging being the transverse and longitudinal impact parameters (d_0 and z_0) of the reconstructed jet vertex to the primary vertex of the event [95, 96]. The cut point on this variable used to classify a jet as a b-jet is chosen to correspond to a selection efficiency of 70% (with a light jet rejection factor of $\sim$100), and as the tagging relies on tracking in the

Inner Detector the acceptance region is limited to $|\eta| < 2.5$. Efficiency scale factors to correct efficiencies as determined in various Monte Carlo samples to their counterparts in data samples are used after applying the tagging algorithm – this is necessary because although the tag should depend only on the properties of the jet under consideration, in reality there are many external factors that influence the tagging efficiency.

3.4.5. Taus

Taus that decay leptonically ($\sim 35\%$ of the time) produce electrons/muons and neutrinos, and are identified as either electrons, muons or missing momentum in ATLAS. Thus a tau object or tau-jet refers only to a hadronically decaying tau and will generally be denoted as τ_{had} hereafter. Hadronically decaying taus primarily decay to combinations of pions and/or kaons, with combinations containing only one charged hadron ($\sim 50\%$ of tau decays) called 1-prong taus, and combinations containing three charged hadrons ($\sim 15\%$ of tau decays) called 3-prong taus [97]. Reconstruction of a τ_{had} object is therefore the same as for jet objects with some additional requirements. All jet objects depositing $E_{\mathrm{T}} > 10\,\mathrm{GeV}$ in the calorimeter matched to either one ("1-prong") or three ("3-prong") Inner Detector tracks are considered as τ_{had} candidates. The identification algorithm used, `tau_tauLlhTight`, is based on the likelihood ratio between signal and background optimised in a multidimensional phase space, targeting an identification efficiency for real tau-jets of 30% with a background rejection factor against quark/gluon jets of ~ 100 (500) for 1-track (3-track) τ_{had} objects [98]. Dedicated electron and muon veto algorithms (`tau_EleBDTMedium` and `tau_muonVeto`) are then applied to reduce the chances that an electron or a muon will fake a τ_{had}, which reduces fakes for τ_{had} objects with only one charged track. The τ_{had} objects are required to have $p_{\mathrm{T}} > 20\,\mathrm{GeV}$, and lie within $|\eta| < 2.3$.

3.4.6. Transverse Missing Energy

The Missing Transverse Energy ($\vec{E}_{\mathrm{T}}^{\mathrm{miss}}$) is a 2-vector quantity defined in the transverse (xy) plane. It is derived from momentum imbalance in the transverse plane, and is defined primarily from the topological clusters in the calorimeter associated with physics objects on a per bunch crossing basis. The cluster positions in ϕ relative to the interaction point is what allows the $E_{\mathrm{T}}^{\mathrm{miss}}$ to be associated with a direction in the transverse plane. The definition used here is termed `MET_RefFinal_em_tightpp`, and derives from electrons, high-p_{T} jets, low-p_{T} jets and muon objects. In order to contribute a term ($\vec{E}_{\mathrm{T}}^{\mathrm{electrons}}$) to the calculation of missing transverse energy, electrons must be identified via the `ElectronTight++` criteria and have $p_{\mathrm{T}} > 10\,\mathrm{GeV}$. Jets are split into two p_{T} ranges: soft jets with $7\,\mathrm{GeV} < p_{\mathrm{T}} < 20\,\mathrm{GeV}$, with energy calculated at the EM scale; and jets with $p_{\mathrm{T}} > 20\,\mathrm{GeV}$ corrected to the full EM + Jet Energy Scale. As muons do not deposit much energy in the calorimeter, the muon term is taken as the $\vec{p}_{\mathrm{T}}$ of muons in the full acceptance range, $|\eta| < 2.7$, of the Muon Spectrometer. In addition to these objects, a so-called "cell out" term vectorially sums any remaining energy in the calorimeter at the EM scale. Thus the magnitude of

$$\vec{E}_{\mathrm{T}}^{\mathrm{miss}} = -\left(\vec{E}_{\mathrm{T}}^{\mathrm{electrons}} + \vec{E}_{\mathrm{T}}^{\mathrm{soft\ jets}} + \vec{E}_{\mathrm{T}}^{\mathrm{jets}} + \vec{p}_{\mathrm{T}}^{\mathrm{muons}} + \vec{E}_{\mathrm{T}}^{\mathrm{cell\ out}}\right) \quad , \tag{3.4}$$

constitutes the $E_{\mathrm{T}}^{\mathrm{miss}}$, with a typical resolution proportional to $\sqrt{\sum E_{\mathrm{T}}}$ of the event as shown in Figure 3.18.

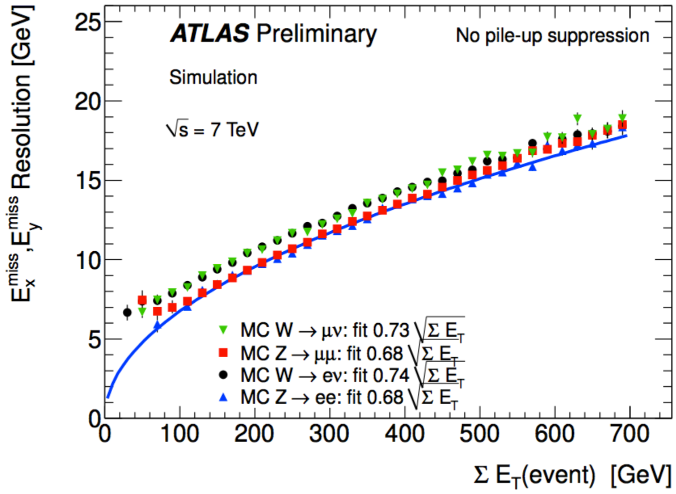

Figure 3.18.: Resolution for x and y components of $E_{\mathrm{T}}^{\mathrm{miss}}$ as a function of the total E_{T} in the event [99].

Chapter 4.

SCT Beam Loss Studies

This chapter covers a study undertaken during the LHC startup period (end of 2009, beginning of 2010) and concerns potential damage to the ATLAS SCT readout chips that would result from the proton beam scraping the beam pipe or a collimator near ATLAS. Such a scenario could be realised as the result of problems related to the steering of the LHC beams around the machine at injection, or as they are brought into alignment for collisions — as the machine was so new and largely untested at this time. The impetus for this study also came, in part, from the 2008 LHC accident, where during the ramping-up of current in the main dipole circuit at the nominal rate of 10 A/s, a resistive zone developed leading to a resistive voltage of 1 V at 9 kA ultimately resulting in the helium leak and subsequent magnet quenches [55]. In the case of loss of control while the LHC was circulating proton beams it was necessary to ensure that in the event of beamloss (prior to dumping the beams) near ATLAS any resulting damage would not shut down the experiment for an extended period of time, or force it to operate without any of its key sub-detectors. As the SCT is important in the reconstruction of charged tracks — without it the tracking resolution and particle identification at ATLAS would be severely crippled.

4.1. Introduction

In the case of loss of control of one or both of the LHC beams during operation, the Semiconductor Tracker (SCT) [100] in the ATLAS detector may be particularly vulnerable. The purpose of this work is to determine the amount of damage the readout electronics of the SCT modules would sustain under such beamloss scenarios.

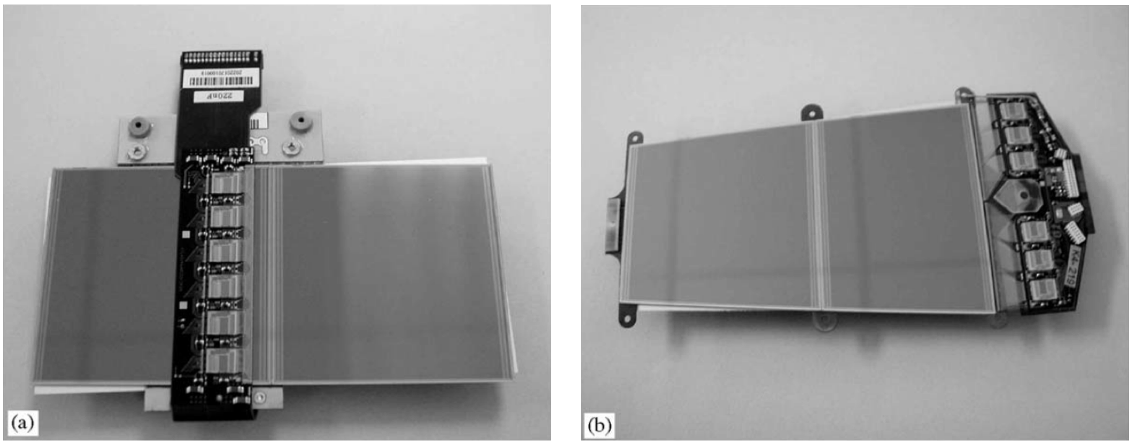

(a) An SCT barrel module [101]. The n-type silicon bulk is instrumented with 768 p-type implants (strips) that run along the length of the module (& parallel to the beam axis). The strips are connected via Al electrodes to 6 `ABCD3T` binary readout chips [102]. i.e. 128 readout channels per chip.

(b) An SCT end cap module [103]. Strips run along the length of the module fanning out such that they lie in the ϕ direction. The end-cap modules have the same number of strips and readout chips as their barrel module counterparts.

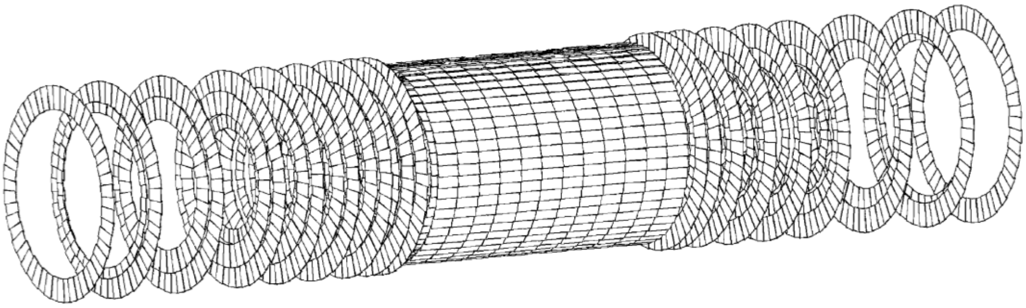

(c) Representation of the arrangement of the SCT outer barrel and end-cap modules within ATLAS [104]. Total length from end-to-end is $\sim$5.6 m.

Figure 4.1.

As discussed in Section 3.2.1 the SCT is a silicon microstrip tracking detector vital for the reconstruction of charged tracks in the inner detector. Close to the ATLAS detector are a pair of collimators designed to shield the inner triplets of superconducting quadrupole magnets from particles produced at the interaction point. Known as the TAS (Target Absorber Secondaries) this collimation system is comprised of two 1.8 m long copper blocks at $18.0 < |z| < 19.8$ m (i.e. either side of the ATLAS cavern) [105].

The two accident scenarios considered most likely were that the proton beam would either scrape the beam pipe in the vicinity of the detector, or scrape the TAS collimator before it reached the detector. In the event that the ATLAS Beam Conditions Monitor

[106] (designed to trigger an abort before such scrapes happen) is not functioning correctly, the resulting flux of secondary particles passing through the SCT would cause much more charge to be collected by the SCT module strips than would be the case under normal operation. The front-end `ABCD3T` readout chips [102] (see Figures 4.1(a) & 4.1(b)) are rated to handle a maximum charge of 5 nC in a 25 ns window collected by any one of these strips. Therefore the 5 nC in a 25 ns limit is used as the threshold beyond which may lead to damage of the readout chips.

In order to determine whether either of these two scenarios would result in more than 5 nC being collected by any of the individual strips of the SCT modules, the amount of charge collected by individual strips of the SCT is determined approximately for each scenario from the full simulation events (Subsections 4.4.1, 4.4.2). However, due to low statistics a method of sampling-with-replacement was developed to more accurately determine the charge per strip distribution (Subsections 4.4.3, 4.4.4). This determination of charge collected per strip was ultimately used to gauge the potential for damage to the SCT front end readout chips under the two scenarios.

4.2. Previous Experimental Studies

The finished SCT modules have previously been subjected to three types of experimental tests: a test beam study; irradiation with a Nd:YAG laser; and bench top hardware tests.

In 2004 the performance of the SCT modules was tested using a ~ 180 GeV pion beam, part of the ATLAS combined test beam [107]. In this case the amount of charge collected by the strips did not (and was not intended to) reach a level at which the front-end readout chips would sustain any damage, so their real-world limitations were not tested.

Two tests of the SCT modules using a Nd:YAG laser [108, 109] were carried out in 2005. The laser light had an energy just above the Si band gap energy (~ 1.1 eV). One of these was a quality assurance test [108] of the barrel modules and, again, did not cause enough charge to be collected by the strips to do any damage. However the second test [109], meant to simulate 'beam splash' effects on the SCT modules, is particularly relevant here. The laser was pulsed at a frequency of 1 kHz, with pulse widths of 6 ns (FWHM) and the bias being applied across the test module ranged between 150 V–400 V. The laser pulses covered single strips at a time and charge collection of order 2-3μC/6 ns resulted.

The `ABCD3T` readout chips connected to these strips failed unless the bias voltage was set at 150 V, the minimum of the range. This amount of charge is approximately three orders of magnitude above what a single channel on a readout chip is designed to carry.

In August 2009, further hardware tests attempted to verify the 5 nC/25 ns/channel limit and deliver fatal charge doses to the chips. It was found that above this threshold, individual channels within the readout chips did indeed fail, and the channels either side of the damaged one became particularly noisy for ~ 15 mins, but the rest of the chip functionality was retained. The readout chips would survive provided charge collection is less than 5 nC/25 ns/channel but were shown to always fail if the charge collected is greater than $\sim$ 2-3 μC/6 ns/channel.

As a result of this previous work, 5 nC/25 ns/channel is taken to be the safe upper limit, beyond which failure is possible but not necessarily guaranteed. The primary aim of the sections that follow is to obtain the amount of charge collected per strip under two plausible simulated beamloss scenarios and to see how it compares with these results.

4.3. Beamloss Scenarios Studied

At nominal luminosity an LHC bunch contains 1.15×10^{11} protons, with these bunches spaced 25 ns apart. Though the bunch spacing has not yet reached this nominal value, the number of protons per bunch has reached, and exceeded the nominal value (see Table 3.1). The protons in a bunch are distributed in an approximately 2D gaussian distribution in the plane transverse to the beam, with the two primary LHC collimators clearing any protons outside 6σ (which is of order a few mm, but dependent on run conditions) of this distribution. For the rest of this study we assume a *moderate beam scrape*, defined here as protons in the outer region of the beam (between 6σ and 3σ) colliding with the beam pipe or the TAS collimator. The number of protons colliding is therefore taken to be $\sim 0.1\%$ of the bunch (1×10^8 protons) — this is approximately the top third of the protons between 3–6σ in the bunch that would be involved in the scrape. Any more than this (i.e. a deviation greater than 3σ) would almost certainly result in a beam dump. However, this moderate scrape assumption is made with the understanding that the final results of the total charge collected per strip can, in principle, be rerun for any number of events. The resulting flux of secondary particles due to such a scrape may conceivably result in a much larger amount of charge being collected than the SCT is able to cope with.

Charge collected by a strip, resulting from a single particle passing through the silicon of a module constitutes an SCT hit. If the hits are the result of protons from a single bunch colliding with the beam pipe or TAS collimator, this charge would be deposited within a 25 ns window (i.e. the minimum bunch spacing at the LHC). It is the total charge collected by any single strip (in 25 ns) that we are concerned with here. In this context an “event” is defined as a single proton colliding with either the beam pipe or the TAS collimator.

The two particular scenarios simulated for such occurrences were: 7 TeV (i.e. the nominal beam energy) protons colliding with the TAS collimator (34,960 simulated events); and 450 GeV (i.e. the LHC injection energy) protons colliding with the beam pipe (65,000 simulated events). The numbers of events listed were the numbers available in the form of `HITS`[1] files containing all the low level information regarding charge deposition in the SCT. These files were produced directly from GEANT4 [82] simulation of *individual* proton collisions with either the beam pipe or TAS collimator with secondary particles showering through the SCT. Now, the actual number of events in such scenarios is assumed to be more like 10^8 per bunch (i.e. $\sim 0.1\%$ of the bunch as previously stated), but due to a combination of time taken and memory constraints the numbers of simulated events are limited to those listed above. The simulated events were produced one proton at a time, as it would be far too computationally intensive to simulate such a large number of events concurrently such that their collective effects on the detector are accounted for. This is the one major point overlooked in this analysis – particularly in relation to the breakdown of the module bias voltage that can occur with too many free charge carriers in the module silicon. This was in fact the case in previous beamloss stress tests of the CMS silicon tracker [110]. Such an effect would protect the ATLAS `ABCD3T` readout chips to some extent as the breakdown of the module bias voltage would lead to less charge being collected, but this effect will not be considered here.

Though any similar beamloss scenario to those studied here would be unlikely in reality, such scenarios are worthy of study because the resulting damage could have the potential to shut down the SCT for an extended period of time. It should be noted that the total and relative probabilities of the two scenarios studied were not assessed.

---

[1] GEANT4 simulated signals in the detector produced using ATLAS geometry `GEO-02-01-00` in ATHENA 14.2.20.1 with configuration tag `e347_s464`.

4.4. SCT Charge Collection Study

The methods discussed in this section were carried out in a general attempt to determine how much charge could be collected by the strips of the SCT modules under the scenarios described in Section 4.3. Subsections 4.4.1 and 4.4.2 focus on the charge distributions of the 65,000 fully simulated beam pipe scrape events. A method of sampling hits from these events ('with replacement') for 10^8 events is developed in Subsections 4.4.3 and 4.4.4 and corresponding results are presented.

Figures 4.2 and 4.3 contain 2D histograms that are functions of *Strip number* and *eta_module*. For a given side (inner-1 or outer-0) of a particular barrel layer (0-3) or end cap wheel (0-8), these two numbers will uniquely label all strips side-by-side in that end cap wheel or barrel layer (see Figures 3.6 and 4.1(c)). The strip number, counts the strips around the ϕ direction, while eta_module labels the modules in η but does not correspond to actual pseudorapidity values defined by the co-ordinate system.

4.4.1. Determining Charge Deposition Using the SCT Digitisation Package

The rest of the analysis was performed using the 450 GeV beam pipe scrape scenario, as this had the most fully simulated events available to use. The final result will be compared with that of the 7 TeV TAS scrape case. The files for the 450 GeV beam pipe scrape events were used as the input and the charge deposition and strip information was saved as ROOT [111] ntuples just before the digitisation step (at which point the charge information is lost).[2] It was done this way because the ntuples will be required for the sampling-with-replacement method described in Subsection 4.4.3. Importantly the digitisation package used accurately represents the module dimensions and the strip positions; it also shares charge deposited over neighbouring strips, creating clusters of strips that all register a signal due to a traversing particle. Using this method, 'charge maps' — 2D histograms of barrel layers and end cap discs weighted by charge, are created, and these are shown in Figures 4.2 and 4.3. The charge per strip was linearly scaled (i.e. multiplied by $\frac{10^8}{\#\text{events}}$) to get an idea of the order of magnitude for the charge per strip after 10^8 events (Figure 4.4).

---

[2] The SCT hits are processed through the `SCT_Digitization` package in ATHENA 14.2.25 with ATLAS geometry `GEO-02-01-00`.

4.4.2. Results Using the SCT Digitisation Method

Figures 4.2 and 4.3 contain the charge maps produced using this method — they are effectively the unrolled layers and wheels shown in Figure 4.1(c). In these layers, the strip number ('strip #') corresponds to the ϕ co-ordinate, and the 'eta_module' value can be thought of as labeling the modules in η (though the numbers are not the actual positions in η). For the 4 end cap wheel sides and 4 barrel layer sides shown, each bin contains the charge for approximately 350[3] strips. Only the outermost and innermost end-cap sides are presented as these will receive the lowest and highest particle fluxes respectively for a given side of the detector. The general direction of the secondary particles can be deduced from the charge maps in Figures 4.2 and 4.3. The initial protons travel from the $-z$ side of the detector to the $+z$ side, colliding with the top of the beam pipe. The outer side of the outer-most end cap wheel on the $-z$ side of the detector (Figure 4.2(a)) gets the least charge, while strips in the inner-most end cap wheel on the $+z$ side (Figure 4.2(c)) collect approximately the same amount of charge as those of barrel layer 1 (Figure 4.3(c)). The greatest amount of charge is collected in barrel layer 0 (Figure 4.3(d)). Only the inner sides (side 0) of the barrel layers are presented as these are representative of the charge maps for the outer sides (side 1).

The number of strips receiving a given charge is plotted (Figure 4.4), with the charges collected by the strips scaled by $\frac{10^8}{65{,}000}$. The other reason for the scaling is to allow comparison with the final charge per strip plot for the sampling-with-replacement method (to be described in Subsection 4.4.3) for 10^8 events.

Though the aforementioned plots are useful for providing the right order of magnitude for the average charge per strip, this is not a valid way of determining the number of strips that collect a charge greater than 5 nC. This is because the distributions for charge per strip plots depend on the number of events being used. Figure 4.5 shows the large shape difference in charge-per-strip distributions between linearly scaling from 10,000 of the fully simulated events as opposed to the 65,000 available. This is primarily due to the fact that for lower numbers of events, some proportion of strips will not collect any charge and hence scaling fails in these cases. Even after it is ensured that all strips collect some amount of charge, the relatively low statistics ensure the scaled distributions will be unreliable at the low and high ends of the charge scale. Ideally this determination of the charge per strip distribution would be done for 10^8 individually simulated events.

---

[3] This large bin size (equivalent to 350 strips) is used simply to make the charge distribution clearer in the figures.

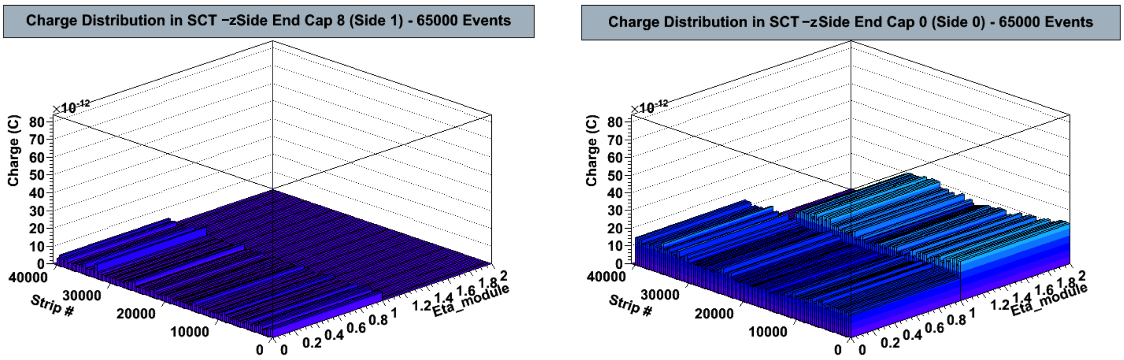

(a) Outer-most end cap wheel, on the $-z$ side. **(b)** Inner-most end cap wheel, on the $-z$ side.

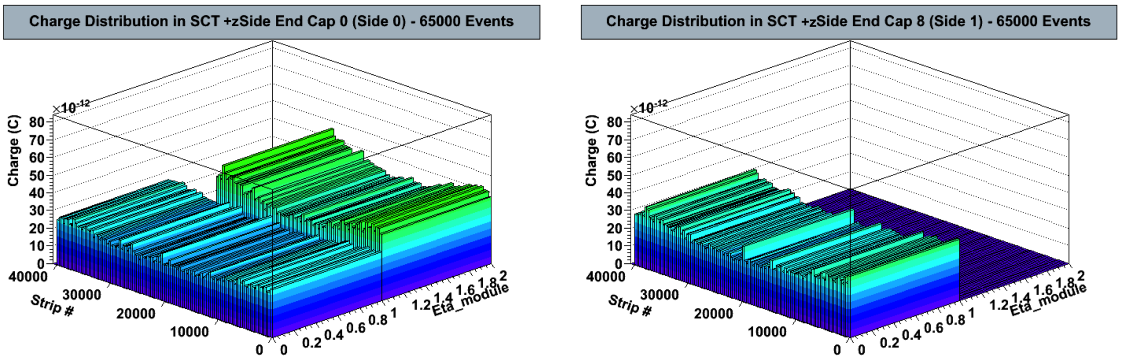

(c) Outer-most end cap wheel, on the $+z$ side. **(d)** Inner-most end cap wheel, on the $+z$ side.

Figure 4.2.: How charge is distributed in the 450 GeV beam pipe scrape scenario on a given side of a selection of end-cap wheels.

Now it would seem that the distributions (appropriately normalised) could be fitted with some simple function (e.g. a Poisson distribution). However, this would not take into account the spread in charge collected per hit, which should follow a Landau distribution up to some cut-off point [112], or the non-uniform distribution of hits in the detector, resulting from the particular scenario being studied. Since the range of concern for maximum charge per strip seems to lie in the tail of the distribution - the number of strips collecting more than 5 nC would be very sensitive to any fit. Therefore a method of sampling with replacement of events, as well as the hit clusters that result from them, seemed to be the most appropriate way to determine the number of strips collecting more than 5 nC of charge for 10^8 events. Full simulation of 10^8 events is not an option, as it would be far too computationally intensive.

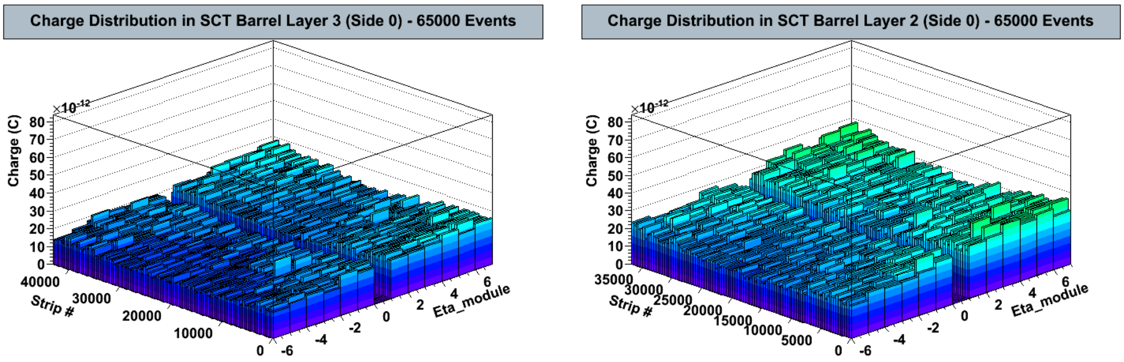

(a) Barrel layer 3 (side 0). **(b)** Barrel layer 2 (side 0).

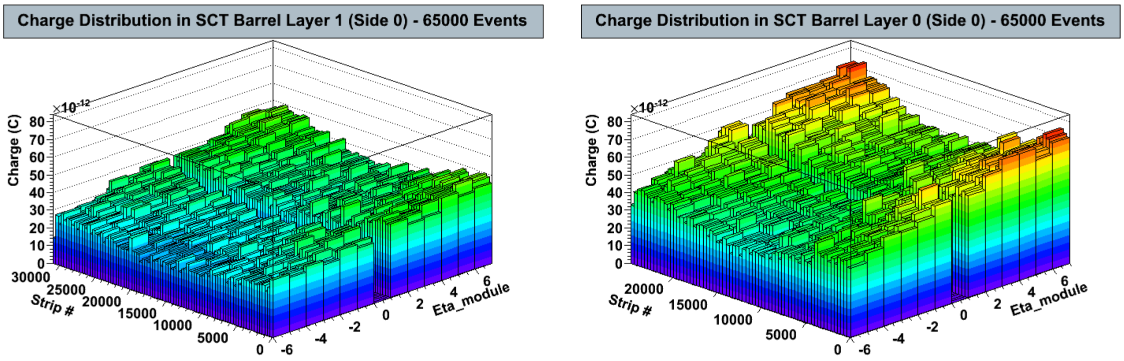

(c) Barrel layer 1 (side 0). **(d)** Barrel layer 0 (side 0).

Figure 4.3.: How charge is distributed in the 450 GeV beam pipe scrape scenario on a given side of a selection of barrel layers.

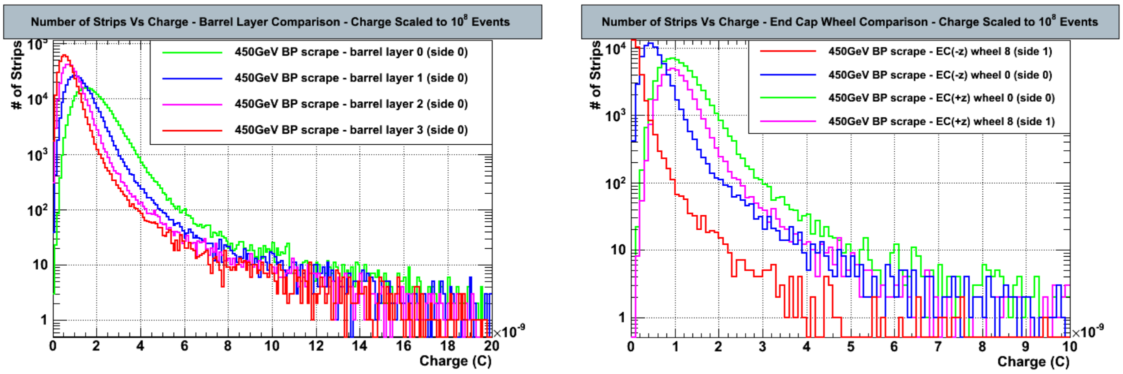

(a) Charge per strip distribution comparison - barrel layers. **(b)** Charge per strip distribution comparison - end cap wheels.

Figure 4.4.: The number of strips collecting a given charge from the charge distributions in Figures 4.2 and 4.3 - charges have been scaled by a factor $\frac{10^8}{65000}$.

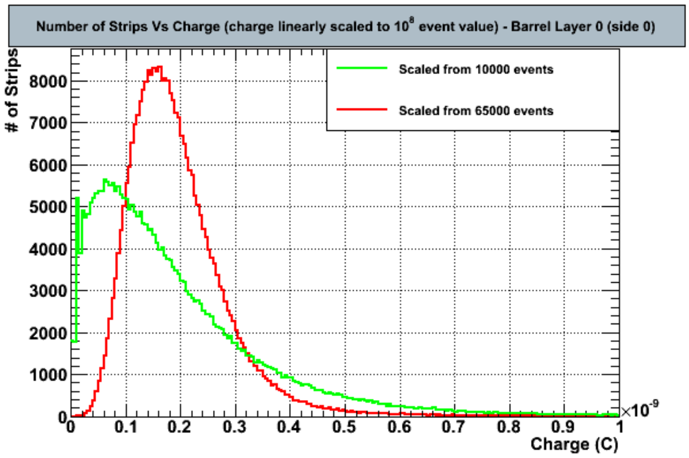

Figure 4.5.: Comparison of number of strips with a given charge for 450 GeV beam pipe scrape case (barrel layer 0). The green line has scaled charges from 10,000 events up to 10^8 and the red is scaled from 65,000 events.

4.4.3. Sampling-with-replacement Method

For this method, the focus was on barrel layer 0 for the 450 GeV beam pipe scrape case, as this was by far the layer in which the most charge was collected in this scenario. The steps of the method are listed below:

- Choose an event at random from the sample of fully simulated events (65,000 in this case).
- If the event produced clusters of strip hits in the relevant barrel layer or end cap wheel.
  - For each of these clusters, *choose a 'new strip'* in the relevant layer/wheel.
  - Assign the charge collected by the centre strip of the cluster to this new strip, and the other charges that make up the cluster to the corresponding adjacent strips.

This is done as many times as required — in our case it will be for 10^8 events.

Selecting A New Strip

Initially each new strip was chosen by sampling[4] the distribution of hits in the relevant layer/wheel. This distribution is shown in Figure 4.6(a). However, upon attempting to validate this method by comparing charge per strip histograms for 65,000 sampling-with-replacement (SWR) events with 65,000 fully simulated events it was found they did not agree (Figure 4.6(b)).

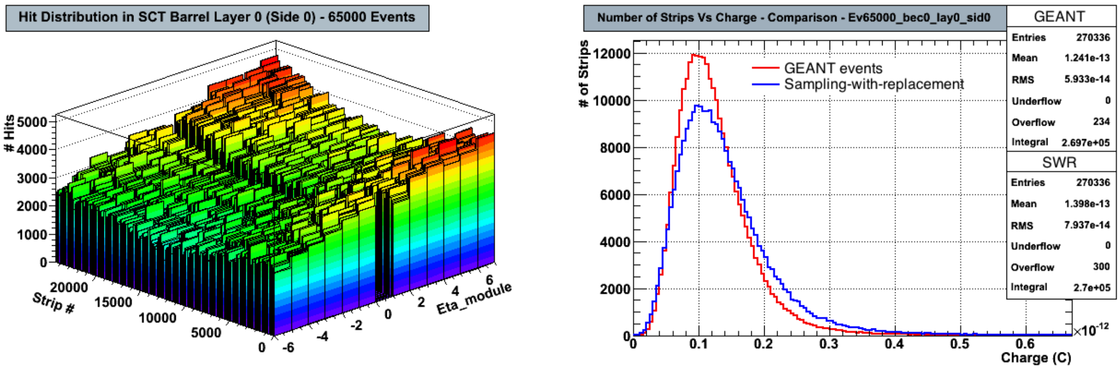

(a) Hit Map for 450 GeV BP scrape, Barrel Layer 0 (side 0) — formed from 65,000 sampling-with-replacement events.

(b) Comparison of "charge per strip" histograms — 65,000 sampling-with-replacement (SWR) events against fully simulated (GEANT4) events. The number of entries in each distribution corresponds to the number of strips in the modules in side 0 of barrel layer 0 ("_bec0_lay0_sid0").

Figure 4.6.: Sampling the hit distribution, (a), to choose a new strip for the sampling-with-replacement method leads to a disagreement in the charge-per-strip distributions, (b).

The reason for this disagreement turned out to be a dependence of cluster size (i.e. the number of strips covered by the cluster) on detector geometry that was not being accounted for. Though the dependence of cluster size on geometry appears relatively minor, not accounting for it results in a broader charge per strip distribution than should be the case (see Figure 4.6(b)). Therefore, the new strips had to be chosen using a different method.

The method settled upon was to choose the new strip by first creating histograms of the cluster size versus the position of the centre strip of the cluster. This requires histograms of 'cluster size Vs strip#' (Figure 4.7(a)) and 'cluster size versus eta_module' (Figure 4.7(b)) for each cluster. Depending on the size of the cluster to be relocated, the

---

[4] Using the `GetRandom2()` function in ROOT.

appropriate 1D slice is obtained from these two histograms and the slices are treated as probability distributions. These distributions are then sampled to get a strip# and eta_module value for the new strip. It should be noted that the very large cluster sizes (covering of order 100 strips) are rare, but do occur and correspond to particles that loop around in the magnetic field or those that simply enter the detector at very shallow angles.

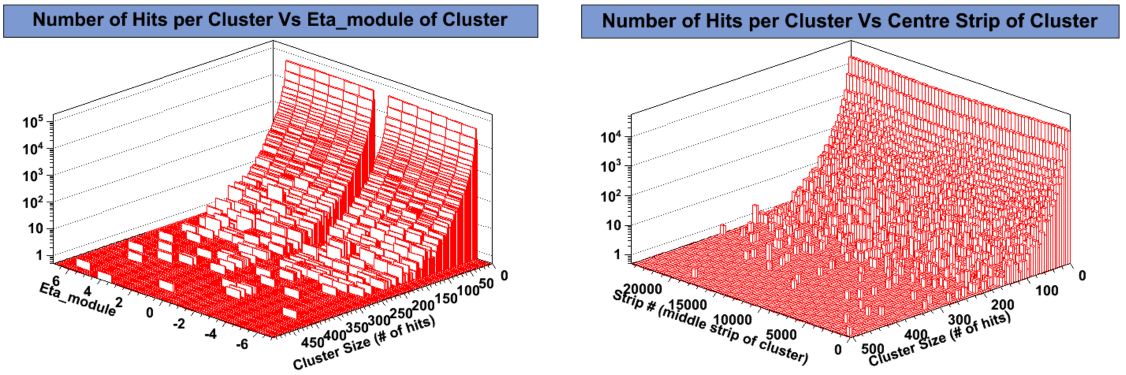

(a) Cluster Size versus Eta_module of Cluster, 450 GeV BP scrape (barrel layer 0, side 0).

(b) Cluster Size versus Centre Strip of Cluster, 450 GeV BP scrape (barrel layer 0, side 0).

Figure 4.7.: Cluster Size vs Position distributions for the total number of clusters used for sampling-with-replacement method.

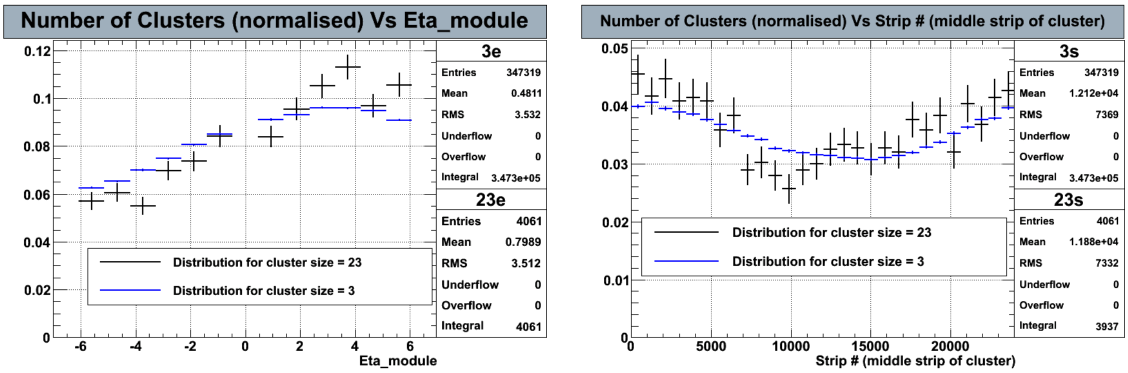

(a) Slices of Figure 4.7(a) at a cluster sizes of 3 (labeled “3e”) and 23 (labeled “23e”).

(b) Slices of Figure 4.7(b) at a cluster sizes of 3 (labeled “3s”) and 23 (labeled “23s”).

Figure 4.8.: Cluster size dependence on position for barrel layer 0, for 450 GeV beam pipe scrape scenario. The area under each slice has been normalised to 1 to facilitate comparison of the slice shapes, with the number of entries corresponding to the number of clusters in each slice.

Figure 4.8 shows the differences in distribution of the number of clusters for two slices (of cluster size 3 and 23) of the 2D histograms in Figure 4.7. Though it is not a large difference, not accounting for this effect is enough to produce the smearing out of the charge per strip distribution that can be seen in Figure 4.6(b). From the above examples it is clear that some information was lost by not accounting for the change in distribution in the barrel layer with cluster size. Validation of this method will be presented next (Subsection 4.4.4), with results for 10^8 sampling-with-replacement events for both scenarios to be shown in Subsection 4.4.5.

4.4.4. Sampling-with-replacement Method Validation

In Figure 4.9 a comparison is made between the charge maps produced using 65,000 sampling-with-replacement events and 65,000 fully simulated events. The plots are again for the 450 GeV beam pipe scrape case, barrel layer 0.

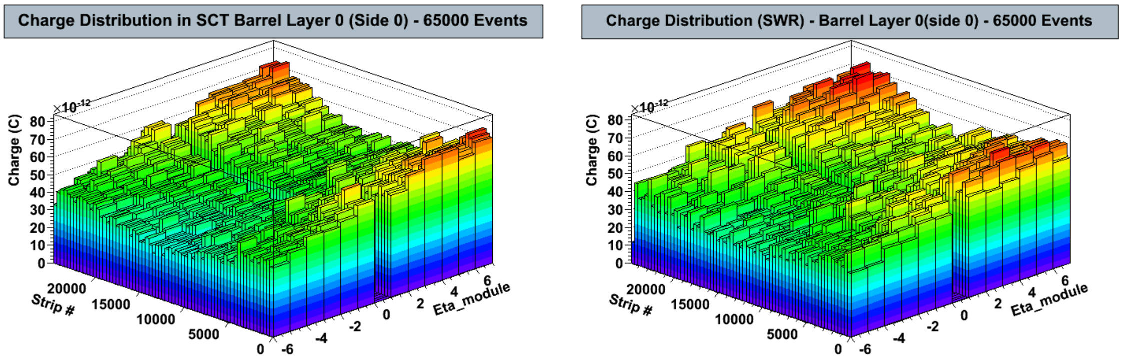

(a) Fully simulated events (65,000) - charge map (barrel layer 0, side 0).

(b) sampling-with-replacement events (65,000) - charge map (barrel layer 0, side 0).

Figure 4.9.: Comparison of charge distributions for fully simulated events, (a), and sampling-with-replacement events, (b). The 450 GeV beam pipe scrape scenario is used.

In Figure 4.10 the charge per strip histograms are compared for 10,000 sampling-with-replacement and fully simulated events (Figure 4.10(a)) and for 65,000 sampling-with-replacement and fully simulated events (Figure 4.10(b)). The plots show good agreement between the charge-per-strip distributions and indicate the method (with the addition of the cluster size consideration) is modelling the events well. This will be discussed further in Section 4.5.

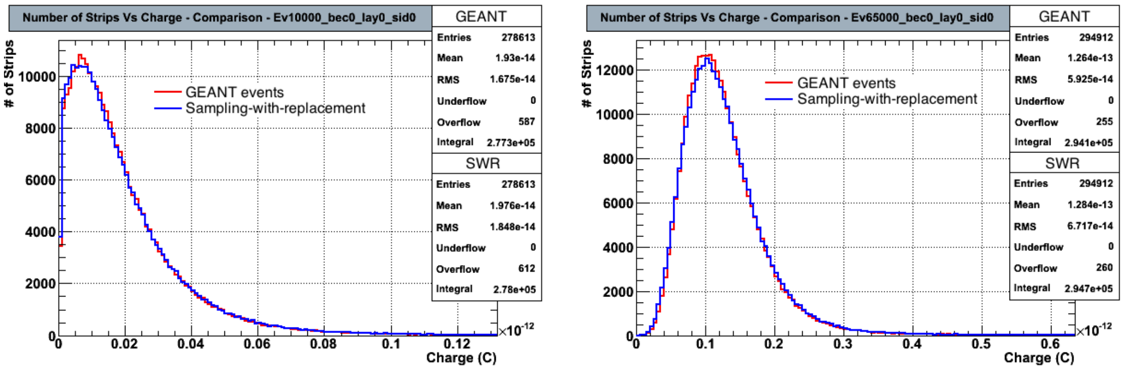

(a) Comparison between fully simulated events & sampling-with-replacement (SWR) events - 10,000.

(b) Comparison between fully simulated events & sampling-with-replacement (SWR) events - 65,000.

Figure 4.10.: Charge-per-strip comparisons in barrel layer 0 (side 0) between fully simulated events and sampling-with-replacement events.

4.4.5. Results Using Sampling-with-replacement Method

Figure 4.11 shows the charge-per-strip distribution resulting from a full 10^8 sampling-with-replacement events. The distribution is plotted with a linear scale (Figure 4.11(a)) for ease of comparison with the previous charge-per-strip distributions (Figures 4.10). A log scale version of the same distribution (Figure 4.11(b)) is also included in order to highlight the tail region of the distribution where higher charges are collected.

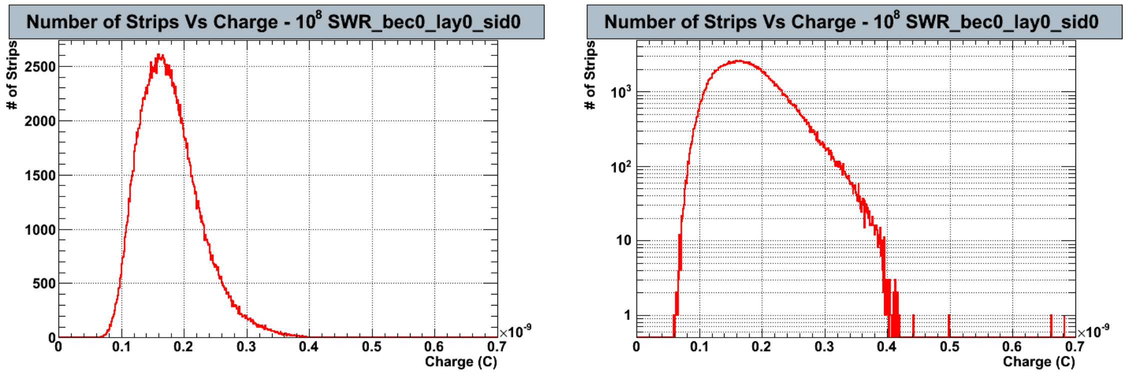

(a) Linear scale.

(b) Semi-log scale.

Figure 4.11.: Number of strips with a given charge - for 10^8 sampling-with-replacement events.

The same sampling-with-replacement procedure (Subsection 4.4.3) used for the 450 GeV beam pipe scrape scenario was also followed for the 7 TeV TAS scrape scenario. The charge map based on the full sample of fully simulated events, for the worst affected layer/disc of the SCT, is presented in Figure 4.12(a), while the (log scale) charge-per-strip distribution is included in Figure 4.12b for comparison with the tail region of 450 GeV beam pipe scrape distribution (Figure 4.11(b)).

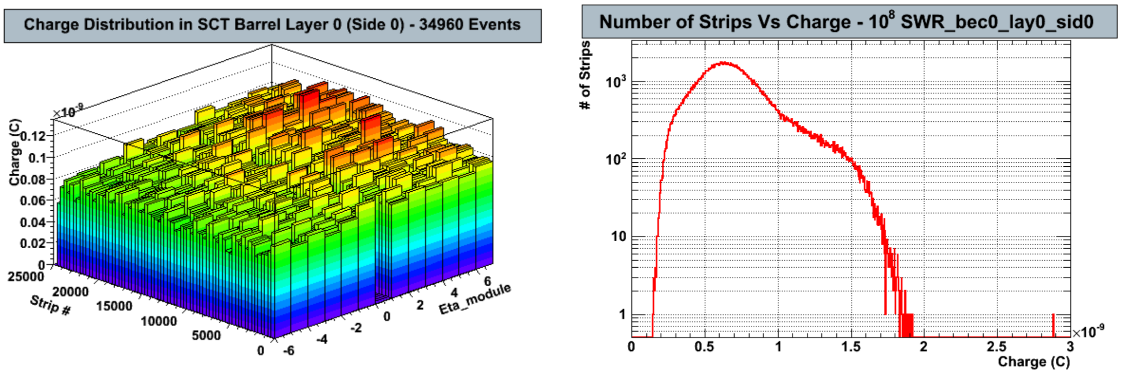

(a) 7 TeV TAS collimator scrape scenario - charge map for the 34,960 fully simulated events available.

(b) 10^8 sampling-with-replacement events for 7 TeV TAS scrape scenario. Plot shows number of strips with a given charge.

Figure 4.12.: Charge map and charge-per-strip plots for the 7 TeV TAS scrape case, for barrel layer 0, side 0.

4.5. Discussion

The focus of the sampling-with-replacement method for the 450 GeV beam pipe scrape scenario has been on the innermost barrel layer side because it collects almost twice as much charge as the next worst hit layer/disc (Figures 4.2(c) and 4.3(c)). Of course a lot depends on the particular scrape scenario, but within the framework developed here the sampling-with-replacement method can always be run on other layers or wheels depending on which is worst hit in any given scenario.

In Figure 4.9 the charge map obtained using the sampling-with-replacement method (Figure 4.9(b)) is compared with the equivalent one produced using the fully simulated events (Figure 4.9(a)) — the distributions appear to be in good agreement in terms of shape and magnitude of charge deposited per bin. A clearer demonstration that the method is working correctly comes by comparing the charge-per-strip histograms, Figure 4.10(b), with Figure 4.6(b), which shows a marked improvement from the sampling-with-replacement performance when cluster size is taken into account. Importantly the method also matches the charge-per-strip distributions for smaller numbers of events –

for example, a comparison of 10,000 sampling-with-replacement events and 10,000 fully simulated events is given in Figure 4.10(a) and they match up well. Since the method reproduces the distributions in cases where the number of events is less than or equal to 65,000 it was considered to be valid to extend it up to 10^8 events — to within any uncertainty resulting from interactions between secondaries, and their collective effects on the detector, which is beyond the scope of this study.

The charge per strip histograms in Figure 4.4 are obtained from finer binned (1 strip = 1 bin) versions of the charge maps from Figures 4.2 and 4.3 — the charge collected by each strip is simply scaled by the factor $10^8/65,000$, as only 65,000 fully simulated events existed. This was done to see if the 5 nC/strip limit was in danger of being breached or whether the charge collected would be orders of magnitude below this. From these distributions it was thought that a number of strips may collect charge of order 5 nC, and this concern was the primary motivation for creating and implementing the sampling-with-replacement method.

Results for 10^8 sampling-with-replacement events (Figure 4.11) show strips receiving a maximum charge of < 0.7 nC - much less than suggested by linear extrapolation from the 65,000 fully simulated events, and below the threshold at which damage would be done to the readout chips. Apart from the 6 strips that receive charges between $0.42 - 0.7$ nC, the distribution seems to end at 0.42 nC. As the number of sampling-with-replacement events is increased the tail of the charge-per-strip distribution gets much thinner, with the number of strips collecting high charge (> 0.7 nC) dropping to zero (Figure 4.11(b)).

In the 7 TeV TAS scrape scenario, barrel layer 0 was again the layer/disc of the SCT in which the most charge was collected (Figure 4.12(a)). Running the sampling-with-replacement method for 10^8 7 TeV TAS scrape events (Figure 4.12(b)) demonstrates that the maximum charge collected by a single strip in the worst hit barrel layer should be < 1.9 nC, in a 25 ns window under the assumption that $\sim 10^8$ protons would collide with the ATLAS TAS collimator per bunch.

4.6. Conclusion

From the 450 GeV beam pipe scrape scenario studied under a moderate scrape assumption, the charge deposited in the strips of the SCT modules *does not* breach the 5 nC threshold, nor does this occur for the 7 TeV TAS scrape scenario – however the charge deposited is of the same order of magnitude as this threshold. A more extreme scrape assumption, say, 10^9 proton collisions would likely begin to damage readout channels. For a beam scrape of 10^8 proton collisions per bunch the strips of the SCT should not collect more than 2 nC per strip. The `ABCD3T` chips of the SCT modules should therefore not incur damaged read-out channels given these scenarios and the assumptions made in this study.

There are two main points that have not been addressed here. The first is whether the assumption of 10^8 proton collisions from a single bunch is realistic, for the purpose of this study a number of collisions (10^8) was chosen in the knowledge that the end result (the charge-per-strip distribution) once obtained, could be reproduced for any number of events required. The 'pile-up' effects from multiple bunches scraping would also add extra complications that would need to be tackled in tandem with the other major point overlooked in this analysis: how charge collection efficiency changes with such large numbers of secondary particles passing through the modules. This was not possible to determine with the hits data and sampling-with-replacement method developed here, as the hits are the result of *single* simulated proton collisions and what is effectively required is to treat all the hits as if they were from the same event.

The fear of LHC beamloss occurring, which was the original motivation for this study, has thankfully not come to pass — in fact after the 2008/2009 repairs, the machine has run flawlessly in the time since this study was conducted. As the LHC ran at 3.5 TeV and 4 TeV beam energies during this period, the fears of damage to the SCT read-out chips were allayed to an extent during this period. However, after upgrades to the LHC over the long shutdown period over 2013–2014, the beam energy is planned to increase to 6.5 TeV which brings the 5 nC/25 ns/channel threshold into focus, and within an order of magnitude of being breached should a collimator scrape occur. The results presented here, and the planned increase in beam energy, have served to motivate further work that addresses two of the main points that could not be covered here: multiple successive bunches scraping the beam pipe or TAS; and the non-linear changes in charge collection efficiency due to such an event. Some of these points are addressed in a new study, where a full simulation of the silicon strip module electrical system is used to determine the behaviour of its elements during a realistic beam loss scenario, with multiple bunches scraping the beam pipe or collimators [113].

Chapter 5.

Light Charged Higgs Search

This chapter covers the $t \to bH^+ \to b\tau^+_{\text{had}}\nu_\tau$ analyses as part of the light charged Higgs search at ATLAS over 2011 [114]. As discussed in Section 2.2.2, electroweak symmetry breaking in the SM is achieved via the Higgs mechanism. However, there is no reason to assume a minimal Higgs sector *a priori*, and charged Higgs bosons (H^+, H^-) are predicted by non-minimal Higgs models. Such models include Two Higgs Doublet Models (the focus of this chapter), as well as models accounting for neutrino masses via Higgs triplets [115–118]. As the SM does not contain any elementary charged scalar particles, the observation of a charged Higgs would be a clear evidence for new physics beyond the SM.

The light charged Higgs search was conducted with $\sim 4.6\,\text{fb}^{-1}$ of ATLAS data collected over 2011 from $\sqrt{s} = 7\,\text{TeV}$ pp collisions. This chapter presents a review of Two Higgs Doublet Models (Section 5.1) as well as a summary of previous experimental searches and constraints on charged Higgs bosons (Section 5.2). An overview of the light charged Higgs search at ATLAS is presented in Section 5.3, with the focus on final states containing hadronically decaying taus. Section 5.4 describes a study conducted to attempt to separate charged Higgs events ($t\bar{t} \to b\bar{b}H^\pm W^\mp$) from the main irreducible SM background ($t\bar{t} \to b\bar{b}W^+W^-$). The methods used to estimate the SM background to the potential charged Higgs signal are summarised in Section 5.5 to provide context for Sections 5.6 and 5.7. Sections 5.6 and 5.7 respectively cover studies into systematic effects on the geometric/kinematic acceptance of the analysis with respect to the MC modelling used, and the rate at which electrons are mis-identified as hadronically decaying taus in $t\bar{t}$ events. Finally, the main exclusion plots for a light charged Higgs decaying to a tau and neutrino are presented in Section 5.8 as a conclusion to the light charged Higgs analyses.

5.1. Two Higgs Doublet Models

Two Higgs Doublet Models (2HDMs) refer to a class of models in which the Higgs sector of the SM, discussed in Section 2.2.2, is extended by adding a second $SU(2)_L$ doublet of complex scalar fields in addition to that introduced in Subsection 2.2.2. i.e. Φ_1 and Φ_2, with $\Phi_1 = U\Phi_2$, where U is some 2×2 unitary operator[1]. This constitutes the simplest non-trivial extension to the SM Higgs sector. Such 2HDMs were originally proposed as a new source of CP violation [119], and this motivation still exists as the SM is not sufficient to account for the level of baryon asymmetry we see in the universe today. Another motivation for such an extension today comes from a requirement in Supersymmetry (SUSY) theories, where higgsino doublets are required to come in pairs (with opposite hypercharge) in order to cancel triangle anomalies [120]. Though the Higgs sectors of these supersymmetric models, as well as their decays and interactions within the scope of the models can be well defined by fixing parameter values, we wish to consider the more general case — one that does not assume supersymmetry, but simply extends the Higgs sector of the SM.

The 'type' of 2HDM refers to the the way in which fermions couple to each of the two Higgs doublets, and there exist three types — known as type-I, type-II and type-III 2HDMs. Type-I 2HDMs only allow Higgs-fermion interactions in which one Higgs doublet couples to both up-type and down-type fermions; while the other Higgs doublet does not couple to fermions at all [121]. In the context of SUSY models, the most commonly discussed Higgs sector is a type-II 2HDM [122], in which up-type quarks and neutrinos couple to one of the Higgs doublets and down-type quarks and charged leptons couple exclusively to the other. The type-III 2HDMs are the most general, and consist of all other 2HDMs — allowing for all possible Higgs-fermion couplings [123]. The main constraints on viable 2HDMs come from limits on possible couplings resulting from neutral Higgs-mediated tree-level flavour changing neutral currents (FCNCs). To avoid FCNCs, all fermions of a given electric charge can couple to at most one Higgs doublet (in a model with multiple scalar doublets) [124]. Another major constraint on parameters in the Higgs potential is that they must lie in regions of parameter space that ensure $U(1)_{EM}$ is not broken [125].

Similar to the form of the potential for the SM Higgs fields (Equation 2.8), the scalar potential for a 2HDM (given the above constraints) is generally expressed as

---

[1] As the Higgs fields self-interact it must be unitary in order to conserve probability in such interactions.

$$
\begin{aligned}
V(\Phi_1,\Phi_2) =& \mu_{11}^2 {\Phi_1}_i^* {\Phi_1}^i + \mu_{22}^2 {\Phi_2}_i^* {\Phi_2}^i - \mu_{12}^2 \left({\Phi_1}_i^* {\Phi_2}^i + {\Phi_2}_i^* {\Phi_1}^i\right) \\
&+ \frac{\lambda_1}{2}\left({\Phi_1}_i^* {\Phi_1}^i\right)^2 + \frac{\lambda_2}{2}\left({\Phi_2}_i^* {\Phi_2}^i\right)^2 + \lambda_3 {\Phi_1}_i^* {\Phi_1}^i {\Phi_2}_i^* {\Phi_2}^i \\
&+ \lambda_4 {\Phi_1}_i^* {\Phi_2}^i {\Phi_2}_i^* {\Phi_1}^i + \frac{\lambda_5}{2}\left[\left({\Phi_1}_i^* {\Phi_1}^i\right)^2 + \left({\Phi_2}_i^* {\Phi_2}^i\right)^2\right] \quad , \qquad (5.1)
\end{aligned}
$$

with real parameters μ_{11}, μ_{22}, μ_{12}, λ_1, λ_2, λ_3, λ_4, λ_5. In the same manner as described in Section 2.2.2 the potential can me minimised with vacuum expectation values for the Higgs fields that will conserve $U(1)_{EM}$ after EW symmetry breaking given by

$$
\langle 0|\Phi_1|0\rangle = \begin{pmatrix} 0 \\ v_1/\sqrt{2} \end{pmatrix} \quad , \quad \langle 0|\Phi_2|0\rangle = \begin{pmatrix} 0 \\ v_2/\sqrt{2} \end{pmatrix} \quad . \qquad (5.2)
$$

The $SU(2)$ doublets, Φ_1 and Φ_2, are written in terms of eight fields (where the vevs have been chosen such that all fields except v_1 and v_2 are set to zero), i.e.

$$
\Phi_1 = \begin{pmatrix} \phi_1^+ \\ (v_1 + \rho_1 + i\eta_1)/\sqrt{2} \end{pmatrix} \quad , \quad \Phi_2 = \begin{pmatrix} \phi_2^+ \\ (v_2 + \rho_2 + i\eta_2)/\sqrt{2} \end{pmatrix} \quad . \qquad (5.3)
$$

Based on the vevs (Equation 5.2) that are set to minimise the potential (Equation 5.1), mass terms for the scalars can be obtained from the terms in the Lagrangian shown in Equations 5.4, 5.5 and 5.6). The masses for the charged scalars are given by

$$
\mathcal{L}_{\phi^\pm \text{ mass}} = \left[\mu_{12}^2 - (\lambda_4 + \lambda_5) v_1 v_2\right] \left(\phi_1^- \ , \ \phi_2^-\right) \cdot \begin{pmatrix} v_2/v_1 & -1 \\ -1 & v_1/v_2 \end{pmatrix} \cdot \begin{pmatrix} \phi_1^+ \\ \phi_2^+ \end{pmatrix} \quad , \qquad (5.4)
$$

where diagonalising the matrix gives a zero eigenvalue which provides the longitudinal degree of freedom for the $W^\pm$, and a non-zero eigenvalue which constitutes the charged

Higgs mass. Similarly, the masses for the pseudo-scalars are given by

$$\mathcal{L}_{\eta\ \mathrm{mass}} = \left[\mu_{12}^2/(v_1 v_2) - 2\lambda_5\right] (\eta_1\ ,\ \eta_2) \cdot \begin{pmatrix} v_2^2 & -v_1 v_2 \\ -v_1 v_2 & v_1^2 \end{pmatrix} \cdot \begin{pmatrix} \eta_1 \\ \eta_2 \end{pmatrix} \quad , \tag{5.5}$$

where one of the pseudo-scalar modes becomes the longitudinal degree of freedom for the Z and the other corresponds to a massive pseudo-scalar Higgs boson. Finally, the two neutral scalar modes are given by

$$\mathcal{L}_{\rho\ \mathrm{mass}} = -\,(\rho_1\ ,\ \rho_2) \cdot \begin{pmatrix} \mu_{12}^2 \dfrac{v_2}{v_1} + \lambda_1 v_1^2 & -\mu_{12}^2 + \lambda_{345} v_1 v_2 \\ -\mu_{12}^2 + \lambda_{345} v_1 v_2 & \mu_{12}^2 \dfrac{v_1}{v_2} + \lambda_2 v_2^2 \end{pmatrix} \cdot \begin{pmatrix} \rho_1 \\ \rho_2 \end{pmatrix} \quad , \tag{5.6}$$

where $\lambda_{345} = \lambda_3 + \lambda_4 + \lambda_5$.

The requirement that $U(1)_{EM}$ remains unbroken after spontaneous symmetry breaking is what allows the definition of the two charged and one neutral states that become the longitudinal degrees of freedom for the $W^\pm$ and Z bosons, and the five "left-over" degrees of freedom as the Higgs bosons. The rotation angle required to diagonalise the matrix for the neutral scalars (Equation 5.6) to get their mass eigenstates is labelled, α, while the angle required to diagonalise the matrices for the charged scalars and pseudo-scalars is labelled β, with

$$\tan\beta \equiv \frac{v_2}{v_1} \quad . \tag{5.7}$$

This ratio of the vevs, $\tan\beta$, is often used to parameterise exclusion limits in 2HDM studies, because it is also proportional to the coupling strength between the Higgs and fermion fields. The problem with such a parameter is that it requires a basis be defined for the the fields, but choosing a particular basis requires some justification, as doing so would set physical couplings — none of which have been measured. Therefore $\tan\beta$ only makes sense if there is some physical way of distinguishing between the two Higgs doublets, such as in a type-II 2HDM. In order to be as model independent as possible, any limit set on the branching ratio of $t \to bH^+$ (considered in this Chapter) should ideally be independent of $\tan\beta$ — however, doing this in reality requires making assumptions about how the charged Higgs decays.

As only the two electrically charged Higgs mass eigenstates will be considered in this chapter, the charged Higgs boson will hereafter be labelled H^+ when describing particle interactions (with charge conjugate interactions involving H^- assumed). For a more complete treatment of the theoretical and phenomenological issues involved in the study of 2HDMs see [126], which has been used extensively as a reference in this section.

5.2. Review Of Charged Higgs Searches and Constraints

Direct searches for charged Higgs bosons have been conducted over the years at LEP [127] and the Tevatron [128], and indirect constraints placed on 2HDMs by precision measurements made at the B-factories (KEK-B, SLAC and CESR). Direct searches rely on high centre of momentum collision energy for on-shell H^+ production while indirect searches and other precision measurements leverage the large integrated luminosities collected at lower collision energies to gain sensitivity to suppressed and higher order processes to which the charged Higgs could potentially contribute. Both methods for accessing H^+ processes are complementary, and consistent results between them allow for a high level of confidence in any exclusion limits set or a larger significance were all experiments to observe the same signal.

Currently the limits on the H^+ mass set by the B-factories are much higher than those from previous direct searches and the LHC must extend the mass range covered by previous searches as well as tighten exclusion limits via a direct search. The LEP lower limit on the mass of a charged Higgs was set by the LEP Higgs Working Group at 78.5 GeV [129] with a 95% Confidence Level (CL) assuming $\mathcal{B}(H^+ \to \tau^+\nu_\tau) + \mathcal{B}(H^+ \to c\bar{s}) = 1$. After the discovery of the top quark at the Tevatron in 1995, searches were separated between: a "light" charged Higgs, where such a Higgs could be produced via $t \to bH^+$ assuming $m_t > m_b + m_{H^+}$; a "heavy" charged Higgs, with $m_{H^+} > m_b + m_t$. Thus, upper limits were placed on the branching ratio $t \to bH^+$ over the light charged Higgs mass range of $\sim 80 - 160$ GeV. A search performed at CDF [130, 131] resulted in the limits shown in Figure 5.1, assuming either $\mathcal{B}(H^+ \to \tau^+\nu_\tau) = 1$ or $\mathcal{B}(H^+ \to c\bar{s}) = 1$, assuming the type-II 2HDM of the Minimal Supersymmetric Standard Model (MSSM). A similar search performed at DØ [132] places upper limits on the branching ratios $\mathcal{B}(t \to bH^+ \to bc\bar{s})$ and $\mathcal{B}(t \to bH^+ \to b\tau^+\nu_\tau)$ — these upper limits are shown for a range of H^+ masses in Figure 5.2.

At the B-factories the primary constraint on the mass of a charged Higgs comes from the measurements of the transition $b \to s\gamma$ (Figure 5.3(b)) in B-meson decay, with

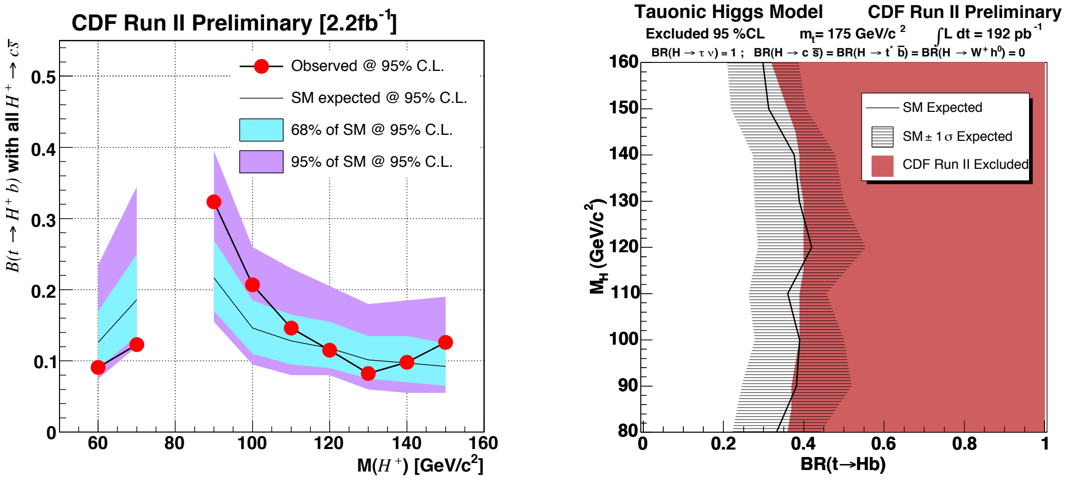

(a) CDF upper limit on $\mathcal{B}(t \to b(H^+) \to b(c\bar{s}))$ [130]. The gap in mass range is due to insensitivity of this analysis for M(H^+) around the W mass.

(b) CDF upper limit on $\mathcal{B}(t \to b(H^+) \to b(\tau^+\nu_\tau))$ [131].

Figure 5.1.: The upper limits set on $\mathcal{B}(t \to bH^+)$ by the CDF Collaboration using $\sqrt{s} = 1.96$ TeV $p\bar{p}$ collisions at the Tevatron, with: $\int \mathcal{L}\,dt = 2.2\,\text{fb}^{-1}$ in (a); $\int \mathcal{L}\,dt = 192\,\text{pb}^{-1}$ in (b).

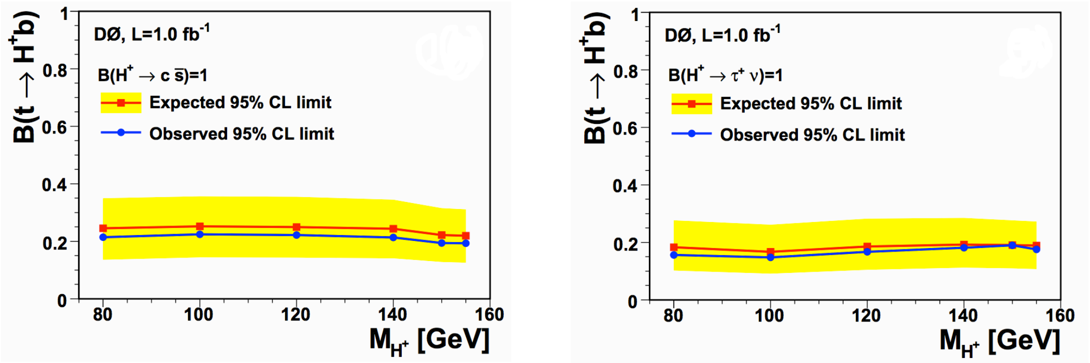

(a) DØ upper limit on $\mathcal{B}(t \to b(H^+) \to b(c\bar{s}))$

(b) DØ upper limit on $\mathcal{B}(t \to b(H^+) \to b(\tau^+\nu_\tau))$

Figure 5.2.: The upper limits set on $\mathcal{B}(t \to bH^+)$ by the DØ Collaboration using $\sqrt{s} = 1.96$ TeV $p\bar{p}$ collisions at the Tevatron, with: $\int \mathcal{L}\,dt = 1.0\,\text{fb}^{-1}$ [128]. Expectation curves for various $\tan\beta$ values are also displayed as a reference in the context of a type-II 2HDM.

additional major constraints coming from measuring $\mathcal{B}(B^+ \to \tau^+\nu_\tau)$, $\mathcal{B}(B^+ \to c\bar{s})$ and $\mathcal{B}(D^+ \to \tau^+\nu_\tau)$.

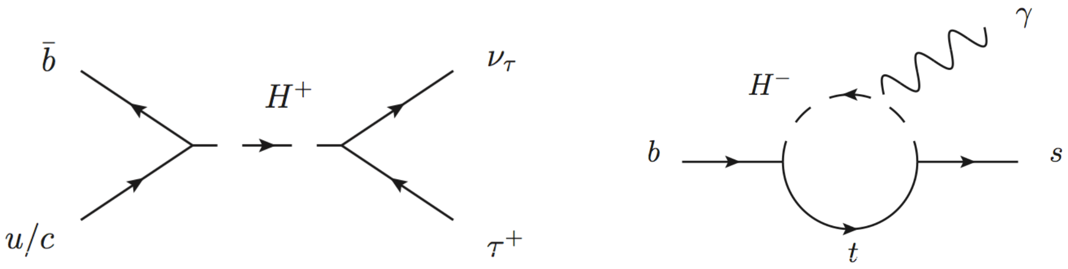

(a) CKM suppressed process with a charged Higgs contributing at tree level.

(b) Higher order process with a charged Higgs contributing at loop level.

Figure 5.3.: Rare processes mediated by a charged Higgs.

The current combined measurement on $\mathcal{B}(b \to s\gamma)$ from the CLEO, Belle and BaBar experiments is $3.43 \pm 0.29 \times 10^{-4}$ [133–135]. This implies a limit on m_{H^+} of at least 300 GeV independent of the type of 2HDM. More recently, the observation of an excess of $\bar{B} \to D^*\tau^-\overline{\nu}_\tau$ decays over the SM expectation by the BaBar Collaboration [136] produces some tension with the SM (at the 3.4σ significance level), and could be an indication of new physics processes affecting these decays. However, the measurement of the $\bar{B} \to D^*\tau^-\overline{\nu}_\tau$ rate combined with the $\bar{B} \to D\tau^-\overline{\nu}_\tau$ rate measurement in the BaBar analysis are incompatible with a charged Higgs from a type-II 2HDMs.

The initial ATLAS search focuses on excluding a light charged Higgs produced via top quarks, independently of the 2HDM type, using the 4.6 fb^{-1} of pp collision data collected at $\sqrt{s} = 7$ TeV in 2011 — this will be the focus of the rest of this chapter. A shift in focus to searches for a “heavy” charged Higgs are currently (at the time of writing) underway at ATLAS, using the increased integrated luminosity collected over 2012 at the increased pp collision energy of 8 TeV. However these searches are beyond the scope of this chapter.

5.3. The ATLAS Charged Higgs Search

During the 7 TeV LHC runs, charged Higgs searches have concentrated on a light charged Higgs produced via top quark decay. The main source of top quarks at the LHC (at 7 TeV) are top quark pairs produced via gluon-gluon fusion ($\sim$80%), with $q\bar{q} \to t\bar{t}$ also contributing ($\sim$20%). The ATLAS searches therefore focus on final states resulting from decays of top quark pairs. The subset of possible final states from $t\bar{t}$ decays most likely to be enhanced if a light charged Higgs exists motivates the object and event selection criteria for the search channels. These search channels correspond to the heaviest lepton pair ($\tau^+\nu$) and the heaviest quark pair ($c\bar{s}$) a light charged Higgs is kinematically allowed to decay to — as these should have the strongest couplings (in general) to the Higgs fields as this is what determines the fermion masses in the first place. Both decays are considered as the charged Higgs may couple preferentially to either quarks or leptons. The four main channels studied in the search for a light charged Higgs assume it decays either as $H^+ \to c\bar{s}$ [137] or $H^+ \to \tau^+\nu_\tau$ [114]. The decay channels and their corresponding final states in terms of the corresponding reconstructed physics 'objects' are listed in Table 5.1. Cases where both top quarks decay to charged Higgs are not considered because the branching ratio for such a process is significantly lower than for a single such decay, as $\mathcal{B}(t \to bW^+) > \mathcal{B}(t \to bH^+)$, with the cross sections for $t\bar{t}$ decaying to $b\bar{b}W^+W^-$, $b\bar{b}H^\pm W^\mp$, $b\bar{b}H^+H^-$ given by:

$$t\bar{t} \to b\bar{b}W^+W^- : \quad \sigma_{bbWW} = \sigma_{t\bar{t}} \times (1-B)^2 \quad , \tag{5.8}$$

$$t\bar{t} \to b\bar{b}H^\pm W^\mp : \quad \sigma_{bbHW} = \sigma_{t\bar{t}} \times 2B(1-B) \quad , \tag{5.9}$$

$$t\bar{t} \to b\bar{b}H^+H^- : \quad \sigma_{bbHH} = \sigma_{t\bar{t}} \times B^2 \quad . \tag{5.10}$$

where $B \equiv \mathcal{B}(t \to bH^+)$ and it is assumed $\mathcal{B}(t \to bW^+) + \mathcal{B}(t \to bH^+) = 1$. The focus for the rest of this chapter is on the final states involving hadronically decaying taus, with leptonically decaying taus covered in a separate analysis. After combining all the tau search channels it is assumed that $\mathcal{B}(H^+ \to \tau^+\nu_\tau) = 1$ — this assumption removes any $\tan\beta$ dependence[2] allowing an upper limit to be placed on the $t \to bH^+$ branching ratio. Taus decay hadronically $\sim$65% of the time and these hadronic decay products are reconstructed as τ_{had} objects in ATLAS (as described in Section 3.4).

Decay Channel	Objects in Final State
$t(\bar{t}) \to bH^+(\bar{b}W^-) \to b\tau^+_{had}\nu_\tau(\bar{b}q\bar{q})$	4 jets, τ_{had}, $E_{\text{T}}^{\text{miss}}$
$t(\bar{t}) \to bH^+(\bar{b}W^-) \to b\tau^+_{had}\nu_\tau(\bar{b}l^-\bar{\nu}_l)$	2 jets, τ_{had}, e/μ, $E_{\text{T}}^{\text{miss}}$
$t(\bar{t}) \to bH^+(\bar{b}W^-) \to b\tau^+_{lep}\nu_\tau(\bar{b}q\bar{q})$	4 jets, e/μ, $E_{\text{T}}^{\text{miss}}$
$t(\bar{t}) \to bH^+(\bar{b}W^-) \to bc\bar{s}(\bar{b}l^-\bar{\nu}_l)$	4 jets, e/μ, $E_{\text{T}}^{\text{miss}}$

Table 5.1.: The decay chains containing a charged Higgs used in the ATLAS search and the reconstructed objects used to select the corresponding final states.

---

[2] As the only effect from $\tan\beta$ in this case would be to change the branching ratio $\mathcal{B}(H^+ \to \tau^+\nu_\tau)$, fixing the branching ratio removes $\tan\beta$ dependence, while not constraining the 2HDM to the extent that fixing $\tan\beta$ would.

5.3.1. Hadronic τ Channels

The two channels in which the tau decays hadronically (the first two rows of Table 5.1) are the focus of the analyses presented here, and the channels will hereafter be referred to as 'τ_{had} + lepton' (Figure 5.4(a)) and 'τ_{had} + jets' (Figure 5.4(b)).

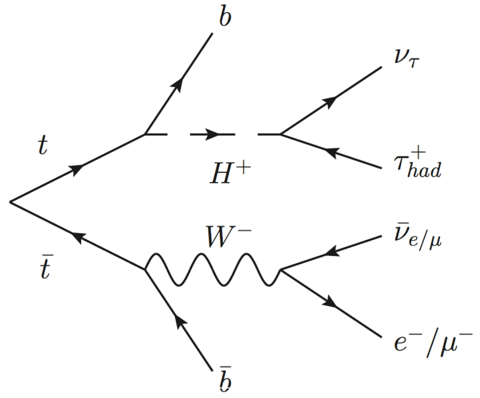

(a) τ_{had} + lepton channel **(b)** τ_{had} + jets channel

Figure 5.4.: Top quark pair decay to τ_{had} final states, where the tau is produced via the the decay of a charged Higgs boson, and the decay of the W defines the channel.

Data

The τ_{had} analyses are based on pp collision data collected by ATLAS in 2011 corresponding to an integrated luminosity of $4.6 \pm 0.2\,\mathrm{fb}^{-1}$. Over 2011, the run conditions changed drastically — particularly before and after an LHC technical stop in September after which β^* (a measure of the amplitude modulation required to focus the beams at the crossing point for collision) was reduced from 1.5 m to 1 m, further squeezing the beams and increasing the collision rate. Thus most of the data used comes from the two final data taking periods, L and M.

Monte Carlo Simulation

The primary MC samples used were produced during the MC11 production campaign of the ATLAS MC production group for the ATLAS top working group. The event generators for the samples use parton showering, hadronisation and underlying event models tuned to 2010 ATLAS data, with the AUET2B parameter set [79] used for

PYTHIA(`v6.425`) [138] and the AUET2 parameter set [80] used for HERWIG(`v6.520`)/JIMMY [139, 140]. The detector modelling is common to all MC samples and is a GEANT4 simulation of the ATLAS detector, while the event/object reconstruction algorithms used are the same as those used for data (as discussed in Section 3.4).

For simulation of the hard interaction, various event generators are used depending on the particular SM process being reproduced. The baseline samples are described here and relevant additional samples used will be mentioned as required. The largest (irreducible) background for the two analyses are SM $t\bar{t}$ events, as these will have the same initial and final states as the $H^\pm$ signal processes.

The modelling of $t\bar{t}$ events is performed with MC@NLO(`v4.01`) [141], which generates the hard interaction that produces the top quark pair at next-to-leading order (NLO). The parameters used for all datasets are the 2010 Particle Data Group values [97], with the exception of the top quark mass. The top quark mass is set at 172.5 GeV[3] and the inclusive $t\bar{t}$ cross section is scaled to the next-to-next-to-leading order (NNLO) prediction of 167 pb [143]. The CT10 [144, 145] parton distribution function sets are used for this sample with the parton showering, hadronisation and underlying event provided using the JIMMY libraries, that model multi-parton interactions, interfaced to the general purpose HERWIG event generator.

Events containing single top quarks produced in the s-channel ($t\bar{b}$ production) and the u-channel (Wt production) are also generated with MC@NLO [146] and HERWIG/JIMMY for shower/hadronisation/underlying event. ACERMC[4](`v3.8`) [148] is used for t-channel (qt and $qt\bar{b}$) single top production (hard interaction) with PYTHIA used for everything else.[5] In the MC used for single top quark production (considered a background in the analysis), approximate NNLO calculations [150–152] predict production cross sections of 64.6 pb, 4.6 pb and 15.7 pb for the t-, s- and u-channels respectively.

Single vector boson (W+jets and Z+jets) production is simulated using ALPGEN(`v2.13`) [153], which is a leading order generator for hard multi-parton processes, interfaced to HERWIG/JIMMY which provides the underlying event. The parton density function set used in this case for both the matrix element calculations, as well as the parton shower evolution, is CTEQ6.1 [154]. The production cross sections of W+jets

---

[3] This was used as the reference top mass value for the entire 2011 ATLAS top working group MC production, and is based on combined CDF and DØ value [142].

[4] A leading order generator optimised specifically for LHC processes, with matrix elements calculated with MADGRAPH `v4` [147]

[5] Note: the “s-”, “t-” and “u-” labels correspond to the Mandelstam variables [149] that describe the four-momenta of the interactions.

and Z+jets samples are rescaled by 1.20 and 1.25, respectively, in order to match NNLO calculations [155, 156].

Diboson events (WW, WZ and ZZ) are generated and hadronised using HERWIG, with the cross sections rescaled by 1.48 for WW, 1.60 for WZ, and 1.30 for ZZ, to match NLO predictions [157].

The signal MC sample consists of $t\bar{t}$ events generated with PYTHIA, in which at least one of the top quarks decays to a charged Higgs with a mass of 130 GeV. Any charged Higgs produced decays exclusively to $\tau\nu_\tau$, with the decay of the τ handled by the TAUOLA(`v1.20`) [158] package. The baseline MC samples used are listed in Table 5.2, along with the cross sections used.

Process	Generator	Cross section (pb)
$t\bar{t}$ with at least one lepton ℓ	MC@NLO	90.6
$t\bar{t}$ with no lepton		76.2
Single top quark t (with ℓ)	ACERMC	20.9
Single top quark s (with ℓ)	MC@NLO	1.5
Single top quark Wt (inclusive)		15.7
$W(\ell\nu)$ + jets	ALPGEN	3.1×10^4
$Wb\bar{b}$ + jets		1.3×10^2
$Z/\gamma^*(\ell\ell)$ + jets, $m(\ell\ell) > 10$ GeV	ALPGEN	1.5×10^4
$Z/\gamma^*(\ell\ell)b\bar{b}$ + jets, $m(\ell\ell) > 30$ GeV		38.7
WW	HERWIG	17.0
ZZ		1.3
WZ		5.5
$t\bar{t} \to b\bar{b}H^\pm W^\mp$ ($m_{H^+} = 130$ GeV)	PYTHIA	–

Table 5.2.: Cross sections for the main SM MC samples and charged Higgs signal sample [3]. In this table, ℓ refers to the three lepton families e, μ and τ. The top mass in the top quark samples is set to 172.5 GeV.

Event Cleaning

Both hadronic tau analyses share common object definitions as presented in Section 3.4. Object overlap removal procedures are also common to both analyses — these ensure that multiple selected physics objects do not overlap geometrically and if they are reconstructed from common detector signals, assigning priority to the most likely object type. However, before overlap removal, event "cleaning" requirements are implemented to produce a subset of events suitable for analysis as follows:

- *(Data only) Event must be included in the 'Good Runs List':* to ensure a high level of data quality, the event must be included in a Luminosity Block (LB) that appears in one of the recommended Good Runs List, which ensures the detector is operating at high efficiency. In this case the list is that recommended by the ATLAS top working group[6].

- *(MC only) Event re-weighting using pileup weights:* weights need to be applied to MC simulated events in order to match the conditions found in data. In the case of pileup re-weighting, Monte Carlo samples which already include pileup interactions are generally produced before or during a given data taking period. As the pileup conditions cannot be known exactly ahead of time, it is necessary to re-weight the Monte Carlo events to match the pileup conditions in data over the relevant runs. In this case the re-weighting is done based on the distribution of the average number of pileup interactions, $<\mu>$, per LB in data. Thus, for a given set of MC, simulated bunch crossings with lower numbers of pileup interactions than the data are given higher weights and those with higher numbers of interactions than the data are given smaller weights until the distributions match. This is done because many other distributions in data cannot be accurately reproduced in MC without accounting for the differences in pileup, $E_{\mathrm{T}}^{\mathrm{miss}}$ and track multiplicity being two key examples.

- *Primary vertex must have more than 4 tracks:* the primary interaction vertex for each bunch crossing is defined as the one with the largest sum of track $|p_{\mathrm{T}}|$. As it is only the primary vertex that is considered for the analysis, this condition ensures that the vertex being considered is consistent with the production of a $t\bar{t}$ candidate event, in terms of track multiplicity (i.e. $b\bar{b}W^{+}W^{-}$).

- *No bad jets or LAr errors:* the event is discarded if a jet, with $p_{\mathrm{T}} > 20\,\mathrm{GeV}$, is consistent with having originated from either non-collision backgrounds or instrumental effects in the calorimeters, such as noise bursts in the LAr hadronic end-cap calorimeter or coherent noise in the EM calorimeter. This requirement is necessary in order to ensure an accurate measurement of $E_{\mathrm{T}}^{\mathrm{miss}}$. Additionally, due to the failure of 6 front end boards in the barrel calorimeter over periods E–H, events with jets and electrons in the range $0.1 < \eta < 1.5$ and $-0.5 < \phi < -0.9$ are also discarded.

---

[6] For reference, this list is designated:
`data11_7TeV.periodAllYear_DetStatus-v36-pro10_CoolRunQuery-00-04-08_Top_allchannels_plus_tau`

Using the objects as defined in Section 3.4, a geometric overlap removal procedure takes place to ensure all objects used for the event selection are isolated and there is no ambiguity regarding object type. e.g. a selected τ_{had} that is also reconstructed and selected as a jet must then be removed from the list of selected jets. The overlap removal procedure and cut values used are those recommended by the ATLAS muon, e/gamma, tau, and jet/$E_{\text{T}}^{\text{miss}}$ combined performance groups for use in 2011 data[7]. Thus, events are discarded if any selected electron and a selected muon have been reconstructed using the same charged track. Selected muons are discarded if they are within $\Delta R < 0.4$ of any jet with $p_{\text{T}} > 25$ GeV and $|\text{JVF}| > 0.75$ — this is to remove muons likely to have originated within jets initiated by b or c quarks. If a τ_{had} candidate is within $\Delta R < 0.2$ of a selected electron or muon it is removed as a τ_{had} candidate. If a jet is within $\Delta R < 0.2$ of a selected τ_{had} the jet is rejected. If a jet is within $\Delta R < 0.2$ of a selected electron the jet is rejected. After this common overlap removal the event selections that maximise the signal significance over the reducible backgrounds (primarily QCD multi-jets) for the two τ_{had} channels are applied.

The τ_{had} + lepton Event Selection

The event selection for the τ_{had} + lepton channel (Figure 5.4(a)) is listed below, using objects as defined in Section 3.4.

1. The event must pass one of the lowest-p_{T} unprescaled[8] single lepton trigger chains, as the high-p_{T} lepton trigers are particularly efficient at removing multi-jet backgrounds (i.e. the majority of events at the LHC). As instantaneous luminosity increased throughout 2011, the lowest-p_{T} unprescaled electron and muon triggers changed with the p_{T} threshold for the single electron trigger increasing from 20 GeV to 22 GeV, while the p_{T} threshold for the single muon trigger remained at 18 GeV throughout the year. The p_{T} thresholds were able to be kept so low due to a tightening of identification requirements for muon and electron trigger objects at the Event Filter level.

2. The event must contain exactly one selected electron or muon, with $E_{\text{T}} > 25$ GeV (if electron) or $p_{\text{T}} > 20$ GeV (if muon), and this electron or muon must be matched ($\Delta R < 0.15$) to a corresponding electron or muon trigger object.

---

[7] As well as MC produced with ATHENA release `v17`.

[8] Prescaling of triggers is the random resetting of a passed trigger to fail, and is done in order to reduce the trigger output rate.

3. The event must contain more than one selected jet, as two b-jets are expected.
4. The event must contain exactly one τ_{had}.
5. The selected τ_{had} must have reconstructed electric charge of opposite sign to that of the selected electron or muon.
6. The scalar sum of the transverse momentum of the tracks associated to the primary vertex, $\Sigma p_{\text{T}}^{track}$, must be greater than 100 GeV. This requirement is included to suppress multi-jet backgrounds due to pile-up, while remaining insensitive to changes in pile-up conditions.
7. The event must contain at least one b-tagged jet.

The τ_{had} + jets Event Selection

The event selection for the τ_{had} + jets channel (Figure 5.4(b)) is listed below, again using objects as defined in Section 3.4.

1. The event must pass a $\tau_{\text{had}} + E_{\text{T}}^{\text{miss}}$ trigger, which specifies a 29 GeV p_{T} threshold for a τ_{had} satisfying the medium ID requirements, as well as missing transverse energy (calculated at the Event Filter level) greater than 35 GeV with no high-p_{T} muons. As luminosity increased over 2011, the trigger was updated for periods L–M to include a requirement of at least 3 level-1 jet objects with $p_{\text{T}} > 10$ GeV to mitigate the increased soft QCD multi-jet backgrounds, without increasing the p_{T} threshold for the τ_{had} trigger object.
2. The event must contain at least four jets.
3. The event must contain exactly one τ_{had} object with $p_{\text{T}} > 40$ GeV matched to a τ_{had} from the list of tau objects that could have triggered the event.
4. The event is vetoed if either a selected electron or selected muon is contained in the event.
5. The event must have $E_{\text{T}}^{\text{miss}} > 65$ GeV.
6. The $E_{\text{T}}^{\text{miss}}$ divided by $\frac{1}{2}\sqrt{\Sigma p_{\text{T}}}$ must be greater than 13 GeV$^{\frac{1}{2}}$. This requirement is optimised in Monte Carlo and is included in order to suppress multi-jet backgrounds and make the selection more robust against increasing pile-up, as $E_{\text{T}}^{\text{miss}}$ is a much smaller proportion of the scalar sum of the p_{T} in QCD multi-jet backgrounds. The

value of 13 $\mathrm{GeV}^{\frac{1}{2}}$ was selected by scanning over the possible cut values using charged Higgs signal, $t\bar{t}$, $W+$jets, and single top MC. The value that maximised the signal ($m_{H^+} = 130\,\mathrm{GeV}$) significance ($s/\sqrt{s+b}$) was chosen [159].

7. The event must contain at least one b-tagged jet.
8. The invariant mass, m_{jjb}, of the system of two jets and one b-tagged jet — using the two highest p_{T} non-tagged jets and highest p_{T} tagged jet — must lie in the range $120 - 240\,\mathrm{GeV}$. This is included as a way to increase the probability that the three jets are coming from a top quark and remove additional QCD multi-jet backgrounds.

An Additional Requirement?

The dominant irreducible background for both the $\tau_{\mathrm{had}}+$lepton and $\tau_{\mathrm{had}}+$jets channels, based on the event selections above, are SM $t\bar{t}$ events. The event selections as listed above, select for $\tau_{\mathrm{had}}+$lepton and $\tau_{\mathrm{had}}+$jets final states from $t\bar{t}$ events, but they are not designed to suppress the SM $t\bar{t}$ background from $t\bar{t}$ events containing a charged Higgs. Therefore it would greatly improve the sensitivity to a potential charged Higgs signal if this irreducible background could in fact be suppressed through some discriminating variable that could be cut on in the event selections. If this could be done, it would greatly increase the final signal significance over the background expectation from the SM. With this in mind it was proposed, in the early stages of the analysis, to explore the possibility of discriminating against SM $t\bar{t}$ events as part of the event selection. This study is presented in Section 5.4.

5.4. SM $t\bar{t}$ Background Separation Study

As the search channels for a light charged Higgs result in final states which are primarily produced by SM $t\bar{t}$ events, such events will dominate the irreducible background to the search (Section 5.3). Irreducible is only used here to refer to background events containing the same final state objects as the signal process under consideration. If possible, it is desirable to increase the signal significance over this SM $t\bar{t}$ background by determining some discriminating variable/s that can be used to separate out $t\bar{t}$ decays involving a charged Higgs. As the initial ($t\bar{t}$) and final ($\tau_{\mathrm{had}}+$lepton or $\tau_{\mathrm{had}}+$jets) states are identical to their SM counterparts for the $H^+ \to \tau^+_{\text{had}}\nu_\tau$ signal channels, two possible strategies for separating the events are evident:

1. The charged Higgs is a scalar boson (spin-0), whereas the W is a vector boson (spin-1). This implies a difference in the angular distributions of their decay products. In this case, that of the τ_{had} in the event relative to the $t\bar{t}$ system.
2. The assumption implicit in the search, that $m_t > m_{H^+} > m_W$, would lead to a softer b-jet momentum spectrum and harder τ_{had} momentum spectrum in charged Higgs events. Thus, one or both of these spectra could be used to discriminate from SM $t\bar{t}$ events.

Of these two options, using the *helicity angle* of the τ_{had} as a way to exploit the difference in spin between the bosons was judged to be most promising as it is independent of m_{H^+}, which is unknown. An investigation into whether this could be used to provide a region of phase space enriched in H^+ signal events was undertaken in MC at “truth” level (i.e. before detector simulation and object reconstruction). Examination of the momentum spectrum of the b-jet produced in association with the charged Higgs is left as a back-up option, and considered a more reliable variable than the τ_{had} momentum spectrum as there is no neutrino involved.

5.4.1. Helicity Angle

In the case of $t \to bW^+$ with $W^+ \to \tau^+\nu_\tau$ and $t \to bH^+$ with $H^+ \to \tau^+\nu_\tau$: if the top quark’s 3-momentum is used as a reference, the *helicity angle* of the τ can be defined as the angle between the 3-momentum of the tau and that of the top quark in the rest frame of the intermediate boson (Figure 5.5). If the τ is produced via $H^+ \to \tau^+\nu_\tau$, there should be no preferred direction for the τ to be emitted in the rest frame of the H^+, as a result the τ and ν should be emitted isotropically in this frame and therefore have a flat distribution in $\cos\theta$. If the τ is produced via $W^+ \to \tau^+\nu_\tau$, the angular distributions will depend on the polarisation of the W^+, which is determined by the $t\bar{t}$ pair and the b quark.

As we will not have experimental access to the 4-momentum of the top quark or that of the intermediate boson, the cosine of the helicity angle of the τ (Figure 5.5) is written as the invariant product of 4-momenta of the final state objects in the top decay:

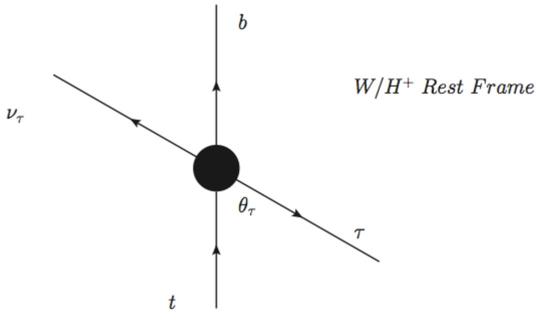

Figure 5.5.: The helicity angle, θ_τ, of the τ in the rest frame of the intermediate boson.

$$\cos\theta_\tau = \frac{p_b \cdot (p_\tau - p_\nu)}{p_b \cdot (p_\tau + p_\nu)} \quad , \tag{5.11}$$

where p is the 4-momentum of the (on-shell) particle in subscript. This expression is used to validate the charged Higgs MC samples produced with the PYTHIA event generator for $t\bar{t} \to b\bar{b}W^-H^+ \to b\bar{b}l^-\bar{\nu}_l\tau^+\nu_\tau$ events in Subsection 5.4.2. The same angle would be used for the τ_{had}+jets channel, however for this study it makes more sense to look at the τ_{had}+lepton channel as the helicity angle of the lepton from the other top decay, $\theta_{e/\mu}$, can also be calculated in the same way for a given event and compared to θ_τ.

5.4.2. MC Generation and Validation

In the ATLAS ATHENA[9] analysis framework, MC events are generated using python files that set up the parameters of the event generation and call the relevant generator packages to be run within the framework, with events output in a standardised ‘generator level’ format. The 2011 ATLAS MC production campaign includes a $t\bar{t}$ charged Higgs sample, with $m_{H^+} = 130\,\text{GeV}$, produced at leading order along with the parton showering and underlying event using PYTHIA. The production and subsequent decay of the $t\bar{t}$ process carried out within the context of a type-II 2HDM, with $\tan\beta$ set to a value of 35, as in this context the branching fraction of a charged Higgs to $\tau\nu$ is highest for large $\tan\beta$ values. In order to ensure that the helicity angle of the tau is indeed sufficiently independent of m_{H^+}, additional MC events using the same parameters as this original charged Higgs MC sample where produced at different mass points. The

---

[9] Version 16.6 was used here.

specific 2HDM used is irrelevant in the case of this study, as events are filtered such that only those containing a single τ_{had} produced from a single charged Higgs in the final state are considered (i.e. relative branching fractions are irrelevant as long as they are non-zero — negating any effects due to $\tan\beta$). All that matters here is the difference in event kinematics between SM $t\bar{t}$ events and $t\bar{t}$ events producing a charged Higgs. As a precaution an extra sample was generated with $\tan\beta = 20$ & $m_{H^+} = 130\,\text{GeV}$ to verify this assumption. The additional samples generated were then run through a package[10] which produces 'truth' MC objects (i.e. particle/jet objects without detector simulation and reconstruction) in a form that can be used for analysis directly from generated events. This includes grouping the hadronic showers into "truth jet" objects, based on the quark/gluon that gave rise to the shower. For each of the three additional H^+ mass points set, 81 GeV, 110 GeV, 150 GeV — 100,000 events were produced in the manner outlined above. In order to ensure the integrity of the generation and processing through the package, a sample of 130 GeV charged Higgs events was also produced and validated against the original sample produced during the central ATLAS production run. Helicity angle distributions for the τ and the e/μ in $t\bar{t}$ events (Figure 5.4) are displayed as 2D histograms below in Figure 5.6.

The angles are taken with respect to the direction of the 3-momentum of the top/anti-top quark when the system is boosted into the rest frame of the corresponding boson — the two top quarks are considered independently of one another. From the plots in Figure 5.6, the first thing to note is that the event distribution for the H^+ samples is flat along the $\cos\theta_\tau$ axis — as expected, there is no preferred direction at which the tau is emitted from the scalar boson. This flat distribution is also independent of the H^+ mass chosen, again, as it should be. The event distribution along the $\cos\theta_{e/\mu}$ axis is common to all plots, peaking at $\cos\theta_{e/\mu} = -0.3$, as this represents electrons or muons from the $\bar{t} \to \bar{b}W^- \to \bar{b}l^-\bar{\nu}_l$ arm of the $t\bar{t}$ decay. Finally, the $\cos\theta_\tau$ distribution for SM $t\bar{t}$ events in Figure 5.6(a) mirrors that of $\cos\theta_{e/\mu}$, as it should. Thus we can be confident that the event kinematics in the MC events generated for this study are properly modelled and can be used to test ways to measure these helicity angles in the real world, where we do not have knowledge of the 4-momenta of the top quarks and bosons.

---

[10] `TruthD3PDMaker` in ATHENA.

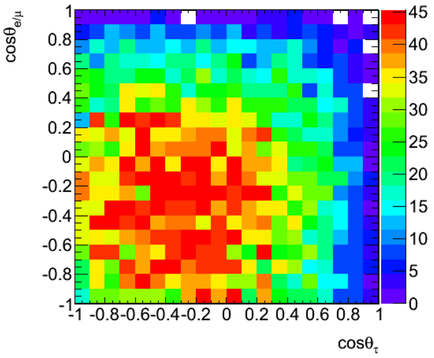

(a) 10,000 SM $t\bar{t}$ events.

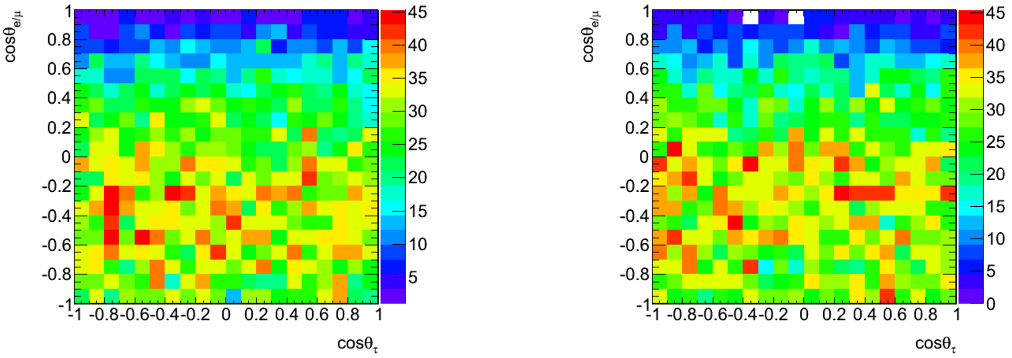

(b) 10,000 H^+ events, with $m_{H^+} = 81\,\text{GeV}$.

(c) 10,000 H^+ events, with $m_{H^+} = 110\,\text{GeV}$.

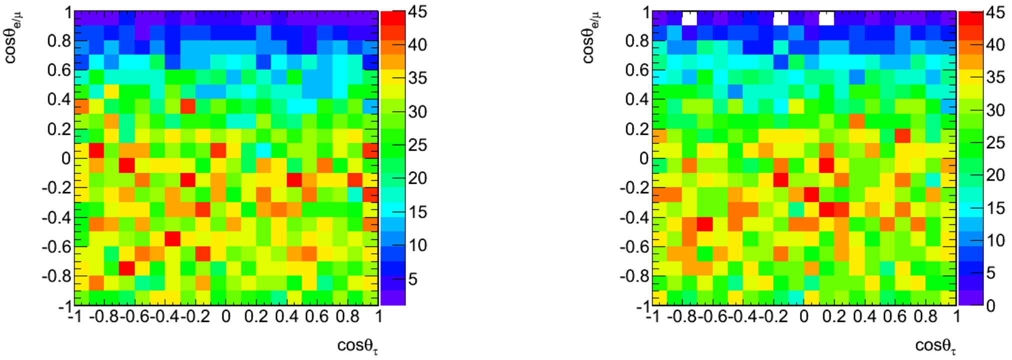

(d) 10,000 H^+ events, with $m_{H^+} = 130\,\text{GeV}$.

(e) 10,000 H^+ events, with $m_{H^+} = 150\,\text{GeV}$.

Figure 5.6.: Cosine of the helicity angle of the lepton, $\cos\theta_{e/\mu}$ ($y-$axis) vs cosine of the helicity angle of the τ, $\cos\theta_\tau$ ($x-$axis).

5.4.3. Helicity Angle Approximation

Having checked that the newly generated MC events are suitable for use in the study we move on to the question of whether the helicity angle of the tau is something that can realistically be measured. The first problem that presents itself when considering

Equation 5.11, is that we do not have access to the 4-momentum of the neutrino that gets produced with the tau. Therefore an approximation for this expression in terms of measurable/known quantities must be used [160, 161]:

$$\cos\theta_\tau \simeq \frac{4\,p_{b\text{-jet}}\cdot p_{\tau_{\text{had}}}}{m_t - m_W} - 1 \tag{5.12}$$

Equation 5.12 requires two assumptions: that the top decay occurs through an on-shell W boson (hence the m_W term); and that the b quark mass be neglected (not too extreme as it is small relative to $m_W/m_{H^+}/m_t$). The on-shell W requirement implies this approximation will break down as the charged Higgs mass moves away from the W mass. So a necessary simplifying assumption to obtain an expression for the helicity angle from observable quantities in a charged Higgs event reintroduces a dependence on charged Higgs mass which is what we were attempting to avoid by using the helicity angle in the first place. This is not ideal, but rather than abandon the idea, a check to see whether the expression 5.12 still provides a useful discriminating variable was performed. Plots corresponding to those in Figure 5.6 are reproduced in Figure 5.7 using the approximation (Equation 5.12).

From Figure 5.7, we see that the approximation quite effectively reproduces distributions 5.6(a) and 5.6(b) ($m_W = 80.4\,\text{GeV}, m_{H^+} = 81\,\text{GeV}$), but breaks down for the heavier charged Higgs masses: $m_{H^+} = 110\,\text{GeV}\,, 130\,\text{GeV}\,, 150\,\text{GeV}$. Nevertheless, there is still some level of discrimination but we will have to be resigned to the variable being mass dependent and almost indistinguishable from the SM $t\bar{t}$ distribution for a charged Higgs mass somewhere in the range 81 GeV – 110 GeV — as can be seen by comparing Figure 5.7(a) with 5.7(b) & 5.7(c).

For the next step, there is a need to account for the fact that the tau decays to hadrons and an additional neutrino, so we must consider the τ_{had} object, or something approximating its 4-momentum, like $p_\tau - p_{\bar{\nu}_\tau}$. The tau decay products cannot be considered in these MC samples due to a technicality — during the production process, tau decays are handled by the TAUOLA package, and therefore the hadronic decay products of the tau (but not the neutrino) are discarded during the event generation stage. However, as we are only working at the generator level and not processing events through the full simulation and reconstruction stages, this TAUOLA simulation of the tau decay does not get invoked. We therefore approximate the 4-momentum of the hadronic

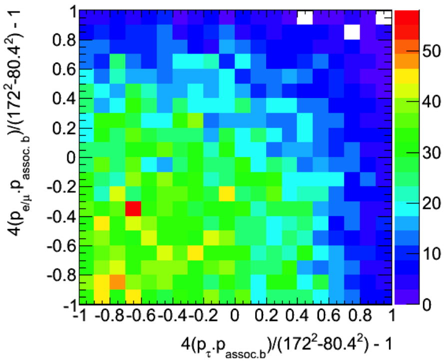

(a) 10,000 SM $t\bar{t}$ events.

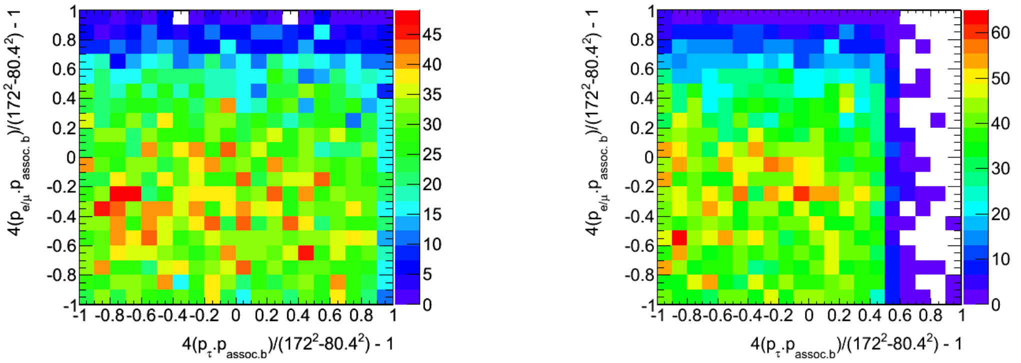

(b) 10,000 H^+ events, $m_{H^+} = 81\,\text{GeV}$.

(c) 10,000 H^+ events, $m_{H^+} = 110\,\text{GeV}$.

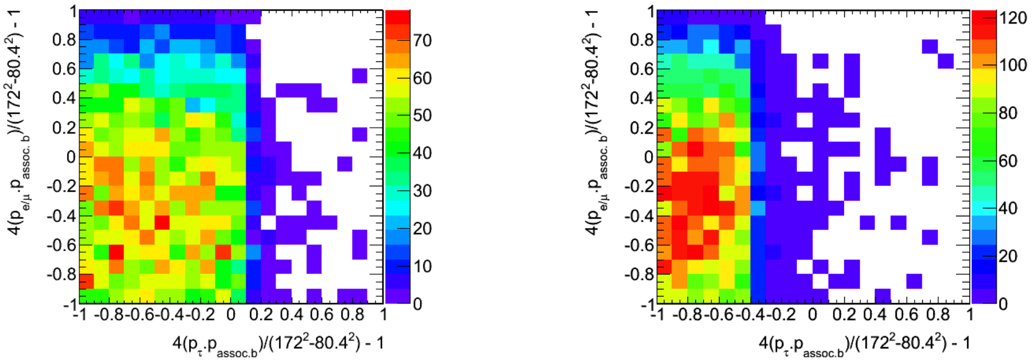

(d) 10,000 H^+ events, $m_{H^+} = 130\,\text{GeV}$.

(e) 10,000 H^+ events, $m_{H^+} = 150\,\text{GeV}$.

Figure 5.7.: Approximation for cosine of the helicity angle of the lepton, $\cos\theta_{e/\mu}$ ($y-$axis) vs cosine of the helicity angle of the τ, $\cos\theta_\tau$ ($x-$axis).

decay products from the tau as $p_{\tau_{\text{had}}} = p_\tau - p_{\nu_\tau}$, realising that this equates to taking a best case scenario (Figure 5.8).

The fact that the tau decays while the e/μ does not, breaks the symmetry of the helicity angle distribution between the two arms of the SM $t\bar{t}$ events further complicating

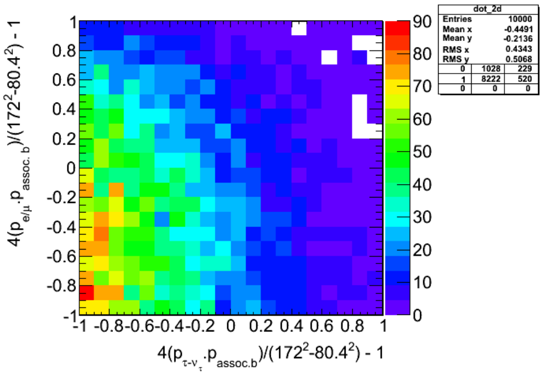

(a) 10,000 SM $t\bar{t}$ events.

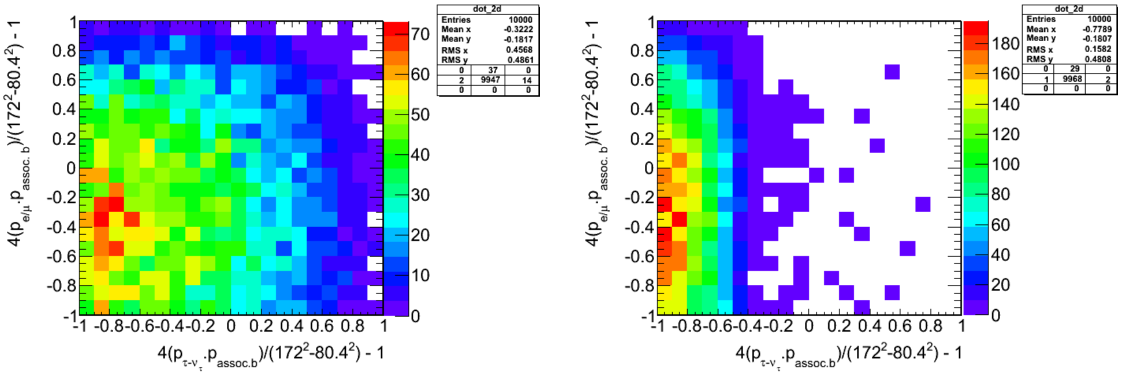

(b) 10,000 H^+ events, $m_{H^+} = 81\,\mathrm{GeV}$.

(c) 10,000 H^+ events, $m_{H^+} = 150\,\mathrm{GeV}$.

Figure 5.8.: Approximation for cosine of the helicity angle of the lepton, $\cos\theta_{e/\mu}$ ($y-$axis) vs cosine of the helicity angle of the τ, $\cos\theta_\tau$ ($x-$axis) using $p_{\tau_{\mathrm{had}}} = p_\tau - p_{\nu_\tau}$ to approximate τ_{had} 4-momentum.

its use as a discriminating variable in the τ_{had}+lepton channel. A point that has also been overlooked until now is that the 4-momentum of the b-jet used is that of the *correct* b-jet, in data there will be no way to ensure that both b-jets are tagged (without large losses in event selection efficiency), let alone matched to the top/anti-top decay from which they were produced. In summary, this approximation of a helicity angle variable does provide some (H^+ mass dependent) discrimination, but we have now arrived at an issue relating to the second strategy listed at the beginning of this section — the b-jet momentum spectrum.

5.4.4. b-jet Assignment

The plots shown so far use the 4-momentum of the b-jet that comes from the same top quark as the associated tau or e/μ as determined from the generator level decay chain (labeled “assoc. b”), however in data it would be much more challenging to assign the correct b-jet to its corresponding lepton, assuming the b-jets are correctly tagged by the `MV1` algorithm to begin with. In order to assign the b-jets in data, they must first be identified and would therefore need to be chosen as the two jets in the event which have the highest `MV1` score — this would add additional inefficiencies outside the scope of this truth level study. Considering the tau arm of the $t\bar{t}$ decay, the event distribution over the expression $p_{\tau} \cdot p_b$ (required for the helicity angle approximation) is plotted for the true b quark associated with the tau (Figures 5.9(a), 5.9(b), 5.9(c)), the closest b quark to the tau in ΔR (Figures 5.9(d), 5.9(e), 5.9(f)), and the b quark with the lower momentum (Figures 5.9(g), 5.9(h), 5.9(i)). Only the $m_{H^+} = 81\,\text{GeV}$ and $m_{H^+} = 150\,\text{GeV}$ samples are used here as they represent the mass extremes of the H^+ masses generated.

The most logical way to assign the b quarks would be to tag their charges, and match the b-jet of opposite sign. This is indeed the method that is envisioned to be used in future, as jet charge identification has begun to be developed for 2012 $\sqrt{s} = 8\,\text{TeV}$ pp collision data [162], however the charge identification for jets at the time of the analysis (2011) was too unreliable to be used here. From the two methods tested here, neither seems particularly useful for assigning the correct b quark to the tau for a low mass H^+ (81 GeV) as the kinematics are too similar to those for b quarks produced in association with the W, and in the case of the SM $t\bar{t}$ events there is no way (except charge identification) to distinguish between the two b-jets by any method as they will have exactly the same kinematics on average. However, for the high mass H^+ (150 GeV), assigning the b quark with the lower momentum to the tau is overwhelmingly the correct choice, indicated by the near identical distribution shown in Figures 5.9(c) & 5.9(i). This highlights an important point, any b-jet assignment would seem to bind us ever tighter (then we already were from using the helicity angle approximation) to a dependence on the charged Higgs mass. If we take the lower momentum b to be that produced with the charged Higgs, as this works for the higher end of the mass range, and look at the p_{T} spectrum of this b quark (Figure 5.10), a further complication arises. The majority of b-jets in the $m_{H^+} = 150\,\text{GeV}$ events would fail the $20\,\text{GeV}$ p_{T} cut on all jets in the event (required to keep the overwhelming level soft QCD backgrounds suppressed to a manageable level). Thus there will be no access to these jets as it will not be possible to include them in the object selection in a reliable way.

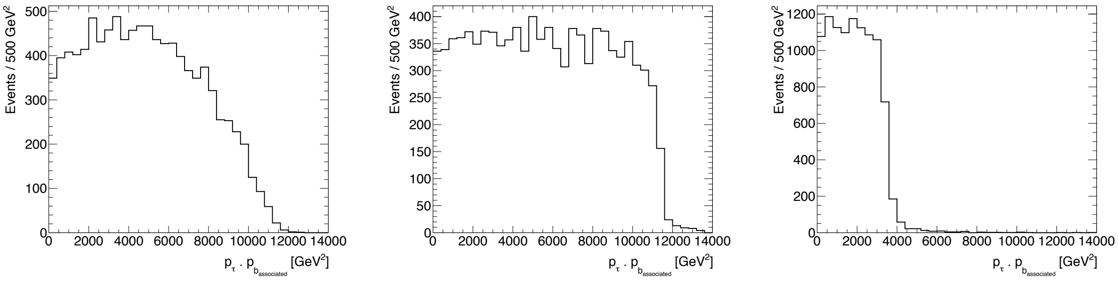

(a) $p_\tau \cdot p_b$ using true associated b — $t\bar{t}$ events.

(b) $p_\tau \cdot p_b$ using true associated b — H^+ events, $m_{H^+} = 81\,\mathrm{GeV}$.

(c) $p_\tau \cdot p_b$ using true associated b — H^+ events, $m_{H^+} = 150\,\mathrm{GeV}$.

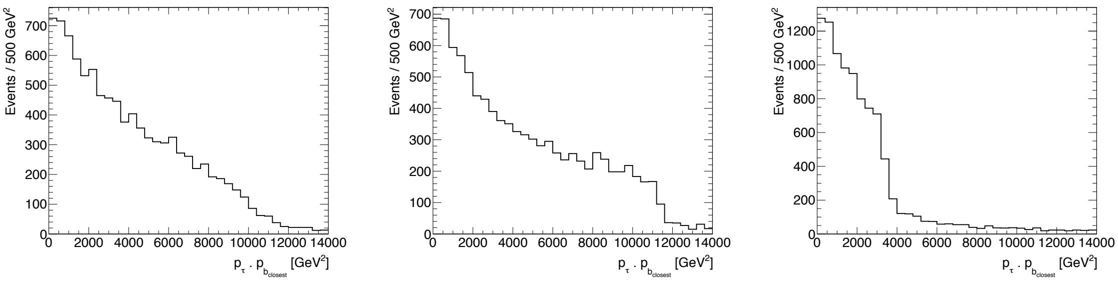

(d) $p_\tau \cdot p_b$ using b with $\Delta R_{\min}(\tau, b)$ — $t\bar{t}$ events.

(e) $p_\tau \cdot p_b$ using b with $\Delta R_{\min}(\tau, b)$ — H^+ events, $m_{H^+} = 81\,\mathrm{GeV}$.

(f) $p_\tau \cdot p_b$ using b with $\Delta R_{\min}(\tau, b)$ — H^+ events, $m_{H^+} = 150\,\mathrm{GeV}$.

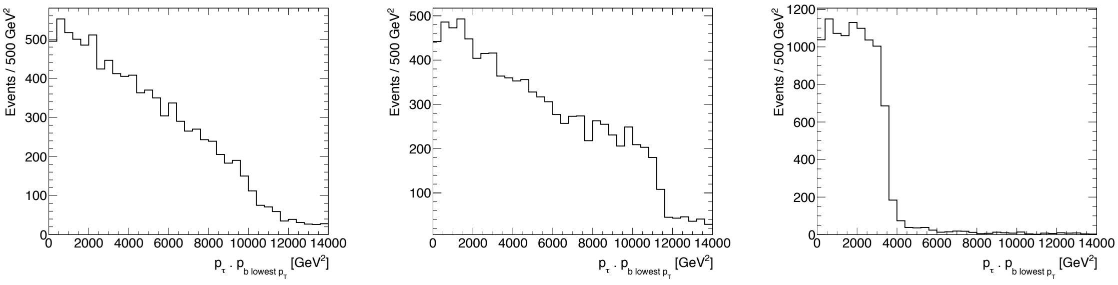

(g) $p_\tau \cdot p_b$ using b with minimum momentum — $t\bar{t}$ events.

(h) $p_\tau \cdot p_b$ using b with minimum momentum — H^+ events, $m_{H^+} = 81\,\mathrm{GeV}$.

(i) $p_\tau \cdot p_b$ using b with minimum momentum — H^+ events, $m_{H^+} = 150\,\mathrm{GeV}$.

Figure 5.9.: Distribution of $p_b \cdot p_\tau$ for different methods for choosing the b quark using 10,000 events.

5.4.5. SM $t\bar{t}$ Separation Study Conclusions

An attempt was made to separate the irreducible SM $t\bar{t}$ background from the H^+ signal events by using the tau helicity angle as a discriminating variable that was independent of m_{H^+}. However the approximations necessary to access the helicity angle experimentally

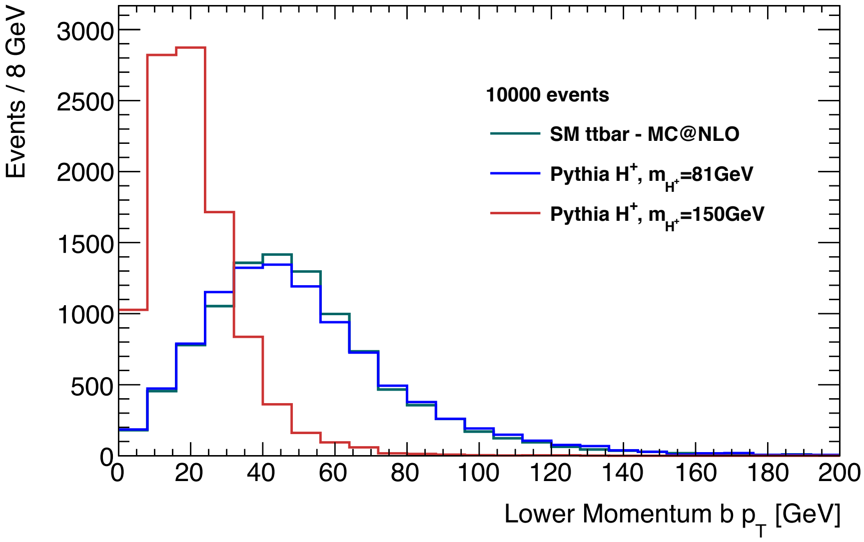

Figure 5.10.: p_T of the b quark with the lower momentum ($|\vec{p}_b|_{min}$).

reintroduce mass dependence into the variable and the realities of a hadron collider environment at LHC energies preclude the precision jet identification required to make even this mass dependent variable reliable. The b-jets could not be assigned reliably, as whether or not they are included in the object selection at all is again dependent on m_{H^+}. Therefore in order to produce the helicity angle approximation one would effectively have to again rely on the unknown H^+ mass, as it affects the b-jet selection, which further hinders the original goal of this study. Though not perfect (i.e. mass independent), the helicity angle approximation could be a useful discriminant. However, it was judged by the charged Higgs group that focus should be shifted to determining the backgrounds and associated uncertainties, for the event selections as they stand, in order to complete the analyses in a timely fashion.

5.5. Irreducible Background, Fakes and Uncertainties

The backgrounds to the charged Higgs signal events after the event selections (Subsection 5.3.1) are split into two categories according to whether they are to be estimated from Monte Carlo or data. Major irreducible backgrounds (i.e. background processes producing the same set of physics objects in the final state as the signal) are determined from the MC samples, whereas all other major backgrounds are estimated from data[11]. For reference the proportion of events from the main irreducible SM backgrounds that pass the event selections are shown in Table 5.3.

Background	τ_{had}+ lepton	τ_{had}+ jets
$t\bar{t}$	76.2%	89.7%
W+ jets	12.7%	6.8%
Wt	6.9%	3.5%
Z/γ^*+ jets	3.7%	–
WW, WZ, ZZ	0.5%	–

Table 5.3.: The proportion of events from SM processes that pass the event selections for the τ_{had} + lepton and τ_{had} + jets channels.

5.5.1. Irreducible Background – Estimated from MC

Due to the inability to suppress the SM $t\bar{t}$ events, they remain by far the dominant background, and the systematic uncertainties on this SM irreducible background must be accounted for through MC studies. The major systematic uncertainties on the SM $t\bar{t}$ events passing the event selections above stem from the MC modelling, with uncertainties due to initial and final state gluon radiation providing the largest contributions, at 13% (τ_{had} + lepton) and 19% (τ_{had} + jets).

The uncertainty on the acceptance of an event due to kinematic and geometric cuts in the object and event selections is the next largest systematic uncertainty on the $t\bar{t}$ MC as it is particularly dependent on slight differences in the $t\bar{t}$ event topology at generator level. The estimate of this uncertainty is provided in Section 5.6, by comparing the different generators and parton shower model combinations available for SM $t\bar{t}$ events for the τ_{had} + lepton and τ_{had} + jets channels.

Other systematic uncertainties arising from the detector simulation and object reconstruction[12] are also evaluated and added in quadrature to the final SM expectation uncertainty. These effects are evaluated by parameterising the source of uncertainty and shifting the parameter up/down by one standard deviation and reapplying the event selection to determine the effect on the events passing the selection. The largest

---

[11] The irreducible background for the τ_{had} + jets channel was estimated both in MC, and through a data-driven "embedding method", where events likely to be $t\bar{t} \rightarrow \mu$ + jets, are selected for in data, and the reconstructed muon is replaced by a simulated τ_{had} object.

[12] With all such uncertainties also propagated through to the calculation of the $E_{\text{T}}^{\text{miss}}$.

uncertainties come from jet reconstruction and b-jet identification, and are parameterised by $|\eta|$ and p_{T}, with: jet energy resolution (10–30%); the jet energy scale (up to 16%); as well as the b-tagging efficiency (5–17%) and b-jet mis-identification probability (12–21%). By comparison, the systematic uncertainties arising from the reconstruction and identification of electrons and muons are small.

5.5.2. Other Backgrounds – Estimated from Data

The backgrounds estimated from data are those in which the final state objects in events that pass the event selections have been mis-identified. There are several reasons for estimating such mis-identification probabilities from data, such as low MC statistics in the signal region, or large systematic differences between such probabilities in data vs MC. The backgrounds considered in the analyses are listed below, and the $e \rightarrow \tau_{\mathrm{had}}$ mis-identification probability will be the focus of Section 5.7.

- *$e \rightarrow \tau_{had}$ Mis-identification Probability*

  The $e \rightarrow \tau_{\mathrm{had}}$ mis-identification probability enters the analyses as a scale factor between the fake rate estimated from data and that determined using MC simulation of $Z \rightarrow ee$ events.

- *Jet$\rightarrow \tau_{had}$ Mis-identification Probability*

  A control sample enriched in $W+$jets events is used to measure the probability for a jet to be misidentified as a τ_{had} object, and this measured probability is used to predict the yield of background events due to jet$\rightarrow \tau_{\mathrm{had}}$ mis-identification. The jet$\rightarrow \tau_{\mathrm{had}}$ mis-identification probability is defined as the number of objects passing the full τ_{had} identification divided by the number prior to requiring identification. This mis-identification probability (parameterised in $|\eta|$ and p_{T}) is evaluated separately for τ_{had} candidates with one or three associated charged tracks at $\sim 7\%$ and $\sim 2\%$ respectively. The contribution to the SM background expectation for the analyses is determined by applying the jet$\rightarrow \tau_{\mathrm{had}}$ misidentification probability to simulated $t\bar{t}$, single top quark, $W+$jets, Z/γ^*+jets and diboson events, all of which are required to pass the full event selection *except for the τ_{had} identification.* For these events, τ_{had} candidates not overlapping with a true hadronically decaying τ or a true electron are considered to be jets mis-identified as taus. The jet corresponding to the τ_{had} objects is removed from the selected jets in the event (as it is being counted as the τ_{had} object), and if the event still passes the event selection it is counted as a background event with a weight given by the mis-identification probability (based on its p_{T} and η).

- *Lepton Mis-identification Probability (τ_{had}+ lepton channel only)*

  This concerns the proportion of non-prompt and/or non-isolated lepton objects that pass the lepton selection criteria (Section 3.4), such as those arising from the decay of hadrons containing b/c quarks, or from photon conversions (more will be said about lepton mis-identification in the following chapter — Section 6.1). The average values of the electron and muon misidentification probabilities were determined to be 18% and 29%, respectively.

- *Contributions from QCD Multi-jet Events (τ_{had}+ jets channel only)*

  Due to the limited statistics available in QCD multi-jet MC samples, and the large systematics effects associated with the MC modelling of such processes in the early stages of 7 TeV running, it is necessary to estimate this background from data for the τ_{had}+ jets selection. The multi-jet background component of the τ_{had}+jets SM expectation is estimated by fitting a template based on the shape of its $E_{\mathrm{T}}^{\mathrm{miss}}$ distribution to data. The template to be fit is generated from a control sample of events in data, using an event selection orthogonal to the baseline selection, that enriches the sample in QCD multi-jet background events. The selection uses all the baseline τ_{had}+jets criteria with the exceptions that: the τ_{had} candidate is required to pass loose tau identification but not the baseline tight tau identification; the reconstruction must not contain a b-tagged jet; and no requirements are placed on the mass of the qqb system (as there are no b-tagged jets). The QCD template, and the sum of the contributions from $t\bar{t}$, single top, diboson, and W+jets luminosity-normalised MC, is then fitted to the $E_{\mathrm{T}}^{\mathrm{miss}}$ distribution in data. The free parameters in the fit are the overall normalisation and the QCD fraction — the individual bins in the $E_{\mathrm{T}}^{\mathrm{miss}}$ template shapes are not free to vary. The resulting QCD multi-jet fraction is shown in Figure 5.11 as a function of $E_{\mathrm{T}}^{\mathrm{miss}}$, the fraction of the SM background expectation is thus estimated to be $\sim$20%.

The magnitudes of the effects on the number of background events from each component, due to systematic uncertainties arising from the data-driven background estimates outlined above, are summarised in Table 5.4.

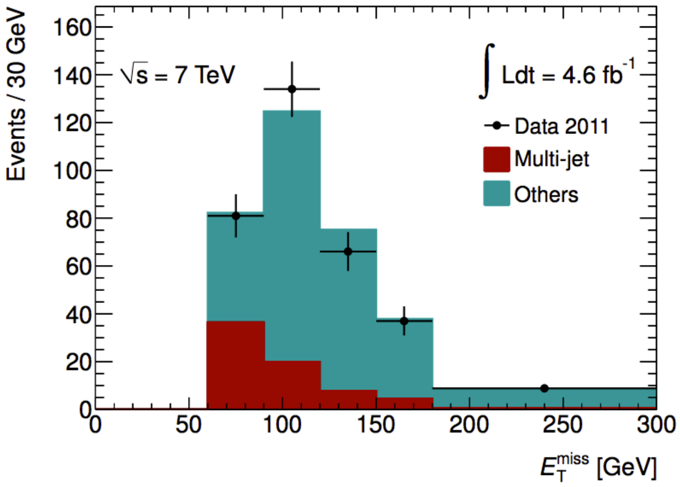

Figure 5.11.: Fit to E_T^{miss} after all selection cuts using two shapes: one for the QCD model and one for all other background processes. [163]

τ_{had}+lepton Background	Total Uncertainty (%)
$e \to \tau_{\text{had}}$ Mis-identification	20
Jet $\to \tau_{\text{had}}$ Mis-identification	26
Lepton Mis-identification	42

τ_{had}+jets Background	Total Uncertainty (%)
$e \to \tau_{\text{had}}$ Mis-identification	22
Jet $\to \tau_{\text{had}}$ Mis-identification	25
QCD Multi-jet Events	36

Table 5.4.: Approximate magnitude of yield uncertainty, based on the estimates of the listed background components from data for each of the τ_{had} analyses.

The magnitude of the relevant systematic uncertainties for SM MC modelling and the applicable detector and reconstruction systematic effects are also included for reference in Table 5.5.

5.6. MC Acceptance Systematic

Charged Higgs MC is used for final limit setting and as a guide to optimise event selection (to the extent possible with the unknown parameters in the model), as seen in Section 5.4.

Source of uncertainty	τ_{had}+ lepton (% effect)	τ_{had}+ jets (% effect)
Luminosity	$\pm\,3.7$	$\pm\,3.9$
Jet energy scale	$^{-8.1}_{+6.2}$	$^{+0}_{-15}\%$
Jet energy resolution	$\pm\,1.5$	$\pm\,4.9\%$
Jet efficiency	$\pm\,0.0$	$\pm\,0.09\%$
b-tagging efficiency	$^{-8.6}_{+8.2}$	$^{+3.6}_{-4.4}\%$
Tau energy scale	$^{+4.2}_{-6.1}$	$\pm\,2.1\%$
Tau ID	$^{-6.7}_{+5.7}$	$\pm\,4.0\%$
Tau eVeto	$^{-2.5}_{+1.5}$	$\pm\,0.11\%$
$E_{\text{T}}^{\text{miss}}$ (cell-out and soft-jet terms)	$^{-0.1}_{-0.3}$	$^{+0.18}_{-0.08}\%$
$E_{\text{T}}^{\text{miss}}$ (pileup effects)	$^{-0.1}_{-0.5}$	$^{+0.25}_{-0.12}\%$
Electron trigger efficiency	$^{-0.9}_{-0.0}$	–
Electron efficiency	$^{-1.7}_{+0.8}$	–
Electron energy scale	$^{-0.5}_{-0.7}$	–
Muon trigger efficiency	$^{-3.1}_{+2.2}$	–
Muon efficiency	$^{-0.8}_{-0.2}$	–
Muon momentum scale	$\pm\,0.1$	–
$t\bar{t}$ cross section, PDF + scale	$^{+7.0}_{-9.6}$	$^{+10}_{-11}\%$
Top Mass	–	$\pm\,1.8\%$
ISR	–	$\pm\,2\%$
FSR	–	$\pm\,19\%$

Table 5.5.: The effect of systematic uncertainties on the predicted Monte Carlo yields of the background sum to the τ+ lepton and τ+ jets channels. The numbers are for illustration only, as the full shape uncertainties are used for setting limits. [163, 164]

The determination of whether or not an observed signal is consistent with $t\bar{t} \rightarrow b\bar{b}W^{-}H^{+}$ events depends on uncertainties associated with the SM MC modelling to which data is being compared. An important factor to consider with the use of SM MC modelling is the uncertainty that arises due to the specific kinematic acceptance region defined by the analysis. Though ATLAS aims to get as close as possible to full 4π coverage in solid angle, this is not technically feasible (see Chapter 3) and so the phase space available to physics processes (in terms of what it is possible to observe) is limited to that defined by the acceptance region of the detector (i.e. the fiducial volume) coupled with the additional object and event selection requirements, such as cuts on p_{T}. If we disentangle ourselves from the efficiencies and uncertainties associated with the reconstruction and identification of physics objects (as these uncertainties are evaluated separately), we can focus on how the event generation and parton shower modelling affect the number of events that fall within the acceptance regions of our H^{+} analyses. An estimate of this acceptance uncertainty on acceptance due to the kinematics of the MC events, as determined by the event generator and parton shower modelling used, is required in order to put forward an accurate prediction of the SM expectation along with all the uncertainties associated with modelling it such that we may draw valid conclusions about any H^{+} signal.

As SM $t\bar{t}$ events form the largest background, a rough estimate of the uncertainty is determined for $t\bar{t}$ events produced using the SM $t\bar{t}$ MC samples available at the time, in addition to the baseline $t\bar{t}$ sample (Section 5.3). This is by no means a complete evaluation of the acceptance uncertainty, as such an evaluation would require the production of large amounts of MC with the contributions from parton distribution function sets, underlying event tunes and parton shower model parameters, all being varied independently. Additionally, the available MC samples generated with both ALPGEN, and POWHEG, interfaced to HERWIG/JIMMY, that would have allowed for independent uncertainties to be placed on the MC generator and parton shower modelling contained incorrect modelling to the tau polarisation. These samples could therefore not be used, as incorrect modelling of the geometric acceptance of the hadronic decay products of the tau will have a large effect on the overall acceptance for both analyses. Thus, in order to provide an estimate of the systematic uncertainty arising from the NLO $t\bar{t}$ generation and the parton shower modelling, the acceptance at each stage of the event selection for $t\bar{t}$ events is compared between MC@NLO interfaced to HERWIG/JIMMY, and POWHEG interfaced to PYTHIA. The acceptance uncertainty for H^{+} signal events (produced using PYTHIA) is estimated using SM $t\bar{t}$ samples, as no other H^{+} samples were available. As the H^{+} signal sample relies on $t\bar{t}$ events generated at LO, a LO SM $t\bar{t}$

sample produced with ACERMC, interfaced to PYTHIA is compared to the baseline NLO $t\bar{t}$ MC.

The particle selection used, is based on the *true* objects from the MC samples used and has been constructed to correspond to the kinematic ranges specified for reconstructed objects in Section 3.4. The selection thus requires electrons to fall within $|\eta| < 1.37$ or $1.52 < |\eta| < 2.47$ with $E_{\mathrm{T}} > 20\,\mathrm{GeV}$ and muons to fall within $|\eta| < 1.37$ with $p_{\mathrm{T}} > 15\,\mathrm{GeV}$. In the case of jets we use "true jet" objects[13] as in Section 5.4 with $|\eta| < 2.5$, while for true τ_{had} objects the visible products from the tau decay are grouped together to form the τ_{had} object, and we require this object lie within $|\eta| < 2.3$. A b-jet is defined as a true jet matched to a b quark (resulting from a top quark decay) within $\Delta R < 0.1$. The missing transverse energy in the event is calculated by the vector sum of momenta in the xy-plane of all the neutrinos in the event.

The event selection cuts follow from Subsection 5.3.1, with modified definitions used where applicable to cover the truth object definitions used here, while event cleaning cuts are unnecessary (only true $t\bar{t}$ MC events are being used) and discarded entirely. No trigger criteria are necessary, however the overlap removal is carried out using the truth objects defined above, as this will affect the acceptance.

In the case of the τ_{had}+ lepton channels the event selection is as follows:

1. Exactly 1 true electron with $E_{\mathrm{T}} > 25\,\mathrm{GeV}$ or 1 true muon with $p_{\mathrm{T}} > 20\,\mathrm{GeV}$
2. Exactly 1 true τ_{had} with $p_{\mathrm{T}} > 20\,\mathrm{GeV}$
3. Opposite sign electric charge (tau,e/μ)
4. ≥ 2 true jet objects, each with $p_{\mathrm{T}} > 20\,\mathrm{GeV}$
5. ≥ 1 b-jet with $p_{\mathrm{T}} > 20$

For τ_{had} + jets channel the selection is:

1. ≥ 4 true jet objects, each with $p_{\mathrm{T}} > 20\,\mathrm{GeV}$
2. Exactly true τ_{had} with $p_{\mathrm{T}} > 40\,\mathrm{GeV}$
3. Exactly 0 true electron or muon objects
4. $E_{\mathrm{T}}^{\mathrm{miss}} > 65\,\mathrm{GeV}$

---

[13] `jet_antiKt4Truth` variables composed of the hadrons resulting from a given shower, but allocated via the anti-k_t algorithm with a scale parameter of 0.4.

5. ≥ 1 b-jet with $p_{\mathrm{T}} > 20$

The uncertainties provided at each cut are binomial errors (Equation 5.13) that assume all selections up to that point constitute a single 'cut' that events will either pass or fail.

$$\sigma(p_c) = \sqrt{\frac{p_c\,(N - p_c)}{N-1}} \quad , \tag{5.13}$$

where N is the total number of events in the $t\bar{t}$ MC sample and p_c is the number of events that pass the selection up to cut c. The percentages of events passing the event selection up to a given cut for the electron and muon channels of the $\tau_{\mathrm{had}}+$ lepton selection are listed in Tables 5.6 and 5.7 respectively. The difference between generators at the end of the selection will be used as an estimate of the 'MC acceptance uncertainty'.

$\tau_{\mathrm{had}} + e$ cut	MC@NLO + HERWIG/JIMMY	POWHEG + PYTHIA	ACERMC + PYTHIA
No cuts	100.00 ± 0.00	100.000 ± 0.000	100.000 ± 0.000
1 e	24.83 ± 0.03	24.26 ± 0.02	24.60 ± 0.04
1 τ_{had}	1.54 ± 0.01	1.52 ± 0.01	1.57 ± 0.01
Opp. Sign	1.27 ± 0.01	1.27 ± 0.01	1.28 ± 0.01
≥ 2 jets	1.13 ± 0.01	1.11 ± 0.01	1.13 ± 0.01
≥ 1 b-jet	1.07 ± 0.01	1.03 ± 0.01	1.06 ± 0.01

Table 5.6.: Percentage of total events that pass up to and including a given cut for $\tau_{\mathrm{had}}+$ electron selection.

$\tau_{\mathrm{had}} + \mu$ cut	MC@NLO + HERWIG/JIMMY	POWHEG + PYTHIA	ACERMC + PYTHIA
No cuts	100.00 ± 0.00	100.00 ± 0.00	100.00 ± 0.00
1 μ	26.15 ± 0.03	25.38 ± 0.03	25.41 ± 0.04
1 τ_{had}	1.41 ± 0.01	1.36 ± 0.01	1.34 ± 0.01
Opp. Sign	1.27 ± 0.01	1.23 ± 0.01	1.20 ± 0.01
≥ 2 jets	1.13 ± 0.01	1.07 ± 0.01	1.07 ± 0.01
≥ 1 b-jet	1.09 ± 0.01	1.02 ± 0.01	1.02 ± 0.01

Table 5.7.: Percentage of total events that pass up to and including a given cut for $\tau_{\mathrm{had}}+$ muon selection.

In order to estimate the systematic uncertainty arising from the $t\bar{t}$ generation and the parton shower, the final acceptance for $t\bar{t}$ events is compared between the baseline NLO

τ_{had}+jets cut	MC@NLO + HERWIG/JIMMY	POWHEG + PYTHIA	ACERMC + PYTHIA
No cuts	100.00 ± 0.00	100.00 ± 0.00	100.00 ± 0.00
≥ 4 jets	63.83 ± 0.02	61.78 ± 0.03	64.17 ± 0.03
1 τ_{had}	3.14 ± 0.01	3.12 ± 0.01	3.32 ± 0.01
0 e or μ	2.85 ± 0.01	2.80 ± 0.01	2.98 ± 0.01
$E_{\text{T}}^{\text{miss}} > 65$ GeV	2.85 ± 0.01	2.80 ± 0.01	2.98 ± 0.01
≥ 1 b-jet	2.79 ± 0.01	2.70 ± 0.01	2.90 ± 0.01

Table 5.8.: Percentage of total events that pass up to and including a given cut for τ_{had}+jets selection.

$t\bar{t}$ sample (MC@NLO interfaced to HERWIG/JIMMY) and POWHEG interfaced to PYTHIA. For the electron and muon channels in NLO SM $t\bar{t}$ events the acceptance uncertainty for the τ_{had}+lepton selection is calculated in Equations 5.14 and 5.15 as the difference between the final acceptance (i.e. after cut 5.) for these two MC samples. The results are quoted as (the acceptance uncertainty) ± (the statistical uncertainty) associated with the number of events in the MC samples used.

$$\tau_{\text{had}} + e \text{ channel:} \quad (1.07 \pm 0.01) - (1.03 \pm 0.01) = 0.04 \pm 0.02 \quad , \tag{5.14}$$

$$\tau_{\text{had}} + \mu \text{ channel:} \quad (1.09 \pm 0.01) - (1.02 \pm 0.01) = 0.07 \pm 0.02 \quad . \tag{5.15}$$

Similarly, for the τ_{had}+jets selection in NLO SM $t\bar{t}$ events the uncertainty is taken from Equation 5.16:

$$\tau_{\text{had}}\text{+jets channel:} \quad (2.79 \pm 0.01) - (2.70 \pm 0.01) = 0.09 \pm 0.02 \quad . \tag{5.16}$$

Thus, for both τ_{had}+lepton and τ_{had}+jets selections the uncertainty is estimated at $\sim 4\%$ ($\tau_{\text{had}} + e$), $\sim 7\%$ ($\tau_{\text{had}} + \mu$) and $\sim 9\%$ (τ_{had}+jets), with the caveat that this does not account for any correlations between generator and parton shower model effects. These uncertainties enter into the analyses as uncertainties on the SM expectation distributions used in the limit calculations to outlined in Section 5.8.

In contrast to the SM $t\bar{t}$ events, the systematic uncertainty arising from the event generator and the parton shower model for the H^+ signal MC is set to the relative difference in acceptance between $t\bar{t}$ events generated with MC@NLO interfaced to HERWIG/JIMMY vs events produced using ACERMC (also a leading-order generator) interfaced to PYTHIA. For the electron and muon channels in this case the uncertainty for the τ_{had}+ lepton selection in LO SM $t\bar{t}$ events is given in Equations 5.17 and 5.18:

$$\tau_{\text{had}} + e \text{ channel:} \quad (1.07 \pm 0.01) - (1.06 \pm 0.01) = 0.01 \pm 0.02 \quad , \tag{5.17}$$

$$\tau_{\text{had}} + \mu \text{ channel:} \quad (1.09 \pm 0.01) - (1.02 \pm 0.01) = 0.07 \pm 0.02 \quad . \tag{5.18}$$

Finally, the acceptance uncertainty for the τ_{had}+ jets selection in LO SM $t\bar{t}$ events is given in Equation 5.19:

$$\tau_{\text{had}}\text{+ jets channel:} \quad (2.79 \pm 0.01) - (2.90 \pm 0.01) = -0.11 \pm 0.02 \quad . \tag{5.19}$$

Therefore the acceptance uncertainty due to the LO event generator and parton shower model for the H^+ signal MC is estimated to be $\sim$1% ($\tau_{\text{had}} + e$), $\sim$7% ($\tau_{\text{had}} + \mu$) and $\sim$11% (τ_{had}+ jets). These H^+ signal sample uncertainties are only estimates to get an idea of the order of the acceptance uncertainty associated with using the signal sample, they are not used for the uncertainty in the SM expectation.

5.7. $e \rightarrow \tau_{\text{had}}$ Mis-identification Probability

This section presents the study conducted into the suitability of the $e \rightarrow \tau_{\text{had}}$ mis-identification probability scale factors derived from $Z \rightarrow ee$ data as they are applied to $t\bar{t}$ events in the phase space defined by the charged Higgs event selections (Subsection 5.3.1). These scale factors are necessary to adjust the mis-identification probability in MC to that obtained from data.

The τ_{had} objects selected here are as described in Section 3.4. As the main tau identification algorithms are optimised to separate hadronic jets initiated by taus from quark and gluon jets, a separate electron veto (EV) was developed to reject τ_{had} candidates if they are more likely to have originated from electrons. The EV, however, is not perfect and there will be some associated mis-identification probability – where a real electron is selected as a τ_{had} object. The mis-identification probability depends on the specific algorithms used in the τ_{had} definition (Subsection 3.4). It is important to determine this mis-identification probability and its uncertainty so that the number of expected events after the charged Higgs event selection is not underestimated. In the case of hadronically decaying taus, the τ_{had} objects usually contain either one or three charged tracks and are described respectively as 1-prong or 3-prong τ_{had} objects. Mis-identified τ_{had} objects primarily come from QCD jets that satisfy the τ_{had} object selection criteria, however in the case of 1-prong τ_{had} objects, the single charged track with its associated energy deposition in the calorimeter can result from an electron. Thus the probability of an electron being mis-identified as a 1-prong τ_{had} must be estimated and accounted for in any analysis involving hadronically decaying taus. It is preferable to determine this $e \to \tau_{\text{had}}$ mis-identification probability in a data-driven way, however, doing so requires a pure sample of electrons from data. The ATLAS tau working group obtain such a sample by employing a tag-and-probe method in data to obtain a pure sample of $Z \to ee$ events that allow for the determination of the $e \to \tau_{\text{had}}$ mis-identification probability (outlined below in Subsection 5.7.1). This allows scale factors to be calculated that correct the mis-identification probability in MC to that observed in data. In the case of the $H^+ \to \tau^+_{\text{had}}\nu_\tau$ search channels, after object and event selection, the remaining τ_{had} objects are overwhelmingly from SM $t\bar{t}$ events. It is therefore necessary to ensure that the data-driven mis-identification probability obtained from $Z \to ee$ events is valid for τ_{had} candidates coming from $t\bar{t}$ events which will have different kinematics.

5.7.1. Tau Working Group Tag & Probe Study In Data

As mentioned above, the selection of a suitably pure electron sample from data that can be used to determine the $e \to \tau_{\text{had}}$ mis-identification probability is achieved using events containing $Z \to ee$ decays [165–167]. These events are selected by requiring:

1. the lowest un-prescaled electron trigger at the EF level;
2. a “tagged” electron object matched to the electron trigger object with $E_{\text{T}} > 30\,\text{GeV}$ and satisfying tight electron identification criteria;
3. a “probe” tau object with $p_{\text{T}} > 20\,\text{GeV}$, but not requiring any additional identification criteria other than it be reconstructed as a 1-prong τ_{had} object;
4. the invariant mass from combining the tag and probe objects 4-momenta must lie in a mass window of $80 - 100\,\text{GeV}$;

5. the tag and probe objects have oppositely charged tracks.

The QCD jet background for this selection is estimated using a data-driven method, known as the "`ABCD`" method, whereby events events are distributed over a 2-dimensional parameter space (using uncorrelated parameters) which is split into 4-regions (A, B, C, and D) by placing a single cut on each parameter. The signal should primarily lie in one of the regions with the QCD background in the signal region estimated by extrapolating from the other three regions with a minimal signal. This estimate is then used to subtract the QCD jet background from the $Z \to ee$ signal region. After this selection, the events remaining contain electrons (produced by Z boson decays) that are reconstructed as τ_{had} objects and the $e \to \tau_{\text{had}}$ mis-identification probability is calculated as

$$P_{\text{data}}(e \to \tau_{\text{had}}) = \frac{N_{\tau_{\text{had}}\text{ candidates passing full event selection, with }\tau\text{ ID and EV}}}{N_{\tau_{\text{had}}\text{ candidates passing full event selection}}} \quad . \tag{5.20}$$

This mis-identification probability is then compared with the corresponding probability obtained from $Z \to ee$ MC, defined as

$$P_{\text{MC}}(e \to \tau_{\text{had}}) = \frac{N_{\tau_{\text{had}}\text{ candidates passing full event selection, with }\tau\text{ ID and EV, matched to true electrons}}}{N_{\tau_{\text{had}}\text{ candidates passing full event selection, matched to true electrons}}} \quad . \tag{5.21}$$

Taking the ratio of the mis-identification probability for data to that for MC and binning by $|\eta^{\tau}|$ regions, "scale factors" are produced (see Table 5.9). These scale factors, $SF = \frac{P_{\text{data}}}{P_{\text{MC}}}$, are intended to correct $e \to \tau_{\text{had}}$ mis-identification probabilities in MC, and are used because they are more robust to slight variations in definition of the $e \to \tau_{\text{had}}$ mis-identification probability used in a given analysis.

5.7.2. Mis-identification Probability Test With $t\bar{t}$ MC

Due to the difficulty in selecting a pure sample of $t\bar{t}$ events decaying to electrons in data and thus determining an $e \to \tau_{\text{had}}$ mis-identification probability directly with $t\bar{t} \to ee$ events, it is necessary to use scale factors derived from $Z \to ee$ events. In order to justify using the tau working group MC-to-data scale factors it is necessary to show that the

$\lvert\eta^{\tau}\rvert$ range	Scale Factor
≤ 1.37	1.28 ± 0.52
1.52–1.37	1.0 ± 1.0
1.52–2.00	0.54 ± 0.36
≥ 2.00	2.76 ± 1.29

Table 5.9.: Scale factors, as calculated by the ATLAS tau working group [168], applied to the $e \rightarrow \tau_{\mathrm{had}}$ mis-identification probabilities in different pseudorapidity regions, for τ candidates with $E_{\mathrm{T}} > 20\,\mathrm{GeV}$ passing the tight likelihood based τ identification (`tau_tauLlhTight`) and medium electron veto (`tau_EleBDTMedium`), as well as overlap removal with any electrons fulfilling the tight identification requirements (`ElectronTight++`). Combined statistical and systematic uncertainties are quoted.

mis-identification probabilities between tau candidates from $Z \rightarrow ee$ events and those from $t\bar{t}$ events are consistent over the kinematic range of the tau candidates (i.e. $|\eta^{\tau}|$ and p_T^{τ}). The purpose of this MC study is simply to justify using the scale factors, determined by the Tau Working Group study (outlined above), for $t\bar{t}$ events — the purpose is *not* to reproduce the Tau Working Group study itself.

The $Z \rightarrow ee$ mis-identification probability in Monte Carlo was obtained using 347,220 $Z \rightarrow ee$ simulated events, produced with ALPGEN, to account for multi-parton interactions produced in conjunction with the Z, and interfaced to HERWIG/JIMMY to provide the underlying event and parton shower modelling. The object definitions and overlap removal mirror those used for the charged Higgs channels (Section 5.3) in order to remain unbiased when comparing mis-identification probabilities. However, the exact same tag-and-probe event selection (Subsection 5.7.1) used for the tau working group analysis was employed here to determine the numerator and denominator in Equation 5.21 for the $Z \rightarrow ee$ sample. The mis-identification probabilities for the $H^{+} \rightarrow \tau_{\mathrm{had}}^{+}\nu_{\tau}$ search channels were determined using SM $t\bar{t}$ events produced using the baseline SM $t\bar{t}$ MC sample for the charged Higgs analyses (Section 5.3). In this case, mis-identification probabilities for the τ_{had}+lepton (based on 238,576 simulated events) and τ_{had}+jets (based on 25,255 simulated events) final states were obtained using the full object selection, overlap removal and event selection used for the charged Higgs search channels (Section 5.3).

The $e \rightarrow \tau_{\mathrm{had}}$ mis-identification probabilities are determined using Equation 5.21, where the numerator is the number of τ_{had} candidates that satisfy the object selection criteria defined in Section 3.4 produced within events that pass the full event selection criteria for either τ_{had}+lepton, τ_{had}+jets or $Z \rightarrow ee$. These τ_{had} candidates must then be truth matched within a cone of $\Delta R < 0.1$ to electrons. The denominator repeats the process required for the numerator but simply removes the identification and electron veto requirements from the τ_{had} candidate selection to provide the total number of electrons that could potentially be selected as τ_{had} candidates in the events (where the event selection incorporates this looser τ_{had} definition). These probabilities are then compared for the two $t\bar{t}$ channels (i.e. $t\bar{t} \to e + e/\mu$ or $t\bar{t} \to e$+jets events) against the $Z \to ee$ events, over the kinematic range of the tau candidates available. These calculated probabilities are displayed in Figure 5.12.

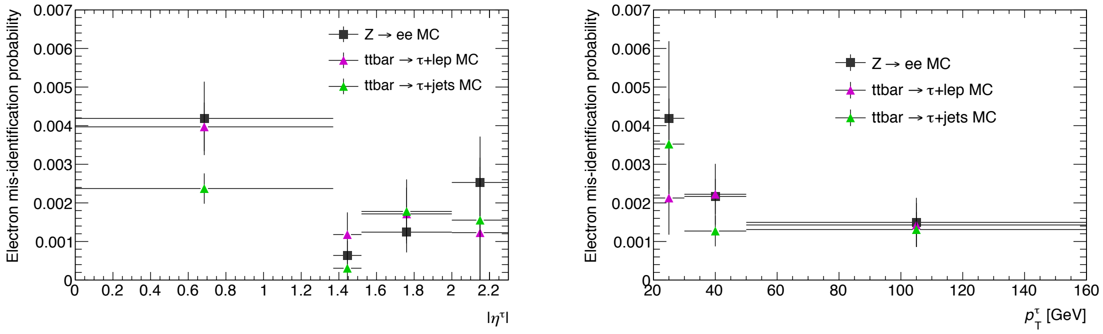

(a) $e \to \tau_{\text{had}}$ mis-identification probability binned by absolute pseudorapidity of the τ_{had} candidate ($|\eta^{\tau}|$). With bins corresponding to: barrel; EM calorimeter crack region; silicon end-cap region; TRT end-cap region.

(b) $e \to \tau_{\text{had}}$ mis-identification probability binned by transverse momentum of the τ_{had} candidate (p_{T}^{τ}).

Figure 5.12.: The $e \to \tau_{\text{had}}$ mis-identification probabilities from MC. Plotted for: $Z \to ee$ MC events using a tag and probe method; $t\bar{t} \to \tau_{\text{had}} + \mu$ and $t\bar{t} \to \tau_{\text{had}} + e$, corresponding to the τ_{had} + lepton H^+ search channel; $t\bar{t} \to \tau_{\text{had}} + jets$ H^+ search channel.

From Figures 5.12(a) and 5.12(b) it can be seen that the $e \to \tau_{\text{had}}$ mis-identification probabilities between $Z \to ee$ MC events and MC events passing selection for the $t\bar{t}$ channels agree within the binomial statistical uncertainties for each bin. As the overall $e \to \tau_{\text{had}}$ mis-identification probability is small ($0.1-0.5\%$) and the stated uncertainties on the scale factors themselves are relatively conservative (Subsection 5.7.1), it is concluded that these factors are valid to use in the $H^+ \to \tau^+_{\text{had}}\nu_\tau$ analyses as listed in Table 5.9. These mis-identification probabilities are applied in the analysis by scaling the MC events passing the event selections in which the selected τ_{had} object is found to have originated from a true electron. With adjustments of the scale factors by $\pm 1\sigma$ used to determine the uncertainty on the number of $e \to \tau_{\text{had}}$ mis-identified events passing the event selections — this uncertainty is added in quadrature to all the others to obtain the total uncertainty on the SM expectation.

5.8. Charged Higgs Limit

The upper limits on $\mathcal{B}(t \to bH^+)$, assuming $\mathcal{B}(H^+ \to \tau^+\nu_\tau) = 1$, are based on a profile likelihood ratio, using the $E_{\mathrm{T}}^{\mathrm{miss}}$ distribution for the τ_{had}+lepton analysis (Figure 5.13) and the $\tau_{\mathrm{had}} + E_{\mathrm{T}}^{\mathrm{miss}}$ transverse mass (m_{T}) distribution for the τ_{had}+jets analysis (Figure 5.14). With m_{T} defined as

$$m_{\mathrm{T}} = \sqrt{2p_{\mathrm{T}}^{\tau} E_{\mathrm{T}}^{\mathrm{miss}}(1 - \cos\Delta\phi)} \ , \tag{5.22}$$

where $\Delta\phi$ is the angle between $\vec{p}_{\mathrm{T}}^{\,\tau}$ and $\vec{E}_{\mathrm{T}}$.

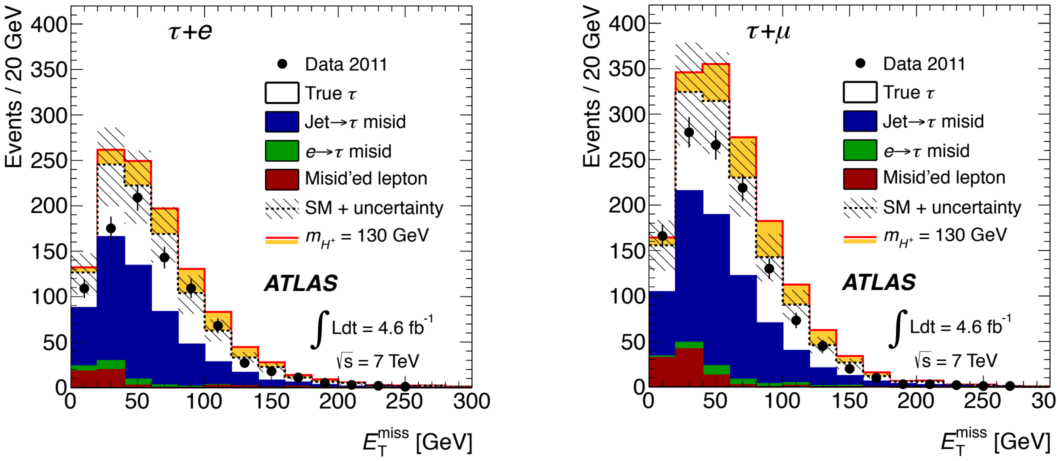

(a) $\tau_{\mathrm{had}} + e$

(b) $\tau_{\mathrm{had}} + \mu$

Figure 5.13.: Data vs expectation from MC and data-driven background estimates for the $E_{\mathrm{T}}^{\mathrm{miss}}$ distribution for the electron (a) and muon (b) channels in the τ_{had}+lepton analyses [114]. Signal MC events for a 130 GeV H^+ have been included assuming $\mathcal{B}(t \to bH^+) = 5\%$ for reference.

These distributions (Figures 5.13 and 5.14) are used to produce a test statistic based on the likelihood ratio, which is used to set the exclusion limits below. The systematic uncertainties for the background expectation (SM) are added in quadrature, and represented by the shaded regions in Figures 5.13 and 5.14, while the statistical uncertainties are shown by error bars on the data points. The likelihood ($\mathcal{L}$) is constructed assuming Poissonian ($\mathcal{P}$) distributed bin content that is a function of the branching ratio $B = \mathcal{B}(t \to bH^+)$, with nuisance parameters, $\boldsymbol{\theta}$, used to describe the effects of the systematic uncertainties:

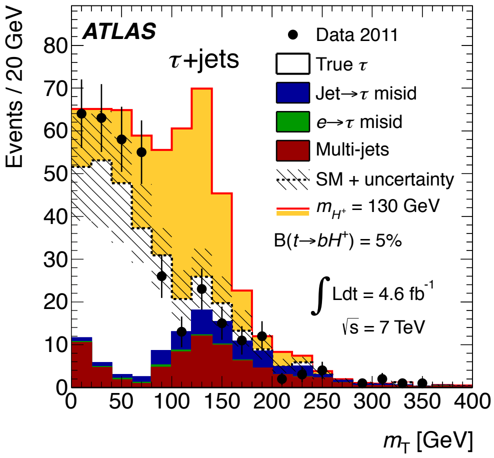

Figure 5.14.: Data vs expectation from MC and data-driven background estimates for the m_{T} distribution in the τ_{had} + jets analysis [114]. Signal MC events for a 130 GeV H^+ have been included assuming $\mathcal{B}(t \to bH^+) = 5\%$ for reference.

$$\mathcal{L}(B) = \prod_{i \,\in\, \mathrm{bins}} \mathcal{P}\left(n_i^{\mathrm{obs}} \mid n_i^{\mathrm{exp}}\right) \prod_{j \,\in\, \mathrm{syst.s}} \mathcal{G}\left(\theta_j\right) \quad , \tag{5.23}$$

where n_i^{obs} is the content of bin i in the distribution observed in the data and n_i^{exp} is the expected content — based on MC (i.e. "True τ" events) and the data-driven background estimates (i.e. "Jet→ τ misid","e→ τ misid", "Misid'ed lepton" and "Multi-jets" events). The systematic effects are set to have Gaussian distributions ($\mathcal{G}$) about their nominal values, which are estimated from the systematics studies conducted for the analyses (as shown in Table 5.4 for the data-driven background estimates, for example). The likelihood ratio is then defined as:

$$\lambda(B) = \frac{\mathcal{L}(B, \hat{\hat{\boldsymbol{\theta}}}_B)}{\mathcal{L}(\hat{B}, \hat{\boldsymbol{\theta}})} \quad , \tag{5.24}$$

where the $\hat{\hat{\boldsymbol{\theta}}}_B$ are the maximum likelihood estimators of the nuisance parameters for a fixed B, while $\hat{\boldsymbol{\theta}}$ and $\hat{B}$ are the global maximum likelihood estimators of $\boldsymbol{\theta}$ and B, respectively. With the one-sided log likelihood ratio based test statistic q_B defined as

$$q_B = -2\log\lambda(B)\ ,\quad 0 \leq \hat{B} \leq B\ \ , \tag{5.25}$$

note: $\hat{B}$ is forced to be non-negative, as a negative branching ratio estimator would represent an unphysical scenario. Thus, if the branching ratio estimator is less than B at least 95% of the time for a given B, an upper limit at this value for B at a 95% confidence level can be set. Further detail on the limit setting procedure and the one-sided log likelihood ratio based test statistic used can be found here [169], while additional discussion of the role of a test statistic is to be provided in Chapter 6. A profile likelihood ratio is used rather than marginalisation over the systematic uncertainties as there are so many sources of systematic uncertainties in ATLAS, and MC samples are so complex and computationally intensive to produce, it is not feasible to scan over each source.

The upper limits set on the branching ratio for $\mathcal{B}(t \to bH^+)$ by assuming $\mathcal{B}(H^+ \to \tau^+\nu_\tau) = 1$ in each of the two τ_{had} analyses, at 95% confidence level [170, 171], are shown in Figure 5.15. Where the confidence level for excluding the possibility of H^+ events + backgrounds (i.e. the signal + background hypothesis), is the probability, assuming the presence of both signal and background at their hypothesised levels, that the likelihood ratio would be less than or equal to that observed in the data. This is determined for data at eight charged Higgs mass points, $m_{H^+} = 90, 100, 110, 120, 130, 140, 150, 160$ GeV, using new sets of signal MC produced with PYTHIA.

The limit plots (Figures 5.15(a) and 5.15(b)) show the expected exclusion sensitivity (dashed line) of the τ_{had}+lepton and τ_{had}+jets analyses and the $\pm 1\sigma$ (green band) and $\pm 2\sigma$ (yellow band) uncertainties on this expectation. The black points (and solid black lines) represent the 95% confidence limits on the branching ratio exclusion, calculated from data at the eight charged Higgs mass points.

For the τ_{had}+lepton analysis, the data are slightly above the expected exclusion sensitivity over most of the mass range however the results are still consistant with the expected sensitivity of the analysis. The higher sensitivity in the τ_{had}+jets channel is due to the superior discriminating power of the m_{T} distribution as long as the H^+ mass is sufficiently far from the W mass. Assuming $\mathcal{B}(H^+ \to \tau\nu) = 1$, this leads to upper limits on the branching ratio for $\mathcal{B}(t \to bH^+)$ of between 3% and 7% for charged Higgs boson masses (m_{H^+}) in the range $90\,\text{GeV} < m_{H^+} < 160\,\text{GeV}$.

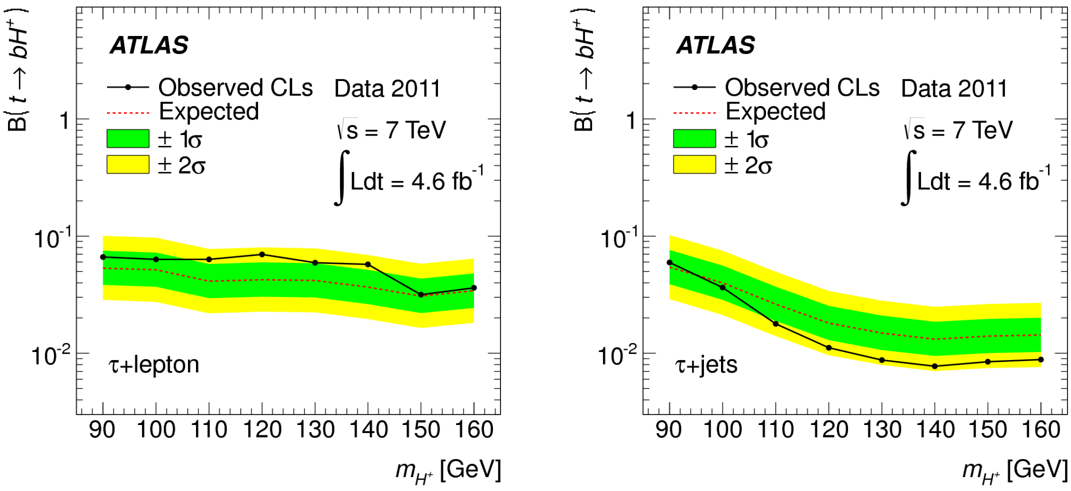

(a) τ_{had} + lepton **(b)** τ_{had} + jets

Figure 5.15.: Exclusion limits for τ_{had} analyses, expected [114]

For the τ_{had}+jets analysis the data agree well with the expected sensitivity, leading to upper limits on the branching fraction $\mathcal{B}(t \to bH^+)$ between 1% and 6% for charged Higgs boson masses (m_{H^+}) in the range $90\,\mathrm{GeV} < m_{H^+} < 160\,\mathrm{GeV}$.

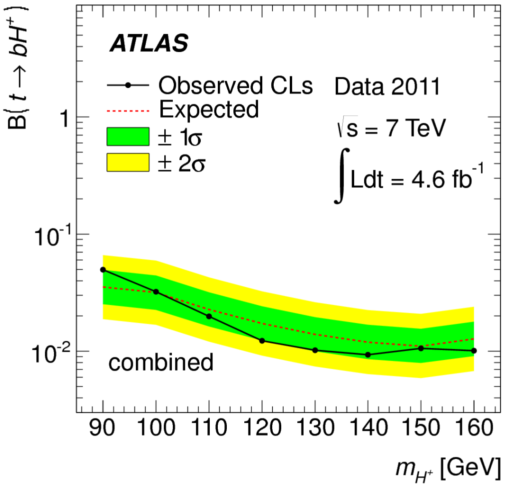

Figure 5.16.: Combined upper limit on $\mathcal{B}(t \to bH^+)$, assuming $\mathcal{B}(H^+ \to \tau^+\nu_\tau) = 1$. [114]

The combined upper limit on the branching ratio, $\mathcal{B}(t \to bH^+)$, set by assuming $\mathcal{B}(H^+ \to \tau^+\nu_\tau) = 1$ is shown in Figure 5.16 with the inclusion of the leptonically decaying τ channel not discussed here. The same profile likelihood ratio is used, but this time using all three of the distributions that offer some discriminating power between signal and background, i.e. m_T^H[14] (τ_{lep}+ jets), $E_{\mathrm{T}}^{\mathrm{miss}}$ (τ_{had}+ lepton) and m_{T} (τ_{had}+ jets). Systematic uncertainties are included as Gaussian terms in the likelihood, but are treated as correlated where appropriate [172].

Over the H^+ mass range covered, $90-160$ GeV, the upper limit on the branching ratio $t \to bH^+$ excluded here varies between $1-4\%$, which is roughly an order of magnitude lower than the previous DØ limits [173]. No inconsistencies with the SM have been observed.

---

[14] Where m_T^H is defined by $(m_T^H)^2 = \left(\sqrt{m_t^2 - \left|\vec{p_T}^{\,l} + \vec{p_T}^{\,b} + \vec{p_T}^{\,\mathrm{miss}}\right|^2} - \vec{p_T}^{\,b}\right)^2 - \left|\vec{p_T}^{\,l} + \vec{p_T}^{\,\mathrm{miss}}\right|^2$.

Chapter 6.

Testing SM Predictions with Inclusive $e^{\pm}\mu^{\mp}$ Events

This chapter presents "An Inclusive Dilepton Analysis" (AIDA) as part of the ATLAS experiment. The main aims of the analysis are to simultaneously measure the $t\bar{t}$, $W^{+}W^{-}$, and $Z/\gamma^{*} \rightarrow \tau\tau$ production cross sections, as well as test the consistency of pp collision data collected at $\sqrt{s} = 7\,\text{TeV}$ with ATLAS in 2011 against the SM prediction. These aims are achieved using events containing an electron and oppositely charged muon in the final state. Such events are chosen with a minimal set of object/event selection criteria such that the analysis is as inclusive as possible. The AIDA method and derivation of cross sections is demonstrated in Section 6.1, while a method to test the consistency of the SM in the phase space defined by AIDA is developed and refined throughout the remainder of the chapter. Section 6.2 outlines the general requirements for conducting a goodness-of-fit test between data and the SM expectation — also covering ideal vs expedient implementations of such a test in the AIDA case. In Section 6.3 a toy study is conducted to contrast these two implementations and identify where improvements could be made to the expedient method. Section 6.4 then covers the resulting steps taken to bridge the gap between the expedient and ideal implementations of this goodness-of-fit test as applied to AIDA and the resulting level of agreement between data and the SM. The chapter concludes with some discussion of outstanding points, and possibilities for the $\sqrt{s} = 8\,\text{TeV}$ data collected by ATLAS in 2012 (Section 6.5).

6.1. An Inclusive Dilepton Analysis

In order to fully exploit the unprecedented collision energies at the LHC, it is necessary to conduct both measurements of SM physics processes as well as model independent searches for new physics, and these can in fact be considered two sides of the same coin. In general, searches for physics beyond the SM must mitigate dominant SM contributions in order to extract any potential signal (as in the case of the charged Higgs for example). Limits imposed on the phase space covered as a result of this requirement (i.e. needing to cut away the dominant SM contributions) necessarily make such searches model *dependent* — as they only allow constraints to be placed on new physics models that make definite predictions in convenient regions of phase space.

Model *independent* searches, on the other hand, need to cover much larger regions of phase space to maximise the chances of discovering any new/unanticipated signal. As a consequence of this, such searches must contend with large contributions from one or more of the dominant SM processes that may swamp any new physics signal. So, although model independent searches are preferable from a physics standpoint because they are unbiased with regard to BSM theories, they are often technically unfeasible. This problem can be mitigated to a degree by choosing observables over which dominant SM processes are well modelled and well separated and then combining SM measurements and a model independent search for new physics — this is the approach taken in An Inclusive Dilepton Analysis (AIDA) at ATLAS. Taking such an approach thus requires accurate modelling/measurement of the dominant SM processes over the entire phase space chosen. This re-measurement is necessary because, in general, other SM measurements are made in isolation from other physics processes to improve sensitivity, and may suffer from systematic effects that are non-obvious in the limited phase space used for those measurements. Such measurements are therefore not ideal for use in a model-independent search approach, where the the SM contributions must all be tightly consistent with one-another over the much larger phase space under consideration. In order to tackle this problem AIDA uses Monte Carlo simulation to perform simultaneous SM cross section measurements of the dominant SM processes in a more inclusive phase space (i.e. an event final state selected by only a minimal set of requirements). Thus the method not only provides multiple simultaneous SM measurements, but also allows their (in)consistency to make inferences about possible new physics in a more model-independent way.

The purpose of this section is to provide a demonstration of this AIDA method for cross section measurements, focusing on aspects most relevant to goodness-of-fit testing of the SM in the context of AIDA which comprise the rest of this chapter (Sections 6.2, 6.3, 6.4). For a far more detailed account of AIDA cross section measurements themselves see [174]. AIDA at ATLAS derives from an equivalent study conducted previously at CDF [175, 176], and in its first iteration uses events containing a prompt electron and an oppositely charged prompt muon ($e^\pm\mu^\mp$). These events are selected from ATLAS data collected in 2011 corresponding to an integrated luminosity of $4.59 \pm 0.08\,\mathrm{fb}^{-1}$ [57], based on an improved luminosity calibration against the van der Meer (vdM) scans[1] conducted by the LHC. This study was completed in 2013 and therefore not available to the analyses presented in Chapter 5. The resulting data distribution in the missing transverse energy and jet multiplicity ($E_{\mathrm{T}}^{\mathrm{miss}}$–$N_{\mathrm{jets}}$) parameter space is then used to simultaneously fit templates produced using MC simulated events. The $E_{\mathrm{T}}^{\mathrm{miss}}$–$N_{\mathrm{jets}}$ parameter space is considered because it naturally separates the three processes with the largest cross sections that produce high-p_{T} $e^\pm\mu^\mp$ events at the LHC — $t\bar{t}$, W^+W^- and $Z/\gamma^* \to \tau\tau$ events for which the invariant mass of the sum of the 4-momenta of the two taus is less than 40 GeV (i.e. $M_{\tau\tau} \geq 40$ GeV). Production cross sections for these three processes, in $\sqrt{s} = 7$ TeV pp collisions are then extracted from these MC template fits.

6.1.1. Event Selection and Template Production

The processes chosen to be measured are $t\bar{t}$, W^+W^- (hereafter WW), and $Z/\gamma^* \to \tau\tau$ [$M_{\tau\tau} \geq 40$ GeV] (hereafter written just $Z/\gamma^* \to \tau\tau$), in final states containing a prompt electron and prompt muon of opposite electric charge, $e^\pm\mu^\mp$ (hereafter $e\mu$). Example Feynman diagrams for these processes are provided in Figure 6.1.

The additional SM processes that produce $e\mu$ final states are not measured here, as their contributions are smaller. As a percentage of the real $e\mu$ events, the relative contributions (from MC) are approximately: 52% ($t\bar{t}$); 30.8% ($Z/\gamma^* \to \tau\tau$); 11.1% (WW); 5.2% (Wt); 0.9% (WZ/ZZ). As a result, Wt and WZ/ZZ processes in which one or more leptons are not reconstructed, are treated as fixed backgrounds, with their distributions over the $E_{\mathrm{T}}^{\mathrm{miss}}$–$N_{\mathrm{jets}}$ parameter space normalised to theoretical expectations.

The object definitions used are those recommended by the ATLAS top reconstruction group and have been outlined in Section 3.4, as they are mostly common to both AIDA and the light charged Higgs searches of Chapter 5. Any differences in object definitions/selection criteria from the previous descriptions will be noted where relevant.

---

[1] Where the changes in luminosity are measured as the proton beams are slowly move through each other in terms of the relative x and y positions of their respective beam spots.

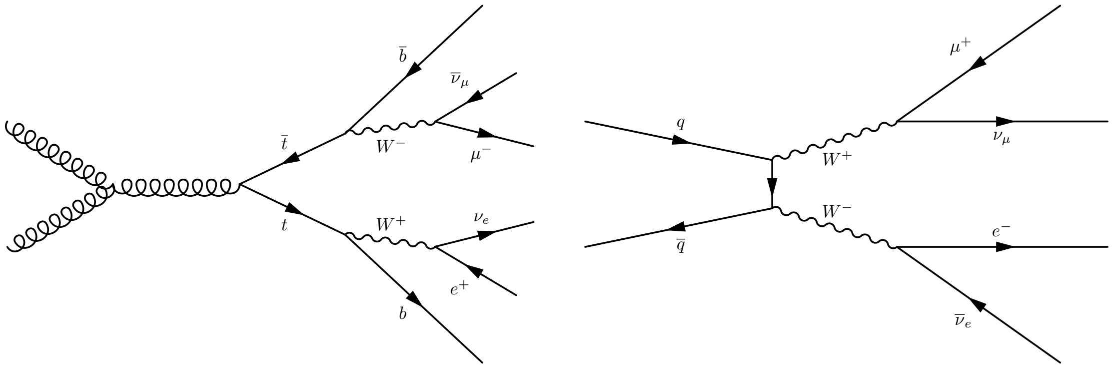

(a) $t\bar{t}$ production and decay to $e\mu$.

(b) WW production and decay to $e\mu$.

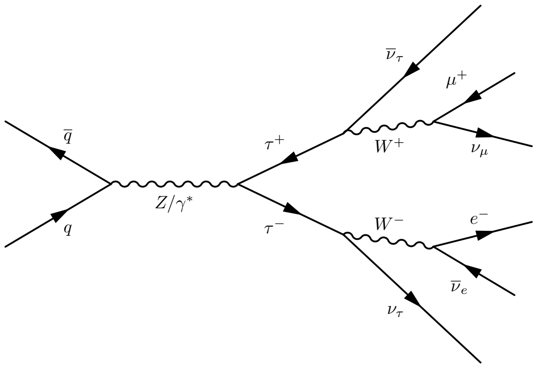

(c) $Z/\gamma^* \to \tau\tau$ production and decay to $e\mu$.

Figure 6.1.: Example Fyeynman diagrams representing decays to $e\mu$ final states for the three signal processes selected.

Event Selection

Events containing an electron and an oppositely charged muon ($e^\pm\mu^\mp$) are selected with a minimal set of requirements to ensure the data sample is as inclusive as possible. This particular final state was chosen because the Drell-Yan production of e^+e^- and $\mu^+\mu^-$ would swamp all other processes were these final states to be used. Opposite sign ee or $\mu\mu$ events also have many more (and varied) backgrounds, however it is envisaged that the same sign dilepton event content will eventually be studied in a similar manner. The event selection proceeds as follows:

1. *Good Runs List (Data and Data-driven Fakes)*
   Events must occur within a lumi-block listed in the top group Good Runs List for 2011 data periods B–M, with MC events reweighted to match the pile-up conditions for these data periods.

2. *Triggers*

   Events must pass the lowest-p_{T} unprescaled single electron or single muon trigger (or both). The notation specifying the triggers is a shorthand used by the experiment — the main takeaway is that "`EF`" specifies the Event Filter level, and the number following `e` or `mu` refers to the E_{T} threshold for the electron or p_{T} threshold for the muon trigger object. The electron trigger requirement is `EF_e20_medium` for periods B–J; `EF_e22_medium` for period K; and either `EF_e22vh_medium1` or `e45_medium1` for periods L–M. The muon trigger requirement is `EF_mu18` for periods B–I; and `EF_mu18_medium` for periods J–M. The "`medium`" tag refers to additional identification requirements that allow the p_{T} thresholds to remain at their relatively low levels (e.g. the lowest threshold for the single electron trigger only increases by 2 GeV over 2011 in spite of the orders of magnitude increase in instantaneous luminosity) without increasing the trigger rate to beyond the ability of the TDAQ system to cope.

3. *Primary Vertex Requirement*

   The primary vertex (i.e. vertex with the highest $\sum p_{\mathrm{T}}^{track}$ in the bunch crossing) must be formed from at least 5 reconstructed tracks.

4. *Overlap Veto*

   If an electron candidate overlaps with a selected muon candidate within an overlap region $\Delta\theta < 0.15$ and $\Delta\phi < 0.15$ the event is discarded. This is to remove $Z \to \mu\mu$ events where one of the muons undergoes bremsstrahlung and the overlapping electron candidates result from photon conversion close to the muon track. This is a much hasher requirement than the standard overlap removal (only requiring that the electron and muon do not share the same track) used in Chapter 5 for example, as neither of those analyses were selecting events with a high-p_{T} muon *and* a high-p_{T} electron.

5. *Exactly one e and one μ*

   An event can contain only 1 selected muon object and 1 selected electron object with one or both of these within $\Delta R < 0.15$ of the corresponding electron or muon trigger object. This trigger matching is necessary to ensure correct calculation of the integrated luminosity.

6. *Mis-measured Jet and LAr Error Vetos*

   Events containing mis-measured jets (due to noise bursts in calorimeters in 2011) are discarded as this will affect the quality of the $E_{\mathrm{T}}^{\mathrm{miss}}$ calculation. Events are also discarded if data integrity errors occurred in the LAr EM calorimeter.

7. *Truth Matching (MC only)*
   The reconstructed electron and muon objects selected must be matched to true prompt electrons and muons. This is to avoid double counting non-prompt electrons and muons, as the rates for these events are to be estimated from data.

8. *Opposite Sign*
   The selected e and μ objects must have opposite electric charge — this requirement largely removes the $Z/\gamma^* \to ee$ and $Z/\gamma^* \to \mu\mu$ backgrounds (and is the reason this $e\mu$ final state was selected)

Monte Carlo

MC simulated events are produced (via the steps described in Section 3.3) as part of the MC11 production campaign [177] by the ATLAS production group (as in Chapter 5, but with updated recommendations from the top working group [178]). The known SM processes that can lead to an $e\mu$ final state are $t\bar{t}$, WW, $Z/\gamma^* \to \tau\tau$, Wt, WZ and ZZ production, and MC samples are used to model each of these processes. The baseline MC samples used for the analysis are listed in Table 6.1, and discussed briefly below along with their reference cross sections. In general the samples are those recommended for use in analyses on 2011 data by the ATLAS top working group, and are the same samples used in the charged Higgs analyses previously described in Subsection 5.3.1.

To simulate pileup resulting from different pp collisions in the same bunch crossing, minimum bias events were generated with PYTHIA using the ATLAS AMBT2B tune [179] and CTEQ6L1 parton distribution functions (PDFs) [180]. Parton showering and underlying event tunes for PYTHIA and HERWIG/JIMMY have also been updated to better match the jet rate data from ATLAS [181].

The baseline sample for $t\bar{t}$ production includes a generator-level filter that requires at least one top quark to decay to produce a W boson which in turn decays to produce an electron, a muon, or a tau with $p_{\mathrm{T}} > 1\,\mathrm{GeV}$. As the branching ratios for semileptonic and dileptonic $t\bar{t}$ decay are 10.5% and 43.8% respectively the filter efficiency for the sample including dileptonic and semileptonic decays is 0.543. The $t\bar{t}$ cross section was normalised to the next-to-next-to leading order (NNLO) cross section of $177.3\,^{+19.0}_{-20.3}\,\mathrm{pb}$

for a top quark mass of 172.5 GeV — using `Top++` [182], which calculates the inclusive top pair production cross section in hadron collisions.

The baseline sample for $Z/\gamma^* \to \tau\tau$ production in association with jets was simulated using SHERPA `v1.4.0` [183] and CT10 PDFs, using the leading order matrix element and parton shower calculation. These samples differ from the previously used $Z+$jets samples (produced with ALPGEN+HERWIG/JIMMY) as the SHERPA sample better models the rapidity distribution of the Z boson. The cross section for $Z/\gamma^* \to \tau\tau$ production was normalised to the QCD NNLO prediction [184] calculated by FEWZ [156] at 1070 ± 54 pb. In both the cross section calculation and MC sample, the invariant mass of the tau lepton pair was required to be greater than 40 GeV, with cases of lower invariant masses to be considered as background.

In addition to the baseline samples for WW production (MC@NLO+HERWIG/JIMMY) are samples containing contributions from: gluon-gluon fusion processes, $gg \to WW$, involving box diagrams; and gluon-gluon fusion induced Higgs boson production and decay to WW^* which has a cross section of 3 pb ($m_H = 125$ GeV), providing a non-negligible contribution to the final state. The total SM cross section for WW production in pp collisions at $\sqrt{s} = 7$ TeV is predicted at NLO to be $44.7^{+2.1}_{-1.9}$ pb [185].

Diboson WZ and ZZ sample cross sections were normalised to NLO calculations performed using MC@NLO and MSTW2008 NLO PDFs [186], at $\sigma^{\mathrm{th}}_{WZ} = 17.83 \pm 1.25$ pb and $\sigma^{\mathrm{th}}_{ZZ} = 5.86 \pm 0.29$ pb. In these MC@NLO calculations the Z boson is required to be on the mass shell [184]. The theoretical cross sections include contributions from both Z and γ^*. In WZ, the W decay is inclusive and Z bosons decay via $Z \to ll$ to produce a pair of electrons, muons, or taus, while in ZZ, one Z decay is inclusive, while the other Z boson decays via $Z \to ll$. Other decay modes not specifically simulated are absorbed by the data-driven fakes estimation (to be described in the next subsection).

The Wt production cross section was normalised to the approximate NNLO prediction of 15.7 ± 1.1 pb [152], which was also evaluated using MSTW 2008 NNLO PDFs. To be misidentified as an $e\mu$ event, contributions from single top production in the s and t channels require a jet or a non-prompt lepton to fake the prompt lepton signature and are therefore also absorbed into the data-driven fakes estimate to be discussed next.

Application of this event selection to the baseline MC samples determines the events used to produce the MC templates, while the selection efficiency (Table 6.2) will be used later for the initial template normalisations.

Physics Process	Notes	Dataset ID	Generator	Hadronization	PDFs
$t\bar{t}$		105200	MC@NLO `v4.01`	HERWIG `v6.520`	CT10
$Z/\gamma^* \rightarrow \tau\tau$		147772	SHERPA `v1.4.0`	SHERPA `v1.4.0`	CT10
WW	μe	105922	MC@NLO `v4.01`	HERWIG `v6.520`	CT10
	τe	105923			
	$e\mu$	105925			
	$\tau\mu$	105926			
	$e\tau$	105927			
	$\mu\tau$	105928			
	$\tau\tau$	105929			
$gg \rightarrow WW$	ee	106011	$gg2WW$ `v3.0`	HERWIG `v6.520`	CT10
	$e\mu$	106012			
	$e\tau$	106013			
	μe	106014			
	$\mu\mu$	106015			
	$\mu\tau$	106016			
	τe	106017			
	$\tau\mu$	106018			
	$\tau\tau$	106019			
$H \rightarrow WW^* \rightarrow ll$		116703	POWHEG	PYTHIA `v6.425`	CTEQ6L1
Wt		108346	MC@NLO `v4.01`	HERWIG `v6.520`	CT10
WZ	+0 parton	107104	ALPGEN `v2.13`	HERWIG `v6.520`	CTEQ6L1
	+1 parton	107105			
	+2 parton	107106			
	+3 parton	107107			
ZZ	+0 parton	107108	ALPGEN `v2.13`	HERWIG `v6.520`	CTEQ6L1
	+1 parton	107109			
	+2 parton	107110			
	+3 parton	107111			

Table 6.1.: Configurations for the baseline Monte Carlo samples used to generate the nominal template distributions in the $E_{\mathrm{T}}^{\mathrm{miss}}$–$N_{\mathrm{jets}}$ parameter space. The dataset ID is an identification tag used internally to refer to the various MC datasets stored on the WLCG.

Physics Process	Theoretical Cross Section (σ^{th})	MC Filter Efficiency (ϵ_f)	Initial Events (pile-up reweighted)	Selected Events	Selection Efficiency (ϵ_s)
$t\bar{t}$	$177.3^{+19.0}_{-20.3}$ pb	0.5426	11,583,234	154,816	0.01336
WW	$44.7^{+2.1}_{-1.9}$ pb	0.0798	1,202,998	92,809	0.07715
$Z/\gamma^* \to \tau\tau$	1070 ± 54 pb	0.1366	1,568,346	9,010	0.00575
Wt	15.7 ± 1.1 pb	1.00	797,009	6,542	0.00821
WZ	18.0 ± 1.3 pb	0.101	139,932	1,333	0.00953
ZZ	5.64 ± 0.28 pb	0.191	90,026	304	0.00338

Table 6.2.: Theoretical cross section for the physics processes modelled as well as the MC filter efficiency for the baseline samples — as MC samples are filtered at generator level to include $e\mu$ events to avoid overlapping with the events containing mis-reconstructed or non-prompt electrons/muons, which are estimated from data. Also listed, are the numbers of pile-up reweighted events that are processed through the event selection, along with the fraction of events that pass the event selection listed above.

Data-driven Fakes Estimate

The estimate of events in data that pass the event selection but contain mis-reconstructed or non-prompt electrons/muons is determined via the "matrix method", which is validated using control regions in the data, with events of this type hereafter termed "fakes". The matrix method is based on selecting two categories of events, using loose (L) and tight (T) lepton selection requirements, and expressing them in terms of the the numbers of real (R) and fake (F) leptons that contribute to each category. Loose electron candidates must satisfy all selection cuts presented in Section 3.4, but with the "`tight++`" identification criteria replaced by "`medium++`[2]" identification criteria and removal of the requirement that the electron be isolated, though a veto is used if the electron is matched to a photon conversion vertex. Loose muon candidates must satisfy all of the muon selection requirements presented in Section 3.4 except that they must not be isolated, i.e. either $E_T(\Delta R < 0.2) \geq 4\,\text{GeV}$ or $p_{\text{T}}(\Delta R < 0.3) \geq 2.5\,\text{GeV}$.

In the case of a single lepton, the number of loose and tight leptons can be written as:

$$N^L = N^L_R + N^L_F \quad , \tag{6.1}$$

$$N^T = N^T_R + N^T_F \quad . \tag{6.2}$$

---

[2] Removes a high threshold cut on TRT hits, and a cut on the value E/p from the `tight++` criteria.

As we are interested in the number of tight leptons that are fakes (N_F^T), we re-write Equation 6.2 in terms of the number of loose leptons multiplied by the efficiencies at which they are selected as tight leptons:

$$N^T = rN_R^L + fN_F^L \quad \& \quad N^L = \frac{N_R^T}{r} + \frac{N_F^T}{f} \quad , \tag{6.3}$$

where r and f are the efficiencies with which real loose leptons and fake loose leptons are selected as tight leptons. These efficiencies themselves are measured using control regions in data where the contribution of real leptons is higher (e.g. Z boson decays to leptons for r), and regions in which the contribution from fake leptons is higher (e.g. QCD multi-jet events for f) [178]. The quantity of interest (N_F^T) can thus be expressed in terms of these efficiencies and quantities of tight and loose leptons as:

$$\begin{aligned} N_F^T &= N^T - N_R^T \\ &= f\left(N^L - \frac{N_R^T}{r}\right) \quad . \end{aligned} \tag{6.4}$$

$$\begin{aligned} \Longrightarrow N_R^T\left(1-\frac{f}{r}\right) &= N^T - fN^L \quad , \\ i.e.\ N_F^T &= N^T - \left(N^T - fN^L\right)\left(1-\frac{f}{r}\right)^{-1} \\ &= N^T - \frac{rN^T - rfN^L}{r-f} \\ &= \frac{f}{r-f}(rN^L - N^T) \quad . \end{aligned} \tag{6.5}$$

The matrix method extends this idea to the case of two leptons (in our case $e\mu$) by expressing N^{TT}, N^{TL}, N^{LT}, N^{LL} in terms of linear combinations of N^{RR}, N^{RF}, N^{FR}, N^{FF}, shown in Equation 6.6.

$$\begin{pmatrix} N^{RR} \\ N^{RF} \\ N^{FR} \\ N^{FF} \end{pmatrix} = \frac{1}{(r_e - f_e)(r_\mu - f_\mu)} \begin{pmatrix} (1-f_e)(1-f_\mu) & -(1-f_e)\,f_\mu & -f_e\,(1-f_\mu) & f_e f_\mu \\ -(1-f_e)(1-r_\mu) & (1-f_e)\,r_\mu & f_e\,(1-r_\mu) & -f_e r_\mu \\ -(1-r_e)(1-f_\mu) & (1-r_e)\,f_\mu & r_e\,(1-f_\mu) & -r_e f_\mu \\ (1-r_e)(1-r_\mu) & -(1-r_e)\,r_\mu & -r_e\,(1-r_\mu) & r_e r_\mu \end{pmatrix} \begin{pmatrix} N^{TT} \\ N^{TL} \\ N^{LT} \\ N^{LL} \end{pmatrix} \tag{6.6}$$

When run on data, with T(T), T(L), L(T), L(L) selections for the electron(muon), the event yield is determined to be 207 ± 158. The uncertainty is derived by taking all combinations of f_e, r_e, f_μ, r_μ adjusted up/down by their respective uncertainties to determine the highest and lowest resulting event yields (i.e. the outer envelope of possible yields), and taking half of this difference to be a conservative estimate.

Templates

Each of the three signal processes produce characteristic transverse missing energy, $E_{\mathrm{T}}^{\mathrm{miss}}$, and jet multiplicity, N_{jets}, distributions. Typical $t\bar{t}$ events have large $E_{\mathrm{T}}^{\mathrm{miss}}$ and high jet multiplicity; WW events tend to have large $E_{\mathrm{T}}^{\mathrm{miss}}$ and relatively low jet multiplicity; while $Z/\gamma^* \to \tau\tau$ events often have low $E_{\mathrm{T}}^{\mathrm{miss}}$ and low jet multiplicity. This is the reason for choosing a two-dimensional parameter space defined by $E_{\mathrm{T}}^{\mathrm{miss}}$ and N_{jets} that naturally separates the contributions from each process as illustrated in Figure 6.2, allowing for the production of these three processes to be measured via a simultaneous fit. Any overlap regions between the processes allow them to constrain each other during the fit, ideally producing globally consistent measurements over the whole space.

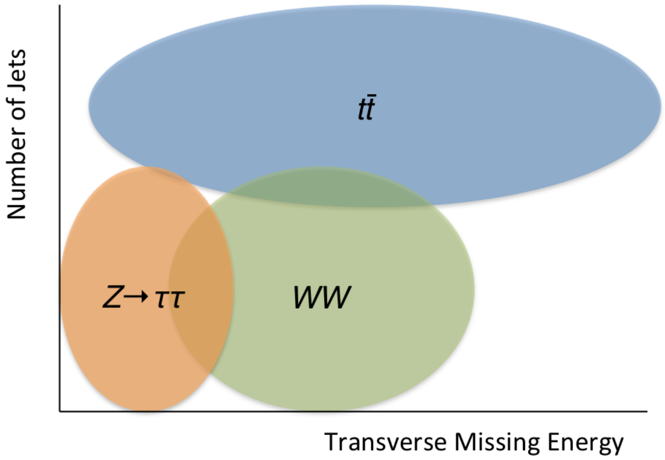

Figure 6.2.: Illustration of how the $t\bar{t}$, WW, and $Z/\gamma^* \to \tau\tau$ processes that produce $e\mu$ final states are naturally separated in the $E_{\mathrm{T}}^{\mathrm{miss}}$–$N_{\mathrm{jets}}$ parameter space.

Templates (2D histograms) in the $E_{\mathrm{T}}^{\mathrm{miss}}$-$N_{\mathrm{jets}}$ parameter space are produced for signal processes ($t\bar{t}$, WW, $Z/\gamma^* \to \tau\tau$) and backgrounds (Wt, WZ/ZZ) using the object and event selection described above, with the fakes template estimated from data. The templates are then all employed in a fit of the three signal templates to data. The $E_{\mathrm{T}}^{\mathrm{miss}}$–$N_{\mathrm{jets}}$ parameter space is divided into just two bins for jet multiplicity, $N_{\mathrm{jets}} = 0$ and $N_{\mathrm{jets}} \geq 1$, requiring reconstructed jet objects to have p_{T} greater than 30 GeV to be counted towards the N_{jets} total. The reason for this compromise in the number of jet bins used stems from the need to use the baseline MC@NLO $t\bar{t}$ MC (for consistency among other ATLAS top group results), which does not correctly model events with high jet multiplicities. However, the proportion of events with high jet multiplicities is small, and adequate signal separation can be achieved with just two jet bins without reducing the sensitivity of the cross section measurements — with the differences between results based on the baseline MC@NLO $t\bar{t}$ MC sample and MC generated with POWHEG interfaced to HERWIG/JIMMY taken as the generator level modelling uncertainty. The $E_{\mathrm{T}}^{\mathrm{miss}}$ is divided into twenty bins from $0 < E_{\mathrm{T}}^{\mathrm{miss}} < 200^{+}$ GeV in increments of 10 GeV, with the last bin containing the overflow. The templates produced with this binning are displayed in Figure 6.3 and their relative contributions can be seen in Figure 6.4 for the two N_{jets} bins.

The normalisation of an MC template (N), Figures 6.3(a)–(e), is determined by scaling to the expected number of events based on the theoretical cross section (σ^{th}), generator filter efficiency (ϵ_f), event selection efficiency (ϵ_s) and integrated luminosity in data ($\int \mathcal{L}\,\mathrm{dt} = 4.59\,\mathrm{fb}^{-1}$):

$$N = \epsilon_f \cdot \epsilon_s \cdot \sigma^{\mathrm{th}} \cdot \int \mathcal{L}\,\mathrm{dt} \quad . \tag{6.7}$$

The MC template normalisations are determined by Equation 6.7 using the values listed in Table 6.2 prior to the fitting procedure (Subsection 6.1.2). The normalisations will be fixed at these values for the Wt and WZ/ZZ templates, whereas the normalisations for the $t\bar{t}$, WW and $Z/\gamma^{*} \to \tau\tau$ templates will be allowed to freely float during the fit — providing the signal yields used to determine the cross sections for the three processes. Note: the fakes template is also fixed during the fit, but with its normalisation determined via the estimate from data.

6.1.2. Fitting to Data

In order to perform the fit to data the template sum is compared to the $E_{\mathrm{T}}^{\mathrm{miss}}$–$N_{\mathrm{jets}}$ event distribution in data (Figure 6.5) via the construction of a *binned likelihood function.* The likelihood in a given bin, i, is taken as a Poisson distribution $\mathcal{P}$,

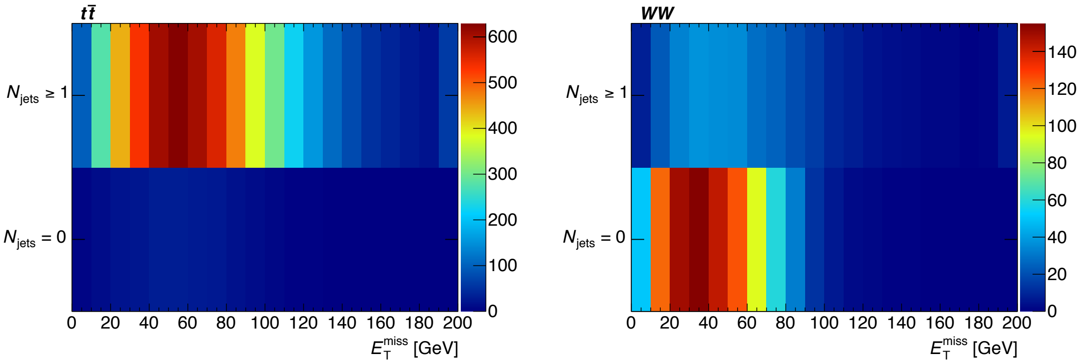

(a) Nominal $t\bar{t}$ MC — 5903 events. **(b)** Nominal WW MC — 1,263 events.

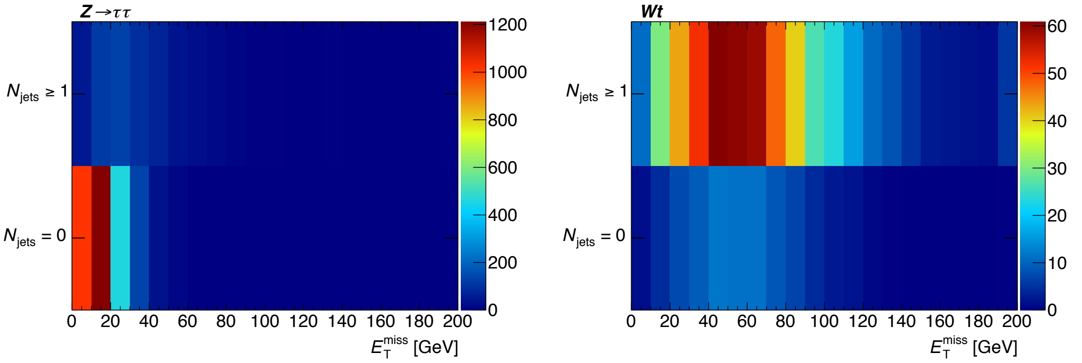

(c) Nominal $Z/\gamma^* \rightarrow \tau\tau$ MC — 3,497 events. **(d)** Nominal Wt MC — 592 events.

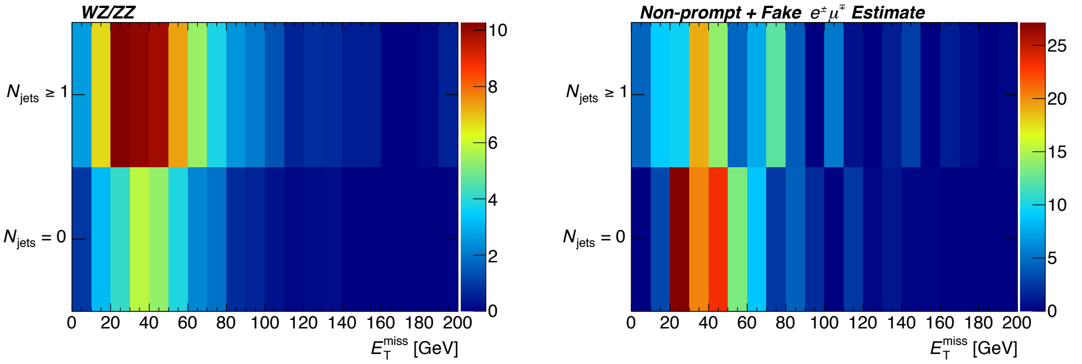

(e) Nominal WZ/ZZ MC — 96 events. **(f)** Fakes estimated from data — 207 events.

Figure 6.3.: E_T^{miss}-N_{jets} templates for signal processes: (a) $t\bar{t}$; (b) WW; (c) $Z/\gamma^* \rightarrow \tau\tau$. Background processes: (d) Wt; (e) WZ/ZZ; (f) fakes.

$$\mathcal{P}\left(N_i^{\text{obs}} \middle| N_i^{\text{exp}}\right) = \frac{\left(N_i^{\text{exp}}\right)^{N_i^{\text{obs}}} \cdot e^{-N_i^{\text{exp}}}}{N_i^{\text{obs}}\,!} \quad , \tag{6.8}$$

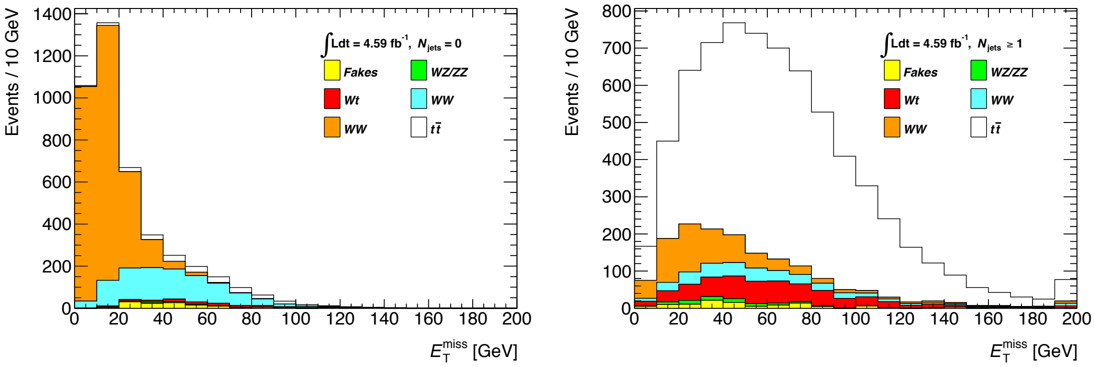

(a) $N_{\text{jets}} = 0$ **(b)** $N_{\text{jets}} \geq 1$

Figure 6.4.: Relative $E_{\mathrm{T}}^{\mathrm{miss}}$ distributions for stacked templates from Figure 6.3.

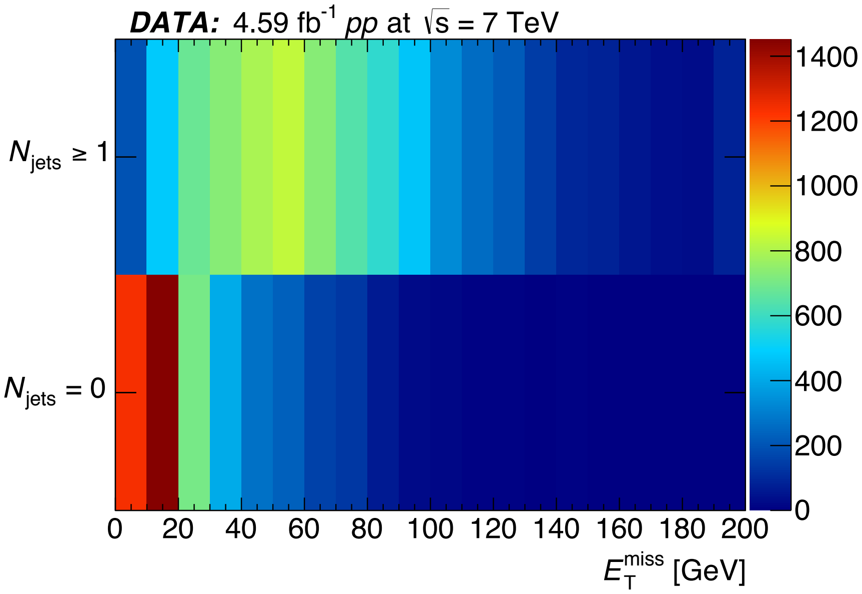

Figure 6.5.: $E_{\mathrm{T}}^{\mathrm{miss}}$–$N_{\text{jets}}$ distribution for $e\mu$ events in data — 12,224 events.

where N_i^{obs} is the bin content of the distribution observed in the data. N_i^{exp} is the expected content, which is a function of $N_{t\bar{t}}$, N_{WW} and $N_{Z/\gamma^* \to \tau\tau}$ — the normalisations of three signal processes that will be allowed to float in the fit. Only these three templates are allowed to float as they are well separated in $E_{\mathrm{T}}^{\mathrm{miss}}$–$N_{\text{jets}}$ space, this is not the case for the other templates, so allowing them all to float in the fit would not allow for a unique minimum in the $-ln(L)$ function. The likelihood function, L, is then taken as the product over all bins:

$$L = \prod_i \mathcal{P}\left(N_i^{\text{obs}} | \, N_i^{\text{exp}}\right) \quad . \tag{6.9}$$

The negative log of the likelihood is minimised using the MINUIT function minimisation tool [187]. During the minimisation the normalisations of the $t\bar{t}$, WW and $Z/\gamma^* \to \tau\tau$ templates (Figures 6.3(a)–(c)) are treated as free parameters, whereas the normalisations of the Wt (Figure 6.3(d)) and WZ/ZZ (Figure 6.3(e)) templates are fixed to their expected values from theory (using Equation 6.7). The fake backgrounds template (Figure 6.3(f)) containing events with non-prompt or misidentified $e\mu$ pairs is left as is, with uncertainties on its normalisation included as a systematic uncertainty. This and all other systematic uncertainties affecting template normalisations are treated as nuisance parameters, and profiled during the fit. This is done by incorporating them into the likelihood function via the expected bin content, N_i^{exp}, along with corresponding Gaussian penalty terms multiplying the likelihood — this is discussed further in Subsection 6.1.3. The normalisations for the $t\bar{t}$, WW and $Z/\gamma^* \to \tau\tau$ templates ($N_{t\bar{t}}$, N_{WW} and $N_{Z/\gamma^* \to \tau\tau}$) that minimise the global negative loglikelihood are used to calculate total cross sections for the three processes in Subsection 6.1.4, after discussion of the treatment of systematic uncertainties in Subsection 6.1.3.

6.1.3. Systematic Uncertainties

Systematic uncertainties affect the cross section measurements through the event yields returned by the fit for the three signal processes. As the events yields determined by the fitting procedure will depend on the normalisations and shapes of the input templates, systematic effects must be evaluated through their effects on both the templates' normalisation and shape. The systematic sources, and their effects on the event yields for $t\bar{t}$, WW, and $Z/\gamma^* \to \tau\tau$ are summarised in Table 6.4.

Sources of Systematic Uncertainty

- *Missing Transverse Energy*

  Uncertainties on the energy scale and energy resolution for leptons and jets are propagated to the leptons and jets used to calculate $E_{\mathrm{T}}^{\text{miss}}$. Additional uncertainties specific to $E_{\mathrm{T}}^{\mathrm{miss}}$ are estimated by varying the energy scale of the 'soft jets' and 'cell out' terms (refer to Equation 3.4).

- *Lepton Reconstruction*

  The systematic uncertainty associated with electron reconstruction, identification and isolation has by far the largest effect on template normalisations — in particular the difference between the efficiency of isolation requirements for electrons in data vs MC. Differences between data and MC are corrected for using scale factors estimated from data, and in the case of the isolation cut efficiency, a tag-and-probe method using $Z+$jets events is used to determine these scale factors. The uncertainty on the scale factors is large due to a systematic difference between the isolation cut efficiency in $Z+$jets events where the scale factors are measured, and the isolation cut efficiency in other types of events, with differing jet activity in regions away from the isolation cone considered [178]. For electron reconstruction in the $t\bar{t}$, WW, and $Z/\gamma^{*} \to \tau\tau$ signal processes, these factors contribute a $\sim 3\%$ template normalisation uncertainty. Scale factors for muon reconstruction and identification, are similarly determined from $Z \to \mu\mu$ events in data using a tag-and-probe method, and these contribute a $\sim 1\%$ uncertainty to the normalisations for the MC templates.

- *Lepton Momentum Scale and Resolution*

  Uncertainties due to simulation of the lepton momentum scale and resolution are evaluated by reconstructing dilepton invariant mass distributions in $Z \to ee$ and $Z \to \mu\mu$ candidate events in data. The lepton momentum scale and resolution in the Monte Carlo are then corrected to obtain consistency with the data.

- *Jet Reconstruction*

  The jet reconstruction efficiency was measured in dijet events in data and MC using a tag-and-probe method [188]. Track-jets are reconstructed using tracks observed in the inner detector as inputs to the jet reconstruction algorithm, and the track jet with greatest p_{T} is defined to be the 'tag' object. A second track-jet opposite in azimuthal angle to the tag track-jet is defined to be the 'probe' object. A matching efficiency is then determined by searching for jets reconstructed from energy deposits in the calorimeter that match the probe track-jet. As track jets and calorimeter jets are reconstructed in independent components of the ATLAS detector, good agreement between data and MC allows the absolute jet reconstruction efficiency to be determined from simulation. Efficiencies measured in data and Monte Carlo agree within 2%, and an uncertainty was assigned to reflect this.

- *Jet Energy Scale*

  The jet energy scale uncertainty consists of sixteen independent JES components which are varied by one standard deviation to evaluate the impact of JES uncertainty on the templates. The total magnitude of JES uncertainty can be seen in Table 6.3 for various η and p_T ranges of individual jets. The uncertainties can be categorised under nine effects: JES calibration method, calorimeter response, detector simulation, physics model and Monte Carlo parameters, relative calibration for jets with $|\eta| > 0.8$, pile-up effects, near-by jets, flavour composition/response, and heavy flavour JES [189].

η region	Maximum fractional JES Uncertainty		
	$p_\mathrm{T} = 20\,\mathrm{GeV}$	$p_\mathrm{T} = 200\,\mathrm{GeV}$	$p_\mathrm{T} \approx 1.5\,\mathrm{TeV}$
$0 \leq \lvert\eta\rvert \leq 0.3$	4.1%	2.3%	3.1%
$0.3 \leq \lvert\eta\rvert \leq 0.8$	4.3%	2.4%	3.3%
$0.8 \leq \lvert\eta\rvert \leq 1.2$	4.4%	2.5%	3.4%
$1.2 \leq \lvert\eta\rvert \leq 2.1$	5.3%	2.6%	3.5%
$2.1 \leq \lvert\eta\rvert \leq 2.8$	7.4%	2.7%	–
$2.8 \leq \lvert\eta\rvert \leq 3.2$	9.0%	3.3%	–
$3.2 \leq \lvert\eta\rvert \leq 3.6$	9.3%	3.5%	–
$3.6 \leq \lvert\eta\rvert \leq 4.5$	13.4%	4.9%	–

Table 6.3.: Summary of the maximum EM+JES jet energy scale systematic uncertainties for different p_T and η regions from MC simulation based study for anti-k_t jets with $R = 0.4$ [189]. Note: for 7 TeV collisions, jets with $p_\mathrm{T} \approx 1.5\,\mathrm{TeV}$ cannot also have large boosts along the z direction.

- *Jet Energy Resolution*

  The jet energy resolution was measured from calorimeter observables in dijet events in data using two different techniques. The resolution is measured by determining the asymmetry of the transverse momenta of the two leading jets [190]. The resolution is also measured by projecting the vector sum of the transverse momenta of the two leading jets onto an orthogonal coordinate system bisecting the azimuthal angle between the jets. For a perfectly balanced dijet event the magnitude of this projection is zero, but several sources may result in a non-zero variance, including instrumentation effects that result in a finite jet energy resolution. These two independent measurements in data agree with predictions from Monte Carlo simulation to within 8%.

- *Jet Vertex Fraction*

  Scale factors are applied to Monte Carlo to correct for differences in efficiencies in data and Monte Carlo of cuts made with respect to the jet vertex fraction [178]. Uncertainties from these scale factors are estimated by varying the fitting and selection criteria in the tag and probe study used to derive the scale factors.

- *Additional QCD Radiation*

  For the $t\bar{t}$ signal process the systematic uncertainty due to modelling of additional QCD radiation is evaluated using the ALPGEN generator interfaced with PYTHIA. The ALPGEN `ktfac` parameter controls the α_S-reweighting scale used to generate additional QCD radiation. The parameter `ktfac` is adjusted from its default value of 1.0 to 0.5 and 2.0. Changes in signal rate and shape are measured and divided by 2 to obtain an estimate of the systematic uncertainty on $t\bar{t}$.

  For the WW and $Z/\gamma^* \to \tau\tau$ signal processes, the choice for parameterisation of the factorisation and renormalisation scale, Q, is varied using ALPGEN. For these two processes a scale factor that multiplies Q can be varied from 1 to $m_Z^2 + p_{T\,Z}^2$ by changing the `iqopt` parameter in ALPGEN. Changes in rate and shape are measured, symmetrised, and assigned as systematic uncertainties. The decision to vary `iqopt` in order to assess the impact of additional QCD radiation on the WW and $Z/\gamma^* \to \tau\tau$ signal processes was made after investigating the variation of several ALPGEN parameters at truth level in WW and Z samples — `iqopt` was found to have the most significant effect on additional QCD radiation [174].

- *Parton Distribution Functions*

  The uncertainty associated with choice of parton distribution functions is evaluated using a range of different PDF sets. For MC samples used to model $t\bar{t}$, WW, and $Z/\gamma^* \to \tau\tau$[3], the envelope of error bands from CT10, MSTW08 and NNPDF 2.3 [191] sets, determined via the procedure described in previous ATLAS studies [192], is used.

---

[3] Due to a bug uncovered in SHERPA `v1.4.0` that affects the stored generator record, ALPGEN reweighted to CT10 is used to compute PDF uncertainties for $Z/\gamma^* \to \tau\tau$.

The PDF related uncertainties fall into two categories: intra-PDF, which is the uncertainty within a given PDF originating from uncertainties on various inputs to the PDF calculation or other uncertainties assigned by the particular PDF authors; and inter-PDF uncertainty, which is the variation observed comparing one PDF to another. The full PDF uncertainty combines the inter- and intra-PDF uncertainty by taking the 'envelope' of the minimum and maximum effects of shifting these values. The envelope of these values is taken as the PDF rate uncertainty, and it is added in quadrature to the shape uncertainty and applied to the final cross section values as the total PDF uncertainty.

- *Event Generator*

  For the $t\bar{t}$ signal process the uncertainty due to the choice of Monte Carlo event generator is evaluated for the $t\bar{t}$ signal sample by comparing the predictions of the baseline sample with those from POWHEG interfaced to HERWIG/JIMMY, and ALPGEN interfaced to HERWIG/JIMMY, all produced using CT10 PDFs. Similarly for WW, the uncertainty due to the choice of MC event generator is evaluated by comparing the predictions of the baseline sample with those from POWHEG interfaced to HERWIG/JIMMY. No generator uncertainty is taken for the $Z/\gamma^* \rightarrow \tau\tau$ sample, due to the incorrect modelling of the Z boson rapidity distribution in the other available ALPGEN+HERWIG/JIMMY sample, produced with the LO CTEQ6L1 PDFs [193].

- *Parton Showering and Fragmentation Model*

  For $t\bar{t}$ and WW, POWHEG samples interfaced to HERWIG/JIMMY and PYTHIA were compared to evaluate uncertainties associated with the choice of model for parton showering and fragmentation. For $Z/\gamma^* \rightarrow \tau\tau$ a comparison is made between SHERPA and ALPGEN samples interfaced to HERWIG. The ALPGEN samples are reweighted at truth level such the Z/γ^* p_{T} and η spectra agree with those produced with SHERPA. This uncertainty is relatively high and is best explained by the choice of isolation requirement imposed on the electron.

- *Theoretical Cross Sections*

  Uncertainties on theoretical cross sections used to model background contributions are treated as template normalisation uncertainties. A 5% uncertainty is assigned to the WZ and ZZ diboson background [157] and for the Wt background the theoretical uncertainty of 7.6% [152] is assumed.

- *Data-driven Background Estimate*

  The combined effects on the fitted signal yields of changes to the normalisation and shape of the 'fakes' template — caused by varying the efficiencies associated with the matrix method by $\pm 1\sigma$. The matrix (in Equation 6.6) produced using these adjusted efficiency values is used to recalculate the fakes template normalisation ($N^{FF} + N^{RF} + N^{FR}$), this new fakes template is then used in a new fit. The outer envelope of the fitted signal yields obtained via this process are taken as a single uncertainty for each of the signal processes, while the efficiencies themselves are taken from [178, 194]. Of the three processes the WW component is found to be the most susceptible to this effect due to its template having a similar shape to the fakes template.

- *Luminosity*

  The uncertainty on the total integrated luminosity is constrained to 1.8% [57]. No shape uncertainty is associated with the luminosity measurement, only a normalisation uncertainty of 1.8% for each template.

Treatment of Template Normalisation Effects

Systematic uncertainties affecting the overall event rate — i.e. affecting template normalisations — are treated as Gaussian constrained parameters in the likelihood function. These factors multiply the likelihood, L (Equation 6.9) such that it becomes

$$L = \prod_{i \,\in\, \text{bins}} \mathcal{P}\left(N_i^{\text{obs}} \mid N_i^{\text{exp}}\right) \prod_{j \,\in\, \text{syst.s}} \mathcal{G}\left(s_j \mid \mu = 0, \sigma = 1\right) \quad . \tag{6.10}$$

This penalises the likelihood as these parameters move away from their nominal values during the minimisation procedure. These parameters, s_j, also enter into Equation (6.8) as the number of expected events N^{exp} will be a function of these s_j, with

$$\mathcal{G}\left(s_j \middle| 0, 1\right) = \frac{1}{\sqrt{2\pi}} e^{-s_j^2/2} \quad , \tag{6.11}$$

$$N^{\mathrm{exp}} = \sum_{\mathrm{k} \,\in\, \mathrm{templ.s}} \sum_{\mathrm{j} \,\in\, \mathrm{syst.s}} N_k \cdot (1 + s_j \cdot \delta_{jk}) \quad . \tag{6.12}$$

The parameters N_k, for $k \in \{t\bar{t},\, WW,\, Z/\gamma^* \to \tau\tau\}$ are the signal event yields, and are allowed to float as free parameters in the fit. These are then used to extract signal cross sections. The N_k values for $k \in \{Wt,\, WW/ZZ\}$ are fixed to their values determined by cross sections set to the Standard Model predictions and efficiencies measured from Monte Carlo samples for Standard Model Wt, WZ, and ZZ production (Figures 6.3(d) and 6.3(e)). The value of N_k when $k =$ "fakes" is the number of $e\mu$ events due to mis-identified and non-prompt leptons in the fakes template (Figure 6.3(f)). The array δ_{jk} encodes the effect on the normalisation of template k due to an adjustment of systematic j by $\pm 1\sigma$, or in cases where more than one parameter must be adjusted — the maximum difference in normalisation is taken.[4] These values (δ_{jk}) are summarised in Table 6.4. In cases where a particular systematic effect does not apply to a particular template its value in the array is simply set to zero.[5] The total effect of the normalisation uncertainty due to the systematic sources is the total uncertainty on the fitted template yields returned by MINUIT after the –loglikelihood minimisation.

Treatment of Template Shape Effects

In order to estimate uncertainties on event yields due to systematic effects on template shapes, MC "pseudo-experiments" are performed. For a given source of systematic uncertainty, s, sets of modified $E_{\mathrm{T}}^{\mathrm{miss}}$–$N_{\mathrm{jets}}$ signal and background templates are produced in which s is varied up and down by its expected uncertainty, while the template normalisation remains fixed to its assumed Standard Model expectation. Pseudo-experiments are performed by fitting the nominal (i.e. no systematic effects applied) templates to these modified templates, termed "pseudo-data".

---

[4] Uncertainties associated with the parton distribution functions are not profiled in the fit, as the PDF uncertainties are not determined using the baseline MC.

[5] Note: as these normalisation uncertainties are incorporated as Gaussian-distributed scale factors, it is necessary to symmetrize each source of uncertainty.

The pseudo-data normalisation for each template process is chosen by randomly fluctuating the nominal normalisation according to a Poisson distribution, providing the number of expected events N_k for each template k. The distribution of these expected events is then obtained according to a probability density function defined by the shape of template k, to create a pseudo-data template. This process is repeated for each template, k, to produce a full pseudo-data sample containing signals and backgrounds. The pseudo-experiment is then performed by fitting the nominal templates to the set of pseudo-data and extracting the event yield for each of the three signal processes. This process is repeated one thousand times to obtain a well defined distribution of $N^{\text{fit}}_{t\bar{t}}$, N^{fit}_{WW} and $N^{\text{fit}}_{Z/\gamma^*\to\tau\tau}$ values.

The difference between the mean value of this distribution and the expected value used to generate the pseudo-data for a given template, ΔN_k, is taken as the uncertainty due to template shape effects of systematic source s. To obtain the final template shape uncertainty, each positive $\Delta N_k/N_k$ value is added in quadrature to obtain the total positive error, and each negative value is added likewise to obtain the negative error. These values are summarised in Table 6.4.

6.1.4. Results and Discussion

One of the primary motivations for performing a simultaneous measurement like this is to have the signal processes well separated in some phase space such that unique global minima of the fit function can be found, but with enough overlap between signal processes that the templates can constrain each other in these overlap regions leading to globally consistent measurements over that space. Once the fitted yields for the signal processes ($N^{\text{fit}}_{t\bar{t}}$, N^{fit}_{WW}, $N^{\text{fit}}_{Z/\gamma^*\to\tau\tau}$) have been determined, cross sections are calculated for: the fiducial phase space, as determined by the kinematic and geometric acceptance of the analysis; and the full phase space.

The measured cross sections for signal process X, in the fiducial phase space ($\sigma^{pp\to X\to e\mu+Y}_{\text{fid}}$), are determined by Equation 6.13.

$$\sigma^{pp\to X\to e\mu+Y}_{\text{fid}} = \frac{N^{\text{fit}}_{X}(\text{fiducial})}{\mathcal{C}\cdot\mathcal{L}_{\text{int.}}} \quad , \tag{6.13}$$

Source of Uncertainty	Effects of Systematic Uncertainties on Event Yields (%)					
	$t\bar{t}$		WW		$Z/\gamma^* \to \tau\tau$	
	Norm.	Shape	Norm.	Shape	Norm.	Shape
ISR/FSR	±0.34	+0.97(−1.51)	±1.12	+4.70(−3.51)	±0.95	+0.70(−1.03)
$t\bar{t}$ generator	±0.87	+0.19(−0.00)		+0.00(−0.36)		+0.00(−0.68)
$t\bar{t}$ PS modelling	±0.23	+0.00(−0.05)		+0.15(−0.00)		+0.00(−0.60)
WW generator		+0.00(−0.80)	±0.53	+4.45(−0.00)		+0.00(−0.95)
WW PS modelling		+0.00(−0.65)	±0.68	+3.50(−0.00)		+0.00(−0.84)
$Z \to \tau\tau$ PS modelling		+0.00(−0.52)		+0.00(−0.59)	±2.40	+0.47(−0.00)
PDF	±0.59	±0.48	±0.10	±1.65	±0.22	±0.81
$E_{\mathrm{T}}^{\mathrm{miss}}$ cellout	±0.01	+0.42(−0.19)	±0.00	+8.14(−9.92)	±0.00	+2.28(−0.19)
$E_{\mathrm{T}}^{\mathrm{miss}}$ pileup	±0.01	+0.05(−0.08)	±0.00	+3.74(−4.51)	±0.00	+1.00(−1.69)
e identification	±3.23	+0.00(−0.04)	±3.24	+0.25(−0.26)	±3.30	+0.00(−0.84)
e trigger	±0.13	+0.04(−0.00)	±0.04	+0.11(−0.11)	±0.14	+0.00(−0.84)
e momentum scale	±0.17	+0.10(−0.00)	±0.19	+0.14(−0.61)	±0.80	+0.00(−0.45)
e momentum resolution	±0.01	+0.07(−0.00)	±0.01	+0.00(−1.16)	±0.12	+0.00(−0.53)
μ identification	±0.79	+0.00(−0.00)	±0.78	+0.00(−0.00)	±0.78	+0.00(−0.00)
μ trigger	±0.00	+0.04(−0.00)	±0.02	+0.01(−0.12)	±0.07	+0.00(−0.86)
μ momentum scale	±0.04	+0.00(−0.05)	±0.03	+0.00(−0.85)	±0.17	+0.00(−0.22)
μ momentum resolution	±0.01	+0.00(−0.07)	±0.00	+0.00(−0.00)	±0.00	+0.00(−0.00)
Jet vertex fraction	±0.82	+0.12(−0.00)	±0.28	+0.00(−1.67)	±0.18	+0.00(−0.34)
Jet energy scale	±0.77	+1.40(−1.42)	±0.65	+0.48(−4.86)	±0.46	+1.42(−3.12)
Jet reconstruction	±0.00	+0.08(−0.00)	±0.00	+0.00(−1.00)	±0.00	+0.00(−0.38)
Jet energy resolution	±0.23	+0.25(−0.00)	±0.18	+0.00(−2.58)	±0.18	+0.00(−0.07)
Fakes	±0.78		±5.60		±0.68	
Luminosity	±1.80	–	±1.80	–	±1.80	–

Table 6.4.: Normalisation and shape systematic effects on event yields returned by the fit, for the three signal processes. Note: the entries in the normalisation columns represent the δ_{jk} terms for the three signal processes.

where N_X^{fit}(fiducial) is the number of events attributed to the specified process by the fit (using systematic uncertainties as they affect events in the fiducial region); $\mathcal{L}_{\text{int.}}$ is the integrated luminosity of the data sample; $\mathcal{C}$ is the ratio of the number of events fulfilling the offline selection criteria to the number of events produced in the fiducial phase space estimated from MC simulation.

The full production cross sections ($\sigma_{\text{tot}}^{pp\to X}$), for the signal processes are obtained by correcting for the kinematic and geometric acceptance of the analysis, as well as the branching ratios for the signal processes to produce $e\mu + Y$ final states, as shown in Equation 6.14.

$$\sigma_{\text{tot}}^{pp\to X} = \frac{N_X^{\text{fit}}(\text{total})}{\mathcal{A}\cdot\mathcal{C}\cdot\mathcal{B}^{X\to e\mu+Y}\cdot\mathcal{L}_{\text{int.}}} \tag{6.14}$$

where N_X^{fit}(total) is the number of events attributed to the specified process by the fit (but this time using systematic uncertainties as they affect the full phase space); $\mathcal{A}$ is the kinematic and geometric acceptance in the fiducial phase space as a fraction of the full phase space; and $\mathcal{B}^{X\to e\mu+Y}$ is the branching fraction to inclusive $e\mu$ final states for the decay channel under consideration, which takes into account the branching fractions of tau decays to electrons and muons. It should be noted that systematic effects due to MC modelling (ISR/FSR, PDF sets, generator, and parton shower), are larger when considered over the full phase space, because they affect the acceptance ($\mathcal{A}$) as well as the selection efficiency ($\mathcal{C}$).

The values used for the cross section determinations (Equations 6.13 and 6.14) are provided in Table 6.5.

Process	$t\bar{t}$	WW	$Z/\gamma^* \to \tau\tau$
Fitted Yield N_X^{fit}	$6,049$	$1,479$	$3,844$
Selection Efficiency $\mathcal{C}$	0.482	0.505	0.496
Acceptance $\mathcal{A}$	0.465	0.390	0.0232
Branching Ratio $\mathcal{B}$	0.0324 ($WW \to e\mu + Y$)	0.0324 ($WW \to e\mu + Y$)	0.0621 ($\tau\ \tau\ \to e\mu$+Y)
Integrated Luminosity $\mathcal{L}_{\text{int.}}$	$4.59\,\text{fb}^{-1}$		

Table 6.5.: The fitted yields, selection efficiencies, acceptance correction factors, and branching ratios to $e\mu$ final states [97] for the three signal processes. The selection efficiencies and acceptance correction factors are extracted from Monte Carlo samples.

Thus, the resulting fiducial and total cross sections as determined by the simultaneous fit in the N_{jets}–$E_{\text{T}}^{\text{miss}}$ parameter space for pp collisions at $\sqrt{s} = 7\,\text{TeV}$ are:

$$\begin{aligned}
\sigma_{\text{fid}}^{t\bar{t}\to e\mu+Y} &= 2,731 \;\pm 42\,(\text{stat.})\;{}^{+125}_{-117}\,(\text{norm.})^{+49}_{-66}\,(\text{shape})\;\pm 22\,(\text{fakes})\;\pm 49\,(\text{lumi.})\;\text{fb}\quad ; \\
\sigma_{\text{fid}}^{WW\to e\mu+Y} &= 638 \;\pm 32\,(\text{stat.})\;{}^{+27}_{-24}\,(\text{norm.})^{+75}_{-84}\,(\text{shape})\;\pm 36\,(\text{fakes})\;\pm 11\,(\text{lumi.})\;\text{fb}\quad ; \\
\sigma_{\text{fid}}^{Z/\gamma^{*}\to\tau\tau\to e\mu+Y} &= 1,690 \;\pm 35\,(\text{stat.})\;{}^{+71}_{-66}\,(\text{norm.})^{+51}_{-95}\,(\text{shape})\;\pm 12\,(\text{fakes})\;\pm 30\,(\text{lumi.})\;\text{fb}\quad .
\end{aligned} \tag{6.15}$$

$$\begin{aligned}
\sigma_{\text{tot}}^{t\bar{t}} &= 181.2 \;\pm 2.8\,(\text{stat.})\;{}^{+8.5}_{-7.8}\,(\text{norm.})^{+3.3}_{-4.3}\,(\text{shape})\;\pm 1.4\,(\text{fakes})\;\pm 3.3\,(\text{lumi.})\;\text{pb}\quad ; \\
\sigma_{\text{tot}}^{WW} &= 53.3 \;\pm 2.7\,(\text{stat.})\;{}^{+2.2}_{-2.0}\,(\text{norm.})^{+6.2}_{-7.0}\,(\text{shape})\;\pm 3.0\,(\text{fakes})\;\pm 1.0\,(\text{lumi.})\;\text{pb}\quad ; \\
\sigma_{\text{tot}}^{Z/\gamma^{*}\to\tau\tau} &= 1,174 \;\pm 24\,(\text{stat.})\;{}^{+60}_{-54}\,(\text{norm.})^{+35}_{-66}\,(\text{shape})\;\pm 8\,(\text{fakes})\;\pm 21\,(\text{lumi.})\;\text{pb}\quad .
\end{aligned} \tag{6.16}$$

The systematic uncertainties shown in Equations 6.15 and 6.16 have been broken up to represent the relative contributions from effects propagated through effects on the templates' normalisations and shapes, as well as the contribution due to uncertainties in the fakes template.

These agree with the standalone measurements that have been conducted to date: $\sigma^{t\bar{t}} = 177 \pm 18\,\text{pb}$ [195] ; $\sigma^{WW} = 51.9 \pm 4.9\,\text{pb}$ [196] ; $\sigma^{Z/\gamma^{*}\to\tau\tau} = 1,066 \pm 170\,\text{pb}$[6] [197].

The cross section measurements themselves are based on a simultaneous fit to data (Figure 6.5), however this does not imply that they are not being affected by processes in the data that are not being modelled. Such processes could be affecting the goodness-of-fit globally, yet still allowing the fit to return event yields corresponding to cross sections that agree with SM expectations. Therefore, we would also like to test how well the data itself agrees with the SM expectation over the $E_{\text{T}}^{\text{miss}}$–$N_{\text{jets}}$ parameter space used for the fit, in case the fit to data is masking some overall tension or outright disagreement with the SM that could be an indication of new physics.

---

[6] This dedicated ATLAS $Z/\gamma^{*} \to \tau\tau$ production cross-section measurement was determined using $e\mu$ events in the fiducial region where $66\,\text{GeV} < M_{\tau\tau} < 116\,\text{GeV}$ and is therefore corrected by a factor of 1.1 to compare it directly with the $Z/\gamma^{*} \to \tau\tau$ cross-section measured here for $M_{\tau\tau} > 40\,\text{GeV}$.

Checking this would first involve testing the consistency of the data with the expectation under the SM hypothesis as modelled by the nominal templates used for the fit. As the systematic effects on the template shapes and normalisations dominate the uncertainty for the AIDA method, which is to be expected over such a large phase space — if the shape and normalisation effects could be combined, an expectation for the SM and its associated uncertainty (in the fiducial phase space defined by AIDA as represented by the templates), can be determined.

6.2. How to Test Goodness-of-Fit Between Data and the SM in AIDA?

In order to provide some quantitative measure of the level of agreement between data and the expectation under the SM hypothesis it is necessary to perform a *goodness-of-fit* statistical test [198]. This requires three steps:

1. **Define a test statistic**
   In order to determine the goodness-of-fit between data and its expectation under a particular hypothesis some measure of "distance" away from the expectation must be defined. This measure is known as the test statistic and it is a function of the data and the model being tested. As the SM hypothesis is not being tested with respect to any particular alternative hypothesis, no claim can be made about the power of the test, and as such the choice of test statistic is somewhat arbitrary.[7] As the AIDA analysis is based on 2D histograms, a χ^2-like[8] test statistic, T, is used – defined as:

$$T_{\text{Data}} = \frac{1}{N_{\text{bins}}} \sum_{i=1}^{N_{\text{bins}}} \frac{(n_i^{\text{Data}} - n_i^{\text{Nominal MC}})^2}{n_i^{\text{Nominal MC}}} \quad , \tag{6.17}$$

   where n_i is the total number of events in bin i.

---

[7] Unlike in Section 5.8, where the test statistic was based on the likelihood ratio that tested a range of hypothesised branching ratios

[8] The term "χ^2-like" is used because strictly speaking the test statistic chosen would not be expected to follow a χ^2 distribution due to systematic effects.

2. **Determine the underlying distribution for the test statistic**
   The main challenge in conducting such a goodness-of-fit test is determining the underlying distribution of T, which will be some function of the model and its associated uncertainties. In the complex case of the SM at ATLAS – the "model" consists of myriad MC simulated events with systematic effects ranging from uncertainties on the cross sections and parton distribution functions of the colliding protons (when generating events) to uncertainties on jet reconstruction efficiency and trigger rates (associated with the detector).

3. **Map the test statistic to a p-value**
   Once the underlying distribution for the test statistic has been determined, it can be used as a reference for how well the data agrees with the model being tested. This is done by forming a p-value defined as

$$p\text{-value} = \int_{T_{\text{Data}}}^{\infty} \phi_T \, \mathrm{d}T \tag{6.18}$$

   where the probability density function (ϕ_T) for the test statistic is the normalised distribution obtained in step 2, produced by varying all parameters defining what "The Standard Model" looks like in the ATLAS detector within their associated uncertainties. Then, for each variation, the test statistic for a new set of this "pseudo-MC" with respect to the SM expectation as defined by the choice of nominal MC (listed in Table 6.1) is evaluated.

The most challenging of these steps, particularly in the context of AIDA, is determining the underlying distribution of the test statistic (step 2). An outline of the *ideal but unfeasible* method for doing this in the AIDA case is provided below (Subsection 6.2.1). This ideal is then contrasted with the implementation of a *expedient but incomplete* method used as the first step towards determining this distribution in Subsection 6.2.2. The remainder of the chapter will focus on how to bridge the gap between these two methods.

6.2.1. Ideal Application In AIDA

In AIDA, the SM hypothesis is represented by the combination of the set of templates used in the fitting procedure. These templates are produced using the nominal MC samples listed in Table 6.1. Each of the templates has an associated *template shape uncertainty*[9] and *template normalisation uncertainty*[10], and these are the result of both statistical (bin-by-bin fluctuations and fluctuations in the overall normalisation) as well as systematic effects in the MC. Systematic effects are introduced at each step in the chain required to produce such templates: parton distribution functions → event generation → parton shower modelling and hadronisation → detector simulation → object/event reconstruction → object/event selection. Systematic uncertainties from either theoretical (e.g. uncertainties on parton distribution function parameters) or experimental (e.g. uncertainties on scale factors that correct electron trigger efficiency for MC to that observed for data) sources are present at every stage in the MC modelling. The quantities responsible for these systematics are listed in Table 6.4, along with how their uncertainties propagate through the cross section analysis to a percentage uncertainty on the fitted event yields for the signals due to template normalisation and shape uncertainties. It should be noted from the systematics treatment in the AIDA cross section measurements that the shape effects are treated in a very different manner to the normalisation effects. Not only are the shape effects considered to be independent of one another, but they are also treated independently of the normalisation effects – while this is a reasonable assumption to make in the context of the cross section measurements (with cross-checks to back it up), it makes determining a single test statistic distribution using shape *and* normalisation effects difficult.

In an ideal world this problem could be overcome if the *pdf*s for all the systematics were known, as well as the correlations (if any) between systematics. This would result in some multi-dimensional *pdf* in systematics space that could simply be sampled in order to choose random values for each quantity with an associated systematic uncertainty. The chosen values for these quantities could then be used to produce updated MC samples to be re-run through the object and event selections. The resulting updated MC template set could then be compared to the nominal (i.e. templates produced with quantities set at their nominal values) MC template set using the test statistic, T. Repeating this process for new choices for the systematics would allow the "true" underlying distribution of T to be built up.

While this method would produce an accurate distribution for the test statistic that would account for all the uncertainties present in modelling the SM expectation, this method is not even close to being technically feasible due to the massive computing

---

[9] The uncertainty over how the events contributing to the template are distributed between the bins.

[10] The uncertainty over the total number of events that make it into the template.

resources that would be required, along with the fact that it is obviously unreasonable to expect a *pdf* describing the uncertainties to be known with certainty.

6.2.2. Expedient Application In AIDA

As the ideal method outlined above is unrealistic, what could be a first step to approximating the distribution for T? Since the normalisation uncertainties profiled during the fitting procedure are assumed uncorrelated (Section 6.1), with Gaussian *pdf*s, and the uncertainty on template normalisations listed in Table 6.4 for shifts of $\pm 1\sigma$ – this seems like a good place to start. A distribution for T can be constructed relatively simply by producing sets of "pseudo-MC" templates by adjusting the normalisations of the nominal MC templates (Figure 6.3). The steps to produce what constitutes a single set of pseudo-MC are as follows:

- For each MC template, t_k (with $k \in$ templates}), and each systematic uncertainty on the template normalisation, δ_j (with $j \in \{\text{systematics}\}$), scale the template integral, N_k, by $\sum\limits_j (1 + s_j \cdot \delta_{jk})$ for randomly selected s_j with Gaussian *pdf*, $\mathcal{G}(s_j \mid 0, 1)$ (smearing due to systematic effects on template normalisation).

- Poisson fluctuate N_k separately for each k (statistical fluctuation in total number of events).

- Randomly fill new templates, u_k, based on the original template shapes, with the N_k events (bin-to-bin statistical fluctuations/migration of events).

- A pseudo-MC histogram (used to calculate a value for T) is thus defined in the $E_{\mathrm{T}}^{\mathrm{miss}}$–$N_{\mathrm{jets}}$ parameter space as the template sum $\sum\limits_k u_k$.

- This template sum will have a value:

$$T_{\text{Pseudo-MC}} = \frac{1}{N_{\text{bins}}} \sum_{i=1}^{N_{\text{bins}}} \frac{(n_i^{\text{Pseudo-MC}} - n_i^{\text{Nominal MC}})^2}{n_i^{\text{Nominal MC}}} \quad .$$

This process is repeated for 10,000 sets of pseudo-MC and the resulting distribution is displayed in Figure 6.6. In addition, the values of T for data (Equation 6.17) as well as the fit-to-data (shown for reference) are displayed with respect to this distribution, where the data histogram used is that displayed in Figure 6.5. The fit-to-data is carried out as described in Section 6.1, with only the systematic effects on template normalisation considered during the minimisation of the negative loglikelihood. The test statistic value for the sum of the templates (post-fit) is displayed in magenta for a fit over the full range in Figure 6.6, and fits over four sub-ranges in Figures 6.7 and 6.8. The test statistic for the post-fit templates will naturally always lie in between the nominal template sum and the data this sum is being fit to, and is shown only for reference. The proportion of pseudo-MC to the right hand side of the data line represents the p-value for the data under the limitations and assumptions used here.

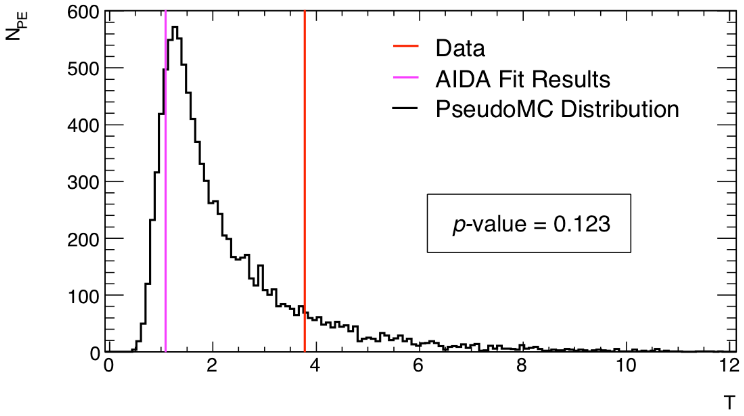

Figure 6.6.: Underlying distribution for T from 10,000 pseudo-MC sets (where $\mathrm{N_{PE}}$ is the number of pseudo-experiments conducted).

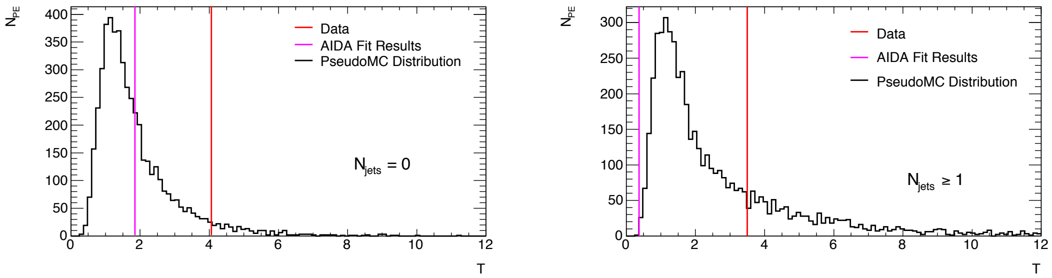

(a) Distribution for T with $N_{\mathrm{jets}} = 0$ (5000 sets pseudo-MC)

(b) Distribution for T with $N_{\mathrm{jets}} \geq 1$ (5000 sets pseudo-MC)

Figure 6.7.: Underlying distribution for T from 5,000 pseudo-MC sets in N_{jets} sub-regions (where $\mathrm{N_{PE}}$ is the number of pseudo-experiments conducted).

The p-value calculated for data in Figure 6.6 is 12.3%, and would correspond to a level of agreement with the SM expectation of $1 - 2\sigma$ (gaussian equivalent) over the binned $E_{\mathrm{T}}^{\mathrm{miss}}$–$N_{\mathrm{jets}}$ parameter space. Figures 6.7 and 6.8 contain the distributions when the parameter space is limited to $N_{\mathrm{jets}} = 0/N_{\mathrm{jets}} \geq 1$ and $E_{\mathrm{T}}^{\mathrm{miss}} \leq 30\,\mathrm{GeV}/E_{\mathrm{T}}^{\mathrm{miss}} > 30\,\mathrm{GeV}$

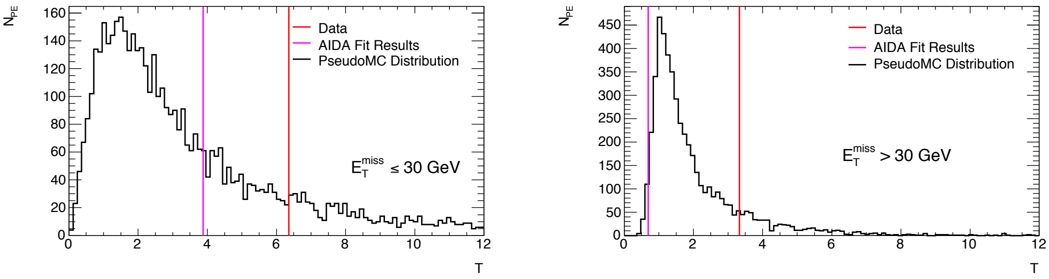

(a) Distribution for T with $E_{\mathrm{T}}^{\mathrm{miss}} \leq 30\,\mathrm{GeV}$ (5000 sets pseudo-MC)

(b) Distribution for T with $E_{\mathrm{T}}^{\mathrm{miss}} > 30\,\mathrm{GeV}$ (5000 sets pseudo-MC)

Figure 6.8.: Underlying distribution for T from 5,000 pseudo-MC sets in $E_{\mathrm{T}}^{\mathrm{miss}}$ sub-regions (where $\mathrm{N_{PE}}$ is the number of pseudo-experiments conducted).

respectively. This is done to see if the level of agreement evident from Figure 6.6 differs for a specific region, e.g. the low $E_{\mathrm{T}}^{\mathrm{miss}}$ region for example, which is associated with large uncertainties in high pile-up conditions. The p-values for data calculated from these distributions are as follows: 6.7(a) 4.7%; 6.7(b) 21.9%; 6.8(a) 13.3%; 6.8(b) 12.0%. A lower level of agreement occurs in the case of $N_{\mathrm{jets}} = 0$, where the $Z/\gamma^* \to \tau\tau$ events provide the dominant contribution.

Though this gives a useful first estimate for the level of agreement — there does not appear to be large global disagreement between data and the SM expectation — this method is unable to incorporate systematic effects on the template shapes. Including such additional uncertainties would act to spread out the test statistic distribution, improving the level of agreement with data. Thus, in order to include these shape effects, some kind of compromise is required between this expedient method and the ideal scenario discussed above (Subsection 6.2.1). To identify points in the analysis where improvements could be made, a toy example is used to contrast the ideal case with the expedient. A toy example must be used for this as this is the only way the ideal situation described can be implemented – as full knowledge of the shape dependence on systematics must be known. This example is presented next (Section 6.3) and breaks down not only the process of determining the underlying distribution for the test statistic, but the differences in the evaluation of systematic effects on the fitting procedure as well.

6.3. Comparing Expedient vs Ideal Systematics Treatment in a Toy Study

In order to provide a platform to highlight the differences between an ideal situation and the state of the goodness-of-fit test as discussed in Section 6.2, a toy model of each case is constructed. This should provide some insight into the most efficient way to bridge the gap between the two cases, as complete control can be exercised over any introduced systematic effects. The specific example chosen to illustrate the point consists of two templates, A and B, and the aim is to evaluate the systematic uncertainties as they affect the number of fitted events as well as the goodness-of-fit test statistic distribution. The templates' shapes and normalisations are set to be functions of two sources of systematic uncertainty defined by parameters, s_1 and s_2.

In the "expedient" method, the steps taken to evaluate the uncertainties follow those used for the AIDA fitting procedure and systematics treatment (Subsections 6.1.2 & 6.1.3) with the test statistic distribution determined as stated in Subsection 6.2.2, without accounting for shape effects.

The "ideal" method will account for shape and normalisation effects simultaneously, producing corresponding distributions to those of the expedient method, and will also consider additional information such as possible correlations between the systematics themselves which cannot be included in the expedient method.

The purpose of this example is not in any way intended to prove that the expedient method for determining goodness-of-fit is wrong but simply to demonstrate that while the AIDA method works for evaluating the uncertainties as they apply to the cross section measurements it cannot be easily extended to produce a complete test statistic distribution. This is because in addition to the omission of shape effects there may exist cases where the inability to account for possible (unknown or unanticipated) correlations between systematic effects can also affect the test statistic distribution. The argument being made here is of the form: if there exists a *reasonable*[11] toy example in which producing a valid test statistic distribution requires treating systematic shape and normalisation effects together; as we do not *a priori* know how such effects may be correlated in reality in the case of ATLAS and AIDA, such combined effects should

---

[11] Reasonable is taken to mean that in all cases, the template fitting procedure will converge about a single central value regardless of systematic effects on template shape and normalisation.

not be ignored and must be accounted for in the determination of a valid test statistic distribution.

The results shown correspond to the following toy example containing an A template and a B template, where their shapes and normalisations are functions of the two "systematics". The parameters set for this example are as follows: as before, Gaussian distributions are chosen for the *pdf*s of the two systematics about their nominal values,

$$\mathcal{G}(s_1) = e^{-s_1^2/2} \quad , \tag{6.19}$$

$$\mathcal{G}(s_2) = e^{-s_2^2/2} \quad . \tag{6.20}$$

An array δ_{jk} contains the corresponding shift in template normalisation due to a 1σ shift of a systematic. The particular values have no reason for being chosen other than the fact that some specific values are required for the example, and the fit converges for all sets of pseudoMC using values of order 5–10% under this example.

$$\begin{aligned} \delta_{1A} &= 0.05 \quad , & \delta_{1B} &= 0.1 \quad , \\ \delta_{2A} &= 0.05 \quad , & \delta_{2B} &= 0.1 \quad . \end{aligned} \tag{6.21}$$

As in AIDA, the template normalisations therefore take the form:

$$N_A = 5000 \cdot (1 + s_1 \cdot \delta_{1A}) \cdot (1 + s_2 \cdot \delta_{2A}) \quad , \tag{6.22}$$

$$N_B = 15000 \cdot (1 + s_1 \cdot \delta_{1B}) \cdot (1 + s_2 \cdot \delta_{2B}) \quad . \tag{6.23}$$

The number of events in the "nominal" templates ($s_1 = s_2 = 0$) was chosen to be of order a few thousand ($N_A = 5,000$ and $N_B = 15,000$) so that statistical fluctuations stemming from randomly filling the histograms is not a major contributor to the overall uncertainty, which will be dominated by the systematic effects (as in the case of AIDA).

Template shape functions are defined as 2D Gaussians ($\mu_A = 0.5, \sigma_A = 0.2$; $\mu_B = 0, \sigma_B = 0.5$) with additional functional dependence on the systematics built-in. These are normalised and used as the probability density functions when filling the templates:

$$Shape_A = 1 + e^{-\left(\frac{(x-0.5)^2}{2\cdot 0.2^2} + \frac{(y-0.5)^2}{2\cdot 0.2^2}\right)} + (0.1)\cdot(1-xy)\cdot(s_1+s_2) \quad , \tag{6.24}$$

$$Shape_B = 1 + e^{-\left(\frac{x^2}{2\cdot 0.5^2} + \frac{y^2}{2\cdot 0.5^2}\right)} + (0.1)\cdot(1-xy)\cdot(s_1+s_2) \quad . \tag{6.25}$$

The shapes are of the form of: (a constant term) + (a Gaussian term) + (a systematic dependence term). Again, all slightly contrived, but the template shapes are now dependent on the *same* systematics parameters that affect the normalisations. The same dependence on s_1 and s_2 has been used for both templates A and B, i.e. the term of the form $(1-xy)\cdot(s_1+s_2)$. This form was chosen so that it *does* matter whether or not s_1 and s_2 are correlated, and the coordinate dependence means the effect is most pronounced at $x = y = 0$. The corresponding nominal ($s_1 = s_2 = 0$) templates are shown in Figure 6.9.

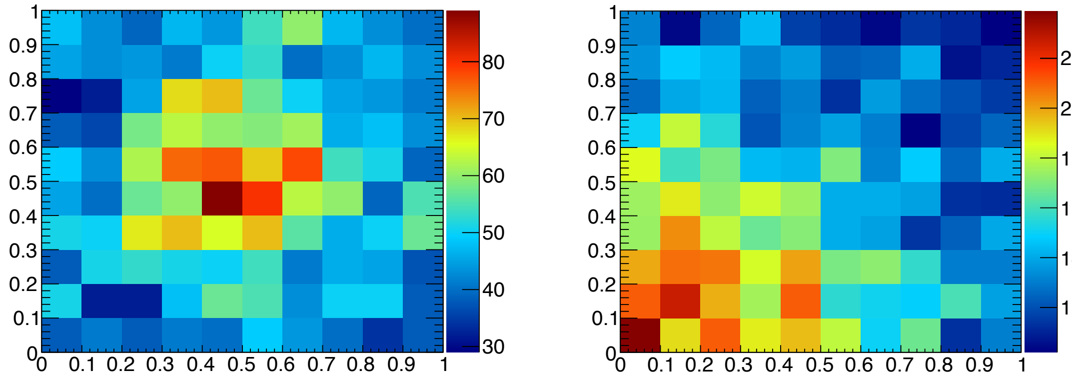

(a) Nominal A Template: $N_A = 5,000$, $Shape_A = 1 + exp\left\{-\left(\frac{(x-0.5)^2}{2\cdot 0.2^2} + \frac{(y-0.5)^2}{2\cdot 0.2^2}\right)\right\}$

(b) Nominal B Template: $N_B = 15,000$, $Shape_B = 1 + exp\left\{-\left(\frac{x^2}{2\cdot 0.5^2} + \frac{y^2}{2\cdot 0.5^2}\right)\right\}$

Figure 6.9.: The two nominal templates, A and B, initially filled via a random sampling of the two shape functions (Equations 6.24 and 6.25).

6.3.1. Expedient Method Applied In Toy

This method reproduces that used to evaluate the effects of normalisation/template shape effects due to systematic uncertainties on the fitted event yields as discussed in Section 6.1, as well as the expedient method used for evaluating the test statistic distribution considering only normalisation effects discussed in Subsection 6.1.3 and 6.2.2 respectively. The aim here is merely to reapply the AIDA method for evaluating systematics effects to the toy example.

First the systematics as they affect the template normalisations are considered. The distributions produced for the number of fitted events for the templates A and B using pseudo-experiments determine the normalisation effects on the fit due to the two systematics. The steps involved in a single pseudo-experiment are as follows:

1. Choose random values for s_1 and s_2 from their Gaussian *pdf*s (Equations 6.20).
2. Produce a set of "pseudo-data" by scaling the template for A by the factor $(1 + s_1 \cdot \delta_{1A}) \cdot (1 + s_2 \cdot \delta_{2A})$ and for B by $(1 + s_1 \cdot \delta_{1B}) \cdot (1 + s_2 \cdot \delta_{2B})$.
3. Poisson fluctuate the *total* number of events the new templates A and B, keeping template shape the same.
4. Perform the fit of the nominal templates ($s_1 = s_2 = 0$) to this pseudo-data set via minimisation of the negative log of the likelihood (Equation 6.10).
5. Histogram the number of events returned by the fit for A and B.

Next, the variation in the number of events returned by the fit due to the effects of the systematics on template *shape* is evaluated. This is again quantified using pseudo-experiments, but this time "switching off" the normalisation parameters (i.e. $\delta_{jk} = 0$ for $j = 1, 2$, $k = A, B$). The systematics effects on shape are determined as follows:

1. Shift s_1 by $\pm 1\sigma$ from its nominal zero value, based on its assumed *pdf* (while keeping $s_2 = 0$).
2. Produce new shape-adjusted templates for A and B with this shift, normalised to the number of events in the nominal templates.
3. Perform pseudo-experiments to determine the number of events returned by the fit using the shape-adjusted A and B templates.

4. Use the difference between the mean of the $\pm 1\sigma$ distributions to the nominal result as the shape uncertainty due to s_1 for A and B.

5. Repeat steps 1—4 for s_2.

Finally the test statistic distribution is constructed — as this method is identical to that of Subsection 6.2.2, it will not be repeated here.

6.3.2. Expedient Results In Toy

Template Fit Results

The resulting normalisation and statistical uncertainties on the number of events are shown in Figure 6.10 for 10,000 pseudo-experiments with uncertainties simply taken to be the RMS of the distribution as a percentage of the mean. In this case the combined normalisation and statistical uncertainty evaluated via the pseudo-experiments is determined to be 14.45% for template A and 11.65% for template B. As the systematics are chosen independently, we would expect their effect combined effect on the pseudo-data to be $\sqrt{2 \times 0.1^2 + 2 \times 0.05^2} = 15.81\%$, if the there was no overlap between the templates. However, even though the shapes of A and B are not being altered, the global shape $(A + B)$ will change as the normalisations of A and B are altered — which will affect the event yields determined by the likelihood fit. This additional effect is the result of overlap between A and B in the xy-plane of the templates, and is the reason it is important to have processes well separated when performing such fits.

Shape effects are presented in Figure 6.11, again using 10,000 pseudo-experiments for each systematic.

Though the shape dependence contributes negligibly to the uncertainty of the number of events returned by the fit – this dependence may still significantly affect the goodness-of-fit test statistic distribution which is calculated bin-by-bin, however this cannot be accounted for using this method.

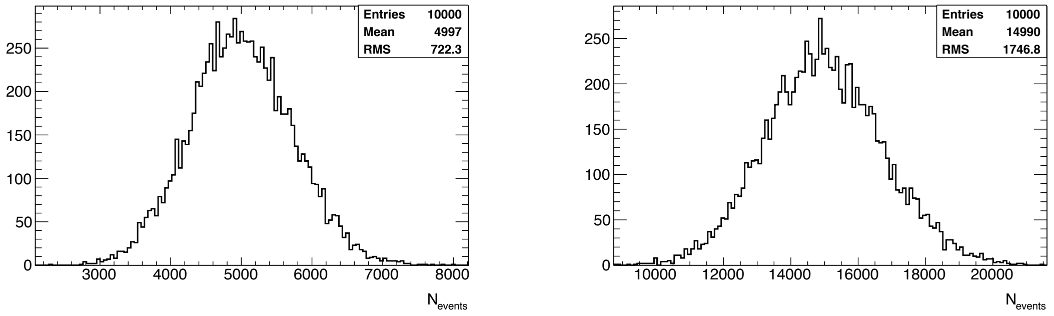

(a) N_A distribution, with normalisation and statistical uncertainty: $\frac{722.3}{4997} = 0.1445$

(b) N_B distribution, with normalisation and statistical uncertainty: $\frac{1746.8}{14990} = 0.1165$

Figure 6.10.: Pseudo-experiment distributions for the event yields returned by the fit based on template normalisation uncertainties. The y-axis represents the number of pseudo-experiments returning a given event yield.

Test Statistic Distribution

The corresponding test statistic distribution for the expedient method is displayed in Figure 6.12. As previously mentioned, there is no way to account for the effect due to template shapes on this distribution, using this method.

6.3.3. Discussion of Expedient Example

In the expedient case above, the total uncertainty on the number of events returned by the fit is estimated by adding the shape uncertainties in quadrature to the normalisation and statistical uncertainties. The assumptions inherent in the treatment of systematics under this method are: the systematics themselves are uncorrelated with one another; the systematic effects on template normalisation are uncorrelated with each other; the systematic effects on template shape are uncorrelated with each other; template shapes and template normalisations are uncorrelated. However, in this case the shape uncertainties on the fitted event yields are negligible. The normalisation uncertainties on the fitted event yields are 14.5% on A and 11.7% on B.

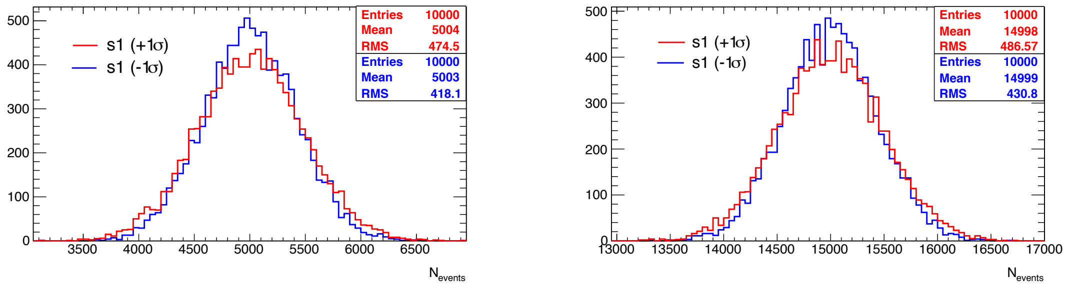

(a) s_1 signal A shape uncertainty negligible: $\frac{5004-5000}{5000} = +0.0008(+1\sigma)$; $\frac{5003-5000}{5000} = +0.0006(-1\sigma)$

(b) s_1 signal B shape uncertainty negligible: $\frac{14998-15000}{15000} = -0.00013(+1\sigma)$; $\frac{14999-15000}{15000} = -0.00007(-1\sigma)$

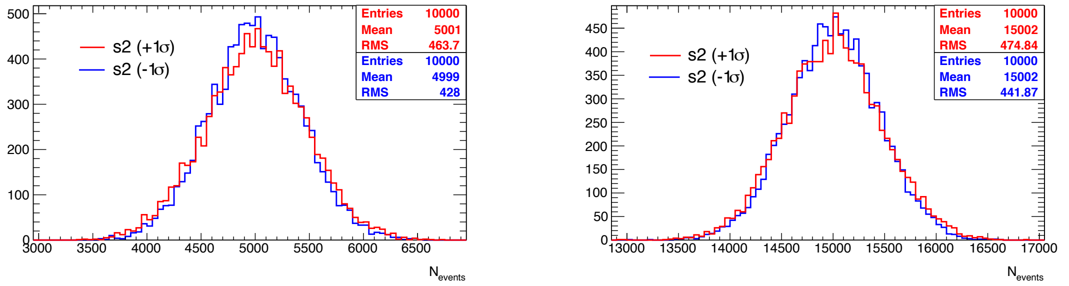

(c) s_2 signal A shape uncertainty negligible: $\frac{5001-5000}{5000} = +0.0002(+1\sigma)$; $\frac{4999-5000}{5000} = -0.0002(-1\sigma)$

(d) s_2 signal B shape uncertainty negligible: $\frac{15002-15000}{15000} = +0.00013(+1\sigma)$; $\frac{15002-15000}{15000} = -0.00013(-1\sigma)$

Figure 6.11.: Pseudo-experiment distributions for the event yields returned by the fit for shape adjusted templates, with no systematic template normalisation uncertainties included. The y-axis represents the number of pseudo-experiments returning a given event yield.

6.3.4. Ideal Method Applied In Toy

For this method a single distribution for the number of fitted events that incorporates all the shape and normalisation dependence is produced for A and B. Each pseudo-experiment is conducted as follows:

1. Randomly select values for s_1 and s_2 based on their assumed *pdf*s.
2. Produce a new set of pseudo-data based on selected values of s_1 and s_2 that the nominal templates will be fit to.
3. Calculate the test statistic between nominal templates and pseudo-data set.
4. Fit nominal templates to the pseudo-data set using Equations 6.8 and 6.9, as normalisation systematics no longer need to be incorporated into the likelihood.

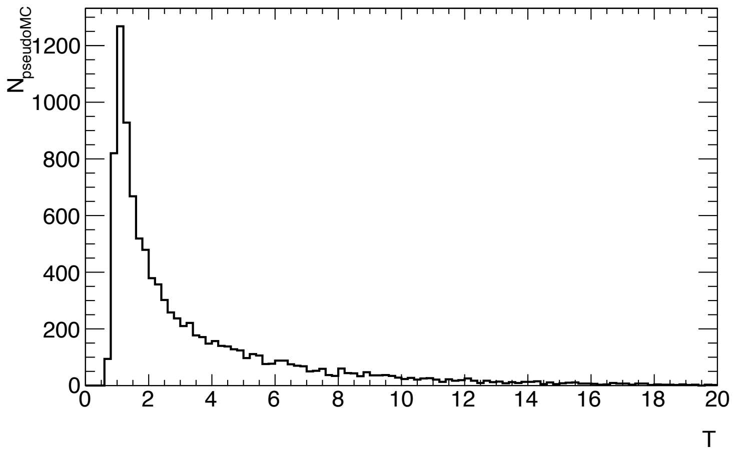

Figure 6.12.: Test statistic distribution for nominal templates from 10,000 pseudo-experiments, using the expedient method.

In addition to selecting s_1 and s_2 independently (uncorrelated case) as in Equation 6.20, the positively correlated and anti-correlated cases are also considered in which s_1 and s_2 are randomly selected from the normalised 2D distributions shown in Figures 6.13(a) and 6.13(b). This is done for completeness such that differences resulting from such correlations (between the systematics themselves) can also be brought to light.

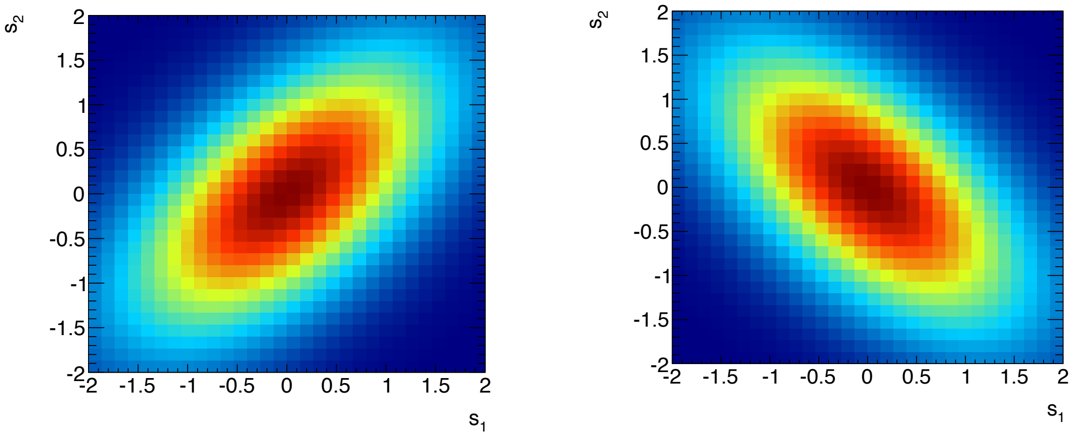

(a) s1,s2 correlated *pdf*. **(b)** s1,s2 anti-correlated *pdf*.

Figure 6.13.: Illustration of the 2D *pdf* functions used to select parameters s_1 and s_2 to test effects due to correlated/anti-correlated systematics.

6.3.5. Ideal Results In Toy

Template Fit Results

In the case where s_1 and s_2 are assumed to be uncorrelated the uncertainty on the number of events based on the distributions for 10,000 pseudo-experiments are shown in Figure 6.14. The same plots are also shown under the assumption that s_1 and s_2 are correlated (anti-correlated) in Figure 6.15 (Figure 6.16).

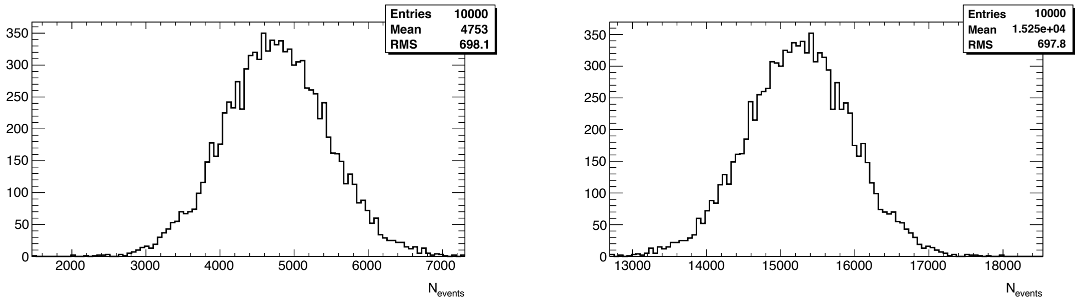

(a) $\Delta N_A = \frac{698}{4753} = 0.147$ **(b)** $\Delta N_B = \frac{698}{15247} = 0.046$

Figure 6.14.: Pseudo-experiment distributions for N_A and N_B with s_1, s_2 uncorrelated.

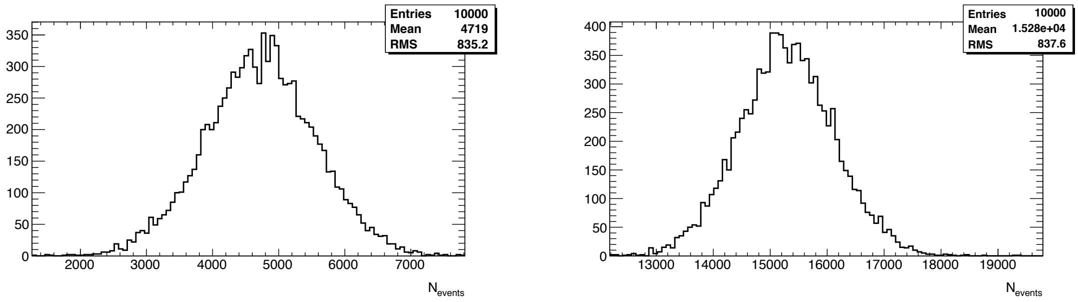

(a) $\Delta N_A = \frac{835}{4719} = 0.177$ **(b)** $\Delta N_B = \frac{838}{15282} = 0.055$

Figure 6.15.: Pseudo-experiment distributions for N_A and N_B with s_1, s_2 correlated.

We see that the uncertainty on the number of events returned by the fit for A (14.7%), in the case of uncorrelated s_1,s_2 (Figure 6.14), is similar to the value obtained by applying the AIDA method (14.5%). However, the uncertainty on the number of events returned by the fit for B (4.6%) is much lower than in the case of the AIDA method (11.7%), as expected due to the larger impact of the shape effects on the fit for template B. For the case with s_1, s_2 correlated (Figure 6.15) the uncertainties are A (17.7%), B (5.5%); while in the case of s_1, s_2 anti-correlated we get A (13.1%), B (4.1%) — as expected due

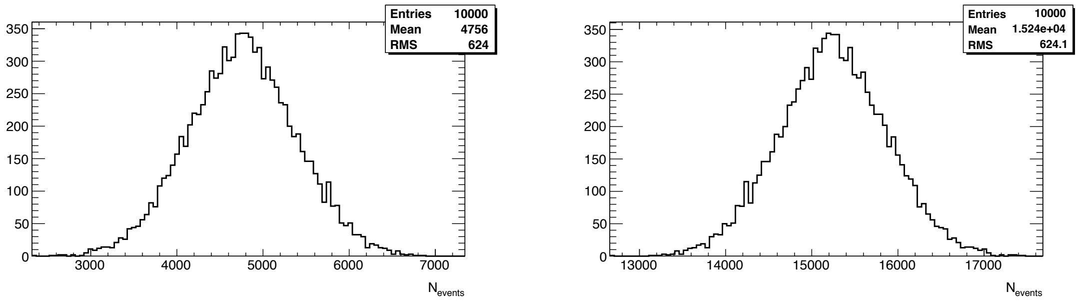

(a) $\Delta N_A = \frac{624}{4756} = 0.131$ **(b)** $\Delta N_B = \frac{624}{15244} = 0.041$

Figure 6.16.: Pseudo-experiment distributions for N_A and N_B with s_1, s_2 anti-correlated.

to the $(s_1 + s_2)$ shape dependence and normalisation dependence, which both decrease if s_1 and s_2 have opposite signs.

It should be stressed that the differences here do not imply anything about the validity of the AIDA cross section measurements as the toy example has explicitly included correlations between shape and normalisation effects due to the *same* systematics. These plots are simply included for completeness and to demonstrate that in the ideal case, shape and normalisation systematic effects would naturally be combined in the cross section analysis as well as used for determination of the test statistic distribution.

Test Statistic Distribution

Figure 6.17 provides the test statistic distribution in the three cases (s_1, s_2 uncorrelated, correlated, anti-correlated). As is clear from Figure 6.17(a), accounting for shape effects can drastically alter the underlying distribution of the test statistic casting doubt on any conclusions one might draw regarding the overall goodness-of-fit reached via the expedient method.

6.3.6. Discussion of Ideal Example

The only assumption inherent in the treatment of systematics under this method is the relationship between the systematics themselves, they are therefore considered when uncorrelated, correlated or anti-correlated with each other. Choosing this relationship is something that cannot be avoided because the probability distribution for an uncertainty will obviously be unknown to a large extent (and generally be assumed to be gaussian).

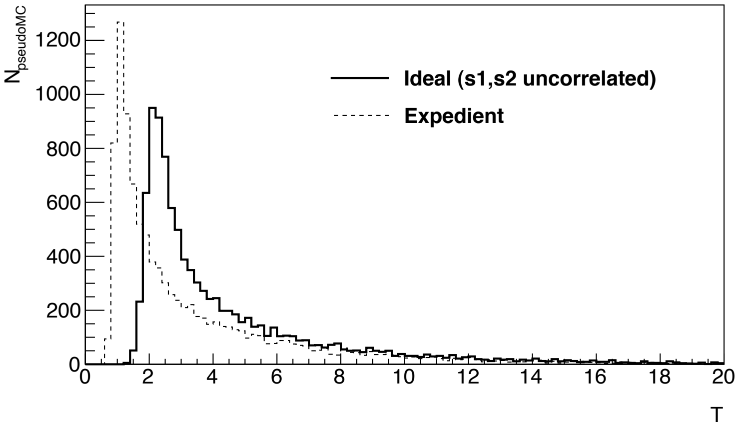

(a) Test statistic distribution for s1, s2 uncorrelated. Figure 6.12 underlaid for comparison.

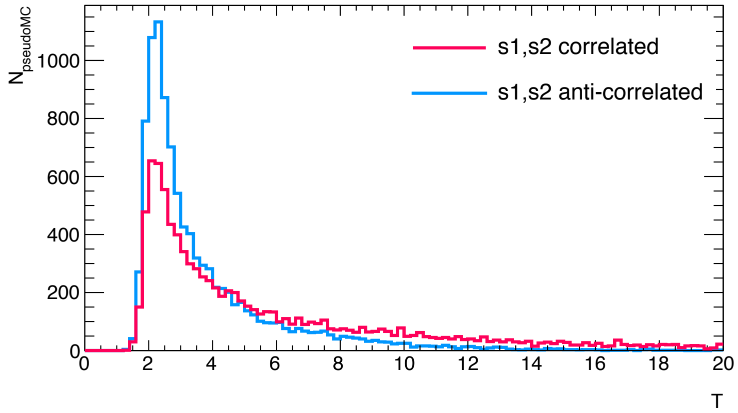

(b) Test statistic distribution for s1,s2 correlated/anti-correlated.

Figure 6.17.: Test statistic distributions for 10,000 pseudo-experiments for the three cases where the parameters s_1 and s_2 are uncorrelated, correlated and anti-correlated.

However, no other assumptions are made, the parameters and functional dependencies are *inputs* to the toy model and do not relate to the method used to determine their effects.

In terms of the uncertainties on the fitted number of events in this ideal case, as one would expect from the shape dependence on $(s_1 + s_2)$, the uncertainty increases as we go from s_1, s_2 anti-correlated to uncorrelated to positively correlated. We also see that the systematic uncertainty due to shape effects is wildly underestimated in the expedient method, as the distribution of the sum of two Gaussian distributed random variables $(s_1 + s_2)$, will have a variance $(\sigma^2_{s_1} + \sigma^2_{s_2})$, which cannot be accounted for because the effects on the shape one gets treating them separately are far smaller than when considering them together. Even if the systematics themselves are uncorrelated, their *effects* on template shape are correlated. In the case of process B, the expedient method also overestimates the uncertainty due to the systematics' effect on the normalisation, $\sim$12% as opposed to 5% in the ideal case. This is because the strength of the shape effect (which depends on $s_1 + s_2$, and is correlated with the change in normalisation) is maximum when $x = y = 0$, which is also where the Gaussian used for this template peaks, and therefore the likelihood will be maximised through improving the fit in this region, favouring template B. Such phenomena are invisible to the expedient method. That is, the normalisation uncertainty for B is lower in the ideal case than the expedient one because of *shape effects*, that cannot be incorporated in the expedient case.

Considering the test statistic distribution (Figure 6.17(a)), even though the uncertainties as they affect the number of events are larger in the expedient case, this has no bearing on the test statistic distribution, which is in fact narrower, and closer to nominal ($T = 0$) than in the ideal case. Such a drastic difference, even though the estimated shape and normalisation uncertainties as they affect the number of events for A and B are similar under both methods (and in fact a lot smaller for template B), is what we wish to avoid in reality.

So while the independence of the systematics themselves can be justified to an extent as we know the sources, their *effects* on template shape and normalisation cannot be treated independently if the test statistic distribution is to be relied upon to produce a valid measure of the goodness-of-fit with the SM.

6.4. Back to AIDA

From the toy example above it is clear that including shape effects to whatever extent possible, while still considering the systematic sources themselves independent of one another in order to remain consistent with the cross section analysis, would be beneficial in terms of the accuracy of an AIDA goodness-of-fit measurement.

Due to the difficulty in producing MC and the number of systematics being considered in the case of AIDA, any kind of full treatment as conducted in the toy example is unrealistic. However, it would seem that replacing the method by which new templates were produced in the toy example (step 2 of Subsection 6.3.4) by some procedure that can utilise the shape-adjusted templates used in the cross section analysis would be a rather efficient way to combine shape and normalisation effects, to produce a single test statistic distribution in the case of the SM in AIDA. Thus, in order to move some of the way to accounting for shape effects and bridge the gap as highlighted in the toy example, the existing templates corresponding to the shape systematics adjusted up/down by 1σ (produced to evaluate shape effects as they affect the cross section analysis) are re-used here. Due to the limited template sets available an attempt is made to interpolate between them, and this process carried out in addition to the normalisation systematic procedure used in Subsection 6.2.2. However, any correlations between shape effects due to different systematics cannot be accounted for using these templates and therefore the effects due to the different systematics on the shapes are simply averaged over in the method outlined below (Subsection 6.4.2).

6.4.1. Bin-by-bin Interpolation Used

The interpolation procedure to be employed here is carried out assuming uncorrelated Gaussian-distributed systematics, and using the two $\pm 1\sigma$ templates. For a given systematic, s, a random value, α, is drawn from the Gaussian distribution $\mathcal{G}(s) = e^{-\frac{s^2}{2}}$. A new interpolated template is produced for this systematic using its corresponding $\pm 1\sigma$ MC templates, with the bin content determined by the value chosen for α as depicted in Figure 6.18 and quantified in Equation 6.26.

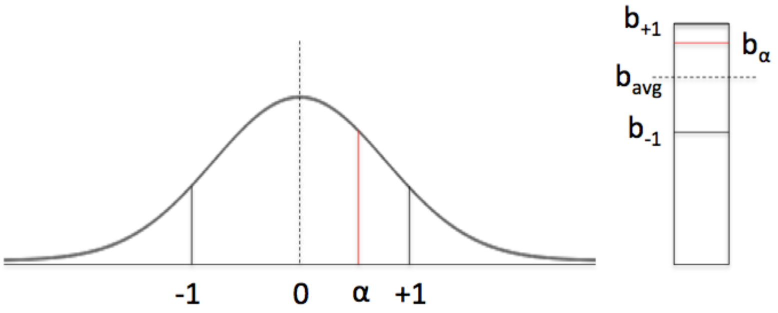

Figure 6.18.: Interpolated bin content assuming s is distributed as $\mathcal{G} = e^{-\frac{s^2}{2}}$

The bin content for each bin in the template corresponding to the systematic shifted up by σ is labeled b_{+1}, and b_{-1} for the systematic shifted down by σ. The bin average is therefore $b_{\text{avg}} = (b_{+1} + b_{-1})/2$, and the bin difference defined as $b_{\text{diff}} = (b_{+1} - b_{-1})$. The interpolated bin value, b_{α}, for a systematic value α randomly selected from the Gaussian above is taken to be:

$$b_{\alpha} = b_{\text{avg}} + \frac{\int_0^{\alpha} \mathcal{G}(x)\, dx}{\int_0^{1} \mathcal{G}(x)\, dx} \cdot \frac{b_{\text{diff}}}{2} \tag{6.26}$$

Equation 6.26 represents the particular type of interpolation used in this case assuming Gaussian-distributed systematic *pdf*s, though more detailed information on the *pdf* for given systematic could be included if available. This interpolation method has been tested using the simple toy example of Section 6.3, in order to validate the code using a case in which the true underlying distribution of the test statistic is known, these tests can be found in Appendix A.

6.4.2. Interpolation Method in AIDA

As a first step towards incorporating shape effects, using the template sets already available (as used to produce the values listed in Table 6.4), interpolation between systematic shape effects (treated independently of one another) and systematic normalisation effects are treated in the following way in order to construct a single set of pseudo-MC and produce a value for the test statistic, T:

- For each systematic source listed in Table 6.6, s_j, choose a random value, α_j, from the Gaussian distribution $\mathcal{G}(s_j) = e^{-\frac{s_j^2}{2}}$.
- Then, for each new template in the set of pseudo-MC, t_k, loop over the systematics, s_j, for which the random values, α_j, have been saved.
  - For each systematic, s_j, get the two shape adjusted templates that correspond to the systematic being shifted up by 1σ and down by 1σ, and then for each bin in the template, t_k:
    - Determine b_{α_j} using Equation 6.26 and add b_{α_j} to the bin content:
  - Scale the new template integral by $\left(\frac{1}{N_{\text{syst.s}}}\right)$ — in order to average over the systematic shape effects.

  - Scale the new template integral by $(1 + \alpha_j \cdot \delta_{jk})$ — in order to incorporate the systematic's effect on normalisation as in the normalisation-only treatment (Subsection 6.2.2).
  - Poisson fluctuate the new template bin-by-bin — in order to incorporate statistical fluctuations as they affect the template shape, as opposed to fluctuating the entire template integral as done in the normalisation only treatment (Subsection 6.2.2).

- Return the value for the test statistic, T, between the sum of the new templates, $\sum_k t_k$, and the sum of the nominal template set:

$$T_{\text{Pseudo-MC}} = \frac{1}{\mathrm{N_{bins}}} \sum_{i=1}^{\mathrm{N_{bins}}} \frac{(n_i^{\text{Pseudo-MC}} - n_i^{\text{Nominal MC}})^2}{n_i^{\text{Nominal MC}}} \quad .$$

The magnitude of the systematic effects on template normalisation implicit in the δ_{jk} terms are shown in Table 6.6. In the case of shape effects due to the event generator or parton shower model used for $t\bar{t}$ and WW, there is not any single continuous parameter that can be adjusted to produce $\pm 1\sigma$ templates, and they are therefore taken from the additional MC template sets available (as opposed to the nominal template sets). For the $t\bar{t}$ generator shape systematic, the $+1\sigma$ template used was generated via the POWHEG method, while the -1σ template was produced with ALPGEN, using HERWIG/JIMMY for the parton shower in both cases. The parton shower shape systematic for the $t\bar{t}$ templates come from POWHEG+HERWIG/JIMMY ($+1\sigma$) and POWHEG+PYTHIA (-1σ). These same generator and parton shower model combinations were used for the WW templates' generator and parton shower shape effects, while $Z/\gamma^* \to \tau\tau$ parton shower and generator uncertainties have been omitted (as in Section 6.2.2) due to limited MC samples. In the case of resolution uncertainties, where only a single shape-adjusted template exists, the $\pm 1\sigma$ template sets are taken to be the same and no interpolation need be carried out. For cross section uncertainties in Wt and WZ/ZZ templates, no corresponding shape uncertainty exists, and thus the $\pm 1\sigma$ template sets are both set to the nominal template sets.

Systematic Source	Template Normalisation Uncertainties				
	$t\bar{t}$	WW	$Z/\gamma^* \to \tau\tau$	Wt	WZ/ZZ
ISR/FSR	0.0034	0.0112	0.0095	0.0000	0.0000
$t\bar{t}$ generator	0.0087	0.0000	0.0000	0.0000	0.0000
$t\bar{t}$ PS modelling	0.0023	0.0000	0.0000	0.0000	0.0000
WW generator	0.0000	0.0053	0.0000	0.0000	0.0000
WW PS modelling	0.0000	0.0068	0.0000	0.0000	0.0000
$Z/\gamma^* \to \tau\tau$ PS modelling	0.0000	0.0000	0.0240	0.0000	0.0000
WZ/ZZ cross section	0.0000	0.0000	0.0000	0.0000	0.0500
Wt cross section	0.0000	0.0000	0.0000	0.0760	0.0000
PDF	0.0059	0.0010	0.0022	0.0000	0.0000
$E_{\mathrm{T}}^{\mathrm{miss}}$ cellout	0.0001	0.0000	0.0000	0.0002	0.0001
$E_{\mathrm{T}}^{\mathrm{miss}}$ pileup	0.0001	0.0000	0.0000	0.0000	0.0000
e identification	0.0323	0.0324	0.0330	0.0308	0.0305
e trigger	0.0013	0.0004	0.0014	0.0012	0.0012
e momentum scale	0.0017	0.0019	0.0080	0.0013	0.0016
e momentum resolution	0.0001	0.0001	0.0012	0.0005	0.0016
μ identification	0.0079	0.0078	0.0078	0.0078	0.0078
μ trigger	0.0000	0.0002	0.0007	0.0001	0.0007
μ momentum scale	0.0004	0.0003	0.0017	0.0003	0.0000
μ momentum resolution	0.0001	0.0000	0.0000	0.0000	0.0000
Jet vertex fraction	0.0082	0.0028	0.0018	0.0054	0.0077
Jet energy scale	0.0077	0.0065	0.0046	0.0062	0.0055
Jet reconstruction	0.0000	0.0000	0.0000	0.0000	0.0001
Jet energy resolution	0.0023	0.0018	0.0018	0.0025	0.0000
Luminosity	0.0180	0.0180	0.0180	0.0180	0.0180

Table 6.6.: Magnitude of effect on $\pm 1\sigma$ shift in systematic value on normalisations of MC templates (i.e. δ_{jk} terms). Note: the uncertainty on the fakes template was taken as a single normalisation uncertainty of 80%, based on its yield uncertainty.

6.4.3. Result

The test statistic distribution built up using this method is presented in Figure 6.19 for 10,000 sets of pseudo-MC and implies a p-value for the data of 14.3%, remaining within 2σ of the SM expectation over the $E_{\mathrm{T}}^{\mathrm{miss}}$–$N_{\mathrm{jets}}$ parameter space.

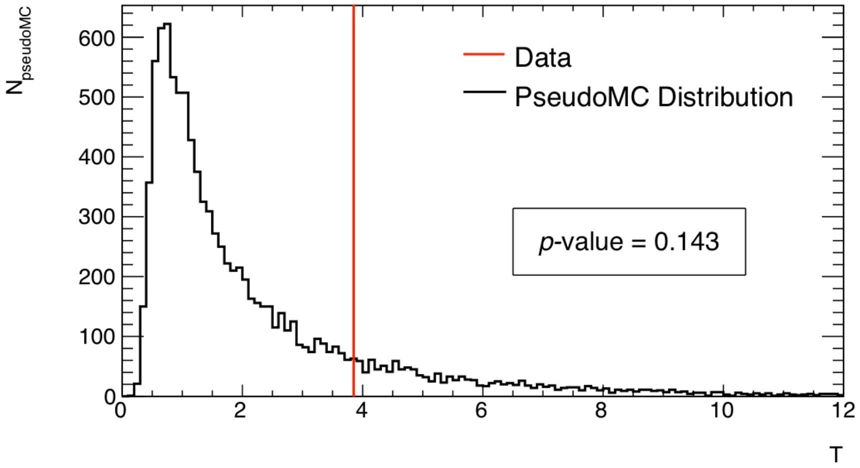

Figure 6.19.: Underlying test statistic distribution including shape and normalisation systematic effects from 10,000 sets of pseudo-MC.

This compares with a p-value of 12.3% (Figure 6.6) when considering only normalisation effects on MC templates. Though slightly higher, the difference is not as large as may have been expected. This may be due to the fact that the systematic shape effects are washed out by statistical fluctuations in the original $\pm 1\sigma$ MC templates themselves. One key point that must be emphasised is that correlations between shape effects were not accounted for in this treatment, as attempting to do so would increase the required number of template sets to $2^{N_{\mathrm{syst.s}}}$, and interpolation in such a higher dimensional space is not as clear as in the case above using only $2 \cdot N_{\mathrm{syst.s}}$ template sets.

6.5. Further Work

The agreement between the SM expectation and the $\sqrt{s} = 7\,\mathrm{TeV}$ ATLAS data for $e\mu$ events over the whole $E_{\mathrm{T}}^{\mathrm{miss}}$–$N_{\mathrm{jets}}$ parameter space is within 2σ as determined using the method discussed in Subsection 6.4.2, which incorporates the systematic effects on shapes and normalisations of the Monte Carlo templates used to model the SM in this parameter space. This level of agreement is put forward cautiously, with the caveats that the PDFs for the systematics were assumed to be Gaussian-distributed and independent of one another. In addition, the validity of the interpolation method used may also be questionable for MC templates with low statistics, as large statistical fluctuations in the templates used for the interpolation convolve statistical and shape effects — though it is not clear how this can be avoided as this is dependent on the number of events available in the specific MC samples.

Looking forward to the $20.3\,\mathrm{fb}^{-1}$ of $\sqrt{s} = 8\,\mathrm{TeV}$ pp collision data collected by ATLAS over 2012, with higher statistics, systematic effects are sure to provide the largest source of uncertainty to future AIDA cross section measurements. In order to ensure such effects are not being overestimated, it may be useful to combine the shape and normalisation effects due to a given systematic source as demonstrated in the toy framework (Section 6.3), through some interpolation procedure for templates modified by a given systematic source (as in Section 6.4). This would both simplify the evaluation of systematic effects for the cross section measurements, and allow for the level of agreement between data and the templates being used to be evaluated globally using the same systematics treatment. Any deviations from the SM expectation (outside of its associated uncertainties) overall could indicate the presence of physics beyond the SM, and additional templates based on MC representing a given theoretical model could be added to the fitting procedure to begin testing these new hypothesis against the SM. The generality of the template-fitting-method also allows for the possibility of measuring other processes simultaneously over any parameter space in which the processes are adequately separated from one another.

Chapter 7.

Conclusions and Future Outlook

This thesis has demonstrated two different approaches to searching for inconsistencies between data the SM expectation. The charged Higgs analyses involved determining whether-or-not there was an excess (over the SM expectation) of top quarks decaying to tau leptons, and whether this was compatible with the hypothesised existence of a light charged Higgs boson. The focus has been on trying to separate the possible charged Higgs signal events from their SM $t\bar{t}$ counterparts, and making sure that the SM backgrounds and their uncertainties are determined accurately in order to maximise the sensitivity to a potential signal. The second approach in the inclusive dilepton analysis, was to determine and implement a method to test the agreement with the SM in a much larger phase space determined by a minimal selection for an electron and oppositely charged muon. The goodness-of-fit test of data against the SM expectation in this case is conducted over the $E_{\mathrm{T}}^{\mathrm{miss}}$–$N_{\mathrm{jets}}$ parameter space chosen to naturally separate the main processes that produce such $e\mu$ final states.

The work presented in this thesis provides no statistically significant evidence for a discrepancy between the SM and data collected by ATLAS in 2011 in either opposite sign $e\mu$ events, or the rate of top quark decay to a tau final state. In fact no inconsistencies with the SM have yet been observed at the LHC experiments, either at $\sqrt{s} = 7\,\mathrm{TeV}$ or $\sqrt{s} = 8\,\mathrm{TeV}$, even as the discovery of the SM Higgs boson reinforces its validity at the energies probed.

Work is beginning on application of the AIDA analysis to the $\sqrt{s} = 8\,\mathrm{TeV}$ pp collision data collected by ATLAS over 2012, and there are many possible directions measurements based on the AIDA framework could take. Current proposals are to add a measurement of associated single top quark production (Wt), and extend the parameter space for the templates to include a third N_{leptons} axis — removing the requirement of an oppositely charged electron and muon. This would increase the number of processes that could be measured to include $t\bar{t}W$, $t\bar{t}Z$, WZ, ZZ, $W+\text{jets}$, and $Z+\text{jets}$ production. Combining treatment of template shape and normalisation effects, using some interpolation between sets of systematically adjusted templates, would also allow the goodness-of-fit for data to be measured in conjunction with the cross section to ensure the fit to data is valid.

Further searches for a charged Higgs in the ATLAS $\sqrt{s} = 8\,\text{TeV}$ dataset concentrate on a heavy charged Higgs ($m_{H^+} > m_t$) due to the increased sensitivity provided by the higher predicted cross sections for H^+ events at 8 TeV (and beyond) and the much larger data set ($20.3\,\text{fb}^{-1}$) collected in 2012. Any further limits placed on a light charged Higgs will likely be inferred from improved measurements of SM top quark processes made possible with the increased statistics.

When the LHC resumes operation after the long shutdown period over 2013/2014, the pp collision energy is expected to be $\sqrt{s} = 13\,\text{TeV}$ — opening up a large amount of phase space for the production and decay of new particle states that could exist in addition to the SM particles. With upgrades to ATLAS proceeding on schedule, there will be much more physics to come.

Appendix A.

Interpolation in the Toy Example

The bin-by-bin interpolation discussed in Section 6.4 is tested on the toy model described in Section 6.3. This test is simply to check that the interpolation method works as expected, and that the resulting test statistic distribution is indeed closer to the true distribution than in the case where no interpolation is performed. The interpolation relies on the random selection of the parameters α_1, α_2 for each systematic source s_1, s_2. The method is tested by selecting the parameters α_1, α_2 from: a flat probability distribution between the -1σ and $+1\sigma$ shape adjusted templates – Figure A.1(a); as well as from Gaussian distributions truncated to various degrees, i.e. $(-1\sigma, +1\sigma)$, $(-1.1\sigma, +1.1\sigma)$, $(-1.2\sigma, +1.2\sigma)$, $(-2\sigma, +2\sigma)$, $(-3\sigma, +3\sigma)$, $(-10\sigma, +10\sigma)$ – Figures A.1(b)–(h).

As expected, the interpolation method produces a test statistic distribution much closer to the true distribution (labeled "Ideal method" in the figures). As there is no particular justification for truncating the probability distribution for the systematic parameters (α), the Gaussian used in Section 6.4 is allowed to run out to $\pm 10\sigma$ (as in Figure A.1(h)).

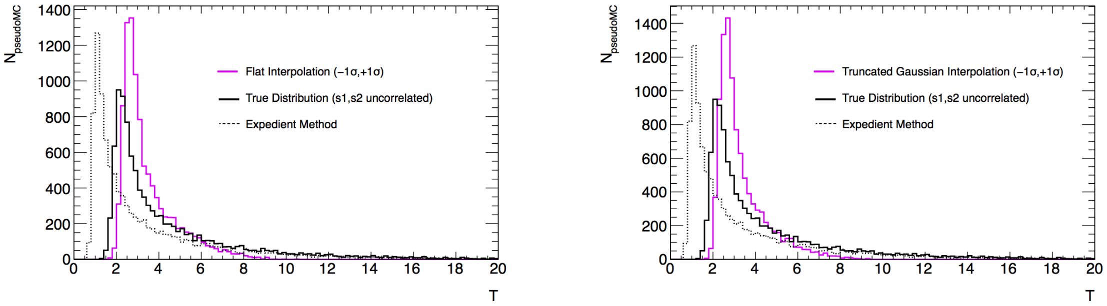

(a) Flat Distribution $(-1\sigma, +1\sigma)$.

(b) Truncated Gaussian Distribution $(-1\sigma, +1\sigma)$.

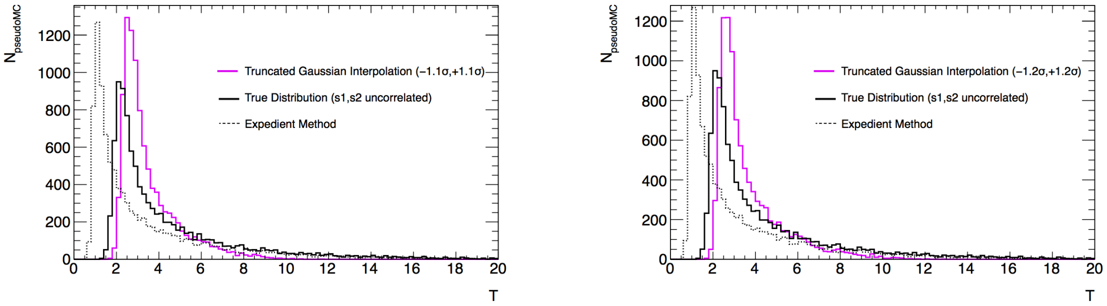

(c) Truncated Gaussian Distribution $(-1.1\sigma, +1.1\sigma)$.

(d) Truncated Gaussian Distribution $(-1.2\sigma, +1.2\sigma)$.

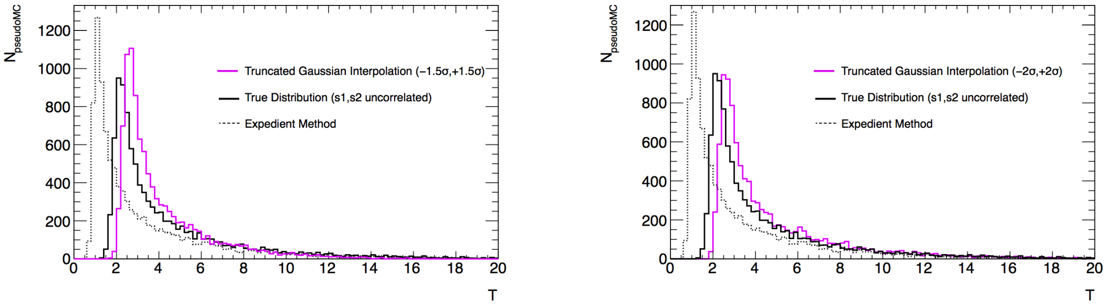

(e) Truncated Gaussian Distribution $(-1.5\sigma, +1.5\sigma)$.

(f) Truncated Gaussian Distribution $(-2\sigma, +2\sigma)$.

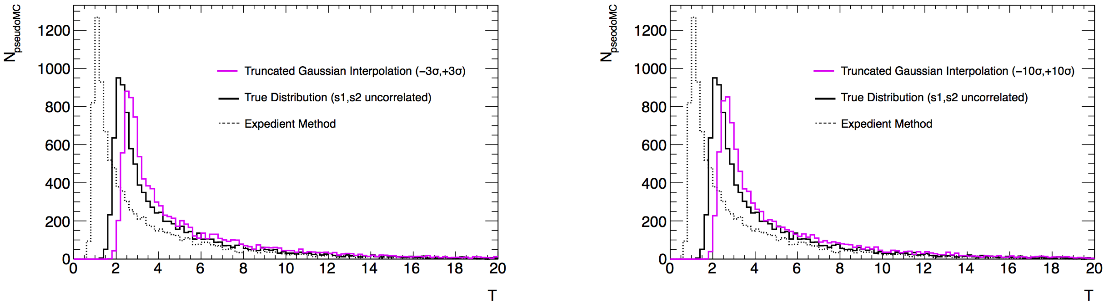

(g) Truncated Gaussian Distribution $(-3\sigma, +3\sigma)$.

(h) Truncated Gaussian Distribution $(-10\sigma, +10\sigma)$.

Figure A.1.: Test statistic distributions in the case of the toy example using the interpolation method, for parameters α_1, α_2 selected from a flat probability distribution (a), and truncated Gaussian distributions (b)–(h).

Bibliography

[1] N. Patel, A. Saavedra, M. White, and B. Yabsley, “Charge deposition in the SCT due to beamloss,” Tech. Rep. ATL-INDET-PUB-2013-002, CERN, Geneva, Aug, 2013. `https://cds.cern.ch/record/1577413`. Cited on page iii.

[2] S. Behar, C. Buszello, P. Czodrowski, A. Ferrari, M. Flechl, S. Hattrem Raddum, C. Isaksson, A. Madsen, A. McCarn, M. zur Nedden, M. Neubauer, N. Patel, D. Pelikan, A. Read, Y. Rozen, and A. Saavedra, “Search for a charged Higgs boson decaying via $H^+ \to \tau_{\text{had}} + \nu$ in $t\bar{t}$ events with one light lepton in the final state using events using $4.6\,\text{fb}^{-1}$ of pp collision data recorded at $\sqrt{s} = 7$ TeV with the ATLAS detector — Supporting note,” Tech. Rep. ATL-PHYS-INT-2012-046, CERN, Geneva, Apr, 2012. `https://cds.cern.ch/record/1442940`. Cited on page iii.

[3] P. Assamagan, C. Bernius, P. Casado, V. Cavaliere, P. Czodrowski, D. Chakraborty, D. Greenwood, A. Ferrari, M. Flechl, S. Hattrem Raddum, A. Kopp, P. Mal, A. McCarn, M. Neubauer, N. Patel, A. Randle-Conde, A. L. Read, G. Rocha de Lima, A. Saavedra, M. Schumacher, and S. Sekula, “Search for charged Higgs bosons in the τ_{had}+jets final state in $t\bar{t}$ decays with $4.6\,\text{fb}^{-1}$ of pp collision data recorded at $\sqrt{s} = 7$ TeV with the ATLAS Experiment — Supporting Note,” Tech. Rep. ATL-PHYS-INT-2012-047, CERN, Geneva, Apr, 2012. `https://cds.cern.ch/record/1442965`. Cited on page iii, 81, and 197.

[4] A. Bangert, D. Benjamin, J. Ferrando, K. Finelli, K. Gellerstedt, H. Khandanyan, M. Kruse, A. Limosani, M. Lisovyi, N. Patel, A. Saavedra, J. Sjölin, and K. Varvell, “An Inclusive Analysis of $t\bar{t}$, WW, and $Z/\gamma^* \to \tau\tau$ Production in the Dilepton Final State at $\sqrt{s} = 7\,\text{TeV}$ with the ATLAS Detector at the LHC,” Tech. Rep. ATL-COM-PHYS-2012-089, CERN, Geneva, Jan, 2012. `https://cds.cern.ch/record/1420072`. Cited on page iv.

[5] E. Noether, “Invariant Variation Problems,” *Gott.Nachr.* **1918** (1918) 235–257,

`arXiv:physics/0503066 [physics]`. Cited on page 8.

[6] H. Greaves and T. Thomas, "The CPT theorem," *arXiv e-prints* (Apr., 2012) , `arXiv:1204.4674 [math-ph]`. Cited on page 8.

[7] C. Wu, E. Ambler, R. Hayward, D. Hoppes, and R. Hudson, "Experimental Test of Parity Conservation in Beta Decay," *Phys.Rev.* **105** (1957) 1413–1414. Cited on page 8.

[8] J. Christenson, J. Cronin, V. Fitch, and R. Turlay, "Evidence for the 2 pi Decay of the k(2)0 Meson," *Phys.Rev.Lett.* **13** (1964) 138–140. Cited on page 8.

[9] M. Schwartz, *Quantum Field Theory and the Standard Model*. Quantum Field Theory and the Standard Model. Cambridge University Press, 2013. `http://books.google.com/books?id=HbdEAgAAQBAJ`. Cited on page 11.

[10] P. Z. Skands, "QCD for Collider Physics," `arXiv:1104.2863 [hep-ph]`. Cited on page 11.

[11] M. Han and Y. Nambu, "Three Triplet Model with Double SU(3) Symmetry," *Phys.Rev.* **139** (1965) B1006–B1010. Cited on page 11.

[12] S. Glashow, "Partial Symmetries of Weak Interactions," *Nucl.Phys.* **22** (1961) 579–588. Cited on page 13.

[13] S. Weinberg, "A Model of Leptons," *Phys.Rev.Lett.* **19** (1967) 1264–1266. Cited on page 13.

[14] A. Salam and J. C. Ward, "Electromagnetic and weak interactions," *Phys.Lett.* **13** (1964) 168–171. Cited on page 13.

[15] Gargamelle Neutrino Collaboration, F. Hasert *et al.*, "Observation of Neutrino Like Interactions Without Muon Or Electron in the Gargamelle Neutrino Experiment," *Phys.Lett.* **B46** (1973) 138–140. Cited on page 13.

[16] UA1 Collaboration, G. Arnison *et al.*, "Experimental Observation of Isolated Large Transverse Energy Electrons with Associated Missing Energy at $s^{1/2} =$ 540-GeV," *Phys.Lett.* **B122** (1983) 103–116. Cited on page 13.

[17] UA2 Collaboration, M. Banner *et al.*, "Observation of Single Isolated Electrons of High Transverse Momentum in Events with Missing Transverse Energy at the CERN anti-p p Collider," *Phys.Lett.* **B122** (1983) 476–485. Cited on page 13.

[18] UA1 Collaboration, G. Arnison *et al.*, "Experimental Observation of Lepton Pairs of Invariant Mass Around 95-GeV/c^2 at the CERN SPS Collider," *Phys.Lett.* **B126** (1983) 398–410. Cited on page 13.

[19] UA2 Collaboration, P. Bagnaia *et al.*, "Evidence for $Z^0 \to e^+e^-$ at the CERN anti-p p Collider," *Phys.Lett.* **B129** (1983) 130–140. Cited on page 13.

[20] P. W. Higgs, "Broken Symmetries and the Masses of Gauge Bosons," *Phys.Rev.Lett.* **13** (1964) 508–509. Cited on page 13.

[21] F. Englert and R. Brout, "Broken Symmetry and the Mass of Gauge Vector Mesons," *Phys.Rev.Lett.* **13** (1964) 321–323. Cited on page 13.

[22] G. Guralnik, C. Hagen, and T. Kibble, "Global Conservation Laws and Massless Particles," *Phys.Rev.Lett.* **13** (1964) 585–587. Cited on page 13.

[23] ATLAS Collaboration, G. Aad *et al.*, "Observation of a new particle in the search for the Standard Model Higgs boson with the ATLAS detector at the LHC," *Phys.Lett.* **B716** (2012) 1–29, `arXiv:1207.7214 [hep-ex]`. Cited on page 13 and 26.

[24] CMS Collaboration, S. Chatrchyan *et al.*, "Observation of a new boson at a mass of 125 GeV with the CMS experiment at the LHC," *Phys.Lett.* **B716** (2012) 30–61, `arXiv:1207.7235 [hep-ex]`. Cited on page 13 and 26.

[25] J. Thomson, "Cathode rays," *Phil.Mag.* **44** (1897) 293–316. Cited on page 17.

[26] M. Baak, M. Goebel, J. Haller, A. Hoecker, D. Kennedy, *et al.*, "The Electroweak Fit of the Standard Model after the Discovery of a New Boson at the LHC," *Eur.Phys.J.* **C72** (2012) 2205, `arXiv:1209.2716 [hep-ph]`. Cited on page 18.

[27] N. Cabibbo, "Unitary Symmetry and Leptonic Decays," *Phys.Rev.Lett.* **10** (1963) 531–533. Cited on page 18.

[28] M. Kobayashi and T. Maskawa, "CP Violation in the Renormalizable Theory of Weak Interaction," *Prog.Theor.Phys.* **49** (1973) 652–657. Cited on page 18.

[29] Particle Data Group Collaboration, J. Beringer *et al.*, "Review of Particle Physics (RPP): Neutrino Mass, Mixing, and Oscillations," *Phys.Rev.* **D86** (2012) 010001. Cited on page 19.

[30] B. Pontecorvo, "Mesonium and anti-mesonium," *Sov.Phys.JETP* **6** (1957) 429.

Cited on page 19.

[31] B. Pontecorvo, "Neutrino Experiments and the Problem of Conservation of Leptonic Charge," *Sov.Phys.JETP* **26** (1968) 984–988. Cited on page 19.

[32] Z. Maki, M. Nakagawa, and S. Sakata, "Remarks on the unified model of elementary particles," *Prog.Theor.Phys.* **28** (1962) 870–880. Cited on page 19.

[33] S. P. Martin, "A Supersymmetry primer," `arXiv:hep-ph/9709356 [hep-ph]`. Cited on page 21.

[34] S. L. Adler and W. A. Bardeen, "Absence of higher order corrections in the anomalous axial vector divergence equation," *Phys.Rev.* **182** (1969) 1517–1536. Cited on page 21.

[35] S. Treiman, *Current Algebra and Anomalies*. Princeton series in physics. World Scientific, 1985. `http://books.google.com/books?id=bjDSKtbdKoEC`. Cited on page 21.

[36] M. Persic, P. Salucci, and F. Stel, "The Universal rotation curve of spiral galaxies: 1. The Dark matter connection," *Mon.Not.Roy.Astron.Soc.* **281** (1996) 27, `arXiv:astro-ph/9506004 [astro-ph]`. Cited on page 21.

[37] D. Clowe, M. Bradac, A. H. Gonzalez, M. Markevitch, S. W. Randall, *et al.*, "A direct empirical proof of the existence of dark matter," *Astrophys.J.* **648** (2006) L109–L113, `arXiv:astro-ph/0608407 [astro-ph]`. Cited on page 21.

[38] J. L. Feng, "Dark Matter Candidates from Particle Physics and Methods of Detection," *Ann.Rev.Astron.Astrophys.* **48** (2010) 495–545, `arXiv:1003.0904 [astro-ph.CO]`. Cited on page 21.

[39] Supernova Search Collaboration, A. G. Riess *et al.*, "Observational evidence from supernovae for an accelerating universe and a cosmological constant," *Astron.J.* **116** (1998) 1009–1038, `arXiv:astro-ph/9805201 [astro-ph]`. Cited on page 22.

[40] Supernova Cosmology Project Collaboration, S. Perlmutter *et al.*, "Measurements of Omega and Lambda from 42 high redshift supernovae," *Astrophys.J.* **517** (1999) 565–586, `arXiv:astro-ph/9812133 [astro-ph]`. Cited on page 22.

[41] Supernova Search Team Collaboration, J. L. Tonry *et al.*, "Cosmological results from high-z supernovae," *Astrophys.J.* **594** (2003) 1–24,

`arXiv:astro-ph/0305008 [astro-ph]`. Cited on page 22.

[42] Planck Collaboration, P. Ade *et al.*, “Planck 2013 results. XVI. Cosmological parameters,” `arXiv:1303.5076 [astro-ph.CO]`. Cited on page 22.

[43] L. Evans and P. Bryant, “LHC Machine,” *JINST* **3** (2008) S08001. Cited on page 23.

[44] ATLAS Collaboration, G. Aad *et al.*, “The ATLAS Experiment at the CERN Large Hadron Collider,” *JINST* **3** (2008) S08003. Cited on page 24, 27, 31, 35, 36, 37, 38, 191, and 192.

[45] CMS Collaboration, S. Chatrchyan *et al.*, “The CMS experiment at the CERN LHC,” *JINST* **3** (2008) S08004. Cited on page 24.

[46] LHCb Collaboration, J. Alves, A. Augusto *et al.*, “The LHCb Detector at the LHC,” *JINST* **3** (2008) S08005. Cited on page 24.

[47] ALICE Collaboration, K. Aamodt *et al.*, “The ALICE experiment at the CERN LHC,” *JINST* **3** (2008) S08002. Cited on page 24.

[48] TOTEM Collaboration, G. Anelli *et al.*, “The TOTEM experiment at the CERN Large Hadron Collider,” *JINST* **3** (2008) S08007. Cited on page 24.

[49] LHCf Collaboration, O. Adriani *et al.*, “The LHCf detector at the CERN Large Hadron Collider,” *JINST* **3** (2008) S08006. Cited on page 24.

[50] J. L. Pinfold, “The MoEDAL Experiment – Searching for Highly Ionizing Particles at the LHC,”. `http://dx.doi.org/10.1007/978-90-481-2287-5_21`. Cited on page 24.

[51] I. Bird, K. Bos, N. Brook, D. Duellmann, C. Eck, *et al.*, “LHC computing Grid. Technical design report,” Tech. Rep. CERN-LHCC-2005-024, 2005. Cited on page 24.

[52] J. Haffner, “The CERN accelerator complex. Complexe des accélérateurs du CERN.” `http://cds.cern.ch/record/1621894`, Oct, 2013. Cited on page 25 and 191.

[53] P. Jenni, “Experimental review of W and Z production and decay at the CERN $p\overline{p}$ collider,” Tech. Rep. CERN-EP-87-226, Dec, 1987. Cited on page 25.

[54] *LEP design report*. CERN, Geneva, 1984. Copies shelved as reports in LEP, PS

and SPS libraries. Cited on page 25.

[55] "Summary of the analysis of the 19 September 2008 incident at the LHC.." http://cds.cern.ch/record/1135729, Oct, 2008. Cited on page 26 and 53.

[56] D. Fournier, "Performance of the LHC, ATLAS and CMS in 2011," *EPJ Web Conf.* **28** (2012) 01003, `arXiv:1201.4681 [hep-ex]`. Cited on page 27 and 197.

[57] ATLAS Collaboration, G. Aad *et al.*, "Improved luminosity determination in pp collisions at $\sqrt{s} = 7$ TeV using the ATLAS detector at the LHC," *Eur.Phys.J.* **C73** (2013) 2518, `arXiv:1302.4393 [hep-ex]`. Cited on page 27, 117, and 134.

[58] G. Aad *et al.*, "Atlas experiment – luminosity public results." https://twiki.cern.ch/twiki/bin/view/AtlasPublic/LuminosityPublicResults, Jan, 2014. Accessed: 2013-11-15. Cited on page 28 and 191.

[59] G. Aad *et al.*, "Atlas stand-alone event displays." https://twiki.cern.ch/twiki/bin/view/AtlasPublic/EventDisplayStandAlone, Aug, 2012. Accessed: 2013-11-15. Cited on page 29 and 191.

[60] J. Pequenao, "Computer generated image of the whole ATLAS detector." http://cds.cern.ch/record/1095924, Mar, 2008. Cited on page 30 and 191.

[61] N. Wermes and G. Hallewel, *ATLAS pixel detector: Technical Design Report*. Technical Design Report ATLAS. CERN, Geneva, 1998. Cited on page 31.

[62] G. Aad, M. Ackers, F. Alberti, M. Aleppo, G. Alimonti, *et al.*, "ATLAS pixel detector electronics and sensors," *JINST* **3** (2008) P07007. Cited on page 31.

[63] ATLAS TRT Collaboration, E. Abat *et al.*, "The ATLAS Transition Radiation Tracker (TRT) proportional drift tube: Design and performance," *JINST* **3** (2008) P02013. Cited on page 32.

[64] A. Vogel, "ATLAS Transition Radiation Tracker (TRT): Straw Tube Gaseous Detectors at High Rates," Tech. Rep. ATL-INDET-PROC-2013-005, CERN, Geneva, Apr, 2013. Cited on page 33.

[65] J. Pequenao, "Computer Generated image of the ATLAS calorimeter." http://cds.cern.ch/record/1095927, Mar, 2008. Cited on page 34 and 191.

[66] *ATLAS calorimeter performance: Technical Design Report*. Technical Design Report ATLAS. CERN, Geneva, 1996. Cited on page 35, 36, and 192.

[67] A. Succurro, "The ATLAS Tile Hadronic Calorimeter performance in the LHC collision era,". Cited on page 36.

[68] ATLAS Collaboration, M. Cascella, "Jet energy scale calibration using photon-jet events in the ATLAS experiment," *Nuovo Cim.* **C034N06** (2011) 274–275. Cited on page 36.

[69] A. Artamonov, D. Bailey, G. Belanger, M. Cadabeschi, T. Chen, *et al.*, "The ATLAS forward calorimeters," *JINST* **3** (2008) P02010. Cited on page 37.

[70] ATLAS Collaboration, "ATLAS muon spectrometer: Technical design report," Tech. Rep. CERN-LHCC-97-22, ATLAS-TDR-10, 1997. Cited on page 37, 39, and 192.

[71] J. Wotschack, "ATLAS Muon Chamber Construction Parameters for CSC, MDT, and RPC chambers," Tech. Rep. ATL-MUON-PUB-2008-006. ATL-COM-MUON-2008-008, CERN, Geneva, Apr, 2008. Cited on page 38.

[72] T. Kono, "Performance and evolution of the ATLAS TDAQ system with pp collisions at 7 TeV," Tech. Rep. ATL-DAQ-PROC-2012-011, ATL-COM-DAQ-2012-116, 2012. Cited on page 40.

[73] ATLAS TDAQ Collaboration, A. Negri, "Evolution of the Trigger and data acquisition system for the ATLAS experiment," *J.Phys.Conf.Ser.* **396** (2012) 012033. Cited on page 41 and 192.

[74] ATLAS Collaboration, A. V. Vaniachine, "ATLAS Detector Data Processing on the Grid," *IEEE Nucl.Sci.Symp.Conf.Rec.* **2011** (2011) 104–107. Cited on page 41.

[75] ATLAS Collaboration, G. Aad *et al.*, "Charged-particle multiplicities in pp interactions measured with the ATLAS detector at the LHC," *New J.Phys.* **13** (2011) 053033, `arXiv:1012.5104 [hep-ex]`. Cited on page 43 and 44.

[76] A. Buckley, J. Butterworth, S. Gieseke, D. Grellscheid, S. Hoche, *et al.*, "General-purpose event generators for LHC physics," *Phys.Rept.* **504** (2011) 145–233, `arXiv:1101.2599 [hep-ph]`. Cited on page 43.

[77] M. Dittmar, S. Forte, A. Glazov, S. Moch, S. Alekhin, *et al.*, "Working Group I: Parton distributions: Summary report for the HERA LHC Workshop Proceedings," `arXiv:hep-ph/0511119 [hep-ph]`. Cited on page 44.

[78] F. Caola, S. Forte, and J. Rojo, "HERA data and DGLAP evolution: Theory and phenomenology," *Nucl.Phys.* **A854** (2011) 32–44, `arXiv:1007.5405 [hep-ph]`. Cited on page 44.

[79] ATLAS Collaboration, "Charged particle multiplicities in pp interactions at $\sqrt{s} = 0.9$ and 7 TeV in a diffractive limited phase-space measured with the ATLAS detector at the LHC and new PYTHIA6 tune," Tech. Rep. ATLAS-CONF-2010-031, ATLAS-COM-CONF-2010-031, 2010. Cited on page 44 and 79.

[80] ATLAS Collaboration, "First tuning of HERWIG/JIMMY to ATLAS data," Tech. Rep. ATL-PHYS-PUB-2010-014, ATL-COM-PHYS-2010-858, 2010. Cited on page 44 and 80.

[81] GEANT4 Collaboration, S. Agostinelli *et al.*, "GEANT4: A simulation toolkit," *Nucl. Instrum. Meth.* **A506** (2003) 250–303. Cited on page 44.

[82] J. Allison, M. Asai, G. Barrand, M. Donszelmann, K. Minamimoto, *et al.*, "The GEANT4 Visualisation System," *Comput.Phys.Commun.* **178** (2008) 331–365. Cited on page 44 and 57.

[83] J. Pequenao and P. Schaffner, "A computer generated image representing how ATLAS detects particles." `http://cds.cern.ch/record/1505342`, Jan, 2013. Cited on page 46 and 192.

[84] T. Cornelissen, M. Elsing, S. Fleischmann, W. Liebig, E. Moyse, and A. Salzburger, "Concepts, Design and Implementation of the ATLAS New Tracking (NEWT)," Tech. Rep. ATL-SOFT-PUB-2007-007. ATL-COM-SOFT-2007-002, CERN, Geneva, Mar, 2007. Cited on page 45.

[85] W. Lampl, S. Laplace, D. Lelas, P. Loch, H. Ma, *et al.*, "Calorimeter clustering algorithms: Description and performance," Tech. Rep. ATL-LARG-PUB-2008-002, ATL-COM-LARG-2008-003, 2008. Cited on page 45.

[86] ATLAS Collaboration, "Performance of primary vertex reconstruction in proton-proton collisions at $\sqrt{s}$ =7 TeV in the ATLAS experiment," Tech. Rep. ATLAS-CONF-2010-069, ATLAS-COM-CONF-2010-070, 2010. Cited on page 47.

[87] ATLAS Collaboration, G. Aad *et al.*, "Electron performance measurements with the ATLAS detector using the 2010 LHC proton-proton collision data," *Eur.Phys.J.* **C72** (2012) 1909, `arXiv:1110.3174 [hep-ex]`. Cited on page 47.

[88] ATLAS Collaboration, "Muon reconstruction efficiency in reprocessed 2010 LHC proton-proton collision data recorded with the ATLAS detector," Tech. Rep. ATLAS-CONF-2011-063, ATLAS-COM-CONF-2011-068, 2011. Cited on page 48.

[89] T. Lagouri, D. Adams, K. Assamagan, M. Biglietti, G. Carlino, *et al.*, "A Muon Identification and Combined Reconstruction Procedure for the ATLAS Detector at the LHC at CERN," *IEEE Trans.Nucl.Sci.* **51** (2004) 3030–3033. Cited on page 48.

[90] ATLAS Collaboration Collaboration, G. Aad *et al.*, "Measurement of the muon reconstruction performance of the ATLAS detector using 2011 and 2012 LHC proton-proton collision data," `arXiv:1407.3935 [hep-ex]`. Cited on page 49 and 192.

[91] M. Cacciari, G. P. Salam, and G. Soyez, "The Anti-k(t) jet clustering algorithm," *JHEP* **0804** (2008) 063, `arXiv:0802.1189 [hep-ph]`. Cited on page 48.

[92] ATLAS Collaboration, "Jet energy scale and its systematic uncertainty in proton-proton collisions at sqrt(s)=7 TeV in ATLAS 2010 data," Tech. Rep. ATLAS-CONF-2011-032, ATLAS-COM-CONF-2011-053, 2011. Cited on page 49.

[93] ATLAS Collaboration, T. Barillari, "Jet energy scale uncertainties in ATLAS," *J.Phys.Conf.Ser.* **404** (2012) 012012. Cited on page 49.

[94] D. W. Miller, A. Schwartzman, and D. Su, "Pile-up jet energy scale corrections using the jet-vertex fraction method," Tech. Rep. ATL-PHYS-INT-2009-090, CERN, Geneva, Sep, 2009. Cited on page 49.

[95] ATLAS Collaboration, "Commissioning of the ATLAS high-performance b-tagging algorithms in the 7 TeV collision data," Tech. Rep. ATLAS-CONF-2011-102, ATLAS-COM-CONF-2011-110, 2011. Cited on page 49.

[96] ATLAS Collaboration, "b-jet tagging calibration on c-jets containing D^{*+} mesons," Tech. Rep. ATLAS-CONF-2012-039, ATLAS-COM-CONF-2012-020, 2012. Cited on page 49.

[97] Particle Data Group Collaboration, K. Nakamura *et al.*, "Review of particle physics," *J.Phys.* **G37** (2010) 075021. Cited on page 50, 80, 138, and 199.

[98] ATLAS Collaboration, F. Friedrich, "Tau Lepton Reconstruction and Identification at ATLAS," `arXiv:1201.5466 [hep-ex]`. Cited on page 50.

[99] ATLAS Collaboration, G. Aad *et al.*, "Performance of Missing Transverse Momentum Reconstruction in Proton-Proton Collisions at 7 TeV with ATLAS," *Eur.Phys.J.* **C72** (2012) 1844, `arXiv:1108.5602 [hep-ex]`. Cited on page 51 and 192.

[100] ATLAS SCT Collaboration, J. N. Jackson, "The ATLAS semiconductor tracker (SCT)," *Nucl.Instrum.Meth.* **A541** (2005) 89–95. Cited on page 53.

[101] A. Abdesselam, T. Akimoto, P. Allport, J. Alonso, B. Anderson, *et al.*, "The barrel modules of the ATLAS semiconductor tracker," *Nucl.Instrum.Meth.* **A568** (2006) 642–671. Cited on page 54.

[102] F. Campabadal, C. Fleta, M. Key, M. Lozano, C. Martinez, *et al.*, "Design and performance of the ABCD3TA ASIC for readout of silicon strip detectors in the ATLAS semiconductor tracker," *Nucl.Instrum.Meth.* **A552** (2005) 292–328. Cited on page 54 and 55.

[103] ATLAS Collaboration, A. Abdesselam *et al.*, "The ATLAS semiconductor tracker end-cap module," *Nucl.Instrum.Meth.* **A575** (2007) 353–389. Cited on page 54.

[104] ATLAS SCT Group, "ATLAS SCT Gallery – Detector Layout." `http://atlas.web.cern.ch/Atlas/GROUPS/INNER_DETECTOR/SCT/gallery/layout/sct_silicon.jpg`, Dec, 2002. Cited on page 54.

[105] A. Gorisek, "The ATLAS beam condition monitor commissioning," Tech. Rep. CERN-2008-008, 2008. Cited on page 54.

[106] V. Cindro, D. Dobos, I. Dolenc, H. Frais-Kolbl, H. Frais-Koelbl, *et al.*, "The ATLAS beam conditions monitor," *JINST* **3** (2008) P02004. Cited on page 55.

[107] F. Campabadal, C. Fleta, M. Key, M. Lozano, C. Martinez, *et al.*, "Beam tests of ATLAS SCT silicon strip detector modules," *Nucl.Instrum.Meth.* **A538** (2005) 384–407. Cited on page 55.

[108] K. Hara, M. Minagawa, T. Kuwano, K. Nakamura, Y. Nakamura, *et al.*, "Test of ATLAS SCT barrel modules with Nd:YAG laser," *Nucl.Instrum.Meth.* **A541** (2005) 122–129. Cited on page 55.

[109] K. Hara, T. Kuwano, G. Moorhead, Y. Ikegami, T. Kohriki, *et al.*, "Beam splash effects on ATLAS silicon microstrip detectors evaluated using 1-W Nd:YAG laser," *Nucl.Instrum.Meth.* **A541** (2005) 15–20. Cited on page 55.

[110] M. Fahrer, G. Dirkes, F. Hartmann, S. Heier, A. Macpherson, *et al.*, "Beam-loss-induced electrical stress test on CMS silicon strip modules," *Nucl.Instrum.Meth.* **A518** (2004) 328–330. Cited on page 57.

[111] R. Brun and F. Rademakers, "ROOT: An object oriented data analysis framework," *Nucl.Instrum.Meth.* **A389** (1997) 81–86. See also `http://root.cern.ch/`. Cited on page 58.

[112] W. Leo, *Techniques for Nuclear and Particle Physics Experiments: A How-To Approach*. U.S. Government Printing Office, 1994. `http://books.google.com/books?id=8VufE4SD-AkC`. Cited on page 60.

[113] P. Rose, A. Grillo, V. Fadeyev, E. Spencer, M. Wilder, *et al.*, "Simulation of the ATLAS SCT barrel module response to LHC beam loss scenarios," *JINST* **9** (2014) C03012. Cited on page 69.

[114] ATLAS Collaboration, G. Aad *et al.*, "Search for charged Higgs bosons decaying via $H^+ \to \tau\nu$ in top quark pair events using pp collision data at $\sqrt{s} = 7$ TeV with the ATLAS detector," *JHEP* **1206** (2012) 039, `arXiv:1204.2760 [hep-ex]`. Cited on page 71, 78, 110, 111, 113, and 194.

[115] F. del Aguila, J. de Blas, A. Carmona, and J. Santiago, "Neutrino physics beyond neutrino masses," *Fortsch.Phys.* **58** (2010) 675–681, `arXiv:1003.5799 [hep-ph]`. Cited on page 71.

[116] J. Valle, "Brief neutrino physics update," `arXiv:hep-ph/0310125 [hep-ph]`. Cited on page 71.

[117] R. N. Mohapatra and G. Senjanovic, "Neutrino Masses and Mixings in Gauge Models with Spontaneous Parity Violation," *Phys.Rev.* **D23** (1981) 165. Cited on page 71.

[118] M. Magg and C. Wetterich, "Neutrino Mass Problem and Gauge Hierarchy," *Phys.Lett.* **B94** (1980) 61. Cited on page 71.

[119] T. D. Lee, "A Theory of Spontaneous T Violation," *Phys. Rev. D* **8** (Aug, 1973) 1226–1239. Cited on page 72.

[120] A. Djouadi, "The Anatomy of electro-weak symmetry breaking. II. The Higgs bosons in the minimal supersymmetric model," *Phys.Rept.* **459** (2008) 1–241, `arXiv:hep-ph/0503173 [hep-ph]`. Cited on page 72.

[121] H. Haber, G. Kane, and T. Sterling, "The Fermion Mass Scale and Possible Effects of Higgs Bosons on Experimental Observables," *Nuclear Physics B* **161** no. 2-3, (1979) 493 – 532. Cited on page 72.

[122] J. F. Donoghue and L.-F. Li, "Properties of Charged Higgs Bosons," *Phys. Rev. D* **19** (Feb, 1979) 945–955. Cited on page 72.

[123] T. P. Cheng and M. Sher, "Mass-matrix Ansatz and Flavor Nonconservation in Models with Multiple Higgs Doublets," *Phys. Rev. D* **35** (Jun, 1987) 3484–3491. Cited on page 72.

[124] S. L. Glashow and S. Weinberg, "Natural Conservation Laws for Neutral Currents," *Phys. Rev. D* **15** (Apr, 1977) 1958–1965. Cited on page 72.

[125] N. G. Deshpande and E. Ma, "Pattern of Symmetry Breaking with Two Higgs Doublets," *Phys. Rev. D* **18** (Oct, 1978) 2574–2576. Cited on page 72.

[126] G. Branco, P. Ferreira, L. Lavoura, M. Rebelo, M. Sher, *et al.*, "Theory and phenomenology of two-Higgs-doublet models," *Phys.Rept.* **516** (2012) 1–102, `arXiv:1106.0034 [hep-ph]`. Cited on page 75.

[127] DELPHI Collaboration, J. Abdallah *et al.*, "Search for charged Higgs bosons at LEP in general two Higgs doublet models," *Eur.Phys.J.* **C34** (2004) 399–418, `arXiv:hep-ex/0404012 [hep-ex]`. Cited on page 75.

[128] CDF Collaboration and D0 Collaboration, P. Gutierrez, "Review of charged Higgs searches at the Tevatron," *PoS* **CHARGED2010** no. FERMILAB-CONF-10-540-E, (2010) 004. Cited on page 75, 76, and 193.

[129] A. G. Holzner, "Searches for charged Higgs bosons at LEP," `arXiv:hep-ex/0105045 [hep-ex]`. Cited on page 75.

[130] CDF Collaboration, T. Aaltonen *et al.*, "Search for charged Higgs bosons in decays of top quarks in $p\bar{p}$ collisions at $\sqrt{s} = 1.96\,\text{TeV}$," *Phys.Rev.Lett.* **103** (2009) 101803, `arXiv:0907.1269 [hep-ex]`. Cited on page 75 and 76.

[131] CDF Collaboration, R. Eusebi, A. Hocker, and P. Tipton, "A search of charged Higgs in the decay products of pair-produced top quarks,". `http://www-cdf.fnal.gov/physics/new/top/2005/ljets/charged_higgs/higgs/V2/HiggsAnalysis_publicV2.html`. Cited on page 75 and 76.

[132] D0 Collaboration, "A search for charged Higgs boson in $t\bar{t}$ events,".

http://www-d0.fnal.gov/Run2Physics/WWW/results/prelim/TOP/T70/. Cited on page 75.

[133] CLEO Collaboration, Chen, S. and others, "Branching Fraction and Photon Energy Spectrum for $b \to s\gamma$," *Phys. Rev. Lett.* **87** (Dec, 2001) 251807. http://link.aps.org/doi/10.1103/PhysRevLett.87.251807. Cited on page 77.

[134] Belle Collaboration, P. Koppenburg *et al.*, "Inclusive Measurement of the Photon Energy Spectrum in $b \to s\gamma$ Decays," *Phys. Rev. Lett.* **93** (Aug, 2004) 061803. http://link.aps.org/doi/10.1103/PhysRevLett.93.061803. Cited on page 77.

[135] BABAR Collaboration, B. Aubert *et al.*, "Measurements of the $B \to X_s\gamma$ branching fraction and photon spectrum from a sum of exclusive final states," *Phys.Rev.* **D72** (2005) 052004, arXiv:hep-ex/0508004 [hep-ex]. Cited on page 77.

[136] BaBar Collaboration, J. Lees *et al.*, "Evidence for an excess of $\bar{B} \to D^{(*)}\tau^-\bar{\nu}_\tau$ decays," *Phys.Rev.Lett.* **109** (2012) 101802, arXiv:1205.5442 [hep-ex]. Cited on page 77.

[137] A. Martyniuk and U.-k. Yang, *A Search for a Light Charged Higgs Boson Decaying to $c\bar{s}$ at $\sqrt{s} = 7$ TeV*. PhD thesis, Manchester U., 2011. Presented 28 Oct 2011. Cited on page 78.

[138] T. Sjostrand, S. Mrenna, and P. Z. Skands, "PYTHIA 6.4 Physics and Manual," *JHEP* **0605** (2006) 026, arXiv:hep-ph/0603175 [hep-ph]. Cited on page 80.

[139] G. Corcella, I. Knowles, G. Marchesini, S. Moretti, K. Odagiri, *et al.*, "HERWIG 6: An Event generator for hadron emission reactions with interfering gluons (including supersymmetric processes)," *JHEP* **0101** (2001) 010, arXiv:hep-ph/0011363. Cited on page 80.

[140] J. Butterworth, J. R. Forshaw, and M. Seymour, "Multiparton interactions in photoproduction at HERA," *Z. Phys. C* **72** (1996) 637, arXiv:hep-ph/9601371. Cited on page 80.

[141] S. Frixione and B. R. Webber, "Matching NLO QCD computations and parton shower simulations," *JHEP* **0206** (2002) 029, arXiv:hep-ph/0204244. Cited on page 80.

[142] Tevatron Electroweak Working Group, CDF Collaboration, D0 Collaboration, "Combination of CDF and D0 Results on the Mass of the Top Quark," arXiv:0808.1089 [hep-ex]. Cited on page 80.

[143] M. Aliev, L. H, U. Langenfeld, S. Moch, P. Uwer, and M. Widermann, "HATHOR – HAdronic Top and Heavy quarks crOss section calculatoR," *Comput. Phys. Commun.* **182** (2011) 1034, arXiv:hep-ph/1007.1327. Cited on page 80.

[144] H. L. Lai *et al.*, "New parton distributions for collider physics," *Phys. Rev. D* **82** (2010) 074024, arXiv:1007.2241 [hep-ph]. Cited on page 80.

[145] M. Guzzi, P. Nadolsky, E. Berger, H.-L. Lai, F. Olness, *et al.*, "CT10 parton distributions and other developments in the global QCD analysis," arXiv:1101.0561 [hep-ph]. Cited on page 80.

[146] S. Frixione, E. Laenen, P. Motylinski, and B. R. Webber, "Single-top production in MC@NLO," *JHEP* **0603** (2006) 092, arXiv:hep-ph/0512250 [hep-ph]. Cited on page 80.

[147] J. Alwall, P. Demin, S. de Visscher, R. Frederix, M. Herquet, *et al.*, "MadGraph/MadEvent v4: The New Web Generation," *JHEP* **0709** (2007) 028, arXiv:0706.2334 [hep-ph]. Cited on page 80.

[148] B. P. Kersevan and E. Richter-Was, "The Monte Carlo event generator AcerMC version 2.0 with interfaces to PYTHIA 6.2 and HERWIG 6.5," arXiv:hep-ph/0405247. Cited on page 80.

[149] S. Mandelstam, "Determination of the pion - nucleon scattering amplitude from dispersion relations and unitarity. General theory," *Phys.Rev.* **112** (1958) 1344–1360. Cited on page 80.

[150] N. Kidonakis, "Next-to-next-to-leading-order collinear and soft gluon corrections for t-channel single top quark production," *Phys. Rev. D* **83** (2011) 091503. Cited on page 80.

[151] N. Kidonakis, "Next-to-next-to-leading logarithm resummation for s-channel single top quark production," *Phys. Rev. D* **81** (2010) 054028. Cited on page 80.

[152] N. Kidonakis, "Two-loop soft anomalous dimensions for single top quark associated production with a W^- or H^-," *Phys. Rev. D* **82** (2010) 054018. Cited on page 80, 121, and 133.

[153] M. L. Mangano, M. Moretti, F. Piccinini, R. Pittau, and A. D. Polosa, "ALPGEN, a generator for hard multiparton processes in hadronic collisions," *JHEP* **0307** (2003) 001, `arXiv:hep-ph/0206293`. Cited on page 80.

[154] J. Pumplin, D.R. Stump, J. Huston, H.L. Lai, P. Nadolsky and W.K. Tung, "New Generation of Parton Distributions with Uncertainties from Global QCD Analysis," *JHEP* **07** (2002) 012. Cited on page 80.

[155] R. Gavin, Y. Li, F. Petriello, and S. Quackenbush, "W physics at the LHC with FEWZ 2.1," `arXiv:hep-ph/1201.5896`. Cited on page 81.

[156] R. Gavin, Y. Li, F. Petriello, and S. Quackenbush, "FEWZ 2.0: A code for hadronic Z production at next-to-next-to-leading order," *Comput. Phys. Commun.* **182** (2011) 2388, `arXiv:hep-ph/1011.3540`. Cited on page 81 and 121.

[157] J. Campbell, R. K. Ellis, and C. Williams, "Vector boson pair production at the LHC," *JHEP* **1107** (2011) 018, `arXiv:1105.0020`. Cited on page 81 and 133.

[158] Z. Was and P. Golonka, "TAUOLA as tau Monte Carlo for future applications," *Nucl. Phys. Proc. Suppl.* **144** (2005) 88. Cited on page 81.

[159] S. Sekula, "tau(had) + jets: Object and Event Selection." Private communication, Nov, 2011. Cited on page 85.

[160] R. K. Ellis, W. J. Stirling, and B. Webber, "QCD and collider physics," *Camb.Monogr.Part.Phys.Nucl.Phys.Cosmol.* **8** (1996) 1–435. Cited on page 90.

[161] D. Eriksson, G. Ingelman, J. Rathsman, and O. Stal, "New angles on top quark decay to a charged Higgs," *JHEP* **0801** (2008) 024, `arXiv:0710.5906 [hep-ph]`. Cited on page 90.

[162] "Jet Charge Studies with the ATLAS Detector Using $\sqrt{s} = 8$ TeV Proton-Proton Collision Data," Tech. Rep. ATLAS-CONF-2013-086, CERN, Geneva, Aug, 2013. Cited on page 93.

[163] P. Assamagan, C. Bernius, P. Casado, V. Cavaliere, P. Czodrowski, D. Chakraborty, D. Greenwood, A. Ferrari, M. Flechl, S. Hattrem Raddum, A. Kopp, P. Mal, A. McCarn, M. Neubauer, N. Patel, A. Randle-Conde, A. L. Read, G. Rocha de Lima, A. Saavedra, M. Schumacher, and S. Sekula, "Search for charged Higgs bosons in the $\tau_{\text{had}}+$jets final state in $t\bar{t}$ decays with $4.6\,\text{fb}^{-1}$ of pp collision data recorded at $\sqrt{s} = 7$ TeV with the ATLAS Experiment — Supporting

Note," Tech. Rep. ATL-COM-PHYS-2012-082, CERN, Geneva, Jan, 2012. Cited on page 99, 100, 194, and 198.

[164] S. Behar, C. Buszello, P. Czodrowski, A. Ferrari, M. Flechl, S. Hattrem Raddum, C. Isaksson, A. Madsen, A. McCarn, M. zur Nedden, M. Neubauer, N. Patel, D. Pelikan, A. Read, Y. Rozen, and A. Saavedra, "Search for a charged Higgs boson decaying via $H^+ \to \tau_{\text{had}} + \nu$ in $t\bar{t}$ events with one light lepton in the final state using events using $4.6\,\text{fb}^{-1}$ of pp collision data recorded at $\sqrt{s} = 7$ TeV with the ATLAS detector — Supporting note," Tech. Rep. ATL-COM-PHYS-2012-083, CERN, Geneva, Jan, 2012. Cited on page .

[165] P. Czodrowski and A. Straessner, *Search for Charged Higgs Bosons with the ATLAS Detector at the LHC*. PhD thesis, Dresden, Tech. U., Dresden, Jul, 2013. Presented 18 Jul 2013. Cited on page 106.

[166] ATLAS Collaboration, "Measurement of the Mis-identification Probability of τ Leptons from Hadronic Jets and from Electrons," Tech. Rep. ATLAS-CONF-2011-113, ATLAS-COM-CONF-2011-067, 2011. Cited on page 106.

[167] Bedikian, S and Czodrowski, P and Demers, S and Kraus, J and Kroseberg, J and Mader, W and Prudent, X and Straessner, A, "Determination of the Electron-Tau Mis-identification Probability with a Tag-and-Probe Method," Tech. Rep. ATL-COM-PHYS-2011-188, CERN, Geneva, Feb, 2011. `https://cdsweb.cern.ch/record/1331802`. Supporting Document for ATLAS-CONF-2011-113. Cited on page 106.

[168] ATLAS Tau Working Group, "Systematics for Electron Misidentification Probability." `https://twiki.cern.ch/twiki/bin/viewauth/AtlasProtected/TauSystematicsWinterConf2012#Systematics_for_Electron_Misiden`, Dec, 2011. NB. These correction factors and uncertainties can be used for physics analyses. We do not preclude updates to these numbers, and continue to look for ways to improve the measurement. Cited on page 108 and 198.

[169] G. Cowan, K. Cranmer, E. Gross, and O. Vitells, "Asymptotic formulae for likelihood-based tests of new physics," *Eur.Phys.J.* **C71** (2011) 1554, `arXiv:1007.1727 [physics.data-an]`. Cited on page 112.

[170] A. L. Read, "Presentation of search results: The CL(s) technique," *J.Phys.* **G28** (2002) 2693–2704. Cited on page 112.

[171] T. Junk, "Confidence level computation for combining searches with small statistics," *Nucl.Instrum.Meth.* **A434** (1999) 435–443, `arXiv:hep-ex/9902006 [hep-ex]`. Cited on page 112.

[172] M. Flechl, S. Hattrem Raddum, and A. Read, "Combined limits for $H^+ \to \tau\nu$ in $t\bar{t}$ decays with 4.6 fb^{-1} of pp collision data recorded at $\sqrt{s} = 7$ TeV with the ATLAS experiment — Supporting Note," Tech. Rep. ATL-PHYS-INT-2012-044, CERN, Geneva, Apr, 2012. Cited on page 114.

[173] D0 Collaboration, V. Abazov *et al.*, "Search for charged Higgs bosons in top quark decays," *Phys.Lett.* **B682** (2009) 278–286, `arXiv:0908.1811 [hep-ex]`. Cited on page 114.

[174] K. Finelli, *An Inclusive Analysis of Top Quark Pair, W Boson Pair, and Drell-Yan Tau Lepton Pair Production in the Dilepton Final State from Proton-Proton Collisions at Center-of-Mass Energy 7 TeV with the ATLAS Detector*. PhD thesis, Duke U., Aug, 2013. Presented 21 Aug 2013. Cited on page 117 and 132.

[175] S. Carron, D. Benjamin, M. Coca, and M. Kruse, "A global analysis of the high-pT dilepton sample using 360 pb-1 of run 2 data," *CDF Public Note* **8146** (2006) 1. Cited on page 117.

[176] CDF Collaboration, A. Abulencia *et al.*, "Cross section measurements of high-p_T dilepton final-state processes using a global fitting method," *Phys. Rev. D* **78** (Jul, 2008) 012003. Cited on page 117.

[177] ATLAS Collaboration, "New ATLAS event generator tunes to 2010 data," Tech. Rep. ATL-PHYS-PUB-2011-008, ATL-COM-PHYS-2011-329, 2011. Cited on page 120.

[178] B. Acharya *et al.*, "Object selection and calibration, background estimations and MC samples for the Summer 2012 Top Quark analyses with 2011 data," Tech. Rep. ATL-COM-PHYS-2012-499, CERN, Geneva, May, 2012. Cited on page 120, 124, 130, 132, and 134.

[179] ATLAS Collaboration, "ATLAS tunes of PYTHIA 6 and Pythia 8 for MC11," tech. rep., 2011. Cited on page 120.

[180] D. Stump, J. Huston, J. Pumplin, W.-K. Tung, H. Lai, *et al.*, "Inclusive jet production, parton distributions, and the search for new physics," *JHEP* **0310** (2003) 046, `arXiv:hep-ph/0303013 [hep-ph]`. Cited on page 120.

[181] ATLAS Collaboration, "New ATLAS event generator tunes to 2010 data," Tech. Rep. ATL-PHYS-PUB-2011-008, CERN, Geneva, Apr, 2011. Cited on page 120.

[182] M. Czakon and A. Mitov, "Top++: A Program for the Calculation of the Top-Pair Cross-Section at Hadron Colliders," `arXiv:1112.5675 [hep-ph]`. Cited on page 121.

[183] T. Gleisberg *et al.*, "Event generation with SHERPA 1.1," *JHEP* **02** (2009) 007. Cited on page 121.

[184] J. Butterworth, E. Dobson, U. Klein, B. Mellado Garcia, T. Nunnemann, J. Qian, D. Rebuzzi, and R. Tanaka, "Single Boson and Diboson Production Cross Sections in pp Collisions at $\sqrt{s} = 7\,\text{TeV}$," Tech. Rep. ATL-COM-PHYS-2010-695, CERN, Geneva, Aug, 2010. Cited on page 121.

[185] J. Campbell, E. Castaneda-Miranda, Y. Fang, N. Kauer, B. Mellado, *et al.*, "Normalizing Weak Boson Pair Production at the Large Hadron Collider," *Phys.Rev.* **D80** (2009) 054023, `arXiv:0906.2500 [hep-ph]`. Cited on page 121.

[186] A. Martin, W. Stirling, R. Thorne, and G. Watt, "Parton distributions for the LHC," *Eur.Phys.J.* **C63** (2009) 189–285, `arXiv:0901.0002 [hep-ph]`. Cited on page 121.

[187] F. James and M. Roos, "Minuit: A System for Function Minimization and Analysis of the Parameter Errors and Correlations," *Comput.Phys.Commun.* **10** (1975) 343–367. Cited on page 129.

[188] ATLAS Collaboration, "Jet energy resolution and selection efficiency relative to track jets from in-situ techniques with the ATLAS Detector Using Proton-Proton Collisions at a Center of Mass Energy $\sqrt{s} = 7\,\text{TeV}$," Tech. Rep. ATLAS-CONF-2010-054, ATLAS-COM-CONF-2010-056, 2010. `https://cds.cern.ch/record/1281311`. Cited on page 130.

[189] ATLAS Collaboration, G. Aad *et al.*, "Jet energy measurement with the ATLAS detector in proton-proton collisions at $\sqrt{s} = 7$ TeV," *Eur.Phys.J.* **C73** (2013) 2304, `arXiv:1112.6426 [hep-ex]`. Cited on page 131 and 198.

[190] G. Romeo, A. Schwartzman, R. Piegaia, T. Carli, and R. Teuscher, "Jet Energy Resolution from In-situ Techniques with the ATLAS Detector Using Proton-Proton Collisions at a Center of Mass Energy $\sqrt{s} = 7$ TeV," Tech. Rep. ATL-COM-PHYS-2011-240, CERN, Geneva, Mar, 2011. Cited on page 131.

[191] R. D. Ball, V. Bertone, S. Carrazza, C. S. Deans, L. Del Debbio, *et al.*, "Parton distributions with LHC data," *Nucl.Phys.* **B867** (2013) 244–289, `arXiv:1207.1303 [hep-ph]`. Cited on page 132.

[192] ATLAS Collaboration, G. Aad *et al.*, *Expected performance of the ATLAS experiment: detector, trigger and physics*. CERN, Geneva, 2009. Cited on page 132.

[193] K. Bierwagen, U. Blumenschein, J. F. Grivaz, T. Kanno, S. Meeham, M. Sandhoff, J. Sauvan, and A. Quadt, "Measurement of the cross section for jets produced in association with Z bosons," Tech. Rep. ATL-COM-PHYS-2012-735, CERN, Geneva, Jun, 2012. Cited on page 133.

[194] B. Abi, S. Allwood-Spiers, W. H. Bell, G. Brooijmans, C. Buttar, V. Dao, J. Ferrando, D. E. Ferreira de Lima, K. J. Grahn, J. M. Katzy, A. Khanov, L. Mijović, F. Rizatdinova, M. Saleem, F. Spano, and D. Urbaniec, "Measurement of the jet multiplicity differential cross section in di-lepton decays of $t\bar{t}$ events with the ATLAS detector.," Tech. Rep. ATL-COM-PHYS-2011-1742, CERN, Geneva, Dec, 2011. Cited on page 134.

[195] ATLAS Collaboration, G. Aad *et al.*, "Measurement of the cross section for top-quark pair production in pp collisions at $\sqrt{s} = 7$ TeV with the ATLAS detector using final states with two high-pt leptons," *JHEP* **1205** (2012) 059, `arXiv:1202.4892 [hep-ex]`. Cited on page 139.

[196] ATLAS Collaboration, "$Z \to \tau\tau$ cross section measurement in proton-proton collisions at 7 TeV with the ATLAS experiment," Tech. Rep. ATLAS-CONF-2012-006, CERN, Geneva, Feb, 2012. Cited on page 139.

[197] ATLAS Collaboration, G. Aad *et al.*, "Measurement of W^+W^- production in pp collisions at $\sqrt{s} = 7$ TeV with the ATLAS detector and limits on anomalous WWZ and $WW\gamma$ couplings," *Phys.Rev.* **D87** (2013) 112001, `arXiv:1210.2979 [hep-ex]`. Cited on page 139.

[198] F. James, *Statistical methods in experimental physics*. No. ISBN-9789812567956. World Scientific Publishing Company, Incorporated, 2006. `http://books.google.com/books?id=S8N_QgAACAAJ`. Cited on page 140.

List of Figures

List of Tables